University of Nottingham
UK | CHINA | MALAYSIA

Topographical and chemical characterisation of temperature controlled on-surface reactions

Michael Clarke, MSc (Hons)

Thesis submitted to the University of Nottingham
for the degree of Doctor of Philosophy

School of Physics and Astronomy
University of Nottingham
October 2024

Abstract

On-surface synthesis, the process of producing covalently bonded structures from molecular building blocks confined on a surface, is a research theme worthy of investigation as it offers a route towards the fabrication of nanoscale two-dimensional devices. Alongside the potential applications within the burgeoning field of nanoelectronics, confining materials to surfaces allows the use of a variety of surface analysis techniques. Scanning probe microscopy, for example, can reveal with unrivalled detail mechanistic information about the progress of reactions in general. Developing our understanding of these processes can allow for the formation of more precise and complex structures 'on-surface' and may pave the way for developing new methodologies within solution phase synthesis.

In this thesis, a variety of molecular species, confined to two-dimensions by supporting substrates, are investigated, and the self-assembled structures formed following deposition, and subsequent temperature-induced reaction steps, are characterised. Particular emphasis is placed on Ullmann-type coupling reactions, a versatile and oft-utilised route to covalent bonding on surfaces. The work described within this thesis takes place predominantly under ultra-high vacuum (UHV) conditions, utilising a variety of surface-sensitive techniques: primarily scanning tunnelling microscopy (STM), but also X-ray spectroscopy techniques such as X-ray photoelectron spectroscopy (XPS), near-edge X-ray absorption spectroscopy (NEXAFS) and X-ray standing wave (XSW) analysis. Each of the chapters describing the experimental results aims to develop our understanding of the mechanisms underlying the behaviours of molecules on surfaces and particularly on the kinetic properties of reactions, in order to better facilitate more efficient and selective synthetic pathways.

The species covered in this thesis span a broad range, and demonstrate the

breadth of utility for this type of 'surface science' based approach. Firstly, the formation of a polymer based upon a diketopyrrolopyrrole (DPP) is studied. This monomer unit possesses aryl-halide groups to facilitate on-surface covalent coupling and is functionalised with alkyl chains which drive the self-assembly of both the monomer material prior to reaction and the domains of polymeric material following on-surface synthesis. The self-assembled structure of close-packed domains of the monomer units, and the ordered polymers, are investigated and characterised using STM and XPS.

Secondly, two groups of larger molecular species are investigated: a series of porphyrin-based nanorings, and porphyrin-doped polymer chains, which serve as a precursor to a target porphyrin-graphene nanoribbon. Both are formed *via* novel in-solution synthesis, and require vital on-surface characterisation to accompany the in-solution chemistry and to confirm the successful synthesis of these materials. Both are investigated *via* STM, with morphological characterisation of the nanorings *via* this technique crucial to understanding the cyclic structure and flexibility of the molecules. For the graphitic nanoribbon species, our focus is the inclusion of porphyrin species within graphene nanoribbons to create porphyrin-fused graphene nanoribbons (PGNRs). A combination of scanning tunnelling microscopy (STM) and photoelectron spectroscopy (PES) techniques are used to characterise the novel porphyrin-fused graphene nanoribbon. This nanoribbon is formed on-surface from a linear polymer consisting of regularly spaced Ni-porphyrin units linked by sections of aryl rings which fuse together during the reaction to form graphitic regions between neighbouring Ni-porphyrin units.

Lastly, a temperature-programmed PES study of brominated tetraphenyl porphyrin is conducted, with a novel Arrhenius analysis opening a pathway to empirical measurement of kinetic properties of reactions. This is enabled *via* temperature-controlled continuous XPS measurement, and the reaction is also characterised by stepwise STM, NEXAFS and XPS. A comparison is made between the properties of the Ullmann-type coupling reaction on both Au(111) and Cu(111) surfaces.

The work described in this thesis develops atop the existing literature for the stepwise analysis of surface-confined covalent reactions, and demonstrates the

flexibility of surface-confined techniques such as STM for their unrivalled molecular resolution. The combination of STM with X-ray spectroscopic techniques underpins much of the work and displays the strength of combined topographic and chemical characterisation when analysing the evolution of a system, and demonstrates novel ways in which these techniques can be used to further our understanding of on-surface synthesis.

List of Publications

1. *On-surface polymerisation and self-assembly of DPP-based molecular wires* - **M. Clarke**, A. Bellamy-Carter, F. Malagreca, J. Hart, S. P. Argent, J. N. O'Shea, D. B. Amabilino and A. Saywell, Mol. Syst. Des. Eng., 2023, 8, 681–689. DOI https://doi.org/10.1039/D2ME00232A

2. *Template-Directed Synthesis of Strained meso-meso-Linked Porphyrin Nanorings* - J. M. Van Raden, J. R. Deng, H. Gotfredsen, J. Hergenhahn, **M. Clarke**, M. Edmondson, J. Hart, J. N. O'Shea, F. Duarte, A. Saywell and H. L. Anderson, Angew. Chemie - Int. Ed., 2024
DOI https://doi.org/10.1002/anie.202400103

3. *Bending a Photonic Wire Into a Ring* - H. Gotfredsen, J.-R. Deng, J. Raden, M. Righetto, J. Hergenhahn, **M. Clarke**, A. Bellamy-Carter, J. Hart, J. O'Shea, T. Claridge, F. Duarte, A. Saywell, L. Herz and H. Anderson, Nature Chemistry, 14, 1436–1442, 2022. DOI https://doi.org/10.1038/s41557-022-01032-w

4. *Covalent Template-Directed Synthesis of a Spoked 18-Porphyrin Nanoring* - M. A. Majewski, W. Stawski, J. M. Van Raden, **M. Clarke**, J. Hart, J. N. O'Shea, A. Saywell and H. L. Anderson, Angew. Chemie - Int. Ed., 2023, DOI https://doi.org/10.1002/anie.202302114

5. *Porphyrin-fused graphene nanoribbons* - Q. Chen, A. Lodi, H. Zhang, A. Gee, H. I. Wang, F. Kong, **M. Clarke**, M. Edmondson, J. Hart, J. N. O'Shea, W. Stawski, J. Baugh, A. Narita, A. Saywell, M. Bonn, K. Müllen, L. Bogani and H. L. Anderson, Nat. Chem., 2024, 16, 1133–1140. DOI https://doi.org/10.1038/s41557-024-01477-1

6. *On-surface synthesis of Ni-porphyrin doped graphene nanoribbons* - M. Edmondson, **M. Clarke**, J. O'Shea, Q. Chen, H.L. Anderson and A. Saywell, *ACS Nano*, DOI:10.1021/acsnano.4c09188.

7. *Inter- and intra-molecular on-surface synthesis: covalent coupling and ring-closing on Au(111) and Cu(111)* - E.S. Frampton, **M. Clarke**, M. Edmondson, A. Gray, J. Bradford, L. Warwick, and A. Saywell - in preparation.

8. *Experimental Demonstration of a Spectral Fingerprint for the Saddle and Inverted Conformations of Porphyrins on Copper* - E.S. Frampton, **M. Clarke**, M. Edmondson, A. Gray, J. Bradford, D.A. Duncan, A. Preobrajenski, and A. Saywell - Submitted to Chem Comm.

9. *At Which Temperature Does a Reaction Occur?* - **M. Clarke**, Eleanor S. Frampton, M. Edmondson, A. Gray, J. Bradford, L. Warwick, and A. Saywell - in preparation.

Acknowledgements

I would like to open the acknowledgments by thanking my Supervisor, Alex, who ensured that my PhD was overall an enjoyable experience and provided a great deal of professional guidance. On top of his great depth of understanding in the field of nanoscience, he is an excellent teacher and has helped me wrap my head around topics that quite frankly would otherwise be beyond me. Most importantly, Alex has been a thoroughly decent and understanding person, sometimes a rare quality in an academic supervisor, and I hold him in the highest esteem as an individual.

Everyone in the nanoscience group has been great to work with, and I can honestly say that my colleagues have been the best part of my PhD experience. If only every workplace had such wonderful people as Felipe, Connor, Will, Sofia, and Tyler (also Freddie it was nice to meet you). The other senior academics, Phil and Brian (particularly Phil thanks to his guidance during my end of year reports) have also been very helpful and instructive. Special mention has to go to the wonderful people of the Saywell group, principally Matt, who taught me more or less everything I know, plus a bunch of extra stuff I have forgotten. Ailish, Liv and Joe have brought a lot of much-needed variety and enthusiasm into C20 which previously consisted of me and Matt sitting around grumbling; truly three absolute gems.

Other people in physics I really need to thank are Abi, who was extremely supportive and helpful during my first year when I really had absolutely no clue, Ellie, who's been kind enough to host us at MAXIV on multiple occasions and whose hallon-catching abilities are the stuff of legend, and David, who was generous enough to give me eons of beamtime experience and countless (often repeated) instruction on how the machines actually work.

I would also like to thank my mom, who has been a rock as always, and my brother, who I would probably still like even if we weren't related. I must most importantly thank my partner Klara, who has made these years the happiest of my life.

Contents

Chapter 1

Introduction

1.1 Motivation for the study of on-surface synthesis

When you tell people you're doing a PhD in nanoscience, they are generally impressed. Nanoscience and the quantum world have been lodged firmly in the public zeitgeist as an exciting area of physics, encouraged by speculative media reeling off a litany of stories telling of dizzying multiverses and hi-tech nanobots. While the reality may be a far cry from the snappy dialogue and tremendous spectacle of a blockbuster film, there is little doubt that nanoscience is a field that captures the imagination. Thankfully the field is also very interesting in practical terms too, as many of the day-to-day accomplishments do indeed resemble the spectacular imaginings of science fiction; much as the touch screens and wireless communication found decades earlier in Star Trek now proliferate in everyday life, so too has single-atom resolution become a commonplace feature in the world of nanoscience.

For me, fundamentally, the capacity of a device like a scanning tunnelling microscope (STM) to image individual atoms is truly exciting. Scanning probe microscopy (SPM) is one of a family of techniques that boast impressive spatial resolution, on the order of picometers, allowing for topographic characterisation at an atomic scale previously thought impossible. First achieved in 1983, [1] this defining achievement still impresses today, and is further built upon by our

capacity for single atom manipulation; the famous writing of IBM *via* using single atoms as individual pixels in 1990 [2] led to a multitude of works speculating on lego-style brick-by-brick molecular construction. Whilst this is not quite how chemistry works, the idea of bottom-up (meaning assembly of a larger whole from smaller building blocks) on-surface molecular fabrication is an idea that has led to impressive results, with SPM playing an extremely important role in characterising (and sometimes helping to drive) the development of these on-surface processes. Figure 1.1 demonstrates the multi-step, bottom-up assembly of a graphene nanoribbon, and the capacity of CO functionalised atomic force microscopy (AFM) tips to image individual chemical bonds. The step-by-step approach shown in Figure 1.1a) demonstrates a particularly impressive example of the power of tuning molecular structure and chemistry specifically for on-surface synthesis. Each step of the reaction shown in figure 1.1a) can be characterised with SPM, allowing for a detailed understanding of exactly which steps happen when, illuminating intermediate reaction steps in a way simply not possible on the single-molecule level within in-solution chemistry. Even spectroscopic techniques, which can be used to measure the development of a reaction in real time, cannot provide the level of single-molecule understanding available to STM. The true strength of STM lies in the ability to image the target molecule at each stage of a reaction and understand the chemical developments on a topographic level. Whether it be individual atoms atop surfaces, such as in the case of the IBM spelling (Figure 1.2a)), or the subtle corrugations of the Au(111) herringbone reconstruction (Figure 1.2b)), STM can reveal topographic and intra-molecular details that other techniques cannot. Figure 1.2c) demonstrates the capacity of STM to resolve not only the underlying surface reconstruction, but also atomic resolution of deposited S atoms, revealing a subtle interaction effect between the supporting substrate and the deposited species. Figure 1.2d-f) demonstrates the capacity for STM to capture in precise detail the formation of extended polymer networks on different surfaces, creating insight into the behaviour and reactivity of different substrate materials with respect to reaction progress. Indeed, individual monomers can be resolved inside the polymer structures, giving a clearer picture on how the reaction progresses.

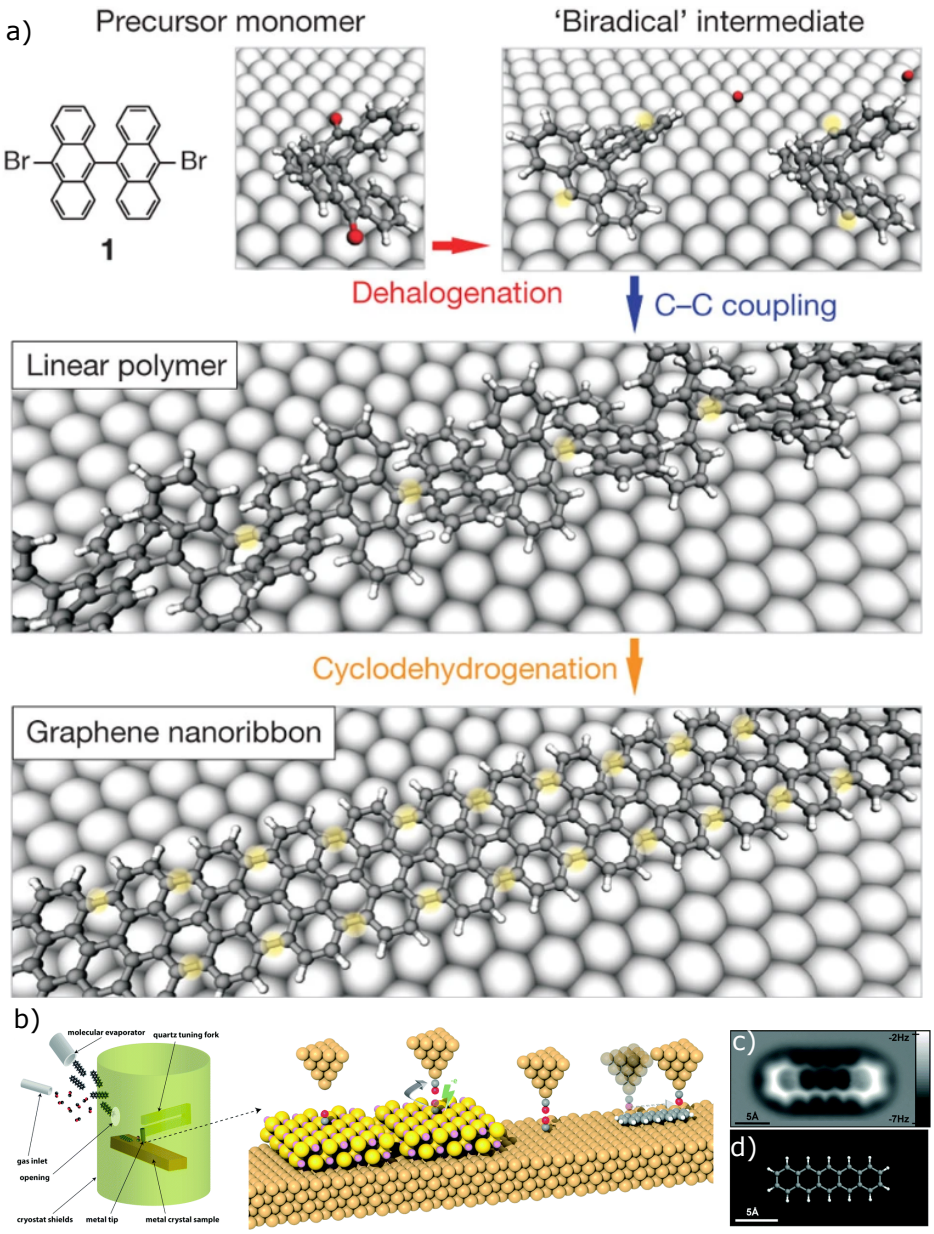

Figure 1.1: a) Step-by-step depiction of the bottom-up synthesis of a graphene nanoribbon. Taken from Cai *et al.* [3] The steps of molecular deposition, tip preparation and imaging of the molecule shown in b), taken from Sweetman *et al.*. [4] c) Constant height AFM image of pentacene (shown in d)), taken with a CO functionalised tip. Taken from Gross *et al.*. [5]

In order to successfully perform these bottom-up assemblies, and to fabricate target devices, such as nanowires, [9] transistors, [10] or even single-atom bits, [11] an understanding of the molecular system must be developed. This begins with the self-assembled structures formed by the deposited molecules. Described by Nobel laureate Jean-Marie Lehn as "chemistry beyond the molecule", [12] self-

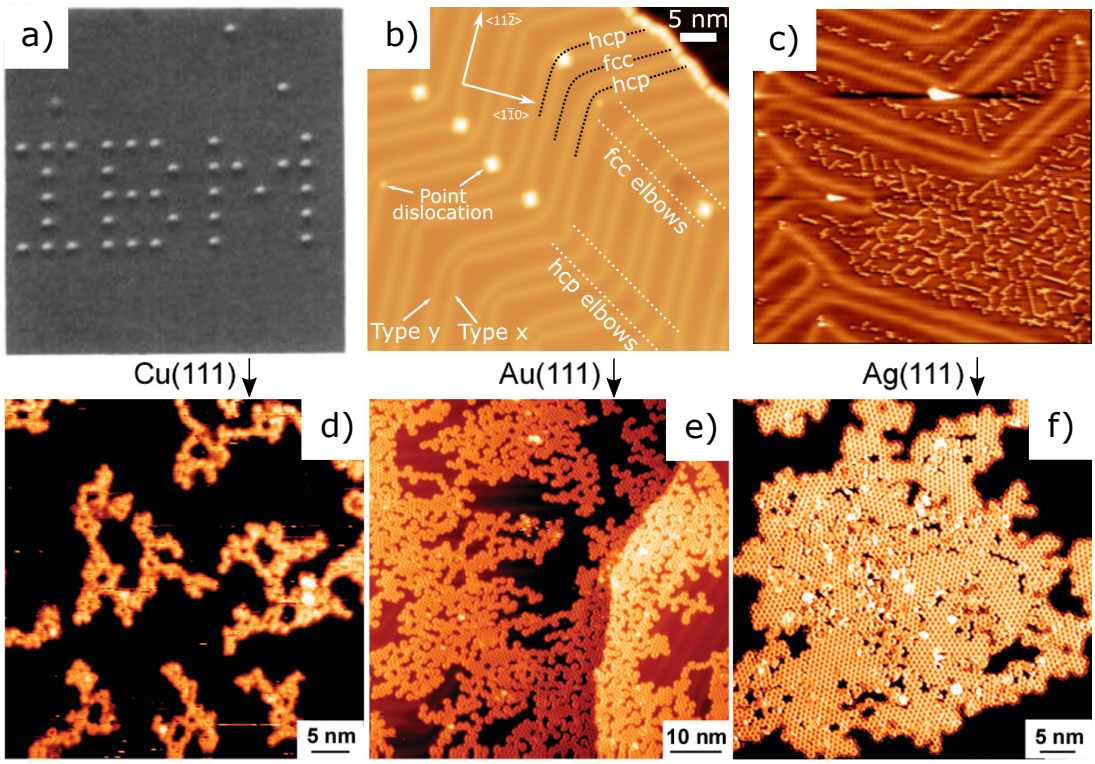

Figure 1.2: a) IBM spelled out using individual Argon atoms on Nickel substrate, captured with STM. Taken from Eigler *et al.* [2] b) The various features of the Au(111) herringbone reconstruction labelled, captured with STM. Taken from Edmondson *et al.* [6] c) The impact of deposited sulphur atoms on the herringbone of Au(111), captured with STM. Taken from Walen *et al.* [7] d) Overview STM images of extended polymer networks on Cu(111), Au(111), and Ag(111). Taken from Bieri *et al.* [8]

assembled structures are of great interest in their own right, informing the behaviour of molecular crystals and soft-matter systems as well as influencing further steps in any on-surface reaction. [13] Of course, following this self-assembled stage, formation of a covalent bond is desirable, as a practical route towards a more thermally stable product. Covalent bonds are important for most practical nanoscience applications, providing a sturdy framework for most nanoscale products, from the nanoribbons shown in Figure 1.1a), to the molecular machines that won Sauvage, Stoddardt and Feringa the Nobel Prize in 2016. [14] A popular choice is the Ullmann-type coupling reaction (see dehalogenation and C-C coupling steps in Fig. 1.1a). In simple terms, the Ullmann-type coupling reaction requires a halogenated precursor to be heated; at a specific temperature,

the halogen-carbon bond will cleave, and two dehalogenated molecules will bond to form a new carbon-carbon chemical bond. The temperature at which this occurs can be tuned by the choice of substrate, halogen or indeed the molecular structure. [15] While the broad brush strokes are understood, there is still much to be determined about this often employed methodology of on-surface covalent bonding.

Frequently, within published literature of on-surface reactions, the temperature at which the reaction occurs is listed. From an experimentalist's point of view this is sensible, as temperatures are relatively straightforward to measure and in principle provide sufficient detail for an experiment to be reproduced (a fundamental tenet of the scientific method). However, this is problematic for a few reasons. Firstly, the inherent complications of measuring temperatures of a sample *in-situ* in a UHV system render these reported temperatures unreliable, with temperatures recorded close-to but not at the position of the sample being investigated. Another key issue is that sample heating rate affects the temperature at which a reaction reaches maximum rate; [16] the different heating setups in each system could lead to starkly different ramp rates, and details of temperature ramp rates and annealing times are rarely reported within published scientific literature. Each of these factors can affect reaction progress and deprive a stated "reaction temperature" of meaning. If activation energies for reactions are stated, they are usually calculated *via* density functional theory (DFT) computational approaches (such as nudged elastic band (NEB DFT), to be described in more detail in section 2.2.3.), which while an extremely useful and versatile tool, should be informed by experimental data, not taken to be a 'black-box' with universal predictive powers. Ultimately, to gain deeper insight into reaction pathways, it is useful to develop a picture of the morphological and chemical changes to a system as the reaction progresses. This is why, in this thesis, I focus on the marriage of STM with chemically sensitive spectroscopic techniques, in order to develop a thorough understanding of reaction development. The aim of this thesis is to improve the understanding of the process of on-surface reactions, with particular emphasis on Ullmann-type coupling reactions, and to display the unique advantages of on-surface characterisation that only STM can provide.

1.2 Thesis Overview

Within this thesis, I will explore the topic of on-surface self-assembly, and subsequent Ullmann-type coupling reactions, with a variety of techniques, predominantly focussing on partnering the unrivalled topgraphic characterisation of STM with chemically sensitive spectroscopic companion techniques.

Chapter 2 contains an overview of the scientific literature on the key areas of self-assembly and Ullmann-type coupling, identifying common motifs in molecular assembly and interrogating the commonly-held truisms of Ullmann-type coupling on surfaces. Chapter 3 describes the fundamental underpinnings of the key techniques utilised throughout this thesis, with particular emphasis on STM. A variety of photoelectron spectroscopy methods, including X-ray photoelectron spectroscopy (XPS), near edge X-ray absorption fine structure (NEXAFS) and X-ray standing wave (XSW), are also outlined, as they perform well as companion techniques to STM.

In chapter 4, self-assembly and Ullmann-type coupling are examined with STM, *via* stepwise annealing to investigate the bottom-up synthesis of nanowires. The influence of hexyl chains in self-assembly and subsequent polymerisation is considered, with surface-induced chirality playing an important role in reaction progress. Chapter 5 investigates potential alternative methods for realising complex molecular architectures on 2D substrates, namely the deposition of fragile, thermally labile complex molecules formed in solution and deposited *via* electrospray deposition. The molecules featured in this chapter are synthesised in solution using novel pathways, and required the use of STM to determine details of structure morphology. Building on this, chapter 6 features the electrospray deposition of complex molecules which may undergo on-surface synthesis, combining STM with an array of X-ray spectroscopy techniques to further understand the reaction. The final product of this reaction can only be produced on-surface, providing an interesting use case for the bottom-up fabrication of porphyrin-graphene nanoribbons.

Finally, chapter 7 explores combining stepwise XPS and NEXAFS with temperature programmed XPS to analyse an Ullmann-type coupling reaction. A novel form of Arrhenius analysis is employed to determine the kinetic properties

of on-surface Ullmann-type coupling reactions, paving the way for these kinetic properties to be determined and used as a metric for comparing the effect of substrate chemistry and structure in lieu of the aforementioned reaction temperatures. Finally, chapter 8 will tie together the key findings of this body of work and present a conclusion and an outlook considering the future direction of this research field.

Chapter 2

On-surface Reactions

A significant proportion of chemical interactions and reactions are influenced by a surface (supporting substrate). Processes such as corrosion at surfaces, the Redox (reduction-oxidation) chemistry underpinning battery functionality occurs at surfaces, and the entire field of heterogeneous catalysis is mediated by interactions between chemical species at a surface. This chapter provides a background to the field of on-surface synthesis, where the interactions and chemistry of molecular systems, confined to a 2D plane, are studied by techniques which provide atomic and sub-molecular resolution as well as chemical sensitivity. Such an approach allows us to obtain detailed information on the mechanisms underlying such processes. This insight should ultimately provide the tools required to enhance the selectivity and efficiency of such on-surface processes, as well as provide a route to the synthesis of novel molecular materials.

2.1 On-surface Self-assembly

Molecules contain a number of atoms chemically bonded into a single unit. Desirable molecular properties can be incorporated and tuned *via* a large array of synthetic pathways, giving rise to molecules with specific atoms in specific configurations. These molecules can then be deposited onto a substrate, providing 2D confinement, where they subsequently interact with both the substrate and other molecules. Such interactions frequently lead to the formation of two-dimensional (2D) supramolecular structures, the properties of which are determined by the

various configurational aspects of the molecule, the properties of the specific chemical moieties, as well as the order and topography of the extended molecular structure. Observing these 2D on-surface structures can reveal fundamental information about the supramolecular structures found in solution, where the vast majority of molecular synthesis is conducted, and provides insight into molecule-substrate interactions which underpin aspects of heterogeneous catalysis.

Therefore, it is important to understand the various inter-molecular interactions driving these structures. The study of 2D molecular assembly has been facilitated by the development of scanning probe microscopy (SPM) techniques. The theory, operation, and practicalities of SPM are detailed in a later chapter, but the principal benefit is to allow real space resolution of molecular assemblies on the single molecule level, and with sub-molecular resolution. [4] In particular, SPM has provided a route to 'seeing' the patterns produced by molecules at the solid-vacuum and solid-liquid interface, and here I will provide details of the intermolecular interactions and examples from the literature. [17, 18]

2.1.1 Van der Waals Interactions

Molecular interactions can dictate the shape of an on-surface molecular assembly; the most universal of these is the van der Waals interaction. The van der Waals interaction is a name given to a group of intermolecular interactions: London, Debye and Keesom interactions. These each stem from a different dipole interaction: instantaneous-induced dipole (London), permanent-induced dipole (Debye) and permanent-permanent dipole (Keesom). Permanent dipoles can be understood as molecules with significant electronegativity differences between atomic species, leading to an imbalanced charge distribution. These induce a dipole in a neutral molecule or atom *via* interaction between the electron density on the neutral body and the charge on the permanent dipole. In the case of an instantaneous-induced dipole, an atom can simply be conceived as a dispersion of electron density around a nucleus. An instantaneously induced dipole can occur when this electron density is unevenly distributed around the nucleus. As the electron density of all atoms and molecules can become non-uniform at any time, due to the constant motion of electrons, when two atoms/molecules are close

enough to interact (typically <1 nm), these temporary fluctuations in electron density in one body can induce a dipole in the other body, and thus lead to an induced dipole in each body, giving rise to one of the three constituent interactions that make up the van der Waals force, the London interaction. Due to this third interaction type being possible with all atomic and molecular species, van der Waals forces are universal, and hence play a role in all self-assembly; the attractive nature of these interactions drives the formation of close-packed structures, a common self-assembly motif even in the absence of other molecule-molecule interactions. These interactions are attractive.

The van der Waals interactions between molecules can be described by the empirically derived Lennard-Jones potential, as shown:

$$V_{LJ}(r) = 4\epsilon[(\frac{\sigma}{r})^{12} - (\frac{\sigma}{r})^{6}], \tag{2.1}$$

where ϵ defines the lowest potential energy of the curve, σ is the distance at which the intermolecular potential between the particles is zero, and where r is the distance between the two particles. σ relates to the potential minimum ϵ via the following equation:

$$\epsilon = 2^{\frac{1}{6}}\sigma. \tag{2.2}$$

Two elements are accounted for in this model: the extremely short range Pauli repulsive force represented by the $\frac{1}{r^{12}}$ term, and the attractive interactions which give rise to the van der Waals attraction. The range of these attractive forces decays as $\frac{1}{r^6}$. Figure 2.1 demonstrates this simple model graphically, and it can be seen that in the example used, two particles with a σ value of 3.4 Å and a well depth of 0.01 eV exhibit an attractive region which extends less than 1 nm - this is smaller than the width of many of the molecular species of interest: for example, the diameter of a single tetraphenyl porphyrin molecule is larger than the attractive van der Waals regime, and thus molecular interactions stabilised by VdW forces results in close-packed structures. It is important to note that the force experienced by a molecule within range of the van der Waal's potential represented in this graph is given by $F = -\frac{dU}{dr}$. Hence, while the repulsive region labelled in the figure is an area in which the force is repulsive, there will still be an overall attractive potential so long as $U_{vdW} < 0$.

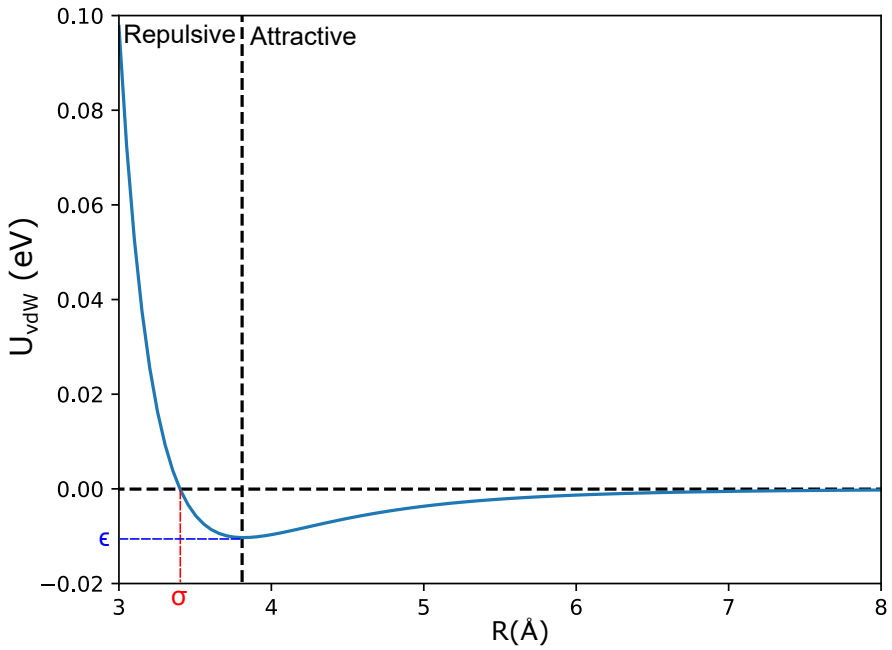

Figure 2.1: A Lennard-Jones potential showing the variation of van der Waals interaction potential energy(V_{vdW}) with distance between bodies (R) in blue.

In some cases, van der Waals forces are the dominant interaction, such as the frequently observed interactions between hydrocarbon chains, [19–21] spherical or quasi-triangular molecule close-packed structures, [22, 23], and graphene nanoflakes. [24] For a spherical molecule, van der Waals interactions have no preferential direction, but as demonstrated in each of the examples given, the conformation of the molecule on the substrate can drive the direction and shape of the molecular ordering. A diagrammatic representation of van der Waals interactions is shown in Figure 2.2a). It is important to note, that when dealing with the interactions between large supramolecular structures formed of many molecules (e.g. interactions between two quasi-infinite 2D sheets of material), the range of van der Waals interactions can increase, with potential energy varying with $\frac{1}{R^2}$ or even $\frac{1}{R}$, depending on the shape of the materials. [25] This is due to large scale molecular assemblies effectively functioning as extended materials and thus can apply a macroscopic lens to understanding van der Waals interactions. The interactions of these larger structures can be determined through use of the Hamaker constant, but this only applies to macroscale interactions.

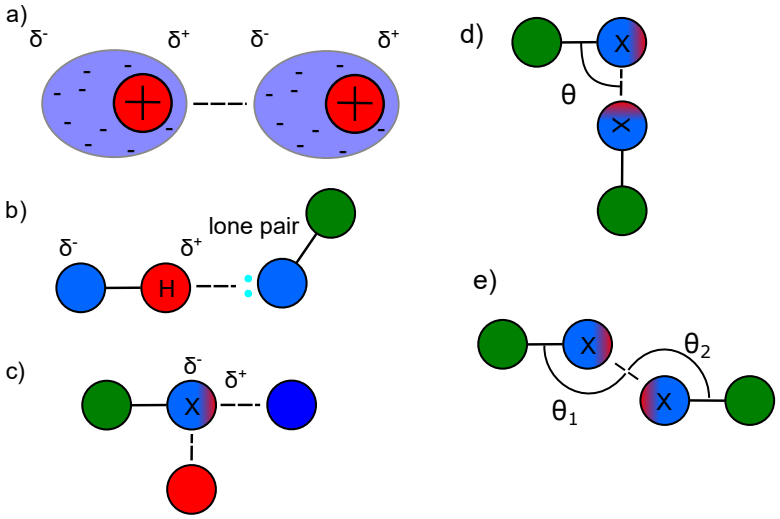

Figure 2.2: a) Van der Waals forces between two atoms due to a dipole formation. b) Hydrogen bonding between a hydrogen atom covalently bonded to an electronegative atom, and the lone pair electrons on a separate electronegative atom. c) The unequal charge distribution of a halogen atom covalently bonded to another atom leads to two possibilities for a halogen bond: side bonding with electropositive ligands, forward bonding with electronegative ligands. d) The first type of halogen-halogen bonding, where the two halogens are at right angles. e) The second type of halogen-halogen bonding, only possible when θ_1=θ_2.

In this thesis van der Waals, will only be considered in the short range. Due to their universal nature, van der Waals interactions form an important part of on-surface self-assembly in general, the attractive nature driving commonly seen agglomeration. Even when not the defining interaction in a structure, van der Waals plays a role and is often a competing force in any self-assembled structure.

2.1.2 Hydrogen Bonding

Hydrogen bonds arise when a hydrogen atom is covalently bonded to an electronegative atom, such as nitrogen or oxygen. This is another common self-assembly motif, and is sometimes found alongside van der Waals interactions, driving lattice formation. [26] An elementary understanding of hydrogen bonding can be obtained from a consideration of dipole interactions. The difference in electronegativity between H and the other atomic species causes a dipole to form, as a partial positive charge ($\delta+$) is induced on the hydrogen, and an opposite par-

Bond Type	Interaction Strength (eV)
van der Waals	∼0.02
Hydrogen	0.02-0.5
Halogen	0.05-1.9
Metal-Organic	0.5-2.0
Covalent	∼3-10+

Table 2.1: Example values for bond strength of typical on-surface interactions. [27, 28]

tial negative charge is induced in the electronegative atom. The hydrogen atom is then strongly attracted to a second, separate electronegative atom, forming the hydrogen bond; this is not a simple dipole interaction, and is a true bond formation.

Hydrogen bonding is a highly directional interaction, unlike van der Waals, as the hydrogen interacts with a lone pair of the electronegative atom, making the bond oriented along the direction of these orbitals. This is shown in Figure 2.2b). This allows for a great influence on lattice shape, and is significantly stronger than a typical van der Waals interaction (as shown in Table 2.1). Due to being slightly stronger than van der Waals interactions, and directional, the hydrogen bond has been utilised many times in on-surface self-assembly, for many years. [29] The highly directional nature of the H-bond can cause porous molecular networks to form, [30, 31] which can be used to restrict reaction pathways by limiting surface area available for reaction, enabling a more controlled surface environment for further reactions. This is different to the close-packed structures created when van der Waals interactions are the dominant force. [32] Hydrogen bonding is of interest as a tool for steering the development of supramolecular self-assembled structures due to the relative strength and directionality relative to van der Waals interactions, and these in turn can be used to control the thermodynamics of bottom-up growth of molecular nanostructures. [33]

2.1.3 Halogen Bonding

In a halogen bond, the charge distribution of the halogen atom becomes polarised and results in a non-spherical electrostatic potential, when covalently bonded with another atom, R, with a partial positive charge concentration around the end opposing the covalent bond. This type of bond is very common in extended crystalline structures, but has not been as extensively covered in a two-dimensional environment. [34] Halogen bonding is capable of slightly stronger bonds than our other two examples of noncovalent bonding, as shown in Table 2.1. These are also highly directional bonds, with the halogen bond capable of forming at 90° with positively charged species, and straight on with negative species, as shown in Figure 2.2c). When coordinating with other halogen species, two common angles emerge, as shown in Figure 2.2d-e). [35] Examples of on-surface halogen bonding include porous networks, [36,37] tri-molecular coordination, [38] or other shape-dependent packing. [39] These examples are shown in Figure 2.3.

2.1.4 Metal-organic Bonding

Metal-organic bonds are another alternative for stabilising 2D molecular systems. These interactions often occur between the lone pair in an atom such as O or N, and a metal adatom. Much like the hydrogen bond, these are highly directional, meaning that they too can be used to create self-assembled formations of specific shape and order. As can be seen in Table 2.1, the bond strength of a MO bond has the potential to be higher than other noncovalent interactions, allowing for the creation of relatively stable self-assembled structures. The comparative resilience of these structures, and inherent tunability, makes them useful for a variety of tasks, such as gas capture and catalysis. [41] MO bonds can be formed either with surface adatoms, [42, 43] or *via* codeposition of precursor molecules alongside metal atoms. [44, 45]

2.2 On-surface Synthesis

The inter-molecular bonds described above are strong enough to drive on-surface self-assembly for molecular systems at room temperature, and have the advan-

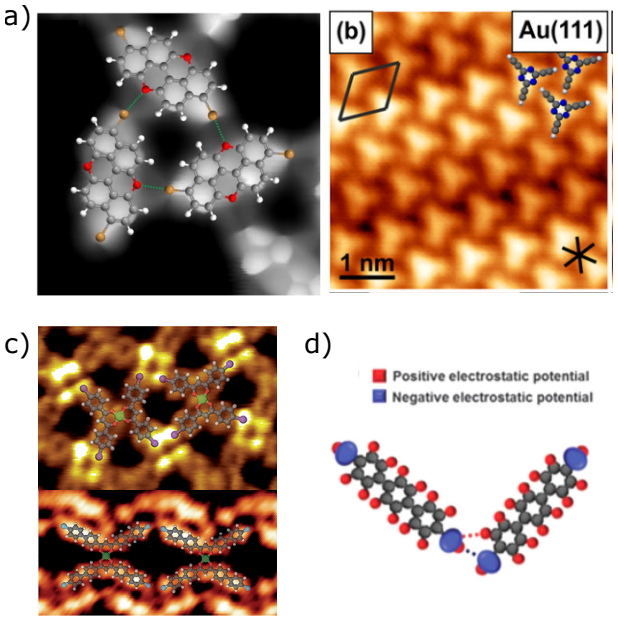

Figure 2.3: Examples of halogen bonding in on-surface self-assembly in the literature. a) Halogen-Oxygen bonding, suggested to be imaged using a CO functionalised tip, taken from Lawrence *et al.*. [40] b) Halogen-Nitrogen bonding on Au(111), taken from Yang *et al.*. [38] c) Halogen-halogen bonding, showcasing extreme differences in packing structure resulting from relatively minor structural changes; in this case, an extension of the phenyl appendage by an additional ring. Taken from Silly *et al.*. [36] d) Halogen-halogen side on bonding between DBTP molecules, taken from Cavallo *et al.* [35], adapted from Zha *et al.*. [39]

tage of reversibility (meaning that the system can be reverted to the original state with relatively similar activation energy), but do not have the requisite strength to withstand significantly higher temperatures. Reversibility is a non-trivial advantage, as the assembled structures can "self-correct" towards uniformity with continual annealing; defects formed by covalent bonding, however, are more permanent. Despite this advantage, many cases require a more stable structure than can be provided by noncovalent interactions. In use cases requiring functionality at room temperature, covalently bonded structures are preferred due to the bond strength being sufficiently high to avoid structural degradation. In order to create more resilient two-dimensional surface structures, stronger bonds must be formed. Covalent bonding commonly involves bond energies ranging from a low point of around 3 eV (and sometimes lower) to over 10 eV. [46–49] For example,

a carbon-carbon single bond is around 3.5 eV, whereas a carbon-oxygen triple bond has an energy of 11.2 eV. Put simply, covalent bonding is a chemical interaction, resulting from two atoms sharing electrons, and thus is much stronger than any of the previously discussed drivers of self-assembly. In this section, different synthetic routes towards covalent bond formation on surfaces will be discussed.

2.2.1 Covalent Coupling

Covalent bonding is useful because it can be used in the formation of organic nanostructures, which are of great interest due to their tunability and general versatility. Covalently bonded structures can be precisely created in bottom-up fashion with controlled and reproducible reaction steps, allowing for greater control over the products. [50] The two-dimensional environment provided by on-surface synthesis can restrict reaction pathways in such a manner as to allow for the creation of novel structures not possible in solution-phase chemistry. This approach is known as a "bottom-up" methodology and is predicated upon the tuning and deposition of molecular building blocks with specific functionality, which can then be annealed to produce a larger structure with a specific function, such as gas capture, or (opto-)electronic properties. [50, 51]

Two routes for on-surface covalent coupling are Glaser coupling and dehydrogenation; example reactions are shown in fig. 2.4. Both reactions feature a molecular building block functionalised with a "leaving group" which detaches from the molecule following activation (usually thermal activated), leaving behind a reactive site available for bonding. Glaser coupling is a form of dehydrogenation, where terminal alkene groups on precursors dehydrogenate (scission of a C-H bond) and form a new covalent bond between monomers. Once the carbon is no longer entirely hydrogen saturated, the carbon radicals (unpaired valence electrons available for bond formation) allow for further bonding. Glaser coupling has been shown to be a practical way of dimerising (or otherwise polymerising) precursor monomers, [52] and has also been shown to be amenable to photoactivation rather than the typical thermal activation used in conventional on-surface covalent bond formation. [53] When used in combination with dehydrogenative coupling,

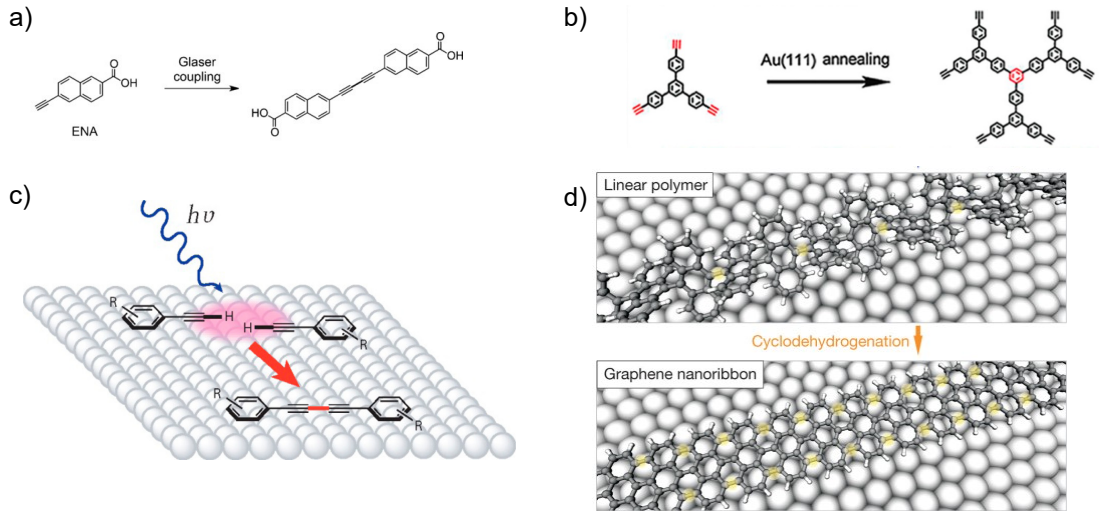

Figure 2.4: A variety of examples of on-surface covalent bonding reactions. a) A typical Glaser coupling dimerisation reaction, taken from Held *et al.* [54] b) An example of a Glaser reaction resulting in an alternative product, taken from Dong *et al.* [55] c) An example of photostimulated Glaser coupling, taken from Gao *et al.*. [53] d) A typical use of dehydrogenative coupling in the synthesis of a graphene nanoribbon, taken from Cai *et al.* [3]

polymer chains of over 100 nm in length have been created. [54] These two methods present significant challenges in precise bottom-up nanomaterial formation, however. Glaser coupling has a large variety of reaction pathways, facilitating the production of a range of unwanted side products, which can lead to an inhomogeneous product. Glaser coupling is also highly surface dependent, with this feature commonplace amongst on-surface reactions. [55] Dehydrogenative alkene coupling has also been shown to have similar issues, having a large number of reaction pathways and being highly dependent on surface chemistry. [56]

2.2.2 Ullmann-type Coupling

Ullmann-type on-surface reactions are a promising approach to coupling a variety of molecular species. The original in-solution Ullmann-type reaction was discovered in 1901 and was defined as a homocoupling reaction between aryl halides, traditionally catalysed by copper. [57] The reaction commonly required elevated temperatures (above 100 °C) [58], but has been encouraged in a variety of environments, and sometimes using a metal other than copper, such as nickel or

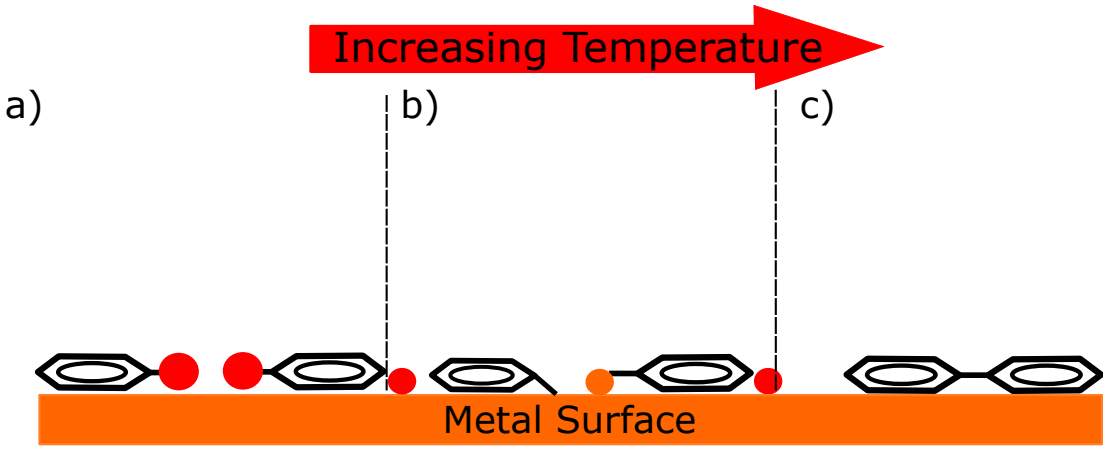

Figure 2.5: A simplified example of an on-surface Ullmann-type reaction. a) Precursor aryl halides deposited on a Cu surface. b) The dehalogenated molecules forming an organometallic intermediate with surface Cu atoms. c) A covalent bond forms between the two monomers.

palladium. [59] The process is generally accepted to proceed in two stages: firstly the precursors undergo halogen disassociation, and *via* the process of oxidative addition (addition of two electrons to the metal from the molecular radicals), a pair of precursors each form an organometallic bond with an atom of the metal catalyst. The second step is a reductive elimination, as the electrons leave the metal, breaking the organometallic structure, and the carbon atoms form a covalent bond. [60]

On a surface, the metal substrate itself activates the reaction, with either an adatom or a surface metal atom forming the organometallic intermediate. [61,62] Primarily, Au(111), Ag(111) or Cu(111) substrates are used, as their efficacy in facilitating Ullmann-type coupling reactions is well documented. [63–65] Figure 2.5 demonstrates a simplified reaction scheme of the on-surface Ullmann-type reaction. As previously described, MOFs are highly directional. [66] They are also often stronger than a typical hydrogen bond, ranging between 0.5-2 eV. [67] In Ullmann-type on-surface coupling reactions, they function as a transient intermediate state. Indeed, on Au(111), the metal-organic state is so short-lived as to be extremely difficult to capture in either STM or XPS. [68] Ullmann-type reactions have the advantage of having a comparatively much lower chance of secondary reactions (when compared to Glaser coupling), leading to a largely uniform product.

This can aid in building larger nanomaterials, such as nanoribbons, with a step-by-step bottom-up assembly. [3] A precursor molecule can also be functionalised with several halogens, enabling the construction of more complex two-dimensional product structures, beyond simple one dimensional chains. [42]

The primary issue with Ullmann-type reactions is that the disassociated halogen atoms do not necessarily desorb from the surface during the reaction and may form islands. These close-packed islands of halogens have previously been found to inhibit the formation of the organometallic intermediate phase and effectively limit the space available to around 30% of the surface. [69] One solution is to construct larger precursor molecules that will form together into a porous lattice; the disassociated bromine atoms have been shown to gather inside these pores and could allow the structure to develop unimpeded if the pore size was sufficiently expanded. [70] In some cases, the disassociated halogens desorb at a temperature very close to that of the disassociation, limiting the impact of this issue. [71] However, the fact remains that the presence of halogen species may adversely affect the reaction progress.

On-surface Ullmann-type coupling has been successfully achieved with various combinations of substrates, halogen functionalisation, and precursor molecules. Predominantly, the surfaces include the coinage metals, Au, Ag and Cu, and the halogens used are often bromine, iodine and chlorine. These combinations of substrate and halogen led to a wide range of different reaction temperatures, as shown in Table 2.2. Table 2.2 contains details of the dehalogenation, organometallic intermediate stage, and covalent bonding as reported within a selection of publications, including a broad range of molecular structures (as diverse as porphyrins, [72], nanoribbon precursors, [3] or simple halobenzene. [73]). Each of these factors affects the progression of a reaction, primarily evidenced in the temperature at which each of the stages is observed. Figure 2.6 displays this information visually. From this, we can see that Au (green) is the least reactive surface, as it consistently features higher reaction temperatures than the Ag or Cu. Also notable is the sparsity of evidence for organometallic structures on Au, indicating the transient nature of an Au based organometallic coordination, if indeed it even features as a stage within the reaction pathway. Both of these

Sub-strate	Halogen leaving group	Dehalogenation Temp (K)	MO Temp (K)	Cova-lent Temp (K)	Ref
Cu(110)	I	300*	300*	500	[73]
Cu(110)	I	300*	300*	398	[74]
Cu(111)	I	300*	300*	475	[8]
Cu(110)	Br	300*	300*	500	[75]
Cu(110)	Br	300*	300*	448	[74]
Cu(111)	Br	300*	300*	n/i	[76]
Cu(111)	Br	240	393	473	[70]
Cu(111)	Br	300*	440	550	[77]
Cu(111)	Br	300*	473	n/i	[65]
Cu(110)	Cl	393	393	458	[74]
Cu(111)	Cl	353	353	433	[78]
Cu(111)	Cl	300*	300*	420	[79]
Ag(111)	I	175	175	300	[80]
Ag(111)	I	300*	300*	575	[8]
Ag(111)	I	<473	473	573	[81]
Ag(111)	Br	400	473	573	[65]
Ag(111)	Br	300*	300*	443	[82]
Ag(111)	Cl	393	393	473	[78]
Ag(111)	Cl	150	150	n/i	[83]
Au(111)	I	393	n/i	393	[84]
Au(111)	I	300*	300*	n/i	[85]
Au(111)	Br	473	n/i	473	[3]
Au(111)	Br	523	n/i	523	[84]
Au(111)	Br	523	n/i	523	[64]
Au(111)	Br	520	n/i	520	[86]
Au(111)	Cl	473	n/i	473	[78]
Au(111)	Cl	453	453	n/i	[83]

Table 2.2: Temperatures for different stages of various Ullmann-type coupling reactions. *reactions that occurred following deposition. n/i = not included in reporting.

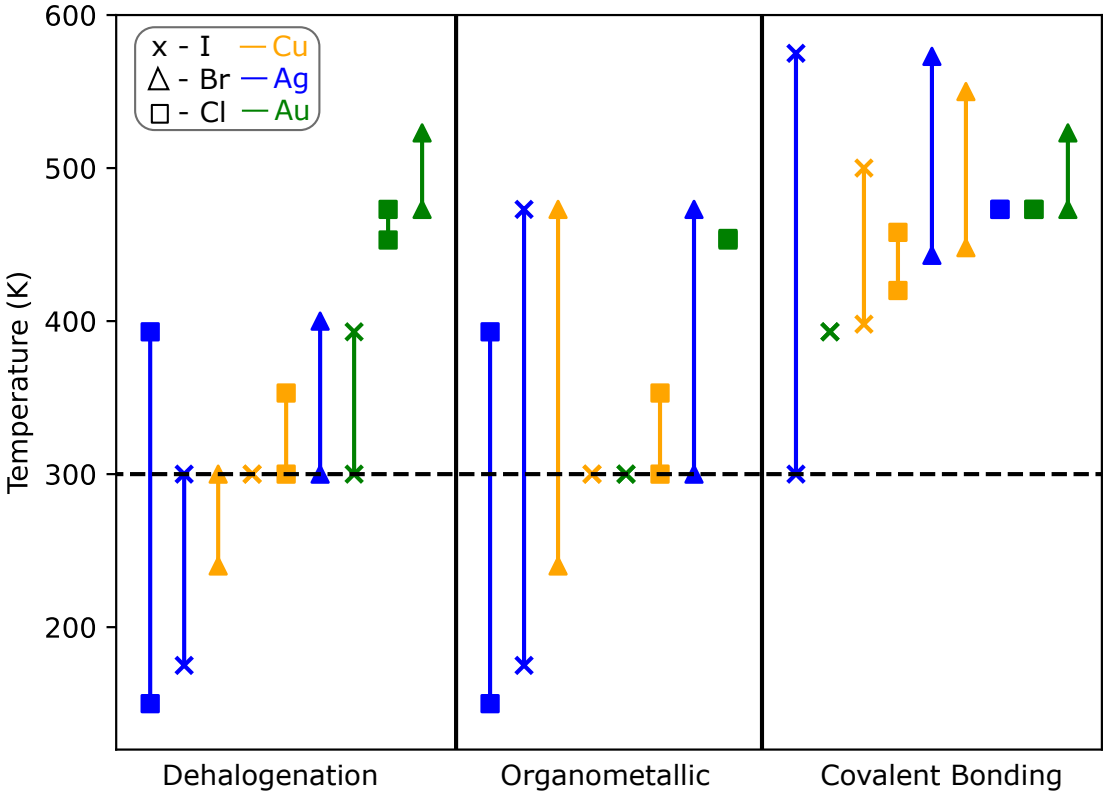

Figure 2.6: The temperatures at which different stages of the Ullmann-type reaction take place on different surfaces with different halogens (as reported in various publications, see Table 2.2). Each line represents the range of reaction temperatures for specific combination of surface and halogen, as indicated by the key.

features are expected, as Au is generally considered to be the least reactive of these metals, due to the high $s-d$ orbital coupling and full d antibonding orbitals. [87] The reactivity of coinage metals is commonly accepted to be Au as the least reactive, then Ag, then Cu; however, this trend is not immediately apparent from the literature survey presented here. Interpretation of the data is hindered somewhat by much of the literature detailing molecular deposition at room temperature, leading to immediate disassociation on Cu and Ag surfaces, but it also likely that the specific nature of the precursor molecule, the deposition conditions, crystallographic plane, and indeed the heating rate (as discussed in Chapter 7) all play a role which may overshadow the expected order of reactivity of the bulk substrate material.

Another notable feature is that, contrary to expectations, Cl does not appear to be the least reactive halogen in Ullmann-type coupling reactions. With regard

to bond strength, Cl-C > Br-C > I-C, and hence we would expect higher reaction temperatures for Cl within on-surface Ullmann-type coupling. However, this does not appear to be the case in the surveyed literature. Obviously, the shape and conformation of any precursor molecule can have a large influence on the prospective reactivity, and applies a degree of variance to the results that confounds any more obvious patterns. Another known impact of the surface on Ullmann-type reactions is the impact of surface geometry. Previous work has shown that step edges are a preferred site for dehalogenation in an on-surface Ullmann-type reaction, meaning that surface preparation with varying levels of surface stepping could result in differing reactivity. [88–91] Other issues include the sheer difficulty of measuring temperature in experiments, particularly in UHV environments; even a sample plate mounted thermocouple, arguably the best available option, is by nature not at the same temperature as the sample itself. Most published work does not report on key features, such as deposition temperature, temperature ramp rate, or duration of anneal, let alone the set-up for measuring the temperature, which can lead to large uncertainties. Prior work has looked into the possibility of encouraging reaction stages during the deposition process, [15] so this uncertainty is of some importance. For thermally activated processes, it could be argued that it would be of more utility to directly measure the activation energy, as opposed to reaction temperature. Hence, a key aim within this work is to look at the reaction mechanism, break it down into individual steps and consider the potential energy surface, as discussed in the next section.

2.2.3 Potential Energy Surfaces and Reaction Pathways

A reaction progresses from products to reactants. This process can be broken down to a series of elementary reaction states. Transition state theory postulates that there exists a transition state between each step; this can be considered as a barrier to the reaction progression, and there can still be a barrier even if the product energy state is lower than that of the reactants. This can be represented visually with a potential energy surface, as shown in Figure 2.7. In a reaction profile, the x-axis is the reaction coordinate; this can be thought of in simple cases as a one dimensional, abstract coordinate showing the progression of a reaction

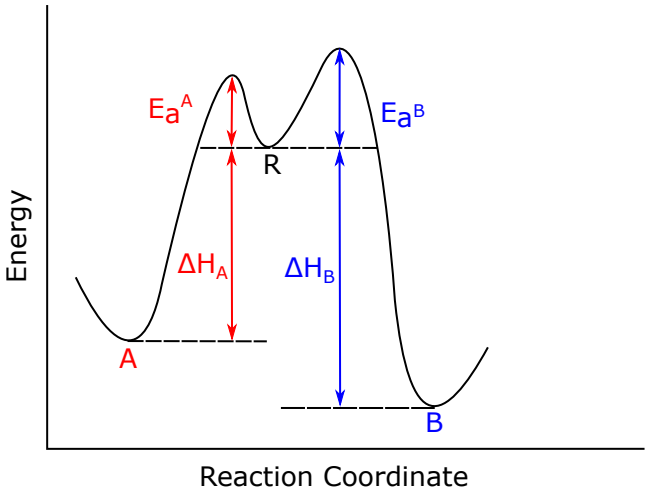

Figure 2.7: Example reaction profile, showing a reactant R with two possible products, A and B.

from reactants to products.

Beginning with reactant R, in this case there are two possible reaction products, A and B. Both R and products A and B sit in a local energy minimum, with energy required to leave. For the transition from R to either of our products, this energy requirement is activation energy E_a^A or E_a^B respectively. Once this barrier is overcome, the reaction may progress to the minimum of the available potential well. Two factors usually determine the outcome of the reaction: the stability of the products (thermodynamic factors) or the rate at which the products form (kinetic factors). In a reversible reaction, if input energy ΔE exceeds both E_a^A and E_a^B, the reactant in the lowest potential well will be preferred, in this case B. This is referred to as a reaction under thermodynamic control. However, if $E_a^A < \Delta E < E_a^B$, product A will preferentially form. This is known as a reaction under kinetic control. Hence, by controlling the thermal condition of the system, products A and B can be selectively formed.

As an example, we can consider the competing models displayed in Figure 2.8 as reported by Grossman *et al.*. [92] With STM, snapshots of a reaction can be taken: after deposition, and after different stages of anneal, revealing different stages of a reaction. If these stages can be identified, perhaps with the use of a complementary technique such as X-ray photoelectron spectroscopy (XPS), the task remains to understand the reaction pathway between these points. In this instance, the 2BPT and 3BPT molecules (trigonal organic molecules possessing

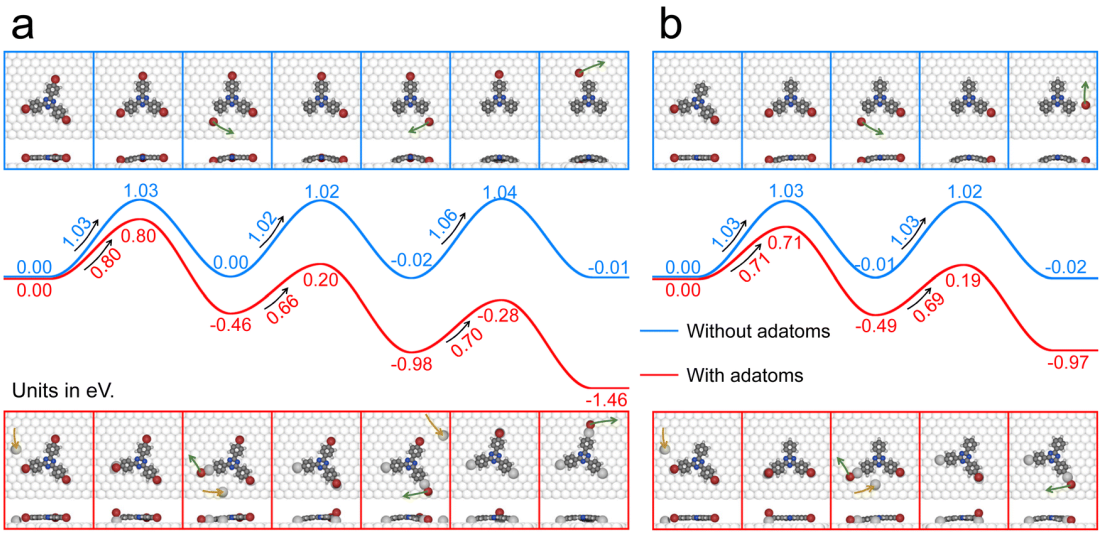

Figure 2.8: DFT calculated energy profiles for the debromination of (a) 3BPT and (b) 2BPT on Ag(111) terraces without (upper part, blue curve) and with (lower part, red curve) Ag adatoms. Taken from Grossman *et al.* [92].

2 and 3 halogenated appendages) are deposited intact onto an Ag(111) surface, as shown in the leftmost box of each pathway. When heated, the molecule dehalogenates, and forms an organometallic intermediate state, before covalently bonding, in a typical Ullmann-type reaction.

The question remains, having observed these stages, what the reaction pathway for these reactions could be. Due to the stepwise nature of STM, the intermediate stages between these snapshots of the reaction condition are unknown. Often, to fill in these gaps, computer simulations are used to determine likely pathways. The most common method currently is the use of density functional theory (DFT), utilising a "nudged elastic band" (NEB) approach. [93, 94] While in simple terms, the reaction coordinate can be imagined as 1 dimensional, in reality many different factors affect the progression of a reaction, and hence when performing NEB DFT, the system is modelled with a potential energy landscape. Conceptually, in the reaction, we have a well-defined starting structure and a product structure. These structures can be optimised using DFT, adjusted to match experimentally gathered information, finding the lowest potential energy for each of these systems. In NEB, a series of points between these two known states are obtained by varying different degrees of conformational freedom. On the path between the two systems, energy barriers will have to be overcome, with

the path with the lowest potential energy trajectory deemed to be the most likely. The elastic band part of the name comes from the manner in which these points are held together, to give adequate spacing along the pathway and by providing an algorithm for allowing the points to search out the pathway with the lowest barrier.

Based on this insight, mechanistic discussions have been invoked to interpret experimental findings. Utilising this technique, Figure 2.8 presents two possible pathways to dehalogenation, with the red pathway incorporating surface adatoms within the reaction mechanism, and blue without. In the leftmost box, the molecule has been deposited intact on the surface. This is set to a potential energy of 0 eV. From here, the simulation calculates the potential energy for subsequent intermediate stages: the interaction of the first halogen with a metal atom or adatom, the dehalogenation of that halogen, and so on. For each stage, the activation energy and resultant potential energy are significantly lower for the model featuring the adatom. Thus, through the use of NEB DFT, the adatom model appears preferable.

Under thermodynamic control, a reaction is reversible, meaning that although one product will be formed preferentially, both products will be formed over the course of the reaction. Previous work has discussed the possibility of a reversible dehalogenation reaction leading to an elongation of reaction time for an Ullmann-type coupling on Au(111), when opposed to a much faster reaction on Ag(111). [95] Fritton *et al.* found that fitting a first order kinetic model to their reaction achieved a good fit to the data and produced values for E_a matching values provided through DFT modelling. On Au(111), however, the debromination was better modelled as thermodynamically controlled, with a model accounting for rehalogenation providing a more accurate fit. If the reaction can indeed in some instances be thermodynamically controlled, the implications for the effect of heating rate and halogen desorption temperature on reaction progress are significant. This issue is specifically addressed in chapter 7.

Given the paucity of information on the fundamental thermodynamic quantities involved in these on-surface reactions in the literature, one of the aims of this thesis is to develop a more detailed understanding of how on-surface reac-

tions progress, linking generalised trends in reactivity (such as the previously noted metal substrate reactivity order) to thermodynamic quantities like activation barriers. A fuller understanding of how molecular structure and substrate choice impacts reactions will increase efficiency and selectivity of future on-surface reactions, and so an understanding of the development of the reaction in a topographic and chemical sense is required. In order to achieve this, high resolution SPM will be utilised in concert with X-ray spectroscopy techniques, to be described in the forthcoming Experimental Techniques, Methods and Materials chapter.

2.2.4 Summary

To summarise, a variety of factors affect the self-assembly of molecules confined to a two-dimensional substrate, with these structures affecting the progression of further on-surface reactions (e.g. covalent bond formation). Bottom-up synthesis of extended organic molecules is of considerable interest, and in this chapter factors affecting the progression of 2D on-surface synthesis have been considered, including factors such as reaction pathways, temperature control, kinetics vs thermodynamics, molecular chemical structure and surface chemistry. With particular focus on Ullmann-type coupling, in this thesis I will further the understanding of these various factors, and their potential influence in synthesising molecules of interest.

Chapter 3

Experimental Techniques, Methods and Materials

In this chapter the primary techniques utilised within this work, scanning tunnelling microscopy (STM), X-ray photoelectron spectroscopy (XPS), near edge X-ray absorption fine structure (NEXAFS) and X-ray standing wave (XSW) will be detailed. The theoretical underpinnings, and basic operation of these techniques is also introduced

3.1 Scanning Tunnelling Microscopy

STM is a scanning probe microscopy technique used to image substrate/adsorbate systems. Conceptually, a sharp metal tip is brought into proximity of a conducting substrate. A bias is applied across the metal tip of the STM and the surface, and the tip is raster scanned across the sample. As the tip moves across the surface, a current flows from tip to sample or vice versa (depending on bias polarity) and is measured. In the most commonly employed measurement mode, the height of the tip above the sample is varied so as to keep the magnitude of the tunnelling current constant. This change in height is interpreted in the zeroth order approximation as the topography of the sample. Due to the single atom tip termination, STM is typically able to obtain sub-Ångstrom lateral resolution and consequently is able to achieve atomic resolution. In the vertical direction the resolution is even finer, due to the extreme sensitivity of tunnel current to

tunnel gap, as explored later, and is on the order of picometers.

3.1.1 Quantum Tunnelling

The fundamental basis of STM operation is the phenomenon of quantum tunnelling. The current between the tip and the surface arises from tunnelling electrons, allowing a measurement of surface topography to take place without making contact with the surface itself; contact here meaning engagement with the extremely close range Pauli repulsion forces between atoms. The quantum tunnelling of electrons which is essential to STM is impossible for a particle considered within the framework of classical mechanics. If we consider the example of a "particle in a box", a particle surrounded on both sides by a potential of magnitude $V_0 >> E$, but finite width, it is forbidden for the particle to escape. However, due to the quantum nature (wave-particle duality) of very small particles, such as electrons, it is possible for them to escape *via* the mechanism of quantum tunnelling. As an electron behaves as both a wave and a particle, it is the wavelike characteristics upon encountering the side of the potential well which allow tunnelling, with the waveform of the particle decaying exponentially into the barrier. If the waveform reaches the other side of the barrier with a non-zero probability (so long as the barrier is finite), there is a chance the particle will be found on the other side of the barrier, as the probability density is the square of this waveform. This is the basic idea behind quantum tunnelling, and is illustrated in Figure 3.1.

In STM, this tunnelling occurs between a sharpened metallic tip (ideally atomically fine), and the substrate/substrate-adsorbate. Modern STM techniques mostly operate with the tunnelling barrier being either vacuum, air, or liquid, depending on experimental requirements. [96] The exponential relationship between tunnel current and distance of the tip from the surface, underpins the spatial resolution of STM and provided catalyst for the development of the technique. [97] The theoretical basis for this result is as follows: an electron of mass m and energy E is approaching a potential barrier of potential $V = V_0$ and width L, as shown in Figure 3.1. The wavefunction of the electron can be considered in three different continuous sections: section i, before the barrier with both the

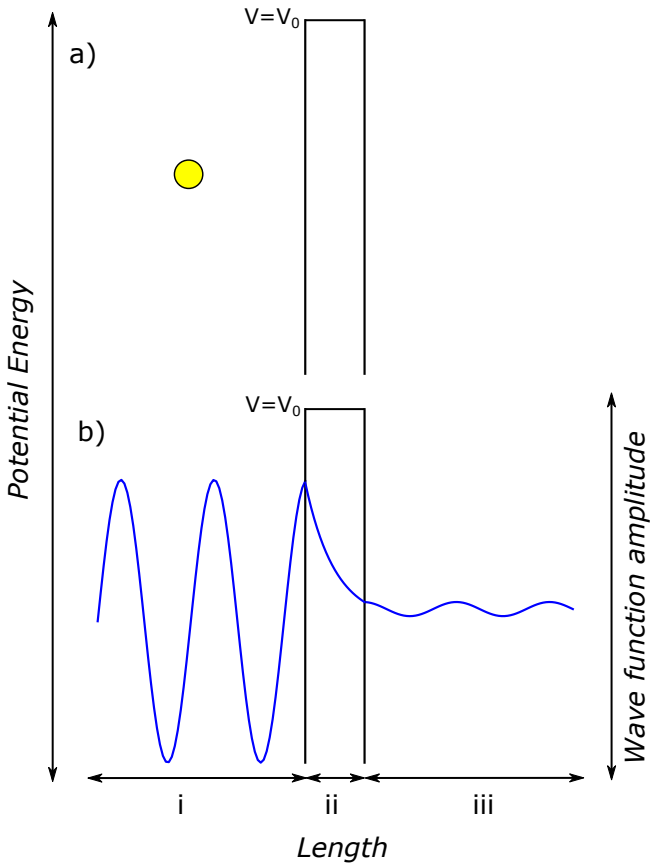

Figure 3.1: a) Shows a classical modelling of an electron facing a potential barrier (shown here by length ii). b) Shows how the quantum nature of the electron allows it to pass the barrier. As the waveform of the electron does not completely decay before reaching the other side of the barrier, the waveform continues beyond the barrier.

original and reflected waves, section ii, over the width of the barrier and section iii, after transmission through the barrier. The wave functions for these three sections can be written as follows:

$$\psi_i = A_0 e^{ikx} + Ae^{-ikx}, \tag{3.1}$$

$$\psi_{ii} = Be^{-\alpha x} + Ce^{\alpha x}, \tag{3.2}$$

$$\psi_{iii} = De^{ikx}, \tag{3.3}$$

where A_0, A, B, C and D are the amplitudes of the respective waves, and the constants k and α are : $k = \sqrt{\frac{2mE}{\hbar}}$, $\alpha = \sqrt{\frac{2m(V_0-E)}{\hbar}}$. ψ_i is the wavefunction for section i, pre barrier. The wavefunction $\psi_i i$ is for section ii, inside the barrier, an impossibility in a classical representation. The wavefunction $\psi_i ii$ is for section iii,

post barrier. At the boundaries between regions i-ii, and ii-iii, the wavefunctions and their first derivatives must be equal. If we set boundary conditions, by taking i-ii boundary as $x = 0$, and ii-iii as $x = L$, we can show the following: At boundary i-ii ($x = 0$):

$$A_0 e^{ikx} + Ae^{-ikx} = Be^{-\alpha x} + Ce^{\alpha x}, \tag{3.4}$$

$$A_0 + A = B + C. \tag{3.5}$$

Taking the first derivative of Eqn. 3.4 :

$$ik(A_0 - A) = \alpha(C - B), \tag{3.6}$$

At boundary ii-iii (x = L):

$$De^{ikL} = Be^{-\alpha L} + Ce^{\alpha L}. \tag{3.7}$$

Taking the first derivative:

$$ikDe^{ikL} = \alpha(Ce^{\alpha L} - Be^{-\alpha L}). \tag{3.8}$$

The tunnelling probability for a specific system is the ratio of the transmitted probability density to the incident probability density. The probability density of a given wavefunction $\psi(x)$ is as follows:

$$\psi(x)_{pd} = |\psi(x)|^2, \tag{3.9}$$

$$|\psi(x)|^2 = \psi(x)^*\psi(x), \tag{3.10}$$

$$\psi(x)^*\psi(x) = (Ae^{+ikx})^* Ae^{+ikx}, \tag{3.11}$$

$$A^*A = |A|^2. \tag{3.12}$$

Hence, the tunnelling probability is given by:

$$T = \left|\frac{D}{A_0}\right|^2. \tag{3.13}$$

Rearranging equations 3.7-3.8, to give us expressions for B and C, gives us the following:

$$C = \frac{D}{2}(1 + \frac{ik}{\alpha})e^{ikl-\alpha L}, \tag{3.14}$$

$$B = \frac{D}{2}(1 - \frac{ik}{\alpha})e^{ikl+\alpha L}, \tag{3.15}$$

Reinserting those into Eqns. 3.5-3.6, we get the following:

$$1 + \frac{A}{A_0} = \frac{D}{A_0}e^{ikl}(\cosh \alpha L - \frac{ik}{\alpha}\sinh \alpha L), \tag{3.16}$$

,

$$1 - \frac{A}{A_0} = \frac{D}{A_0}e^{ikl}(\cosh \alpha L + \frac{i\alpha}{k}\sinh \alpha L). \tag{3.17}$$

Adding Eqn. 3.16 to 3.17 to eliminate $\frac{A}{A_0}$:

$$\frac{D}{A_0} = \frac{2}{e^{ikL}(2\cosh \alpha L + i\frac{\alpha^2-k^2}{\alpha k}\sinh \alpha L)}, \tag{3.18}$$

hence, transmission probability T on an electron tunnelling through a barrier of length L:

$$T = \left|\frac{D}{A_0}\right|^2 = \frac{4}{(4\cosh^2 \alpha L + i(\frac{\alpha^2-k^2}{\alpha k})^2 \sinh^2 \alpha L)}. \tag{3.19}$$

Considering that $\cosh^2 \alpha L = 1 + \sinh^2 \alpha L$, we can write:

$$T = \frac{1}{1 + \frac{1}{4}(\frac{\alpha^2+k^2}{\alpha k})^2 \sinh^2 \alpha L}. \tag{3.20}$$

Reinserting our $\alpha \approx \sqrt{V_0 - E}$ and $k \approx \sqrt{E}$ values:

$$T \approx \frac{1}{1 + \frac{V_0^2}{4E(V_0-E)}\sinh^2 \alpha L}. \tag{3.21}$$

Approximating a large barrier such that $\alpha L >> 1$, we can write the following:

$$T \approx \frac{1}{1 + \frac{V_0^2}{4E(V_0-E)}(\frac{e^{\alpha L}}{2})^2} \approx \frac{16E(V_0 - E)e^{-2\alpha L}}{1 + V_0^2}. \tag{3.22}$$

Hence, the transmission coefficient for a potential barrier of width L, assuming a large barrier, is as follows:

$$T = \left|\frac{D}{A_0}\right|^2 \approx 16\left(\frac{E}{V_0}\right)\left(1 - \frac{E}{V_0}\right)e^{-2\alpha L}. \tag{3.23}$$

The probability of tunnelling and tunnel current are directly proportional, so the current is therefore proportional to the barrier gap by e^{-L}. From Eqn. 3.23, the exponential dependency of tunnel current on the size of the barrier can be seen. This creates extremely fine vertical sensitivity, with STM capable of achieving sub-Ångstrom vertical resolution; for example, a change in distance of 1 nm will typically increase tunnel current by a factor of 10.

3.1.2 Tersoff-Hamman

The wavefunction model described in section 3.1.1 is a useful starting point, but fails to accurately model a complex 3d system, such as that present within an STM. Bardeen [98] developed a general theory of tunnelling between two metal plates as early as 1961, before the STM was invented. In this formulation, each plate is treated independently, avoiding the need to solve the Schrödinger equation for a combined system. This was then translated into an STM scenario by Tersoff and Hamann, by considering the tip and the sample as the different plates. [99] The expression for the tunnel current with this formulation is as follows:

$$I = \frac{2\pi e}{\hbar} \sum_{\mu,\nu} f(E_\mu)[1 - f(E_\nu + eV)] \left|M_{\mu,\nu}\right|^2 \delta(E_\mu - E_\nu), \tag{3.24}$$

where $f(E)$ is the Fermi function, and E the energy of the electronic states on the tip μ and sample ν respectively. V is the applied bias and $M_{\mu\nu}$ is the tunnelling matrix element between tip state ψ_μ and surface state ψ_ν. Considering equation 3.24 in parts can be helpful: $f(E_\mu)[1-f(E_\nu+eV)]$, deals with two Fermi functions, $f(E_\mu)$ and $1-f(E_\nu+eV)$. The first, $f(E_\mu)$ represents the probability of finding an electron in tip state ψ_μ with energy E_μ; $1-f(E_\nu+eV)$ the probability of finding an empty surface state ψ_ν of the same energy. If these are both non-zero, tunnelling from the tip to the sample can occur. It should be noted that the equation in this form only holds for a positive sample bias, which is the circumstance that we will continue to consider here; the alternative for a negatively biased sample is in the original work. [99] Matrix element $\left|M_{\mu,\nu}\right|^2$ represents the probability of these states overlapping, and the final part $\delta(E_\mu - E_\nu)$ ensures that we only consider the case of elastic tunnelling, rendering $I = 0$ if $E_\mu \neq E_\nu$.

The matrix element can be determined by integrating both wave functions and their differentials over an arbitrary surface in the barrier region between the sample and tip:

$$M_{\mu,\nu} = \frac{-\hbar^2}{2m} \int \psi_\mu^* \nabla\psi_\nu - \psi_\nu \nabla\psi_\mu^* \cdot dS. \tag{3.25}$$

In order to evaluate this integral, the surface wave function is expanded:

$$\psi_\nu = \Omega_s^{-\frac{1}{2}} \sum_G a_G e^{(\kappa^2 + |\vec{\kappa_G}|^2)^{1/2} z} e^{i\vec{\kappa_G}\cdot\vec{x}}, \tag{3.26}$$

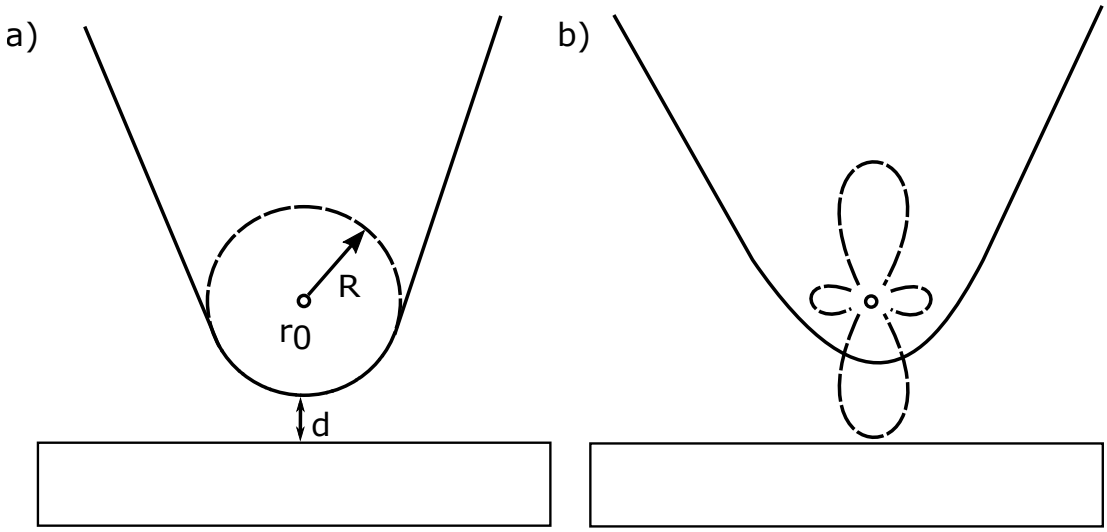

Figure 3.2: a) The basic tunnelling geometry described by Tersoff-Hamman model, featuring spherical s-orbital. b) Possible tip d orbital tunnelling.

where Ω_s is sample volume, $\kappa = \hbar^{-1}(2m\phi)^{1/2}$ is the minimum inverse decay length for the wave function in a vacuum, ϕ is the work function, and $\kappa_G = k_{||} + G$, where $k_{||}$ is the wave vector of the surface state, and G is a reciprocal lattice vector for the surface. The tip is modelled as a spherical potential well, as shown in Figure 3.2a), where R is the radius of curvature of the tip, r_0 is the centre of the curvature, and d is the nearest distance between tip and surface.

In the region between the tip and sample, the wave functions of the tip are of the following spherical form:

$$\psi_\mu = \Omega_t^{-1/2} c_t \kappa R e^{\kappa R} (\kappa \left| r - r_0 \right|)^{-1} e^{-\kappa |r - r_0|}, \tag{3.27}$$

where Ω_t is the volume of the probe, and c_t is a normalisation constant. Assuming the work function is the same for the tip as the surface (reasonable in a case where tip and surface are metal), expanding the wave function from the surface in a similar manner to Eqn. 3.26, and inserting back into Eqn. 3.25, evaluating the expansion term by G (as described by Tersoff and Hamann [99]):

$$M_{\mu,\nu} = \frac{-\hbar^2}{2m} 4\pi \kappa^{-1} \Omega_t^{-1/2} \kappa R e^{\kappa R} \psi_\nu(r_0) \tag{3.28}$$

If we assume low temperature and low bias (meaning the Fermi edge is effectively a step function and the bias is not affecting the Fermi levels of the surface or tip),

equation 3.24 becomes:

$$I = \frac{2\pi e^2 V}{\hbar} \sum_{\mu,\nu} f(E_\mu) \left|M_{\mu,\nu}\right|^2 \delta(E_\mu - E_F)\delta(E_\nu - E_F). \tag{3.29}$$

Inserting Eqn. 3.28 into Eqn. 3.29:

$$I = 32\pi^3 \hbar^{-1} e^2 V \phi^2 D_t(F_F) R^2 \kappa^{-4} e^{2\kappa R} \times \sum_{\nu} \left|\psi_\nu(r_0)\right|^2 \delta(E_\nu - E_F), \tag{3.30}$$

where ϕ is the work function, and D_t is the density of states per unit volume of the tip. This can be simplified such that we can show that:

$$I \propto \sum_{\nu} \left|\psi_\nu(r_0)\right|^2 \delta(E_\nu - E_F). \tag{3.31}$$

Given that $\left|\psi_\nu(r_0)\right|^2$ is the probability density of the surface state wavefunction at the position $r = r_0$, Eqn. 3.31 shows that the tunnelling current is proportional to the local density of states (LDOS), at the Fermi level, at the position of the tip. As this model uses a spherical potential, in a manner resembling an *s*-type orbital, there is no angular dependence. There is also a theoretical lateral resolution limit from *s*-orbital tunnelling of approximately 6-9 Å, due to the radius, R. Experimental work has shown a substantially improved resolution to this, around 2-3 Å. This is due to tunnelling sometimes occurring in states with a higher angular momentum, such as d or p states, elongating the orbitals, as shown in Figure 3.2b). [100] As the tips used are metallic, then there are p and d orbitals available, which is consistent with the increased resolution (as compared to that expected for s orbitals).

3.1.3 The Importance of Bias and Current within STM

The tunnel current flow between an STM tip and the surface and the impact of an applied bias on direction and magnitude can be simply described by an energy level diagram such as that shown in Figure 3.3. Each part of the figure shows a tip and surface for various states of applied bias. In this instance, the tip has a greater work function than the surface ($\phi_t > \phi_s$), and consequently in Figure 3.3a), with 0 applied bias, the vacuum level of the surface E_{Vs} is lower than that of the tip E_{Vt}. When the applied bias is 0 V, the Fermi levels of the surface and tip (E_{fs} and E_{ft} respectively) quickly equilibrate, resulting in

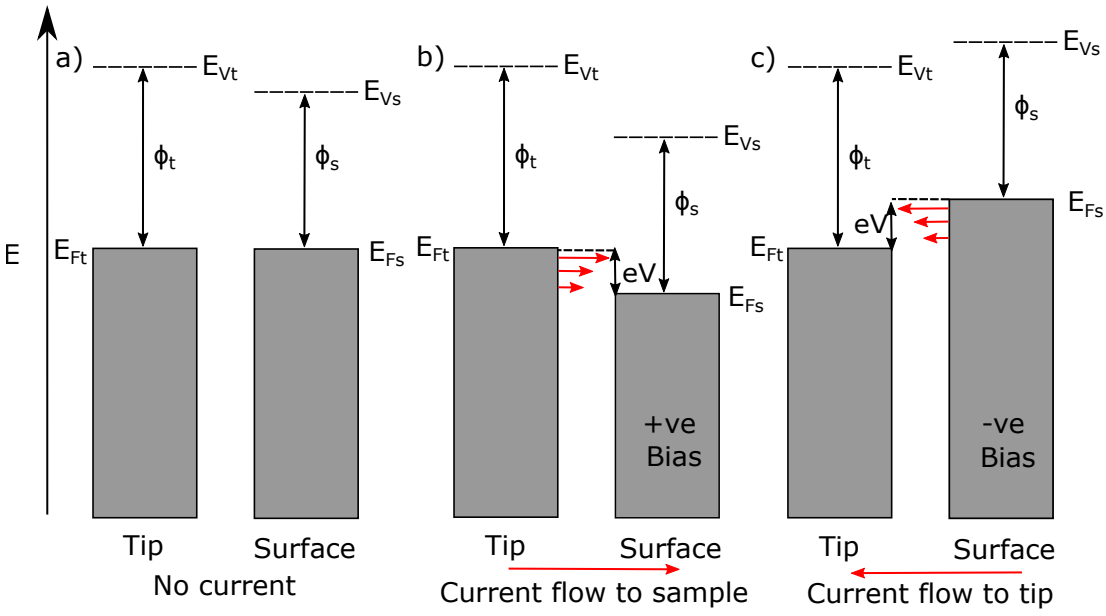

Figure 3.3: a) Energy level diagram showing 0 applied bias - the Fermi levels are equal, so there is no current flow. b) Diagram showing positive applied sample bias, shifting the Fermi level of the sample down relative to the tip, resulting in current flow from tip to surface. c) Diagram showing negative applied sample bias, shifting the Fermi level of the sample up relative to the tip, resulting in current flow from surface to tip.

net zero tunnel current. The Fermi level in a metal is the point at which the probability of finding the state occupied with an electron is 50%, hence when the two Fermi levels are in equilibrium no tunnelling occurs due to there being no overlap between filled states of one side and empty states of the other side. When a positive bias is applied to the sample, as in Figure 3.3b) the Fermi level of the sample shifts down, allowing electron tunnelling into the empty states of the sample. If a negative bias is applied to the surface, as in Figure 3.3c), the surface Fermi level shifts up, allowing electron tunnelling from the surface into the empty states of the tip. Given that we assume the LDOS in the tip remains constant, we can use this mode to examine the filled states of the surface.

When electron tunnelling occurs between a filled state and empty state at the same energy level, energy is conserved (making this elastic tunnelling). Higher energy electrons have a longer decay length, so a higher proportion of the tunnelling electrons will come from states closer to the Fermi level. The higher the

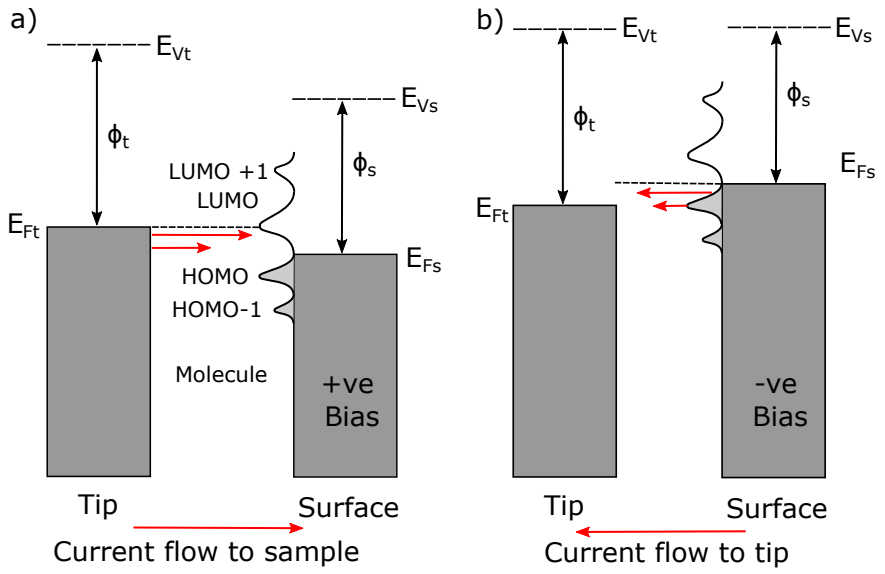

Figure 3.4: a) Energy level diagram showing positive applied bias. The states of the surface and adsorbate are all shifted downward, resulting in tunnel current from the tip into the surface and molecular LUMO and other accessible unoccupied states in the molecules. b) Diagram showing negative applied sample bias, shifting the states of the sample and adsorbate down relative to the tip, resulting in tunnel current flow to the tip from the surface and HOMO (and other accessible occupied states) of the adsorbate.

bias, in positive or negative direction, the greater the shift in the energy levels, allowing more overlap between the filled and empty states of the tip and sample, leading to an increased tunnel current.

When molecules are adsorbed onto the surface, the fundamental theory remains much the same, albeit with additional complexity. On a basic level, adsorbed molecules have discrete energy states which can be tunnelled into or out of; most pertinently, as they are closest to the Fermi level, the highest occupied molecular orbital (HOMO) and lowest unoccupied molecular orbital (LUMO). The states of the molecule both above the LUMO and below the HOMO can also be tunnelled into, depending on bias, and as such are labelled LUMO +1,+2 ... and HOMO −1,−2, etc. These can be tunnelled into in much the same way as the surface states, as shown in Figure 3.4. As the surface and tip are metals, we treat the LDOS in both as homogeneous. While this is not entirely accurate, it is serviceable as an approximation in most instances. Another factor to consider with

molecules adsorbed close to the surface is surface-adsorbate coupling, a common feature in which the orbitals of the surface and adsorbate hybridise, forming a new and different electronic structure. This can lead to the adsorbate exhibiting differing electronic properties on-surface as opposed to in bulk or solution, and most noticeably, the gas phase.

3.1.4 Scanning Tunnelling Spectroscopy

When sufficient positive bias is applied to a surface with a deposited adsorbate, tunnelling occurs into the unoccupied states of the surface and the adsorbate. The higher the bias, the more states can be accessed, and the higher the tunnel current. If we wish to distinguish these states from one another, scanning tunnelling spectroscopy (sometimes referred to as $\frac{dI}{dV}$ spectroscopy) can be utilised. Taking the first differential of Eqn. 3.31, we find:

$$\frac{dI(V)}{dV} \propto \rho_s(E_F - eV), \tag{3.32}$$

where ρ_s is the density of states at the surface. This means that the greater the rate of change of current with respect to increase in bias, the more tunnelling states are available at a given bias value. In terms of experimental implementation, the STM tip is held above the surface in a position dictated by a specified tunnel current set-point. This means leaving the tip in the same location for some time, to reduce creep and drift and ensure the tip remains in the same position during the measurement. The z feedback is then disabled, to prevent tip motion, and the bias is swept through a range of values, with the current measured for each bias value. Taking the gradient of the resultant $I(V)$ would result in the LDOS as a function of bias at the location of the tip. However, numerical differentiation to acquire $\frac{dI}{dV}$ can amplify any noise in the $I(V)$ signal and result in spurious features. A significant improvement in data quality is achieved by applying a small sinusoidal dither to the bias. This results in an oscillating signal in the current channel with the same frequency as the applied bias oscillation. These signals can be separated using a lock-in amplifier. Mathematically, we can consider the lock-in with respect to the reference signal V_{ref} (the applied dither) and output signal V_{out} (the output of the preamp, turning tunnel current into a

voltage); these are defined in basic sinusoidal form as follows:

$$V_{ref} = A_r \sin(\omega_r t + \theta_r), \tag{3.33}$$

$$V_{out} = A_o \sin(\omega_o t + \theta_o), \tag{3.34}$$

where A is the amplitude of each wave, ω is the frequency and θ the phase shift. The lock-in multiplies the output signal by its reference signal, giving:

$$V = A_r A_o \sin(\omega_r t + \theta_r) \sin(\omega_o t + \theta_o). \tag{3.35}$$

Using trigonometric identities, this can be written as:

$$V = \frac{1}{2} A_r A_o \underbrace{\cos((\omega_r - \omega_o)t + (\theta_r - \theta_o))}_{\text{Low frequency}} \underbrace{\cos((\omega_o + \omega_r)t + (\theta_o + \theta_r))}_{\text{High frequency}}. \tag{3.36}$$

Equation 3.36 demonstrates how the combined signal can be considered the sum of two cosine waves, one using the sum of the input frequencies and the other the difference. This signal can be passed through a low pass filter, removing the high frequency term and leaving the following:

$$V = \frac{1}{2} A_r A_o \cos((\omega_r - \omega_o)t + (\theta_r - \theta_o)). \tag{3.37}$$

Given that our reference frequency and the output frequency are the same, it can be further simplified:

$$V = \frac{1}{2} A_r A_o \cos((\theta_r - \theta_o)). \tag{3.38}$$

So our signal, after passing through the lock-in amplifier and the low pass filter, is a DC signal proportional to the amplitude of the output signal. Figure 3.5 showcases how this works in practice. A steeper $I(V)$ gradient is caused by an increased LDOS; this steeper gradient causes a larger amplitude in the output current oscillation, hence by recording the amplitude of the current oscillation, we can more accurately measure the change in LDOS, with much less noise. This technique works best at low temperatures, due to the interference of thermal excitation with the Fermi edge. At very low temperatures ($\sim$4K), the Fermi-Dirac distribution is practically a step function around the Fermi energy, meaning a very immediate change between filled and unfilled states. At higher temperatures, the function becomes more sloped, creating a more blurred Fermi edge and thus reducing the obtainable energy resolution.

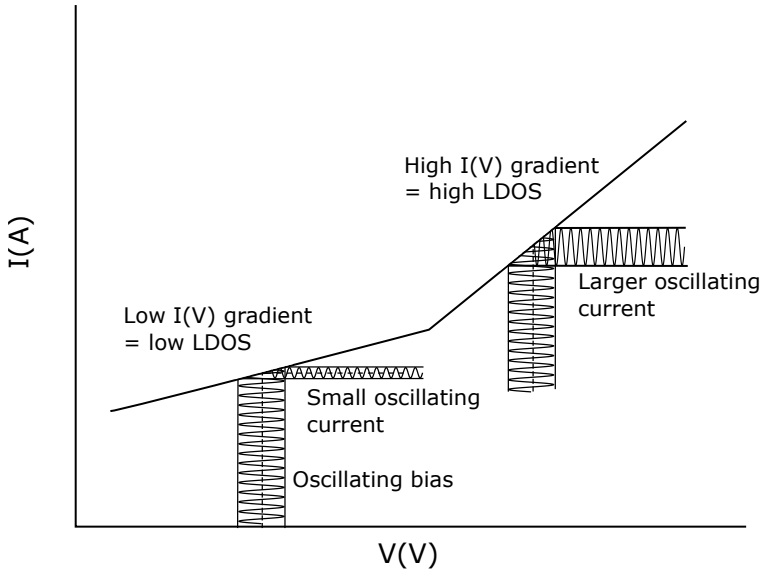

Figure 3.5: Visual representation of the impact of applying an oscillation to the input bias. An oscillating bias results in varying sizes of oscillating current depending on the $I(V)$ gradient, which in turn is affected by LDOS. In $\frac{dI(V)}{dV}$ spectroscopy, this phenomenon is utilised to measure LDOS, by applying a dither to the input bias, and measuring the amplitude of the outgoing current and transmuting into a bias. These signals are then multiplied and then run through a low pass filter, allowing measurement of the amplitude of the tunnel current dither and hence the LDOS.

3.1.5 General STM Operation

Feedback Modes

As mentioned in the opening of this section, the basic function of an STM is described by the rastering of an atomically sharp tip across a biased sample. There are two common modes by which this can be performed: constant height and constant current mode. Constant current mode is the most popular imaging mode of STM, and works by using a feedback system to maintain a constant current as the tip rasters across the surface. Based upon the exponential dependence of tip-sample separation and tunnel current, the Z motion of the tip is adjusted to maintain a specific tunnel current, moving closer to increase the current, and further away to decrease. This Z motion can be approximately mapped to the topography of the surface, as shown in Figure 3.6a). At each point in X and Y,

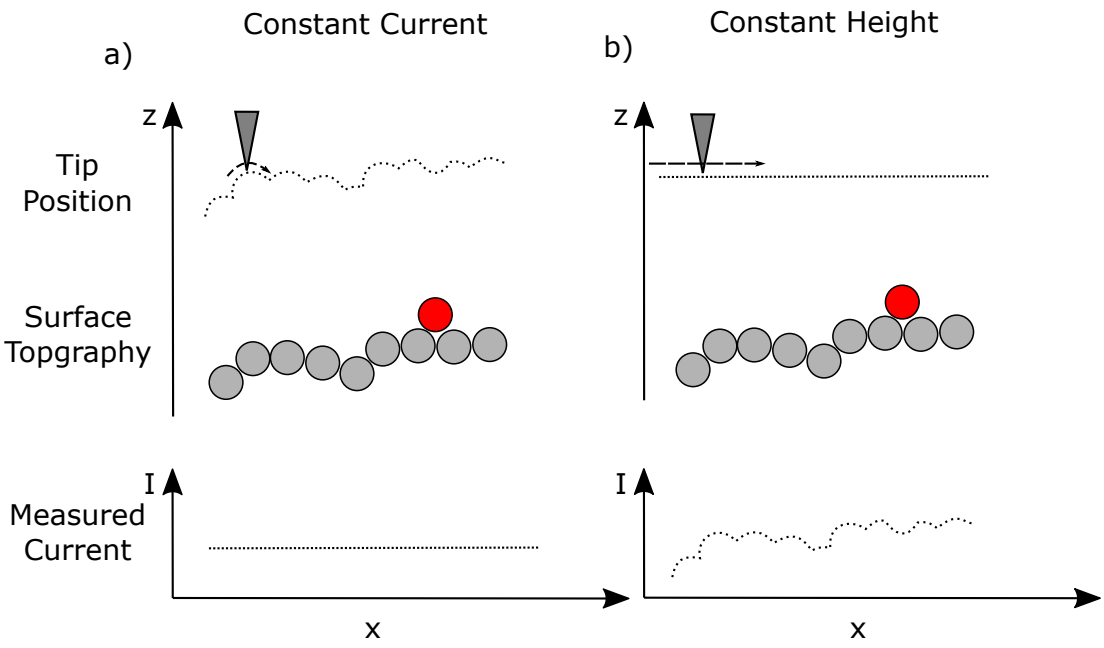

Figure 3.6: The two main modes of STM operation. a) Constant current mode. The most widely implemented mode, feedback loops attempt to keep the tunnel current at a constant set point value, by adjusting the Z position of the tip. These changes in Z position are used to create the image of the surface. b) Constant height mode. In this mode, the tip is kept at a constant Z position and the current varies with the height of the surface. This varying current is used to create the image of the surface. In each, grey circles represent surface atoms, and red circles represent contaminant, with a reduced LDOS relative to the substrate atoms.

the Z position is recorded. Each of these Z positions is arranged into a 2D grid as one pixel each, creating a 2D image of the surface topography. In constant height mode, the tip is held at a constant height, with the current varying as the surface varies in distance from the tip. In this mode, each pixel is a recording of the current value at that particular coordinate, to assemble the full 2D image.

In each of these modes, one issue that arises is that a simple interpretation of tip-height in terms of topographic height breaks down if the LDOS is not constant across the substrate. For a material with a non-uniform LDOS, regions may have a lower LDOS (such as shown in the red circle in Figure 3.6), the apparent height will appear physically lower than the surrounding material; this is due to the fact that the tip will move down to maintain a constant current (accounting for

the lower LDOS). This is why the topography mapped by an STM is referred to as apparent height, as it is in fact mapping the LDOS, which can vary due to reasons other than topography (including changes in chemical composition or local bonding arrangement, within the material). Each mode has its own weaknesses: constant current mode images can exhibit artefacts introduced by the response of the STM feedback loop, and constant height mode by definition, has no mechanism for avoiding large surface features, causing crashing. Crashing is an instance in which the tip and surface strongly interact, often transferring material between the two and damaging both tip and surface. Artefacts caused by feedback are mostly based around reacting too quickly or too slowly to change in LDOS, giving a false impression of the LODS within the tip height. A common form of feedback artefact is so-called "ringing", whereby feedback gain is too high, causing the STM tip to repeatedly overshoot the set point current, oscillating up and down and causing a periodic oscillating artefact on the image. System cooling can help with some image distortion and crashing, as this reduces piezoelectric creep and thermal drift, but avoiding crashing in constant height mode even at very low temperatures is non-trivial, hence constant current is the most popular mode. Regardless of mode, peak STM performance is obtained on atomically flat surfaces, with much emphasis in sample preparation going towards obtaining large, flat terraces.

Tip Motion

STM requires an exceptionally small vacuum gap between tip and sample, and hence requires exceptionally precise control over tip motion. In order to achieve this, whilst also allowing for covering the larger distance from a fully retracted tip position to the sample, STM utilises both fine and coarse motion. Piezoelectric crystal is a material whose lattice expands or contracts when a bias is applied, proportional to the size of the bias. These lattice displacements can be large, or extremely small, making piezos perfect for both fine and coarse motion. Coarse motion in an STM is handled by a slipstick motor, capable of moving the tip the several millimeters clearance required for safe and effective sample and tip transfer. The tip is mounted onto a low friction slide, which is itself placed onto

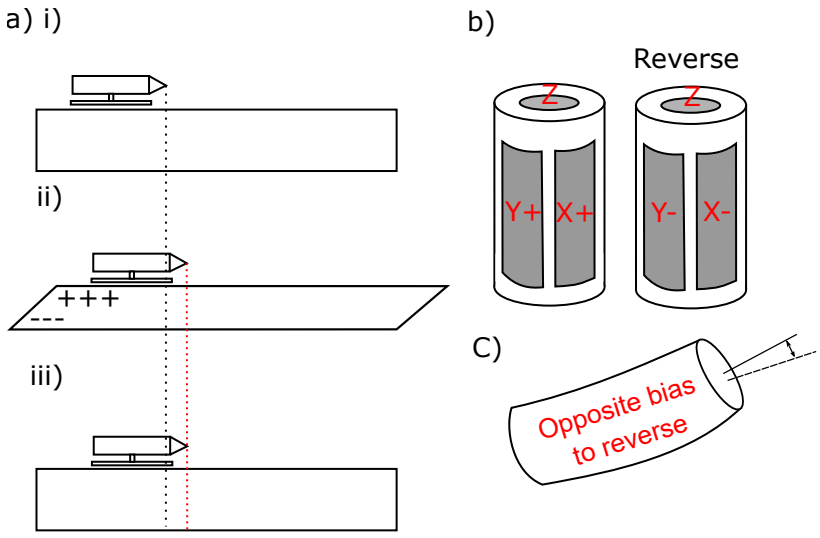

Figure 3.7: a) The mechanism of a piezoelectric slip-stick motor.i) Initially, the mounted tip sits atop the crystal, held in place by friction. ii) The piezo lattice is slowly distorted (shear) *via* the application of opposite biases on each side, carrying the tip with it. iii) The bias is rapidly removed and the piezo returns to the initial shape. The tip remains where it is as it is mounted on a low friction runner. b) A piezoelectric scan tube with mounted electrodes to cause extention/contraction in 4 different directions. c) An example of how the activation of these electrodes can distort the tube and cause the tip to move.

a piezoelectric crystal, as shown in Figure 3.7a)i). To make a coarse step, a large bias is slowly applied to each side of the crystal, such that it elongates, as shown in Figure 3.7a)ii). As the motion of the crystal is slow, the friction holding the tip onto the crystal moves it forward. Once at full extension, the bias is removed, and the stage reverts to the original shape, at which point the tip *slips* due to the low friction runners, and then *sticks*, as shown in Figure 3.7a)iii) when the crystal stops moving. This process can be repeated many times to move the tip the length of the crystal. This is done in X, Y and Z directions, with a separate piezo motor for each, assembled into a stack.

Fine motion is also required, and once again utilises piezoelectric crystal. Fine control of an STM tip requires picometer precision, and with application of appropriate voltages this can be obtained using piezoelectric crystals. One common construction is shown in Figure 3.7b-c), known as a tube scanner. On each quadrant of the crystal tube is an electrode through which voltage can be

applied to manipulate the tip in the X and Y directions, with the Z direction handled by a central electrode. This allows the exceptional, picometer scale lateral and vertical control requisite for STM.

3.2 Photoelectron Spectroscopy

Photoelectron spectroscopy (PES) is a term describing a collection of techniques that exploit the photoelectric effect to determine information about target molecular systems and surfaces. The photoelectric effect, put simply, is the emission of electrons from a material following exposure to photons. Mathematically, this can be described as follows:

$$KE_{max} = h\nu - \phi_s - E_B, \tag{3.39}$$

where KE_{max} is the maximum kinetic energy of the emitted photoelectron, h is Planck's constant, ν is the frequency of the incident photon, E_B is the binding energy of the electron relative to the Fermi level of the substrate, and ϕ_s is the work function of the material. Photoelectric emission only occurs if the energy of the incoming photon is enough to overcome the binding energy holding the electron in place. Hence, we can learn about the electronic structure of a material by encouraging this effect and measuring the kinetic energy of the resultant electrons.

3.2.1 Electronic Structure

Electrons in an atom are organised into discrete orbitals, possessing specific energies. When considering electrons in molecules, there are two distinct categories: those that participate in bonding, and those that do not. The orbitals which do not participate are known as core orbitals; these electrons are the mostly tightly bound to the nucleus, occupy the lowest potential energy molecular orbitals (highest binding energy), and are localised around a specific atom, rather than the molecule as a whole. While these orbitals do not participate in bonding, they can be affected by them, resulting in shifts in binding energy, as discussed later. The orbitals engaged in bonding are the valence orbitals, which delocalise and overlap with the valence orbitals of other atoms. These are associated with the molecule in general, rather than a specific atom.

The valence orbitals for molecules can be split into two categories: HOMOs and LUMOs. HOMOs are the occupied valence states, with the closest to the Fermi level being HOMO, then HOMO -1, HOMO -2 etc. moving further from

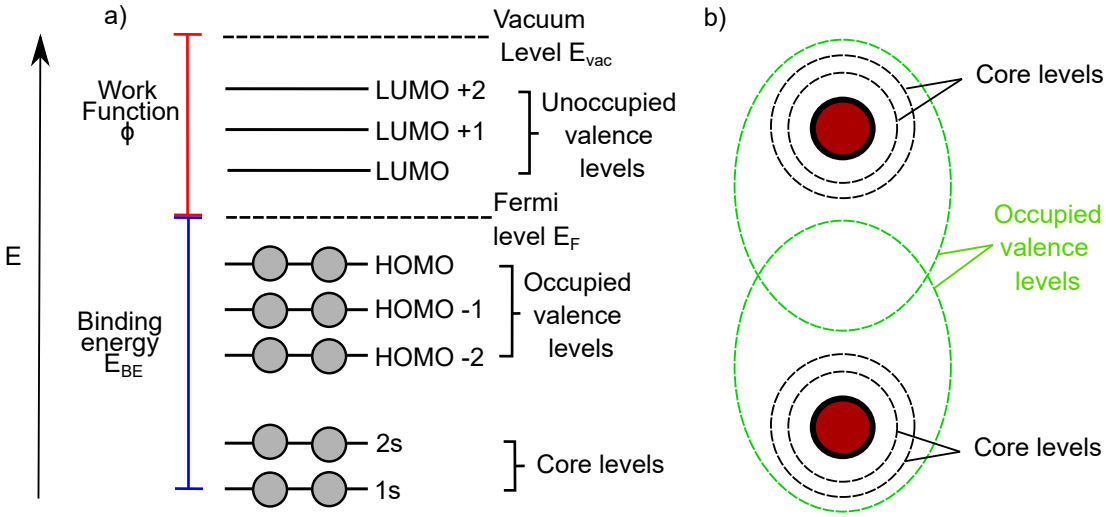

Figure 3.8: a) Example diagram of the energy levels of a molecule. b) Diagram showing the interaction between valence orbitals of atoms in a molecule.

the Fermi level, as shown in Figure 3.8a). The core orbitals are labelled by the quantum numbers required to describe the orbitals, and are written as nl, where n is the number of the shell and l is the angular momentum. In Figure 3.8a), $1s$ and $2s$ are shown, meaning the first and second shells with angular momentum 0 (s shells). We can also see in Figure 3.8a) the meanings of binding energy E_B , and ϕ_s work function: the binding energy is the energy required to raise an electron to the Fermi level E_F, and the work function is the energy required to raise the electron from the Fermi level to the vacuum level E_{vac}. Figure 3.8b) shows the interaction of valence orbitals to form a molecular HOMO, leaving core levels untouched.

3.2.2 XPS

X-ray photoelectron spectroscopy (XPS) is possibly the most widely used photoelectron based surface analysis technique. As a tool, XPS dovetails well with STM, as it provides chemical sensitivity by probing the core levels of atoms, something that STM lacks. XPS can also provide information on the bonding state of the atoms present, allowing for a clearer picture of the chemical environments of a molecule-substrate system.

As XPS accesses the core levels of atoms present, these are not typically orbitals involved directly in bonding. By recording the kinetic energy of ejected

electrons and controlling the energy of the input photons, we can determine the binding energy of these core levels. The binding energy of electronic states is unique to each element, and thus can be used to identify the element present by using a reference table. In practice, we rework equation 3.39 as follows:

$$\underbrace{E_B}_{\substack{\text{Referenced against} \\ \text{known values}}} = \underbrace{h\nu}_{\text{Controlled}} - \phi_a - \underbrace{E_{KE}}_{\text{Measured}}, \tag{3.40}$$

where ϕ_a is the work function of the analyser; the work function of the surface is irrelevant, as the electron's kinetic energy once it escapes to vacuum is the measured variable. Because the fermi level of the sample and the analyser are kept at equilibrium with one another, only the work function of the analyser matters. The influence of the work function on the analyser is in practice a shift of a few eV in the binding energy, which can be compensated for in post-processing. In metals, the Fermi level can be measured in XPS, a step function fitted to this, and this step function shifted to 0. At room temperature, the Fermi edge won't be a clean step function, and more of a gradual slope, but this can be fitted to find the centre of the function in a similar manner. When using a lab source, the resolution of the Fermi level can be too poor to use this method, as the cross section of the metal surface orbitals contributing to the fermi electrons is very small at the photon energies produced by a lab source. In these instances, a known substrate peak with well-defined binding energy is often used for calibration.

Core Levels and Chemical Shifts

While it is the valence orbitals which undergo the most severe change during bonding, forming hybrid orbitals, these changes in electron density across the molecule can perturb the core levels, shifting the binding energy a small amount (frequently of the order ~ 1 eV). Given that the electron density across a molecule can vary greatly from atom to atom, this causes differing levels of perturbation and thus different magnitudes of binding energy shift. This is well demonstrated in Figure 3.9, where each carbon atom in the ethyl trifluoroacetate molecule has a unique combination of covalently bonded atoms, leading to a different chemical shift for each atom. These shifts can be understood with regard to the elec-

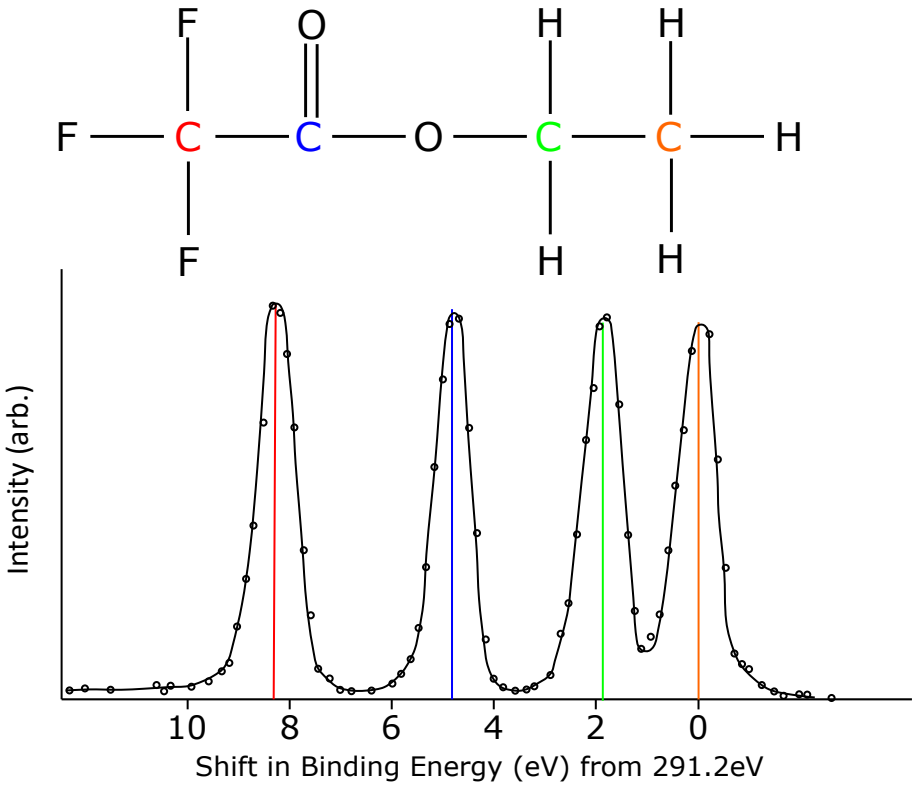

Figure 3.9: XP spectra of an ethyl triflouroacetate molecule, demonstrating how differing chemical environments result in different peak shifts. The colours of each peak relate to a different carbon environment, as labelled by the same colour on the molecular structure above. Based on the work of Siegbahn [101]

tronegativity of the neighbouring atoms; in this instance, the CH_3 group does not neighbour moieties with electronegative character, and here is defined as exhibiting zero chemical shift. Where a carbon atom is surrounded by species with electronegative character a shift in BE is observed; with greater BE shifts arising from higher degrees of electronegative character (e.g. carbon within a CF_3 environment shifts the most, with smaller shifts for C=O and C-O, respectively, as electronegativity of the bonded species decreases). This effect is useful in identifying the chemical environments of the elements present, and most importantly can be used to identify reactions following exterior input (heating, gas dosing etc.), as a peak shift would normally be expected following a reaction which results in a change in the local bonding environment of an atomic species.

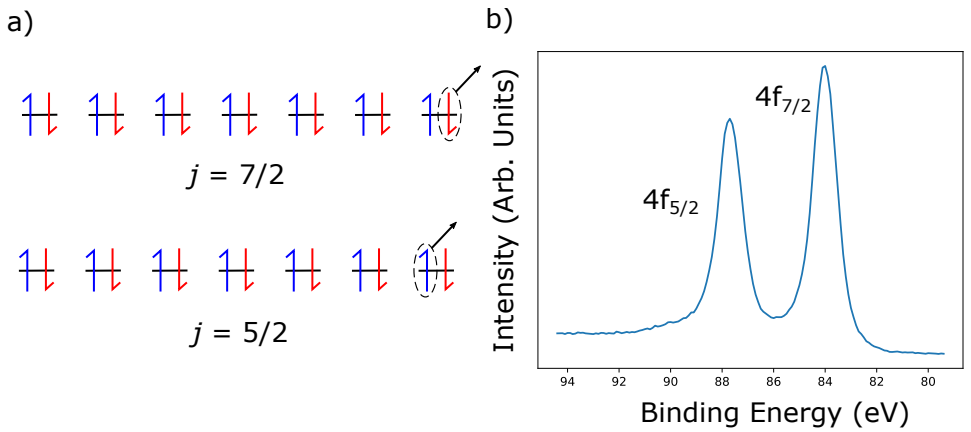

Figure 3.10: Example of spin-orbit splitting in the Au $4f$ orbital. a) Shows the two possible electron structures of the Au $4f$ state following the removal of either an up or down electron. b) XP spectra showing the Au $4f$ region with characteristic split peaks.

Spin-orbit Splitting

Some peaks in XPS are observed to split into two components. This is caused by electron spin, another quantum number alongside the aforementioned n and l, with values of $\pm 1/2$. Electrons in orbitals will form 'up-down' pairs, and interact to conserve total angular momentum j ($j = l + s$). When an electron is removed from an orbital, an unpaired electron in either the up or down state remains. Depending on whether the remaining electron is in up or down state, two different j states can be produced, as shown in Figure 3.10a); this only applies in orbitals where $l > 1$. s orbitals have an angular momentum of 0, and only contain 2 electrons, so the magnitude of j is $1/2$ regardless of the electron ejected.

As these two j states will have different binding energies, two peaks are produced. The relative intensities of these two peaks is determined by the degeneracy (number of electrons) of the state, calculated by $(2j + 1)$. j values and intensity ratios for commonly examined orbitals are shown in Table 3.1 In the example shown in Figure 3.10a-b), the Au $4f$ state has an l value of 3, which leads to j values of $7/2$ and $5/2$, producing the expected intensity ratio of 4:3, and an energy split of 3.7 eV.

Inelastic Effects and Auger Peaks

When considering electrons excited during XPS, it is assumed in a first approximation that the electrons measured are directly excited from the core level to the vacuum, with kinetic energy left over. It is also assumed that the electrons within an atom are unperturbed by the removal of a core electron - this is known as Koopman's theory: that the final state of a system will be the same as the initial state, minus an electron. However, in practice, the formation of a hole in a core state leaves the atom in an unstable state. This leads to internal electron re-arrangement, changing the energy levels of the initial and final state, and thus lowering the apparent kinetic energy of an emitted electron, raising the apparent binding energy. Two phenomena of this kind commonly occur, known as shake-up and shake-off emissions, shown in Figure 3.11a-b). In a shake-up feature, shown in Figure 3.11a), the electron excited from the core level also induces an electron transition from a valence state to an unoccupied state, requiring energy E_{su}. This causes the electron to lose that energy, so appearing to have a higher binding energy. A shake-off emission, as shown in Figure 3.11b), is very similar, but here the secondary electron is also given enough energy to escape the atom. In both instances, the primary photoelectron loses kinetic energy, and so appears to have a higher binding energy.

Another phenomenon which can lead to the emission of electrons from non-core orbitals, is Auger decay. This occurs once an electron has been photoemitted beyond the vacuum level, leaving behind a core hole. An electron from an occupied valence state recombines with the core hole, causing another valence electron

Shell	j values	Intensity ratio
s	1/2	n/a
p	1/2, 3/2	1:2
d	3/2, 5/2	2:3
f	5/2, 7/2	3:4

Table 3.1: Spin-orbit splitting j values and intensity ratios for commonly examined orbitals

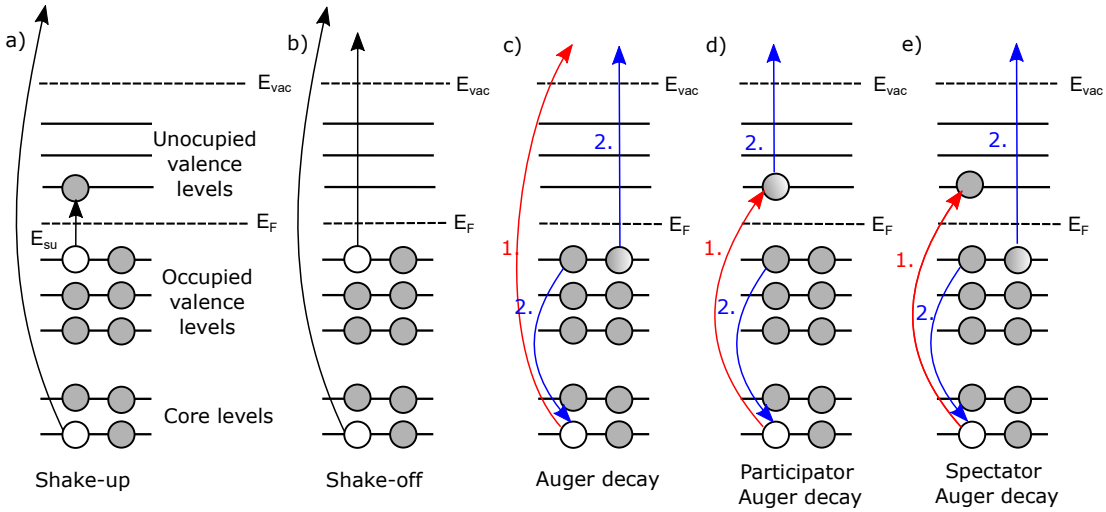

Figure 3.11: a-b) Energy level diagram showing the photoelectric process leading to a) shake-up and b) shake-off emissions. c-e) Shows the processes behind the different kinds of Auger electron emission. d-e) Are known as resonant Auger emissions.

to be released from the atom. These electrons have a set kinetic energy, as the energy given by the core hole decay is identical each time, so one method of identifying an Auger peak in XPS is to alter photon energy and re-scan the same region; an Auger peak will appear to shift in binding energy, as it will have exactly the same kinetic energy independent of the incoming photon.

Two other types of Auger decay exist, occurring if an electron from a core state is not emitted to vacuum immediately, but is excited to an unoccupied valence state. Following this, as an electron from a valence state recombines with the core hole, either the electron that was excited to the previously unoccupied state (participator decay, shown in Figure 3.11d)) or an electron in an occupied state (spectator decay, shown in Figure 3.11e)). These are known as resonant Auger emissions.

Surface Sensitivity

One advantage of XPS for the analysis of 2D surface structures, is the inherent surface sensitivity of the technique. While the X-rays used for XPS are of sufficiently high energy to penetrate a few micrometers into the surface, the electrons released at this depth fail to reach the surface due to inelastic scattering.

The further an electron travels through the bulk, the more likely it is to experience inelastic scattering events, losing energy and thus failing to escape the surface. Those electrons that do retain enough energy to escape, but have still lost some, appear to have a higher binding energy than the true binding energy of their state. As many outgoing photoelectrons experience these events, and lose varying amounts of energy, they make up a broad background of photoelectrons which can be seen in all XP spectra. Inelastic scattering events include phonon production (effectively lattice vibrations) and plasmons (quantized oscillations of electron gas). The intensity of an electron beam I as it travels a distance d through a bulk material can be related to the initial intensity I_0 by:

$$I(d) = I_0 e^{-\frac{d}{\lambda(E)}}, \tag{3.41}$$

where $\lambda(E)$ is the inelastic mean free path. This is dependent on the energy of the excited electron. While the material does influence this slightly, generally the behaviour is the same across all solids. This leads to the creation of a "universal curve" for the inelastic mean free path of electrons in a solid, as shown in Figure 3.12.

3.2.3 NEXAFS

Near-edge X-ray absorption fine structure (NEXAFS) is an X-ray spectroscopy tool useful for examining systems on surfaces. Instead of core states, this technique allows the unoccupied states to be inspected - provided they have an associated resonant Auger transition. In this technique, the photon energy is swept across a range of values, chosen to match the difference between an occupied core level and unoccupied levels (resonance). These unoccupied levels are often more greatly perturbed by changes to the overall electronic structure, than core levels, and thus shifts in NEXAFS can be larger and more obvious than those in XPS, making it a supremely sensitive technique for identifying chemical changes. [102] In this section, I will be considering molecular systems, and hence will refer to LUMO states instead of simply unoccupied states.

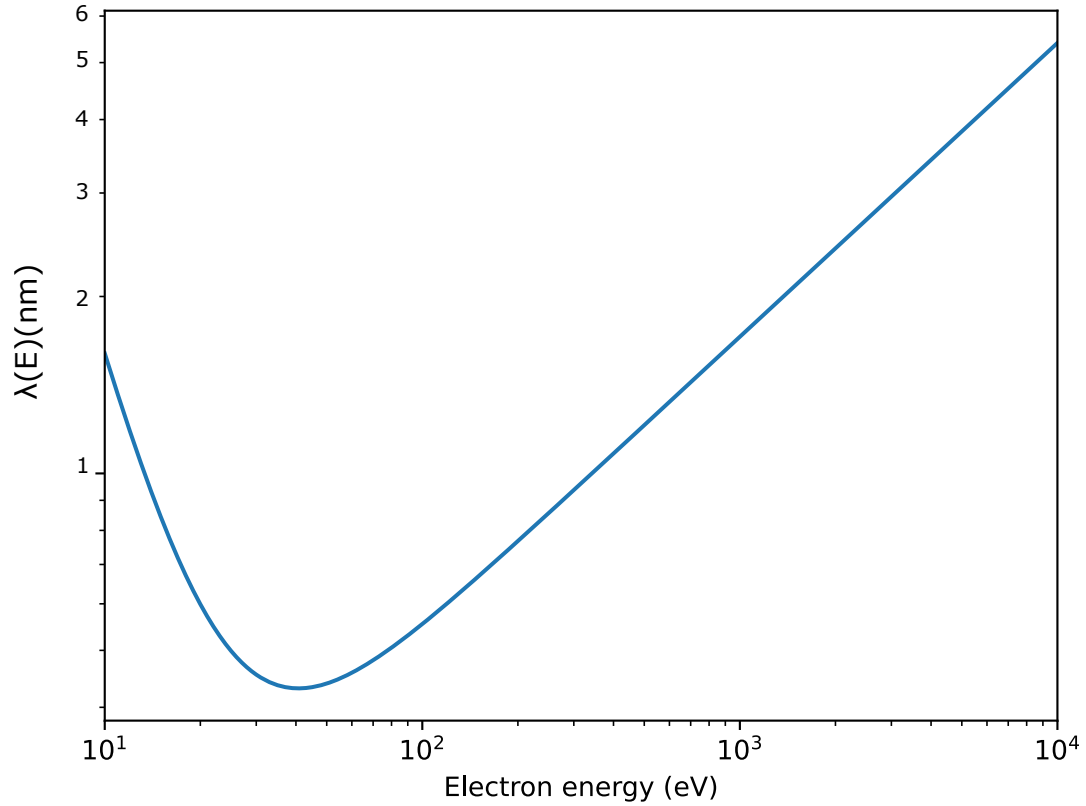

Figure 3.12: The universal curve for the inelastic mean free path of an electron travelling through a solid. This is calculated with the following equation: $\lambda(E) = \frac{143}{E^2} + 0.054\sqrt{E}$

Resonant Auger Measurements

To measure X-ray absorption, which forms the basis of NEXAFS, a variety of signals can be measured. Resonant auger electrons are often used, as they are proportional to the number of electrons excited to a particular energy level, allowing for the measurement of density of states of unoccupied valence orbitals. As these electrons have a specific kinetic energy, they can be easily identified. These emissions are shown in Figure 3.11. Measurement of emitted photons from core-hole recombination is called fluorescence yield detection, and can be used, but is not used in this thesis and thus will not be covered here. Figure 3.13 shows a typical Auger yield (explained in the following section) NEXAFS spectrum and appropriate orbital labels for a light element, such as nitrogen or carbon. In these elements, the orbitals are either π or σ, and so the unfilled valence orbitals may be considered as π^* or σ^* antibonding orbitals. At higher energy levels, the states become closer together, so σ^* orbitals often appear as continuous.

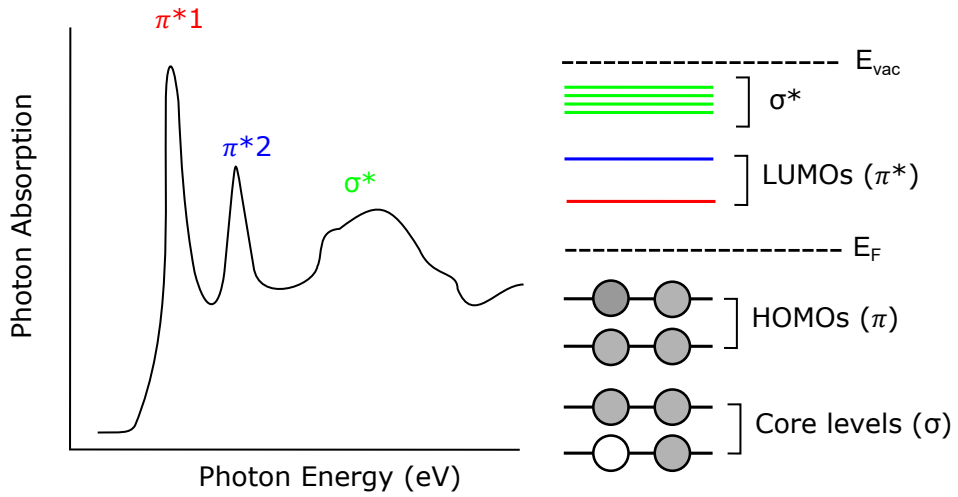

Figure 3.13: Shows a typical NEXAFS spectra and orbital labelling.

Photon Yields

The relationship between the energy of the incident photons and the electron yield is illustrated in Figure 3.14a). Part a) illustrates the changing photoemission peaks as photon energy increases. At photon energy $h\nu_1$, electrons in core levels A and B do not have the requisite energy to escape the material, however electrons in valence band VB do, causing a photoemission peak, as would be seen in XPS. At increased photon energy $h\nu_2$, core level B has enough energy for photoemission, forming a new peak, and the photoemission peak caused by electrons from VB has shifted higher in kinetic energy. At $h\nu_2$ a core hole is created when an electron is excited from core level A to an unoccupied valence state, which results in a resonant Auger decay, giving rise to a peak at this specific photon energy. At $h\nu_3$, all three energy levels have enough energy for photoemission. In this diagram, for simplicity, I have shown the resonant Auger peak disappearing at $h\nu_3$, as the photon energy no longer matches the transition exactly, but inelastically excited electrons may still create the conditions for resonant Auger emission, and so the peak fall off may be more gradual.

There are three common acquisition modes for NEXAFS: total electron yield (TEY), partial electron yield (PEY) and Auger electron yield (AEY). These are effectively setting a window of kinetic energies of which electrons possessing these energies will be recorded; TEY records them all, PEY starts at a particular kinetic energy and records from there onwards, and AEY is a specific window of

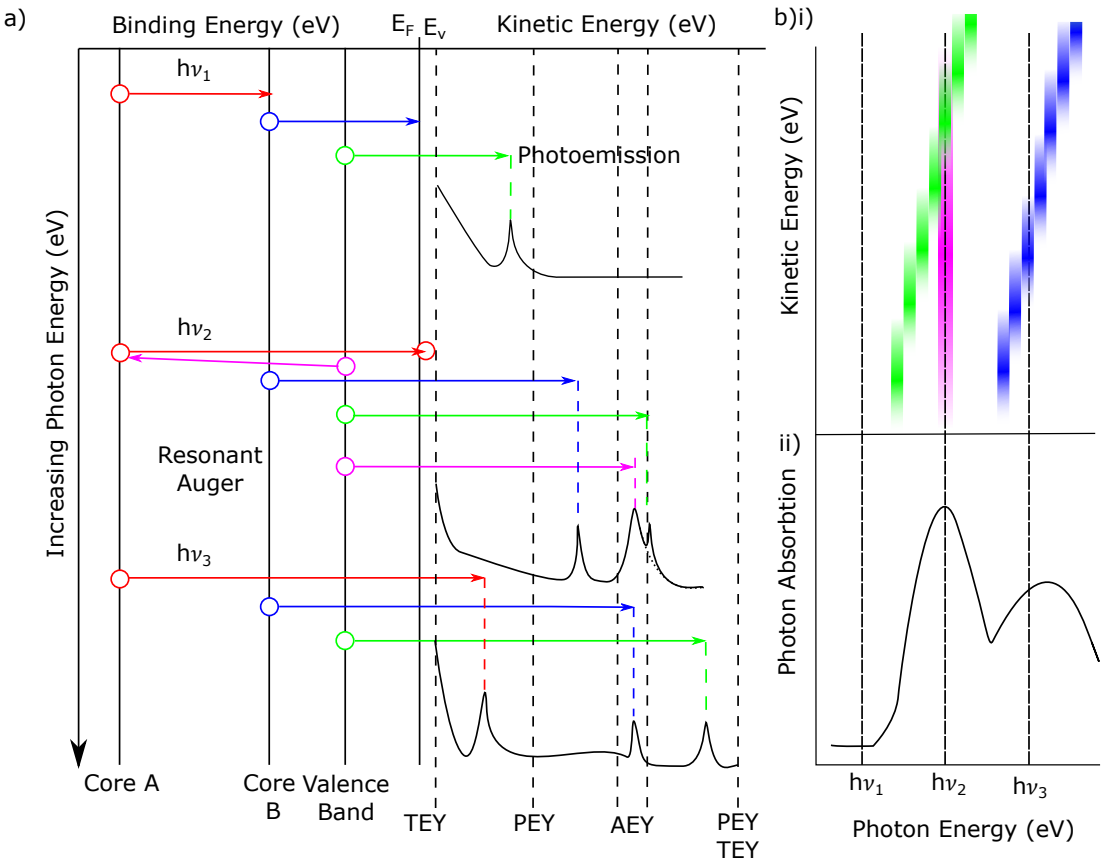

Figure 3.14: a) Energy level diagram and photoemission spectra at different photon energies for an atom containing core levels A and B and valence band VB. As photon energy increases, the kinetic energy of electrons released by direct photoemissions increases. Resonant Auger electrons are not observed until the energy of the incoming photon is correct for the required transition. At the bottom, kinetic energy windows for the three acquisition modes are marked. b) Heat map of example electron intensity at different kinetic energies and photon energies for the energy levels shown in part a), as would be captured during an Auger electron yield measurement, and example NEXAFS spectra. Based on diagram by Stöhr [102].

energies around those expected from a particular Auger emission. In practice, when looking at 2D systems of molecules on surface, Auger electron yield is most appropriate, due to reducing the contribution of bulk electrons, leading to a better signal-to-noise ratio. Auger electron yield is also most appropriate for measuring resonant Auger emission, allowing for unoccupied states to be probed.

AEY does have some issues, however - when photoemission peaks enter the narrow kinetic energy window of an AEY measurement, they can appear as broad peaks. This is shown in Figure 3.14b), where roaming photoemission peaks (here green and blue colour, coded to match transitions from Figure 3.14a)) change in kinetic energy as photon energy increases, leaving a streak across the heatmap in b)i), showing up as peaks in b)ii). When using a hemispherical analyser, at each photon energy, the number of photoemissions at each kinetic energy is recorded, and can be displayed in a heat map like that shown in b)i). These columns are then summed to show the NEXAFS spectra shown in b)ii). Using the heat map, these roaming peaks can be identified and removed, but some systems filter the electrons by kinetic energy and return a single number of counts, eliminating the possibility of identifying these peaks visually. Hence, it can sometimes be useful to set up partial electron yield; if the range of kinetic energies is wide enough, the shifting peak will move across the full range of photon energies, and thus average into the background. With TEY, the contribution from the surface is usually too great for measurements of 2D surface structures.

Angle Resolved NEXAFS

Polarised X-rays have an oscillating electric field in one direction perpendicular to the direction of travel. When the oscillation of the wave is in the same plane as a target orbital's transition dipole moment (TDM), the probability of the transition is increased (resulting in a greater intensity of the resonances observed within NEXAFS). For example, Figure 3.15 depicts an aromatic ring with characteristic aromatic σ^* and π^* TDM orientations, namely σ^* in the plane of the molecule and π^* perpendicular. By varying the angle of incidence, the intensity of peaks associated with excitation to orbitals composed of different bonding orbitals changes: grazing incidence increasing the intensity of the π^* orbital, and normal incidence the intensity of the σ^* orbital. Another useful angle is the so called "magic angle" of 55°, which provides an equal contribution of perpendicular and flat orientation bonds, giving a balanced overview of the states present. This can be explained by considering the angular dependence of absorption intensity,

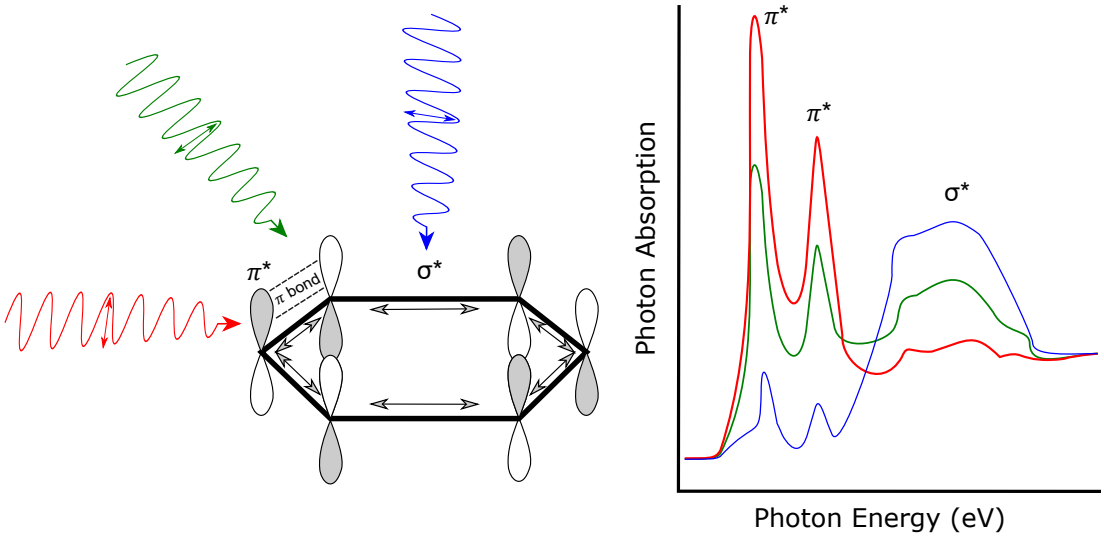

Figure 3.15: The orientations of σ^* and π^* orbitals on an aromatic ring. Three incident X-rays of differing angles, grazing incidence, magic angle and normal incidence, and an example NEXAFS spectra for each angle.

given by the following [103]:

$$I \propto 3\cos^2\theta - 1, , \tag{3.42}$$

setting $I = 0$ and rearranging, we find the following:

$$\theta = \cos^{-1}(\sqrt{\frac{1}{3}}) = 55°. \tag{3.43}$$

By varying the angle of the incident beam, and measuring the intensities of the peaks, information about the orientation of the bond, and hence the orientation of the molecule, can be obtained.

When attempting to discern the angle of the TDM with the surface normal, the vectors can be divided into two types: vector and plane. In Figure 3.15, the π^* orbitals are defined as a vector type, as they are out of the plane of the molecule, and the σ^* is plane type as it is in plane with the molecule. For a given incident angle θ, the expression for the intensity I of a photon absorption peak is given by the following [103]:

$$I = C[PI^{\parallel} + (1 - P)I^{\perp}], \tag{3.44}$$

where C is a constant, P is the polarisation constant (normally around 0.85), $I^{\parallel}$ and $I^{\perp}$ are the intensity contributions of the parallel and perpendicular components respectively. On substrates of three-fold or higher symmetry (111 plane in

FCC crystals such as Ag, Au, and Cu qualify), for vector orbitals these quantities can be calculated as follows [103]:

$$I_v^{\parallel} = A(\cos^2\theta\cos^2\alpha + \frac{1}{2}\sin^2\theta\sin^2\alpha), \tag{3.45}$$

$$= \frac{A}{3}[1 + \frac{1}{2}(3\cos^2\theta - 1)(3\cos^2\alpha - 1)], \tag{3.46}$$

and

$$I_v^{\perp} = \frac{A}{2}\sin^2\alpha, \tag{3.47}$$

and for plane orbitals:

$$I_p^{\parallel} = B(1 - \cos^2\theta\cos^2\gamma - \frac{1}{2}\sin^2\theta\sin^2\gamma), \tag{3.48}$$

$$= \frac{2B}{3}[1 + \frac{1}{4}(3\cos^2\theta - 1)(3\cos^2\gamma - 1)], \tag{3.49}$$

and

$$I_p^{\perp} = \frac{B}{2}(1 + \cos^2\gamma), \tag{3.50}$$

where A and B are normalisation constants, θ is the angle to the surface of the incident ray, and α and γ are the angle of the vector orbital and normal of a plane orbital to the surface normal respectively, as shown in Figure 3.16. An estimate of bond angle can be formed from just two measurements, the grazing and normal incidence spectra. The ratio of the intensity of the resonance peak for the bond at each of these angles can be used to determine bond angle; this is determined by finding the area under a target peak within a NEXAFS spectrum.

Given equations 3.44-3.50, and taking the measured resonance peak intensity at the grazing and normal incidence as I_G and I_N respectively, we can combine as follows for vector orbitals:

$$I_R = \frac{I_G}{I_N} = \frac{\frac{AP}{3}[1 + \frac{1}{2}(3\cos^2\theta_1 - 1)(3\cos^2\alpha - 1] + (1-P)\frac{1}{2}A\sin^2\alpha}{\frac{AP}{3}[1 + \frac{1}{2}(3\cos^2\theta_2 - 1)(3\cos^2\alpha - 1] + (1-P)\frac{1}{2}A\sin^2\alpha}, \tag{3.51}$$

or for plane orbitals:

$$I_R = \frac{I_G}{I_N} = \frac{\frac{2PB}{3}[1 + \frac{1}{4}(3\cos^2\theta_1 - 1)(3\cos^2\gamma - 1] + (1-P)\frac{1}{2}B(1 + \cos^2\gamma)}{\frac{2PB}{3}[1 + \frac{1}{4}(3\cos^2\theta_2 - 1)(3\cos^2\gamma - 1] + (1-P)\frac{1}{2}B(1 + \cos^2\gamma)}. \tag{3.52}$$

We can plot the change in I_R as we vary α or γ, as shown in Figure 3.16. This means an estimate of bond angle can be calculated from just two measurements,

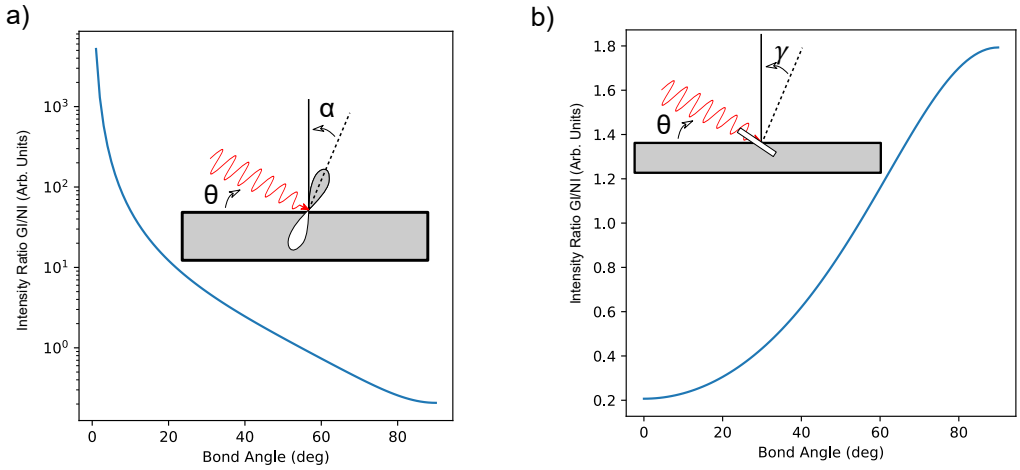

Figure 3.16: a) Plot of the ratio of grazing and incidence peak intensities against the angle of the target vector bond to the surface normal, as defined by Stöhr. [103] Inset is a diagram showing that θ is the angle of the incident ray to the surface, and α is the angle of the vector bond to the surface normal. b) Plot of the ratio of grazing and incidence peak intensities against the angle of the target plane bond normal to the surface normal. Inset is a diagram showing that θ is the angle of the incident ray to the surface, and γ is the angle of the vector bond normal to the surface normal.

however the error margin on this can be large. For further accuracy, measurements can be taken at multiple beam incidence angles. Using Eqn. 3.46, the change in resonance peak intensity can be modelled for different angles of α with changing θ, as shown in Figure 3.17.

With resonance intensities from a range of angles, least squares fitting algorithm can calculate the angle of the bond. This technique is more accurate but requires more measurements, which can be time-consuming. Knowing the angles of particular bonds can be revealing with respect to progressing surface chemistry. Usually, as heat is added to a system, it can progress to a more energetically favourable position, which often features molecules becoming more closely adhered to the surface, increasing molecular flatness. Even when this is not the case, they can form coordination systems that lead to a greater degree of ordering. In cases where the orbitals under investigation are disordered, the angle resolved NEXAFS will return a tilt angle of 55°; deviation from this angle, as a result of heating the molecule-substrate system, is often interpreted as an

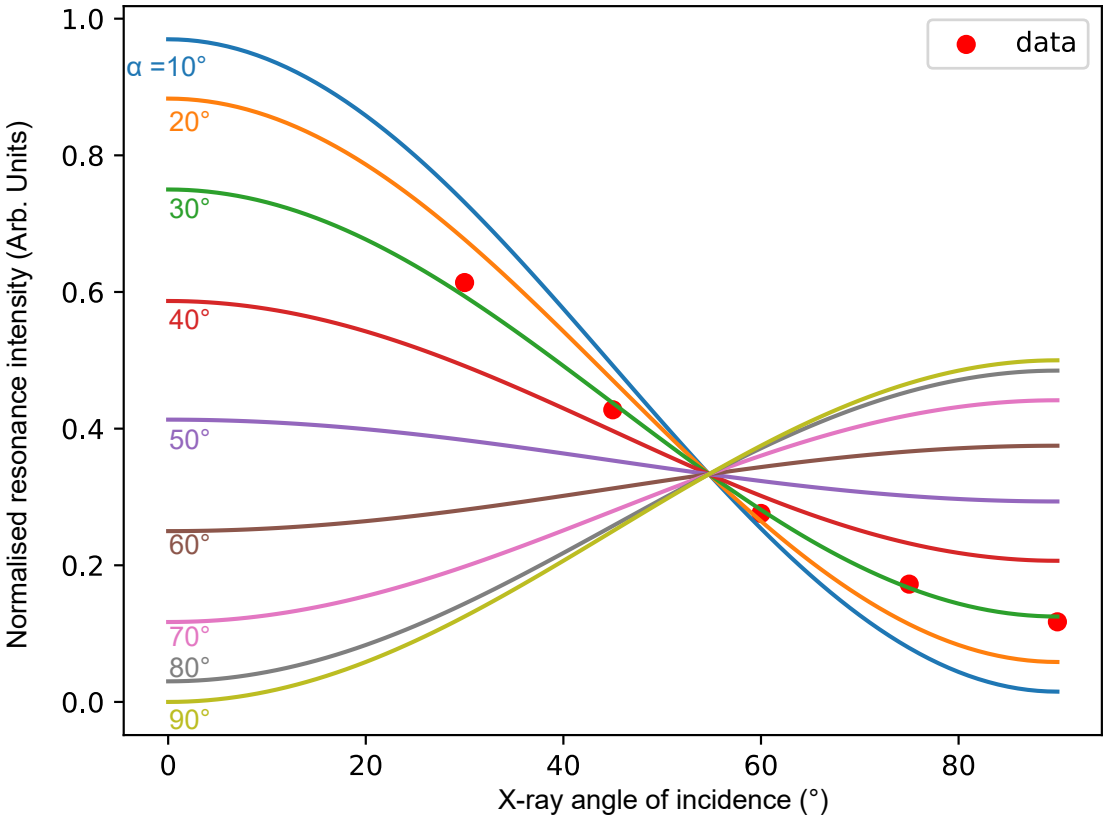

Figure 3.17: Example plot showing the varying resonance intensity with X-ray angle of incidence for a bond angle α varying from 10-90°, with example data. In this instance, the bond angle is estimated to be 29°.

evolution to a more ordered surface state. [104]

NEXAFS probes unoccupied electronic states, providing key information on the changes resulting from the filling of orbitals during chemical reactions. Due to high angular sensitivity, the changing intensity of resonance peaks with the varying angle of incidence can also provide conformational information about the tilt of molecules relative to the surface. Within this thesis, this approach is utilised to examine two on-surface systems in chapter 6 and chapter 7.

3.2.4 XSW

X-ray standing wave (XSW) is an X-ray spectroscopic structural analysis technique that provides sub-Ångstrom structural characterisation of a target species with respect to the substrate. The technique can provide chemically specific structural information, as the chemical sensitivity of XPS is used to identify key species which can provide structural information *via* XSW analysis. As the name

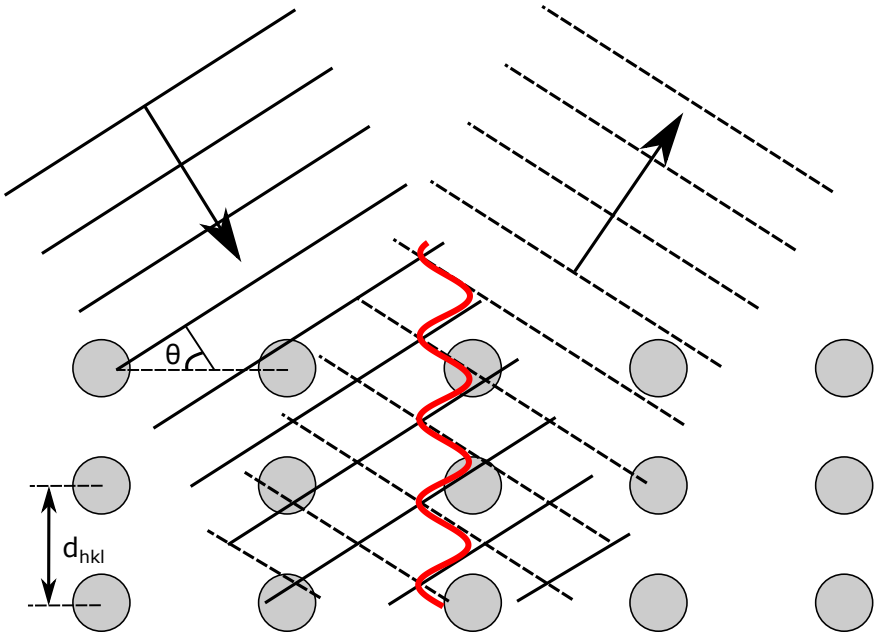

Figure 3.18: Incident and reflected waves forming a standing wave (red) during XSW. Also labelled are the atomic spacing d and angle of incidence θ.

implies, XSW involves the creation of an X-ray standing wave. This is formed by interference between the incident beam and reflected beam, which is created when the Bragg condition has been met, and therefore requires a highly ordered crystalline substrate. A schematic showing the general concept is shown in Figure 3.18.

The Bragg condition is met when an incident X-ray of wavelength λ satisfies the following:

$$n\lambda = 2d_{hkl}\sin\theta, \tag{3.53}$$

where n is the diffraction order, d_{hkl} is the atomic spacing between crystallographic planes (h,k,l) and θ is the angle of incidence for the X-ray beam relative to the surface plane. In this simplistic model, the Bragg condition is satisfied at only one angle θ_B, or energy, E_B. Dynamical diffraction theory is a more advanced approach that takes into account other factors such as multiple scattering and absorbance effects, which lead to X-ray attenuation. With this approach, the Bragg condition is satisfied by a range of angles and energies. [105] The implication of this for XSW is the standing wave exists across this range of energies and angles. By sweeping E or "rocking" θ, the intensity of the reflection forms what is known as a Darwin curve, shown in Figure 3.19a). Also shown in Figure 3.19a)

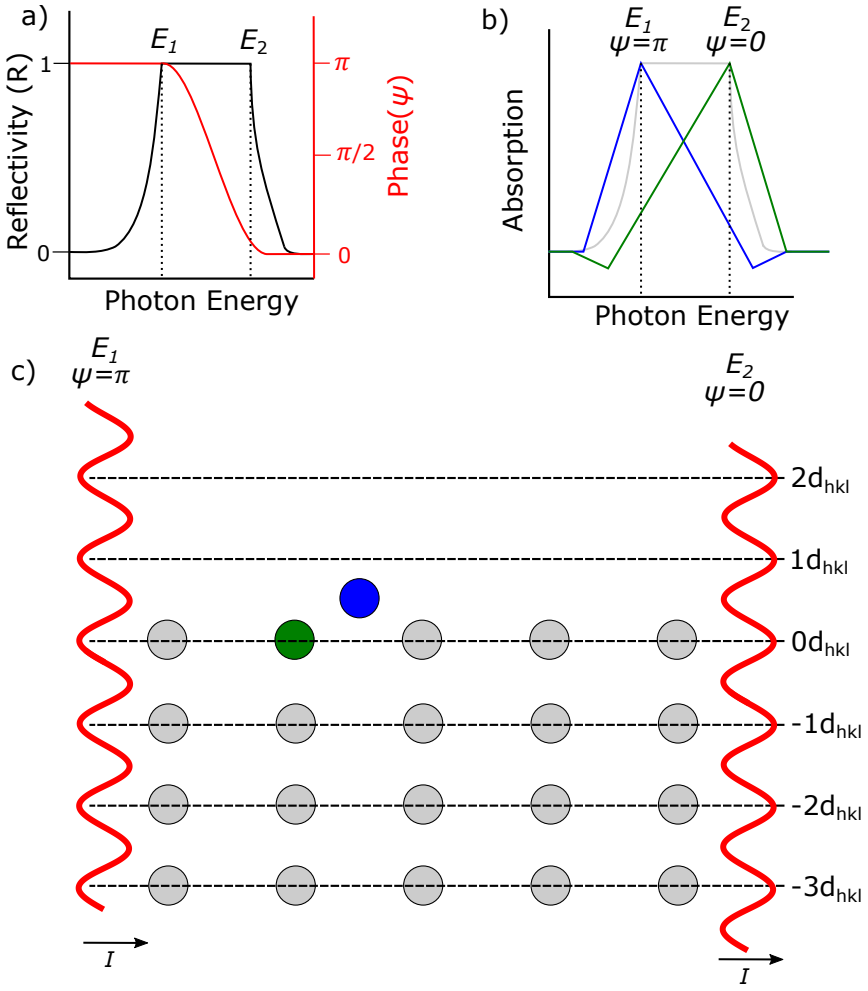

Figure 3.19: a) The Darwin curve (black), showing the change in reflectivity with photon energy over the Bragg condition. Also shown is the variation in phase over this region (red). b) Simplified photon absorption schematic for the atoms shown in c).

is the phase ψ of the standing wave, which varies from π to 0 over the Bragg condition. The reflectivity, the fraction of X-ray intensity reflected by the surface at a given angle, is typically measured by recording the intensity of the reflected spot on a fluorescent screen. In this thesis, normal incidence X-ray standing wave (NIXSW) is the preferred technique, and hence precludes the varying of θ, as the angle must remain constant. Hence, the photon energy is varied. Often, crystallographic planes parallel to the surface are selected; this means that the measured positions can be considered with respect to the surface of the substrate, moving along the normal perpendicularly away from the surface. So, when positions are discussed, they are often referred to as being relative to the surface, typically in

this thesis focussing on the (111) plane of fcc crystals.

At wavelengths similar to half the crystallographic spacing($\frac{\lambda}{2} = d_{hkl}$), the maximum intensity of the reflected X-ray is at $\theta = 90°$ ($\sin 90 = 1$). The nodes of the standing wave shift perpendicularly between the targeted crystallographic planes, as the photon energy is swept through the Bragg condition, as shown in Figure 3.19c). As the node shifts, the X-rays will be absorbed by atomic species as the antinode passes over them, so measuring the absorption gives an indication of the position of the species relative to the targeted crystallographic planes. The X-ray absorbance of a chosen species may be measured *via* several methods, e.g. X-ray fluorescence, photoemission or Auger emission. As the phase shift can be mapped to a vertical position between planes, these absorbance spectra can be used to determine the position of the species, as shown in Figure 3.19b).

If the species is found exactly halfway between the diffraction planes, it will experience a peak in X-ray absorption at the onset of the Bragg condition at photon energy E_1, where $\psi = \pi$, as the antinode of the standing wave is coincident with the atom, as demonstrated by the blue species. The green species experiences a maximum of absorption at photon energy E_2, at the $\psi = 0$ position, as it lies in the bulk reflecting plane. Hence, atoms adsorbed at different distances from the reflecting planes produce distinct X-ray absorption profiles. In the case of measuring photoemission, the resultant photoelectron signal can be collected and analysed similarly to XPS characterization.

Two Beam Derivation

In order to derive meaningful information on the position of atom species from photoelectron yield, we must determine an expression for the intensity of the standing wave at each position above the surface. Given that the intensity of a wave is the absolute square of the amplitude, we begin by considering the amplitude of the standing wave as the superposition of the amplitude of the incident (A_i) and reflected (A_r) waves. Assuming a polarized X-ray beam, we have the following:

$$A_i = E_i e^{2\pi i \vec{K_0} \cdot \vec{r}}, \tag{3.54}$$

$$A_r = E_r e^{2\pi i \vec{K_0} \cdot \vec{r}}, \tag{3.55}$$

where $\vec{K_i}$ and $\vec{K_r}$ are the wave vectors of the incident and reflected waves, $\vec{r}$ is a position vector relating to the direction of travel of the wave, and E_i and E_r are the amplitudes of the electric fields of each wave. Laue's law on elastic scattering in a crystal lattice shows:

$$\vec{K_r} = \vec{K_i} - \vec{G}, \tag{3.56}$$

where $\vec{G}$ is a reciprocal lattice vector. We can then calculate the superposition:

$$A_{sp} = A_i + A_r = E_i e^{2\pi i \vec{K_0}\cdot\vec{r}} + E_r e^{2\pi i \vec{K_0}\cdot\vec{r}}. \tag{3.57}$$

Combining with Eqn. 3.56:

$$A_{sp} = E_i e^{2\pi i \vec{K_0}\cdot\vec{r}}(1 + \frac{E_r}{E_i} e^{-2\pi i \vec{G}\cdot\vec{r}}). \tag{3.58}$$

As stated earlier, I is the absolute square of amplitude, and as the amplitude of the superposition wave is complex, $I_{sp} = A_{sp}A^*_{sp}$. By normalising the magnitude of the incident wave to 1, we can write:

$$I_{sp} = \left| [(E_i e^{-2i\pi\vec{G}\cdot\vec{r}})(E_i e^{2i\pi\vec{G}\cdot\vec{r}})] \cdot [(1 + \frac{E_r}{E_i} e^{2i\pi\vec{G}\cdot\vec{r}})(1 + \frac{E_r}{E_i} e^{-2i\pi\vec{G}\cdot\vec{r}})] \right|, \tag{3.59}$$

$$[(E_i e^{-2i\pi\vec{K_0}\vec{G}\cdot\vec{r}})(E_i e^{2i\pi\vec{K_0}\vec{G}\cdot\vec{r}})] = E_i^2 = 1^2 = 1, \tag{3.60}$$

$$[(1 + \frac{E_r}{E_i} e^{2i\pi\vec{G}\cdot\vec{r}})(1 + \frac{E_r}{E_i} e^{-2i\pi\vec{G}\cdot\vec{r}})] = 1 + \frac{E_r}{E_i} e^{2i\pi\vec{G}\cdot\vec{r}} + \frac{E_r}{E_i} e^{-2i\pi\vec{G}\cdot\vec{r}} + (\frac{E_r}{E_i})^2, \tag{3.61}$$

combining Eqns. 3.59-3.61:

$$I_{sp} = \left| 1 \cdot [1 + \frac{E_r}{E_i} e^{2i\pi\vec{G}\cdot\vec{r}} + \frac{E_r}{E_i} e^{-2i\pi\vec{G}\cdot\vec{r}} + (\frac{E_r}{E_i})^2] \right|, \tag{3.62}$$

$$I_{sp} = 1 + \left|\frac{E_r}{E_i}\right|^2 + 2Re[\frac{E_r}{E_i} e^{-2\pi i\vec{G}\cdot\vec{r}}], \tag{3.63}$$

where Re is the real part of the enclosed number. As E_i and E_0 are both complex, their ratio is also complex and has an associated phase ψ , representing the phase difference between the two waves. This means this term can be rewritten as the following:

$$Re[\left|\frac{E_r}{E_i}\right| e^{i\psi} e^{-2\pi i\vec{G}\cdot\vec{r}}] = Re[\left|\frac{E_r}{E_i}\right| e^{-2\pi i\psi\vec{G}\cdot\vec{r}}]. \tag{3.64}$$

This allows us to use Euler's identity ($e^{i\theta} = \cos\theta + i\sin\theta$) to extract the real part, giving the following:

$$I_{sp} = 1 + \left|\frac{E_r}{E_i}\right|^2 + 2\left|\frac{E_r}{E_i}\right| \cos(\psi - 2\pi(\vec{G}\cdot\vec{r})). \tag{3.65}$$

Given that reflectivity R is given by $\left|\frac{E_r}{E_i}\right|^2$, we can then write:

$$I_{sp} = 1 + R + 2\sqrt{R}\cos\left(\psi - 2\pi(\vec{G}\cdot\vec{r})\right). \tag{3.66}$$

If we consider that $\vec{G}\cdot\vec{r}$ describes the vector direction of the wave onto the crystal planes, we can represent it as the fraction of the distance between the lattice planes and the perpendicular position between the planes, z, giving:

$$I_{sp} = 1 + R + 2\sqrt{R}\cos\left(\psi - \frac{2\pi z}{d}\right). \tag{3.67}$$

This equation describes well the X-ray intensity experienced by a single atomic species at a single well-defined position z. However, in reality, no atomic species lies at an entirely uniform height on the surface; even those that are broadly uniform experience some thermal fluctuation, leading to uncertainty in the position of the species. To account for these multiple positions, the sum of all contributions from different positions, described as the fraction of atoms at each position z, should equal 1, as shown below:

$$\int_0^d f(z)dz = 1; \tag{3.68}$$

combining with Eqn. 3.67:

$$I_{sp} = 1 + R + 2\sqrt{R}\int_0^d f(z)\cos\left(\psi - \frac{2\pi z}{d}\right)dz. \tag{3.69}$$

Within the limits of the integral, both $f(z)$ and $\frac{z}{d}$ take values between 0 and 1. We refer to these terms as coherent fraction, C_f, and coherent position C_p:

$$I_{sp} = 1 + R + 2\sqrt{R}C_f\cos\left(\psi - 2\pi C_p\right). \tag{3.70}$$

The coherent position defines the fractional position of the species between the diffraction planes, and coherent fraction describes the fraction of the species that sits at exactly that position. Hence, a coherent fraction approaching 1 means a highly ordered species sitting in a broadly uniform position. A coherent fraction of 0 renders the coherent position meaningless, but it should not be assumed that no information can be garnered from a low C_f value. In order to understand the more complex situations, we can write the following: [106]

$$C_f e^{2\pi i C_p} = \sum_n C_{fn} e^{2\pi i C_{pn}}, \tag{3.71}$$

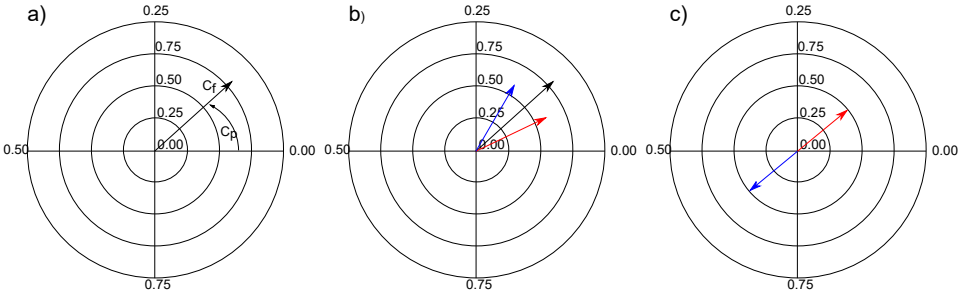

Figure 3.20: a) Argand diagram with labelled directions of C_f and C_p. b) Argand diagram showing two different atomic positions (red and blue) summing to a relatively high coherent fraction (total measured position and fraction = black arrow). c) Argand diagram showing two well-defined atomic positions resulting in a C_f of 0.

where n is the number of discrete z_n positions with weighting C_{fn}. In this form, we can treat the individual components as vectors in an Argand diagram, with a length equivalent to their C_f and angle determined by the phase angle $2\pi C_p$ against the real component. This means we can effectively plot them as vectors with C_p as the angle and C_f as shown in Figure 3.20a).

How these different positions can interact is most straightforwardly demonstrated by scenarios with two positions, as shown in Figure 3.20b-c). In b), the two positions are relatively similar, leading to a high coherent fraction. In c), the coherent positions are opposite, so despite the species being highly ordered, the resultant C_f value is low. The implication of this is that if other techniques (such as STM) describe a highly ordered surface, it can be possible to model the system in such a way as to produce a low C_f value, while remaining highly ordered.

Complexities in XSW Interpretation

As the positional information provided by XSW is relative to the diffraction planes, it is not possible to distinguish which set of planes the species lies between. In Figure 3.19, the blue species could be between $-1d_hkl$ and $0d_hkl$, $0d_hkl$ and $1d_hkl$, $1d_hkl$ and $2d_hkl$ and so on. Lower than this is unlikely, as we are studying molecules adsorbed onto a surface. To distinguish between the available options is not always straightforward, and requires some understanding of the system, perhaps provided by alternative techniques such as NEXAFS, STM, or density

functional theory (DFT) computational modelling.

Another feature of the position information provided by XSW is that it only provides information relative to half the lattice separation d. This is due to equation 3.67 being dependent on the cosine of θ; the value of $\cos\theta$ decreases from 0 to π, but increases again from π to 2π. This means that for values of ψ between 1 and 0, there are two possible positions, e.g. $\cos\frac{\pi}{2} = \cos\frac{3\pi}{2}$. As with the possible differing planes, an understanding of the system is required to deduce which position is correct.

Finally, the standing wave is generated by the bulk of the substrate material. The positions are relative to projections of the bulk layers, not the surface layer - some surface layers, such as Au(111), experience significant reconstruction, causing the surface layer to be different to the bulk crystal. Even in situations with no reconstruction, such as Ag(111), there is often a surface relaxation effect which can cause the surface layer to be different to the bulk. Thankfully, on the most commonly encountered reconstruction in this thesis, the Au(111) herringbone, the effect only causes a drop in coherent fraction of around 0.1. This effect should be considered when considering the results of XSW, particularly when interpreting surfaces with significant reconstruction.

3.3 Summary

In this chapter, the techniques used throughout the experimental work contained within this thesis (STM, STS, XPS, NEXAFS, XSW) have been introduced and explained. Each of these techniques provides a unique insight into the structural, chemical or electronic properties of molecules on surfaces; STM revealing topography, XPS revealing chemical environments, NEXAFS giving insight into both chemistry and orientation, and XSW delivering further structural insights.

Chapter 4

On-surface Polymerisation and Self-assembly of DPP-based Molecular Wires

In this chapter, halogen-functionalised diketopyrrolopyrrole (DPP) precursor monomers are deposited on Au(111) and annealed to initiate Ullmann-type coupling and formation of molecular wires. Of particular interest is the influence of alkyl side chains, the role of surface induced chirality, and the possibility of utilising halogen bonding to drive the formation of self-assembled structures and control the selectivity of the subsequent polymerisation reaction.

4.1 Introduction

An underlying concept of molecular electronics is that the bespoke properties of specific molecular species (e.g. electronic, magnetic, chemical, and optical functionalities) can be incorporated into solid-state devices. Diketopyrrolopyrrole (DPP) is a chemical moiety which may act as both an electron acceptor and donor within organic electronic-devices which has been shown to exhibit a high charge carrier mobility when utilised in extended polymer structures, [10, 107] and has been utilised within organic field effect transistors (OFET) and other nanoelectronic devices. [108] Charge transport within such systems is affected by the local arrangement, and orientation, of molecules and their domains; hence,

the controlled formation of ordered structures is of interest. Additionally, the chirality of the molecular sub-units within ordered structures is also known to influence electronic properties of the materials. [109, 110] Therefore methodologies for controlling these structural arrangements, and techniques which provide molecular level characterisation, are an important facet within the development of molecular-based devices.

The on-surface self-assembly of molecular structures, where non-covalent interactions give rise to local ordering, [67] is a promising approach to studying prototype molecular devices. Scanning probe microscopy techniques (such as scanning tunnelling microscopy, STM, and atomic force microscopy, AFM) have frequently been employed to study such systems as they provide single-/sub-molecular resolution of surface confined molecules. The ordered assembly of domains may be driven by a wide range of intermolecular interactions [13] (e.g. hydrogen-bonding, metal-organic, van der Waals; see section 2.1) and the self-assembly of DPP based species has been achieved *via* functionalisation with alkyl side chains; driving the formation of ordered domains confined to a surface. [111, 112]

Importantly, molecular properties can be changed and enhanced upon polymerisation, and an appropriately designed monomer with specific functional groups may be polymerised into ordered nano or microstructures (with the on-surface synthesis of graphene nanoribbons being an important demonstration of this approach [3]). A range of on-surface synthesis protocols that result in monomer units being covalently coupled under appropriate reaction conditions have been explored (e.g. Ullmann-type reactions [113] amongst others [42, 55, 114–118]) and precursor units possessing acceptor/donor functionality have been covalently coupled to produce individual molecular wires characterised by STM methodologies. [119, 120] These topics are discussed at length in chapters 2 and 3.

In this chapter, I discuss the on-surface synthesis of polymers formed from a halogen-functionalised DPP-monomer on Au(111) under ultra-high vacuum (UHV) as characterised by scanning tunnelling microscopy (STM). Structural characterisation of molecular and polymeric species at different stages of growth within the reaction allow for the identification of the role of molecular chirality

and molecular interactions, driven by alkyl chain and bromine functionalisation of the DPP core, within the observed ordered structures. Specifically, it is shown how the alkyl chains give alignment and order to the DPP polymers and how the thermal stability of these groups is key in maintaining this long-range order.

4.1.1 Br_2Hex_2DPP

The on-surface synthesis of polymeric DPP structures requires a suitably functionalised DPP core. A DPP species functionalised with aryl halide and alkyl chain groups is employed, (*3,6-bis(4-bromophenyl)-2,5-dihexyl-2,5-dihydropyrrolo[3,4-c] pyrrole-1,4-dione*) **Br_2Hex_2DPP**. The chemical structure of **Br_2Hex_2DPP** shown in Figure 4.1a) with dimensions indicated in 4.1b). The nitrogen atom of the DPP core is alkylated with hexyl chains, which have previously been shown to facilitate ordered on-surface self-assembly [111,112], and aryl bromide groups provide access to Ullmann-type covalent coupling reactions on surfaces. [42, 55, 113] It is worth noting that the self-assembly of precursor units may have significant impact upon the reaction pathway of coupling processes [121] and that this approach, amongst others [122] (including alignment to surface features [88, 90] and reactions within molecular pores [61, 123]) offers a paradigm for controlling on-surface synthesis (as discussed in chapter 2). The functionalisation of the DPP core with hexyl chains is selected as a route to modulate the balance of molecule-molecule interactions driven by interactions between the aromatic DPP cores and those driven by alkyl chain interactions. Within three-dimensional structures formed from DPP variants functionalisation with short (e.g. butyl), or no, alkyl chains the self-assembly is driven by interactions between the DPP cores. The inclusion of longer chains (e.g. octyl) results in structures dominated by lamella-type packing of interdigitating alkyl chains. [124] Such a motif is frequently observed within surface confined two-dimensional self-assembly. [125] Here we have obtained, by inclusion of hexyl chains, a balance between interacting DPP cores and between alkyl chains such that the self-assembled structure contains rows of DPP cores (where proximity may allow Ullmann-type coupling) and local ordering of the rows is facilitated by the interdigitated alkyl chains.

A scheme of the on-surface reaction for **Br_2Hex_2DPP** on Au(111) is shown

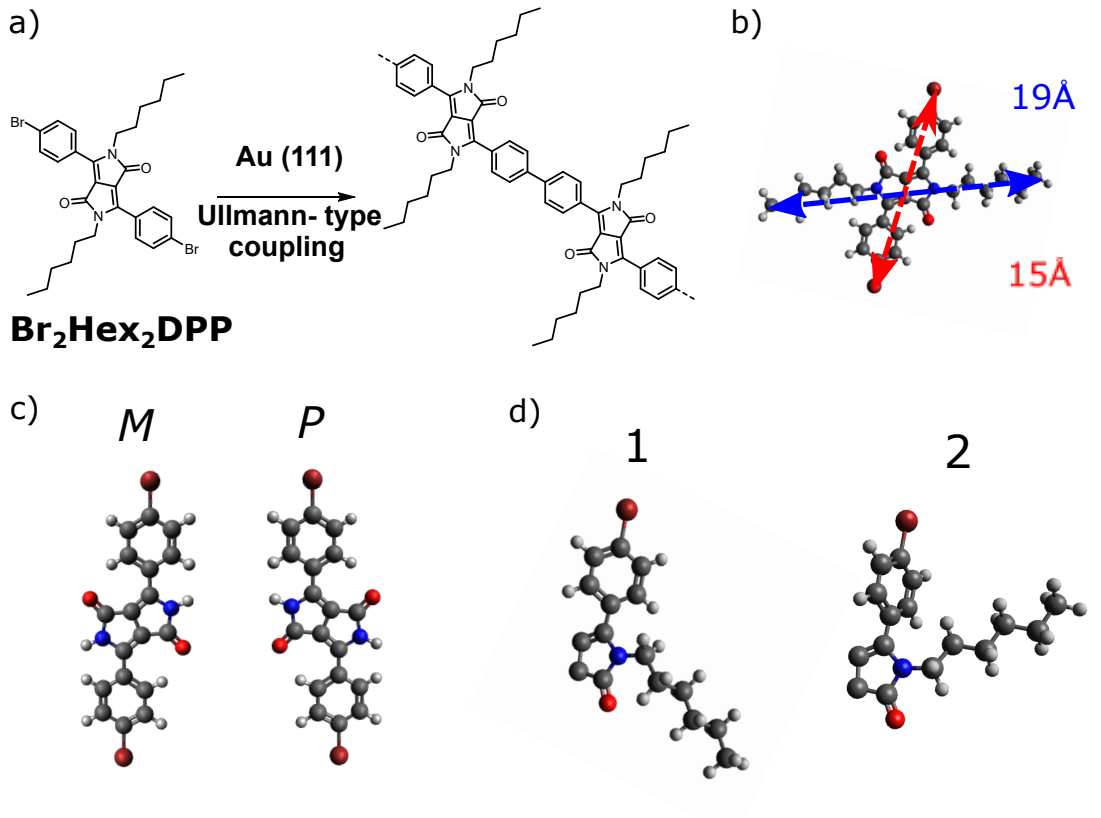

Figure 4.1: a) Scheme of the Ullmann-type coupling reaction expected from heating **Br_2Hex_2DPP** on Au(111). b) Predicted dimensions of a single **Br_2Hex_2DPP** as modelled *via* molecular mechanics geometry optimisation. c) Shows the *M* and *P* chiral arrangements of the molecule as induced by surface interaction. d) Shows the possible alkyl 'arm' positions for **Br_2Hex_2DPP** (the molecule has been truncated to focus on the alkyl chain position – the fragment shown does not represent a stable species).

in Figure 4.1a). The pro-chiral nature [126, 127] of **Br_2Hex_2DPP**, with respect to adsorption on the surface, leads to two enantiomeric chiral species (labelled *M* and *P*, as shown in Figure 4.1c). The high degree of rotational flexibility of the C-C bond between the hexyl side chains and the DPP core leads to the possibility of different conformational isomers of **Br_2Hex_2DPP** being present on the surface. The 'arms' (hexyl side chains) can be considered in one of two orientations: position 1, where the arm is closer to the oxygen atom on the core, and position 2, where the arm points away from the oxygen (see Figure 4.1d)). Each of the two alkyl chains attached to the DPP core can adopt either conformation (1 or 2). Therefore, a single DPP core can exist in four distinct

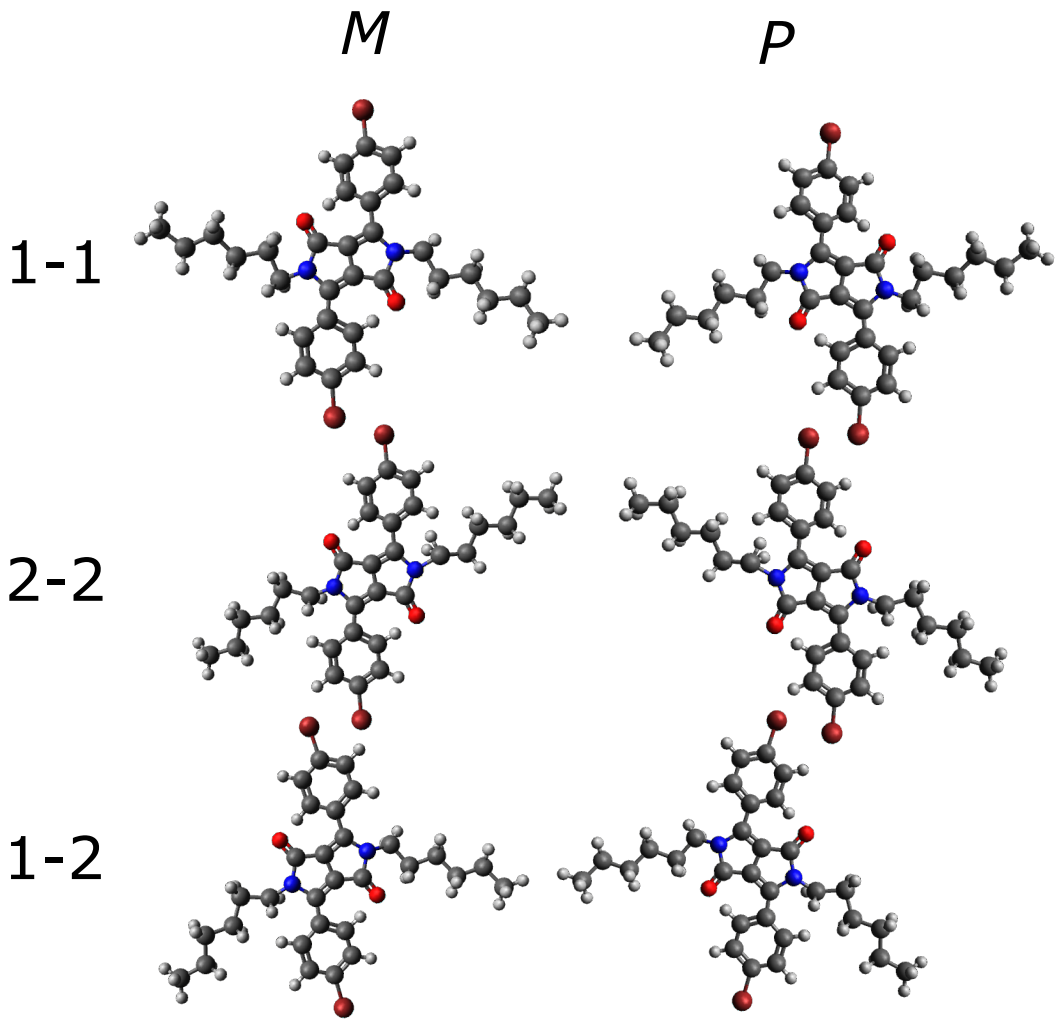

Figure 4.2: Shows all chiral rotomers for **Br_2Hex_2DPP** (1-2 and 2-1 are indistinguishable for molecules adsorbed at a surface).

conformations. Due to the pro-chiral nature of the DPP core, each of the chain conformations is possible for the two core chiralities. On surface, both 1-2/2-1 configurations are identical, so practically there are only three distinguishable surface-confined conformations, 1-1, 2-2 and 1-2, as shown in Figure 4.2.

4.2 Self-assembly and On-surface Synthesis Under UHV

In order to characterise the development of the potential polymerisation reaction occurring following the anneal of the **Br_2Hex_2DPP** species on Au(111), the

system was first examined under "ideal" UHV conditions, as described in the following section. Later, the same experiment is conducted under ambient pressure conditions, in order to determine whether the process may be replicated in a more realistic facsimile of an industrial context.

4.2.1 Experimental Methods

Br_2Hex_2DPP was synthesized by the group of David B. Amabilino, Institut de Ciència de Materials de Barcelona (ICMAB-CSIC), Campus Universitari de Bellaterra, 08193 Cerdanyola del Vallès, Spain.

Structural characterisation was performed *via* STM. Au on mica samples (Georg Albert PVD GmbH) were cleaned *via* cycles of Ar ion sputtering (20 minutes at 0.75 keV, 8.5×10^{-6} mbar) and annealing (300 °C for 20 minutes). Sample cleanliness was determined *via* STM prior to deposition of **Br_2Hex_2DPP**. Thermal deposition was conducted using a Knudsen-type evaporation cell (K-Cell) at a temperature of 190 °C for a period of 2 hours at a pressure of 1×10^{-8} mbar. STM data was acquired using an Omicron STM-1 system, with Nanonis control electronics, operating at room temperature under ultra-high vacuum (UHV) conditions: base pressure $< 2\times10^{-9}$ mbar.

Imaging was performed using electrochemically etched tungsten tips, functionalised with gold during on-surface tip preparation (bias is applied to the sample). Sample annealing is performed *via* resistive heating of a silicon wafer mounted behind the Au/mica sample: Temperature estimates are based upon thermocouple readings from the sample receptor which were calibrated to the sample temperature *via* a combination of pyrometer measurements of the Si wafer and a thermocouple affixed to the sample plate. Samples were annealed to 100 °C, 200 °C, 250 °C and 350 °C with an estimated error of ± 50 °C. This error was determined via pyrometer calibration.

X-ray photoelectron spectroscopy (XPS) was acquired using a SPECS DeviSim near ambient pressure XPS (NAP-XPS) instrument operating in ultra-high vacuum (UHV) mode at a pressure $< 1\times10^{-9}$ mbar. Spectra were measured using a Phoibos 150 NAP hemispherical analyzer with 20 eV pass energy and monochromatic Al Kα X-rays (1486.7 eV). The samples were transported between the STM

and XPS sites using a vacuum suitcase at a pressure $<1\times10^{-10}$ mbar.

4.2.2 Characterization of Self-assembled Monomer Structures

A monolayer coverage of **Br_2Hex_2DPP** on Au(111) was prepared *via* thermal deposition under UHV and RT (room temperature) conditions and subsequently imaged using STM. Figure 4.3a) shows the observed self-assembled structures where a majority and minority phase are observed (minority phase indicated with a white arrow). Within the majority phase, two principal directions are identified (green/blue arrows), with the 'a' axis of the molecular lattice running approximately parallel to the atomic < 1 1 -2 > directions of the Au(111) surface. The measured dimensions of the unit cell, are found to be, a = 1.1 ± 0.1 nm and b = 1.4 ± 0.1 nm; which is in excellent agreement with the proposed model (Figure 4.3b)), with a = 1.2 ± 0.1 nm and b = 1.5 ± 0.1 nm. Each measurement of lattice dimensions is an average of the measurement from the forwards and backwards scans, to correct for drift. The proposed model is a geometry optimised structure based upon the experimentally determined lattice measurement and a consideration of inter and intra-molecular steric effects (to be explained in greater detail in section 4.2.3). The proposed arrangement suggests that the alkyl chains play a role in ordering the observed structures (van der Waals interactions between parallel alkyl chains are known to be a driving force in self-assembled structures [13, 111, 112] – indicated by blue dashed lines in Figure 4.3b)). The self-assembled structure proposed is homo-chiral (either all M or P species present, where M and P are the given nomenclature describing molecules with axial chirality), but the resolution of the STM data precludes identification of molecular chirality within individual domains. However, a consideration of homo- and hetero-chiral domains allows us to discount the presence of hetero-chiral molecular structures due to steric effects (see section 4.2.3). Following deposition, a racemic mixture of the adsorption-induced chiral enantiomers is assumed, with co-existing homochiral domains being formed during self-assembly. This would suggest that homochiral interactions are an important driver of the self-assembled structures, and that the monolayer crystal formed can be consid-

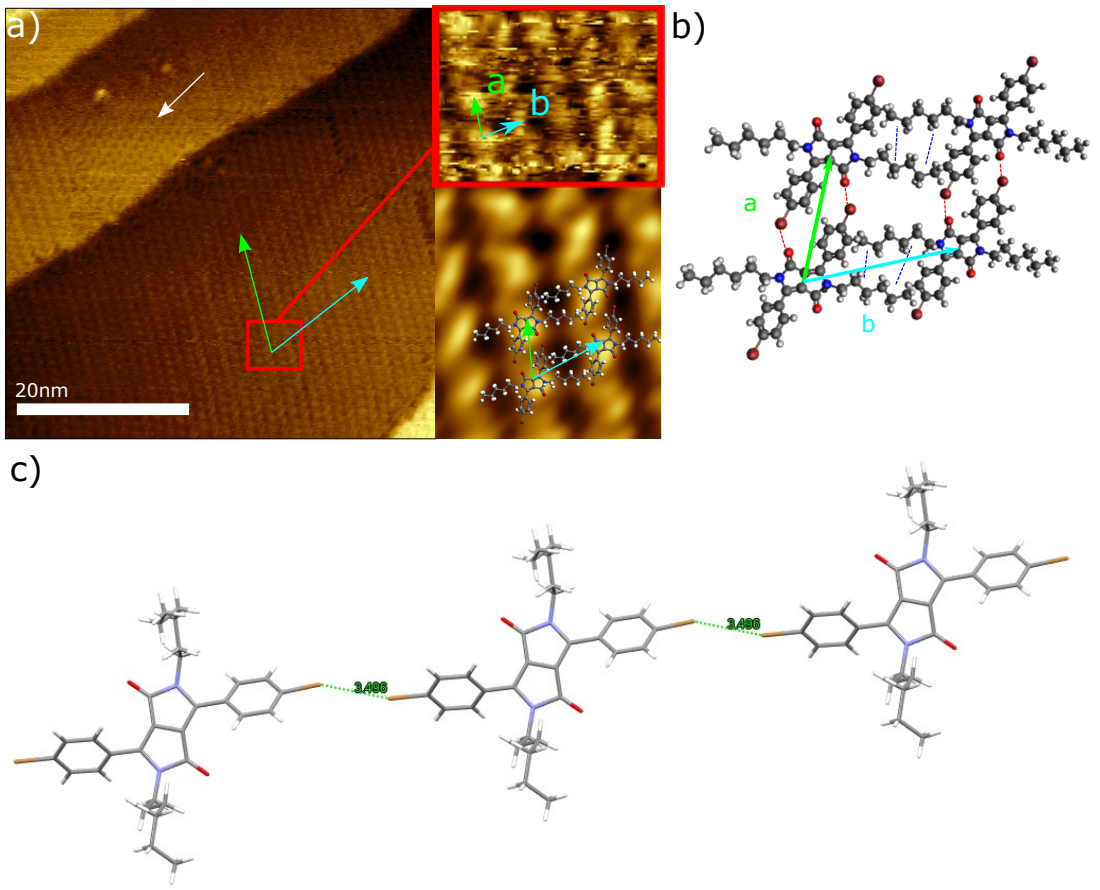

Figure 4.3: a) STM topograph showing self-assembled structures formed by **Br_2Hex_2DPP** following RT deposition (Bias = 2 V, Current =20 pA). Accompanying this is a zoom of a smaller region, paired with a 2D-FFT filtered image of the lattice, with lattice dimensions, a and b, indicated alongside an overlay of proposed molecular structure (a = 1.1 ± 0.1 nm and b = 1.4 ± 0.1 nm). b) Shows the molecular lattice as modelled by molecular mechanics geometry optimisation (a = 1.2 ± 0.1 nm and b = 1.5 ± 0.1 nm). c) Crystal structure of the solid state **Br_2Hex_2DPP** showing halogen-halogen interaction.

ered a conglomerate (overall racemic mixture preserved with distinct homochiral domains present). [126]

Another feature of the proposed self-assembled structure shown in Figure 4.3b) is the potential for halogen bonding between bromine and oxygen atoms attached to the DPP core (dashed red line). In the solid state for this compound, halogen bonding is also involved, this time halogen-halogen. (see Figure 4.3c)). Halogen bonding is highly directional, and may influence molecular self-assembly

via the anisotropic electron distribution around covalently bonded halogens, allowing the strongly electronegative halogen species to interact with another electronegative group by virtue of a small electrophilic region which forms on the halogen atom at the opposite side to the covalent bond. [40, 128]

4.2.3 Molecular Modelling

Molecular models of the observed self-assembled structures were developed *via* a series of steps, utilising well-known self-assembly motifs and measured dimensions from STM images. Before describing the steps, I will provide a brief description of two programs involved: LMAPper [129] is a molecular overlay program that allows molecular models to be loaded directly from .cml files and overlaid to scale onto SPM images, allowing for comparison of the dimensions of surface structures with those of the target molecule. Avogadro [130] is a molecule editor and visualiser that allows for geometry optimisation via the application of models such as universal force field.

Using these programs, steps are shown in Figure 4.4 and can be described as follows: a) measuring molecular lattices acquired from STM *via* an autocorrelation function, b) matching the expected dimensions of **Br_2Hex_2DPP** to features within a 2DFFT filtered image of the lattice using LMAPper, c) modelling these lattices within Avogadro matching the dimensions of the lattice, typically in a 9x9 grid, d) using molecular mechanics to allow the molecules to flex, and constructing a unit cell using the central molecule from the 9x9 grid matching the measured lattice dimensions, e) creating an idealised model based on this unit cell, featuring the rotated rings and flatter arm chains, and f) overlaying this unit cell onto the 2DFFT. Using this method, I was able to determine that the unit cell shown in 4.4e) was the most plausible, as the solution presented by simple molecular mechanics was the most planar, and featured several common self-assembly motifs (alkyl chain interdigitation, halogen bonding, and π-π interactions of aryl rings). This also shows that the chirality of the homochiral domains is not identifiable at this resolution. Other models were considered, as shown in Figure 4.5. As the STM images appear to display an alternating chevron pattern between rows, models featuring alternating conformations were consid-

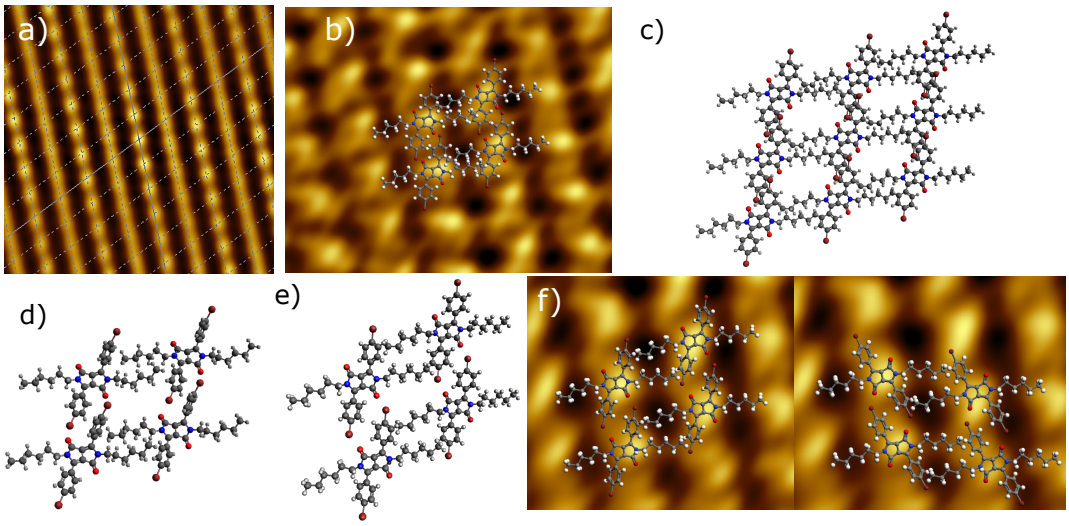

Figure 4.4: a) Measuring the lattice dimensions of the self-assembled lattice from a 2DFFT of the lattice. b) Overlaid simple **Br$_2$Hex$_2$DPP** homochiral molecular model onto a masked 2DFFT of the lattice. c) The molecular model from b) recreated in Avogadro. d) A model unit cell created using the central molecule from the 9x9 grid shown in c), placed at the dimensions measured from the lattice. e) An idealised unit cell created using the motifs of this calculated unit cell. f) This unit cell overlaid onto the 2DFFT filtered image, with both chiralities shown. (Bias = 2 V, Current = 20 pA)

ered. Firstly, the homochiral alternating rotation model considers the possibility of a homochiral lattice, where alternating rows of the molecule are rotated $\sim 90°$ with respect to one another. Secondly, a racemic alternating chirality model was considered, whereby the alternating rows feature molecules of opposing chirality. These models were considered less plausible, as a reasonable degree of planarity was not possible to achieve, as significant sections of the molecule were observed to overlap. Hence, the visually apparent alternating character of the lattice is ascribed to an unusual tip contrast, as it is not strikingly obvious across all images.

4.2.4 On-surface Polymerisation *via* Ullman-type Coupling

To explore the progress of the on-surface polymerisation reaction, the sample was sequentially heated; to 100 °C, 200 °C, 250 °C and 350 °C. The reaction products following heating were characterised by STM, (see Figures 4.6a-c)).

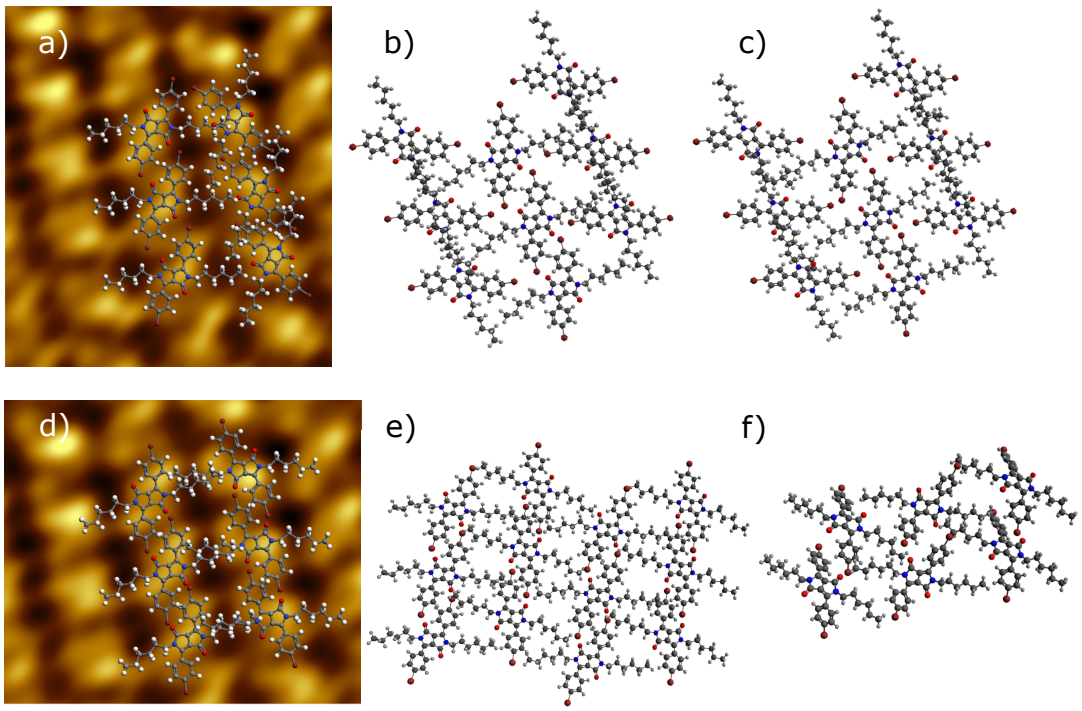

Figure 4.5: a) Overlaid simple **Br_2Hex_2DPP** homochiral alternating rotation model onto a 2DFFT filtered STM image of the molecular lattice. b) The molecular model from a) recreated in Avogadro, with lattice dimensions matching those measured experimentally. c) The molecular model from b) once simple molecular mechanics have been applied; many segments still overlap, in contrast to what would be expected for a surface confined system. d) Overlaid simple **Br_2Hex_2DPP** racemic alternating chirality model onto a 2DFFT filtered image of the molecular lattice. e) The molecular model from d) recreated in Avogadro, with lattice dimensions matching those measured, in 4x3 grid, to create a central molecule for both chiralities. f) The resultant unit cell for a racemic alternating chirality lattice. As can be seen, there are still a great number of possible steric clashes in a proposed "flat" model of this lattice.

Previous studies of aryl-bromides on the Au(111) surface indicate that scission of the C-Br is likely to occur in the range 100-250 °C. [64, 71, 84, 86, 131–136] My results indicate that initial polymerisation occurs at a temperature of 100 °C (Figure 4.6a)); short (1-30 nm length) chains are observed to form distinct ordered domains of varying size. These polymer domains are typically of a smaller size than those seen in the close-packed islands observed before annealing (cf. Figure

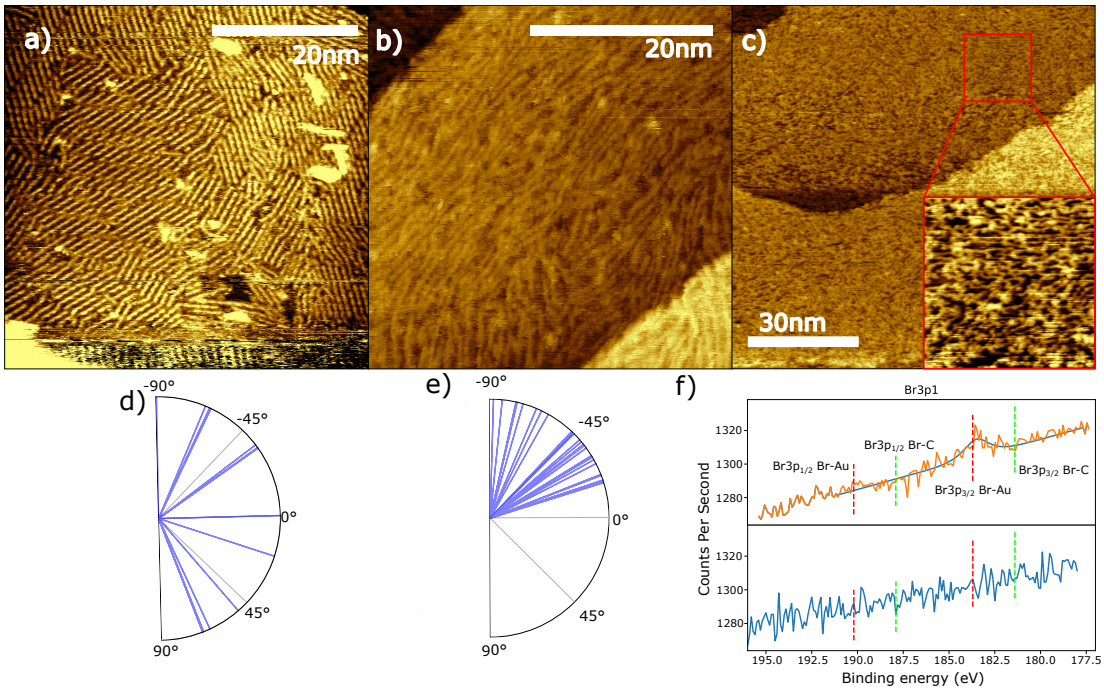

Figure 4.6: STM images of the polymer structures formed following annealing the surface to; a) 100 °C (Bias = 2 V, Current = 40 pA); b) 200 °C (Bias = 2 V, Current = 20 pA); and c) 350 °C (Bias = 2 V, Current = 20 pA). d) Angular orientation of polymer chains in a). e) Angular orientation of polymer chains in b). f) XPS data showing the Br 3*p* region following deposition of **Br_2Hex_2DPP** on Au(111) (orange line, top) and subsequent annealing of the surface to 100 °C (blue line, bottom).

4.3a)). Further discussion of the polymerisation details on the molecular level are provided below. Initially, I focus on the large-scale morphologies observed as a function of temperature.

Following annealing at 100 °C, the polymer domains are observed to run along several directions, with the polymers within each domain being highly aligned. The angular distribution of polymer alignment, relative to the fast-scan direction (x-axis), for the chains in Figure 4.6a) is shown in Figure 4.6d). While there is a high degree of polymer alignment within individual domains, when several images are compared there is no evidence to support a unique relationship between the polymer orientation and the major crystallographic directions of the underlying Au(111) substrate (although my data does not categorically preclude a more subtle interaction with the surface crystallography or the herringbone re-

construction). I propose that the local ordering within the domains, post-anneal, is driven by the initial ordering of the unreacted **Br_2Hex_2DPP** species within close-packed domains, with the proximity of the aryl-bromide groups facilitating covalent coupling.

Similar analysis is performed for the polymer structures obtained after annealing to 200 °C (STM topography shown in Figure 4.6b), with angular distribution shown in 4.6e). In contrast to the range of polymer orientations observed within a single STM image after annealing at 100 °C, additional annealing has resulted in larger domains, where the polymer chains are locally aligned; for example, polymer chains running from the bottom left to the top right of the STM image (shown in Figure 4.6b)) maintain local parallel ordering, but the chain direction varies across the image. I suggest that during the anneal sufficient thermal energy is provided to allow the short polymers to diffuse, producing longer chains which often align with surface structures (such as parallel to step-edges) to maximise the polymer length. Further annealing at 350 °C (Figure 4.6c)) results in a loss of long range ordering of the polymer structure, with local ordering of neighbouring chains (parallel alignment) observed, but with frequent intersection of polymer chains being present. The elevated temperature here may facilitate cross-linking reactions between DPP-polymers as a result of C-H activation in the phenyl rings in the biphenyl units of neighbouring chains. Since there are several positions that may be activated, the inter-chain reactions are expected to lead to a loss of order, as seen for other aromatic systems. [118] The lack of any regular structure supports this hypothesis of non-specific C-C linking with loss of hydrogen.

Our interpretation that the change in structure is due to an on-surface coupling reaction is supported by X-ray photoelectron spectroscopy (XPS) measurements of the Br 3*p* region (Figure 4.6f)) for the as-deposited (orange) and annealed-to-100 °C (blue) samples. Due to spin-orbit splitting, two peaks are expected for each Br environment (1/2 and 3/2). Comparison of the expected binding energies of C-Br and Au-Br species (red and green lines respectively in Figure 4.6f)) with the experimental data indicates that prior to annealing, the Br-C bond within **Br_2Hex_2DPP** is intact. [136] Following annealing to 100 °C

no significant peaks are observed, indicating that the environment of the Br has changed, which is attributed to the cleavage of C-Br bonds. Although no peaks are observed in the Br $3p$ region following annealing, it is likely that the presence of two distinct chemical environments, the expected spin orbit splitting, and the potential for the desorption of Br species at these temperatures [135] will combine to obfuscate any peaks within the noise level of the measurements. As such, the XPS data supports the cleavage of the C-Br but does not necessarily support the complete removal of Br from the surface at 100 °C. In line with several STM studies of Ullmann-type coupling reactions involving bromine functionalised species, there is no evidence within the STM data for Br atoms at the Au substrate following C-Br bond scission [15, 88] (NB related studies involving iodine materials frequently show the presence of iodine atoms [61, 137]).

We now focus on molecular level details of the polymer structures formed after annealing. Figure 4.7a) shows an overview of a domain of the linearly aligned polymer chains formed by heating to 100 °C. There is a clear uniform directionality for chains within the region, alongside discontinuities along the length of the chain (indicated by red arrows). The presence of kinks in predominantly straight chains is likely caused by the adsorption-induced chirality of the **Br_2Hex_2DPP** discussed in Figure 4.1c): the geometry of these kink sites match the chiral models, as shown in Figure 4.8. Figure 4.8a) displays the structure of the proposed homochiral and heterochiral models; the homochiral polymer consists only of one chirality of precursor, whereas the heterochiral model features alternating chirality units along the length of the polymer. The homochiral nature, (M)n or (P)n, is confirmed *via* a comparison with the racemic, P (M P)n M, structure (Figure 4.8b-c)). Alignment of the homochiral polymer structure provides good agreement with respect to the bright/high regions within the topographic STM images (assigned to the aromatic species within the polymer chains), whereas the racemic polymer structure does not spatially align with the observed linear structure of the polymer. The prevalence of kink sites amongst the 100 °C structures was measured to be 1 in 27 (56 kinks identified within a region of 1530 monomer units), implying a largely defect free and enantiopure polymer structure. Domains of homochiral polymers are observed to occur separately to one another, potentially

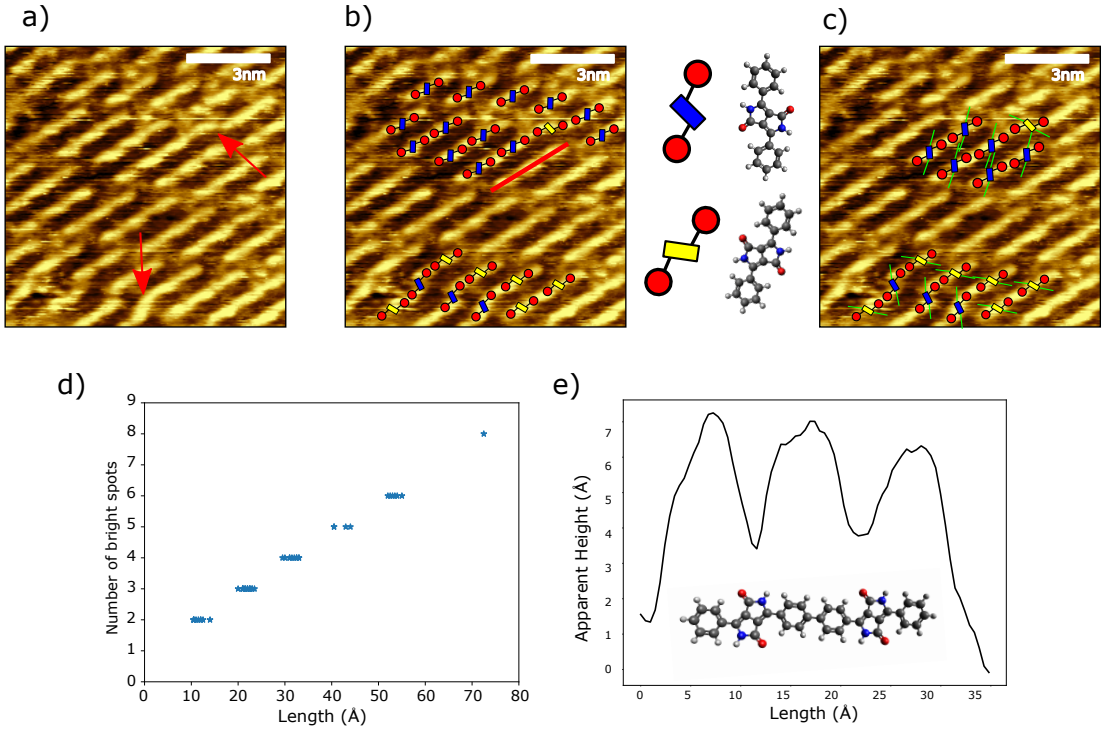

Figure 4.7: a) STM image (Bias = 2 V, Current = 40 pA) of an area of polymer chains formed by heating to 100 °C, kinks within polymers indicated by red arrows. This area is selected due to the presence of a disporportionately high number of kink sites. b) Molecular model overlaid onto the image of polymer chains, with the blue and yellow DPP cores highlighting the two interface enantiomers. c) Simplified model demonstrating the role of alkyl chain interactions in influencing the shape of the domains. d) Plot of the number of visible bright spots within a chain against length of polymer chain. e) Line profile along a polymer chain showing the correspondence between peak positions and molecular structure (line profile position shown by red line in b).

driven by the homochirality of the large self-assembled domains of the unreacted monomer prior to annealing. This may give rise to localised regions with a high proportion of monomers of a single enantiomer that would lead to the observed homochiral reaction products. An overlay of **Br_2Hex_2DPP** monomers onto the structures formed after annealing at 100 °C structures is shown in Figure 4.7b). Here, monomers, dimers, and longer polymers are identified (position of a line profile indicated with a red line - data in 4.7e). Figure 4.7c) demonstrates how the arrangement of the hexyl chain interdigitation (green lines) determines the

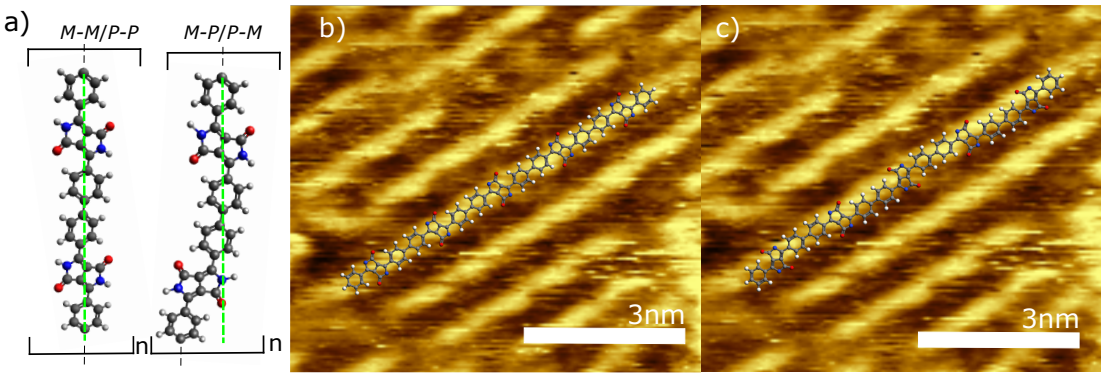

Figure 4.8: a) Scheme showing two possible chiral arrangements of monomers within a polymer. This adsorption-induced chirality could lead to non-linear/kinked polymers [hexyl chains removed for clarity]. b) STM images of the polymer structures formed following annealing of the deposited **Br_2Hex_2DPP** material to 100 °C. Overlays of the proposed molecular structures for a homochiral (a) and a racemic, P-(M-P)n-M, polymer (b). The overlaid structures are positioned such that the bright contrast within the image is aligned to the aromatic regions of the polymer. Good agreement is found for homochiral structure, whereas the racemic structure does not match with the regions of bright contrast. NB hexyl chains have been removed from the molecular structure for clarity. Image parameters: Bias = 2 V, Current = 40 pA.

chain separation (discussed below). Similar to the self-assembled structures prior to annealing, my STM derived model of the chain structure indicates that the linear polymer chains are homochiral. The resolution of the STM data does not allow the chirality (M or P) of the homochiral polymer chains to be determined from a consideration of the chirality of individual monomer units. However, the kinks may be identified as a specific chiral structure, allowing the specific chirality of the covalently coupled linear chains either side of the kink to be identified.

The line profile in Figure 4.7e) shows variations in apparent height along the length of the polymer, resulting in 'brighter' regions (the location the line profile was taken is shown with a red line in high resolution image Figure 4.7b)). The frequency of bright spots is observed to increase linearly with the chain length (see Figure 4.7d)). The separation between the first and last bright features in chains with three bright features is measured to be 2.18 nm ± 0.02 nm, in good agreement with the expected separation of the outer aryl rings within a covalently

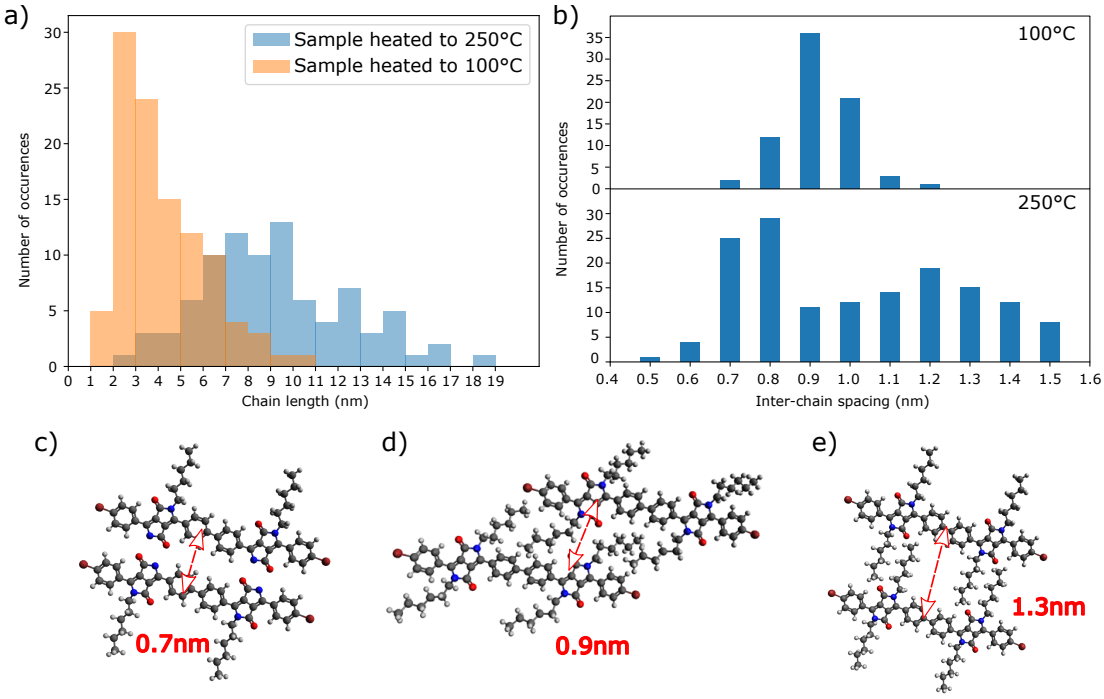

Figure 4.9: a) Histogram showing the distribution of polymer chain lengths following annealing at 100 °C and 250 °C. b) Histogram of chain spacing between polymer rows following annealing at 100 °C and 250 °C. c-e) Models of different hexyl chain configurations, and the corresponding expected chain spacing.

bonded DPP dimer (see line profile - Figure 4.7e)); indicating that under these imaging parameters the DPP units within the polymers appear 'dark'. As can be seen in Figure 4.7d), each additional monomer to the chain adds one additional bright spot (with pairs of phenyl rings forming one indistinguishable peak).

A comparison of the polymers formed after annealing to 100 °C and 250 °C reveals details of additional reactions at higher temperatures and provides information on the thermal stability of the polymers. Figure 4.9a) shows the distribution of the measured chain lengths following annealing at 100 °C and 250 °C, with an average length of 4.14 nm for the chains at 100 °C. The comparatively shorter chain lengths (for the lower temperature anneal) are potentially driven by the initial arrangement of the close-packed structure of the as-deposited monomer material. These close-packed structures bring the reactive Br-aryl groups into close proximity, with only minimal rearrangement being required to facilitate the required bonding geometry. In this respect, the van der Waals interactions between hexyl chains, and halogen bonding, drive both the order of the close-

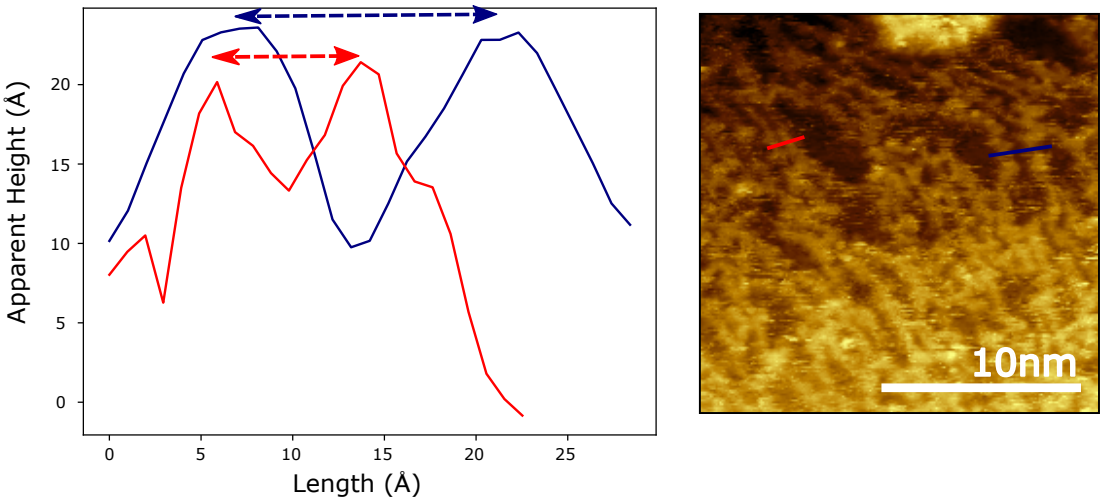

Figure 4.10: Two line profiles demonstrating the separation between polymers (profile locations are indicated within the STM image). The peak-to-peak separation on the red and blue line profiles are 8 Å and 14 Å, respectively. The STM image shows a $\mathbf{Br_2Hex_2DPP}$/Au(111) surface following annealing at 200 °C (Sample bias = 2 V, I(set-point) = 200 pA).

packed structure and the aligned polymers. Heating further, to 250 °C, results in a broadening of the distribution of the measured polymer lengths as well as an increase in the average length to 9.14 nm (as shown in 4.9a)). This observation indicates that the Ullmann-type polymerisation had not progressed to completion following the initial anneal to 100 °C (with the small domains of polymers prohibiting longer chain growth due to local misalignment of the reactive end groups; from the STM data it is not possible to determine if these chains retain Br atoms at their termination).

The role of the hexyl chains in the alignment of the polymer structures is further elucidated by considering the separation between neighbouring polymers. Polymer chain separation was measured by identifying approximately parallel chains and acquiring a line profile perpendicular to the chain's length, as shown in Figure 4.10. From these line profiles, peak-to-peak measurements were used to determine line separation. Measurements were performed for both forwards and backward scans, with an average of the two measurements taken, to minimise the effect of drift. Figure 4.9b) shows the distribution of chain separations following annealing. Following the anneal at 100 °C, the separation of the chains is

broadly uniform, being generally around 0.9-1.0 nm (which is in agreement with a hexyl chain configuration for the polymers with the alkyl chains orientated in the rotamer (2-2) position– see Figure 4.9d) and Figure 4.1d)). This specific chain conformation results in the expected inter-chain separation and could be the cause of the visible diagonal staggering between smaller chains in the more heterogenous domains, as shown in Figure 4.7e). Heating further, to 250 °C, results in a much wider spread of separations (0.7-1.5 nm) with a significant reduction in the minimum separation between polymer chains (around 0.7-0.8 nm). These smaller dimensions are consistent with a process whereby hexyl chains begin to break off at higher temperatures, with a separation of 0.7 nm being consistent with two parallel polymers with no hexyl chains present (Figure 4.9c)). The additional space generated by the loss of alkyl chains may facilitate a conformational change between the two accessible rotamers. Figure 4.9e) shows how an alternative alkyl chain conformation could be expected to stabilise a chain separation of around 1.3 nm. Here, the chains are in the rotamer (1-1) orientation, which increases interchain separation compared to the rotamer (2-2) orientation. The combination of the loss of alkyl chains and conformation change is proposed to stabilise the structures shown in Figures 4.9c) and 4.9e), and is in agreement with the distribution of inter-chain separations shown in Figure 4.9b).

Having successfully shown on-surface synthesis in UHV conditions, I now will now move to a consideration of how to form the same structures under ambient conditions following solution deposition. The motivation for this move from UHV is to create a more suitable environment for scaling up synthesis protocols.

4.3 Self-assembly Under Ambient Conditions

4.3.1 Experimental Method

Br_2Hex_2DPP was successfully deposited onto both highly oriented pyrolytic graphite (HOPG) and Au(111)/Mica from solution *via* drop-casting, and imaged using an Agilent N9448A scanning tunnelling microscope (STM) under ambient temperature and pressure. **Br_2Hex_2DPP** was dissolved in toluene to give concentrations of: 2 μg/ml, 20 μg/ml, 100 μg/ml, 500 μg/ml, 1 mg/ml and 2 mg/ml.

Subsequently, and optionally, nonanoic acid was drop-cast onto the sample to aid with imaging.

4.3.2 Results

As for the self-assembled **Br_2Hex_2DPP** structures seen under UHV conditions, models of possible molecular orientations were produced (Figures 4.11, 4.12 and 4.13). These models were based upon STM measurements of the molecular lattice and by assembling models based on common bonding motifs, such as hexyl chain interactions. Figure 4.11 highlights a commonly seen structure, characterised by rows of bright features with clear horizontal and vertical periodicity ($\sim$1.5 nm and 1 nm respectively). This structure follows expected bonding motifs such as hexyl chain interaction, and bears similarities to those observed under UHV, however in this model there is no obvious indication of halogen bonding. Another notable feature of this structure is that the '2-2' arm conformation is preferred, and is most common across all visible structures. The close-packed structures enabled by this confirmation allow the unit-cell area to be minimised, and potentially explains their prevalence on the surface. An additional structure seen under ambient conditions is shown in Figure 4.12. This structure is of interest as it appears to incorporate the co-deposited nonanoic acid within the assembled structure. This kind of behaviour has been observed previously in self assembled structures of DPP based molecules. [108]

Many other structures were seen at the various concentrations, and on different surfaces, including an unusual hexagonal structure, shown in Figure 4.13. While stable structures were obtained *via* liquid deposition, attempts at thermally initiated polymerisation were unsuccessful. Following drop casting to previously successful monolayer concentration (500 μg/ml), various attempts to anneal the samples to polymerisation were unsuccessful. Methodologies involving heating to 250 °C within an inert gas (nitrogen) tube furnace, under vacuum, and under ambient pressure were attempted. After each method, no resolvable monomer or polymer systems could be identified; the results are shown in Figure 4.14. As can be seen, in most instances material has agglomerated into large indiscernible islands. In the instance of the open air hotplate, most of the material appears to

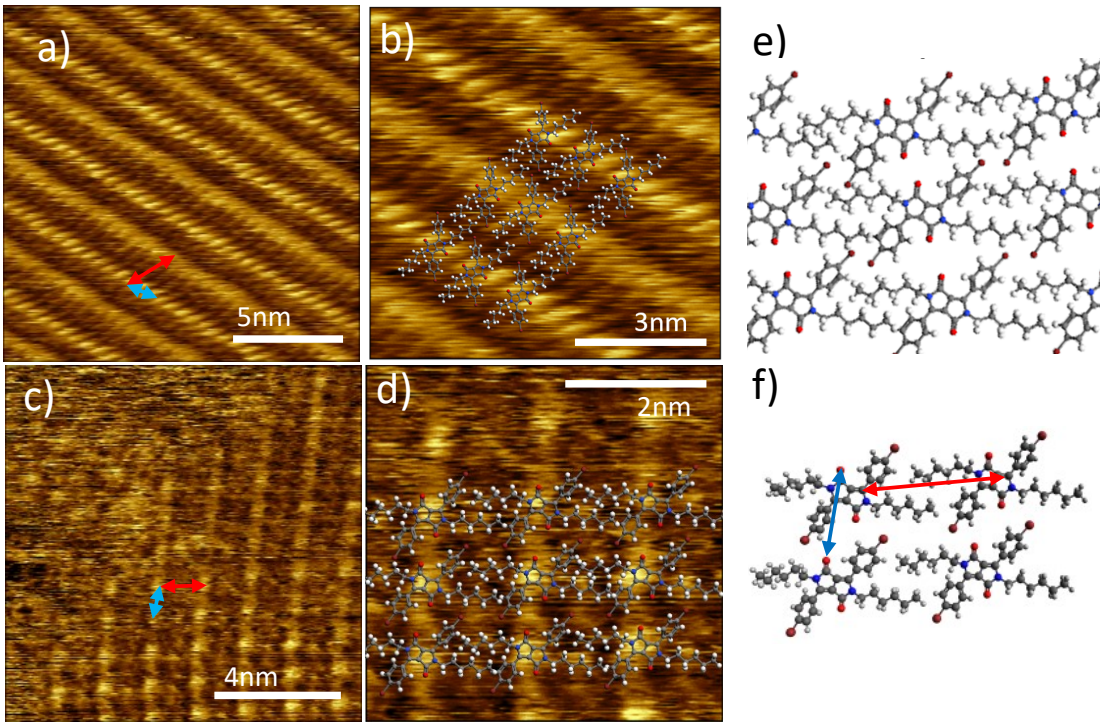

Figure 4.11: a) STM image of a lattice seen at 2 mg/ml **Br_2Hex_2DPP** solution drop cast onto HOPG. Horizontal spacing = 1.49 ± 0.13 nm, vertical spacing 1.07 ± 0.08 nm - (Sample bias = 1 V, Current = 0.05 nA). b) Proposed **Br_2Hex_2DPP** structure overlaid on the structure from a). c) Shows a lattice seen at 500 μg/ml **Br_2Hex_2DPP** solution drop cast onto Au without nonanoic acid present. Horizontal spacing = 1.38 ± 0.09 nm, vertical spacing = 0.94 ± 0.08 nm - (Sample bias = 1 V, Current = 0.05 nA). d) Shows the proposed **Br_2Hex_2DPP** structure overlaid on the structure from c). e) Shows the proposed structure isolated from any background image. f) Shows a single unit cell of this lattice. Horizontal spacing is measured at 1.5 nm, vertical spacing at 1 nm in this model. All overlays created using LMAPper. [129]

have desorbed (Fig. 4.14c)).

In ambient conditions, self-assembled structures were successfully prepared and characterised. Based on the STM images collected, these structures displayed a greater deal of variation than those seen in UHV, possibly impacted by the differing deposition techniques and atmospheric influences. Attempts to initiate the on-surface coupling reaction witnessed in UHV were unsuccessful, with no evidence of polymerisation following similar anneal temperatures to those ex-

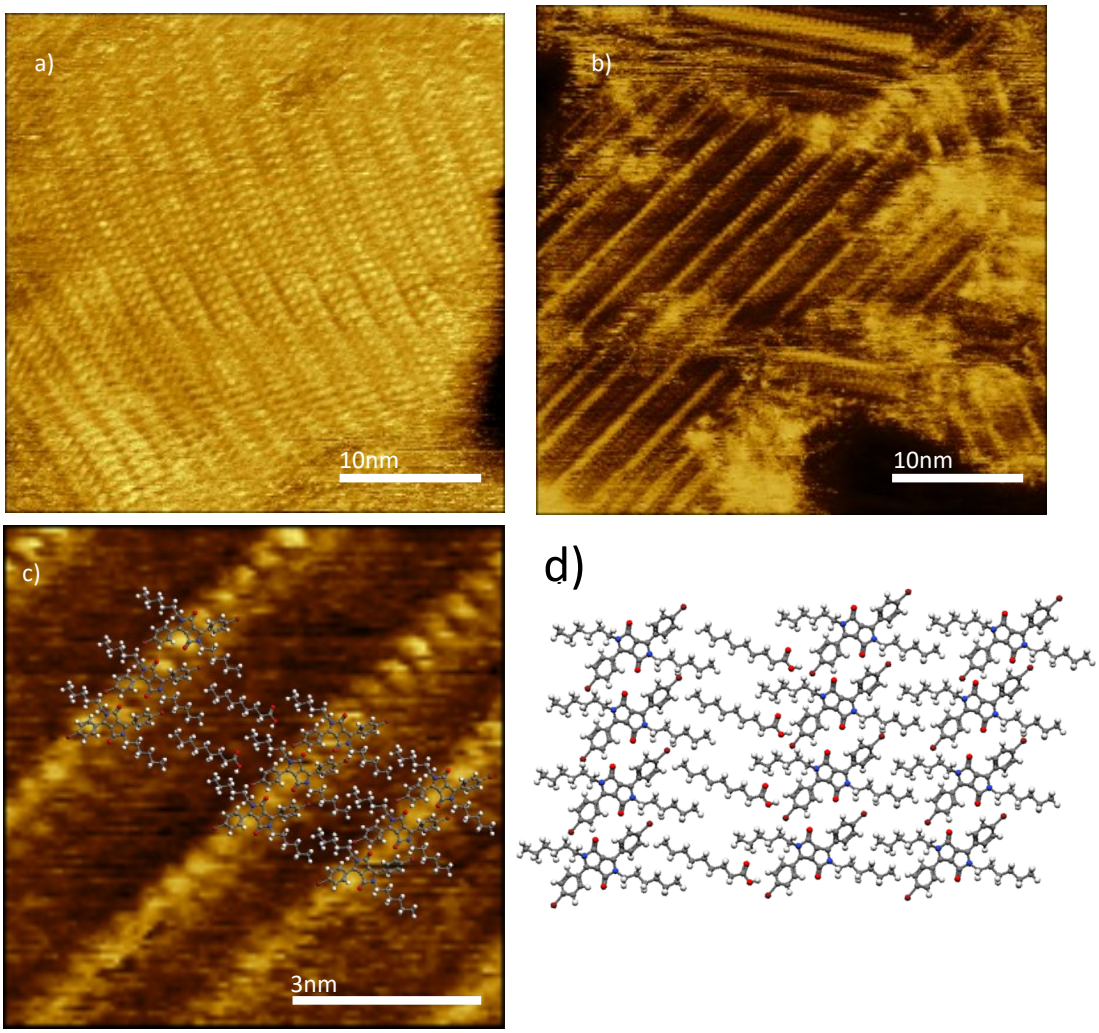

Figure 4.12: a) STM image of a lattice seen at 500 μg/ml **Br$_2$Hex$_2$DPP** solution drop cast onto drop deposited on Au, with nonanoic acid. The horizontal separation is 2.5 $\pm$ 0.1 nm. (Sample bias = 1 V, Current= 0.05 nA) b) Shows a lattice seen at 1 mg/ml **Br$_2$Hex$_2$DPP** solution drop cast onto Au, with nonanoic acid. The larger line spacing is 2.60 $\pm$ 0.08 nm, and the smaller line spacing is 1.75 $\pm$ 0.1 nm. (Sample bias = 1 V, Current = 0.05 nA). c) Shows a proposed **Br$_2$Hex$_2$DPP**/Nonanoic Acid structure superimposed over the structure from b). The separation between the larger spaced lines is as expected for two rows of **Br$_2$Hex$_2$DPP** separated by a single molecule of nonanoic acid, and the separation of the two closer rows is what would be expected if no nonanoic acid were involved. d) Shows the proposed structure.

perienced in STM. These issues are likely a product of the lack of control present in ambient pressure preparation and measurement; contaminants such as water

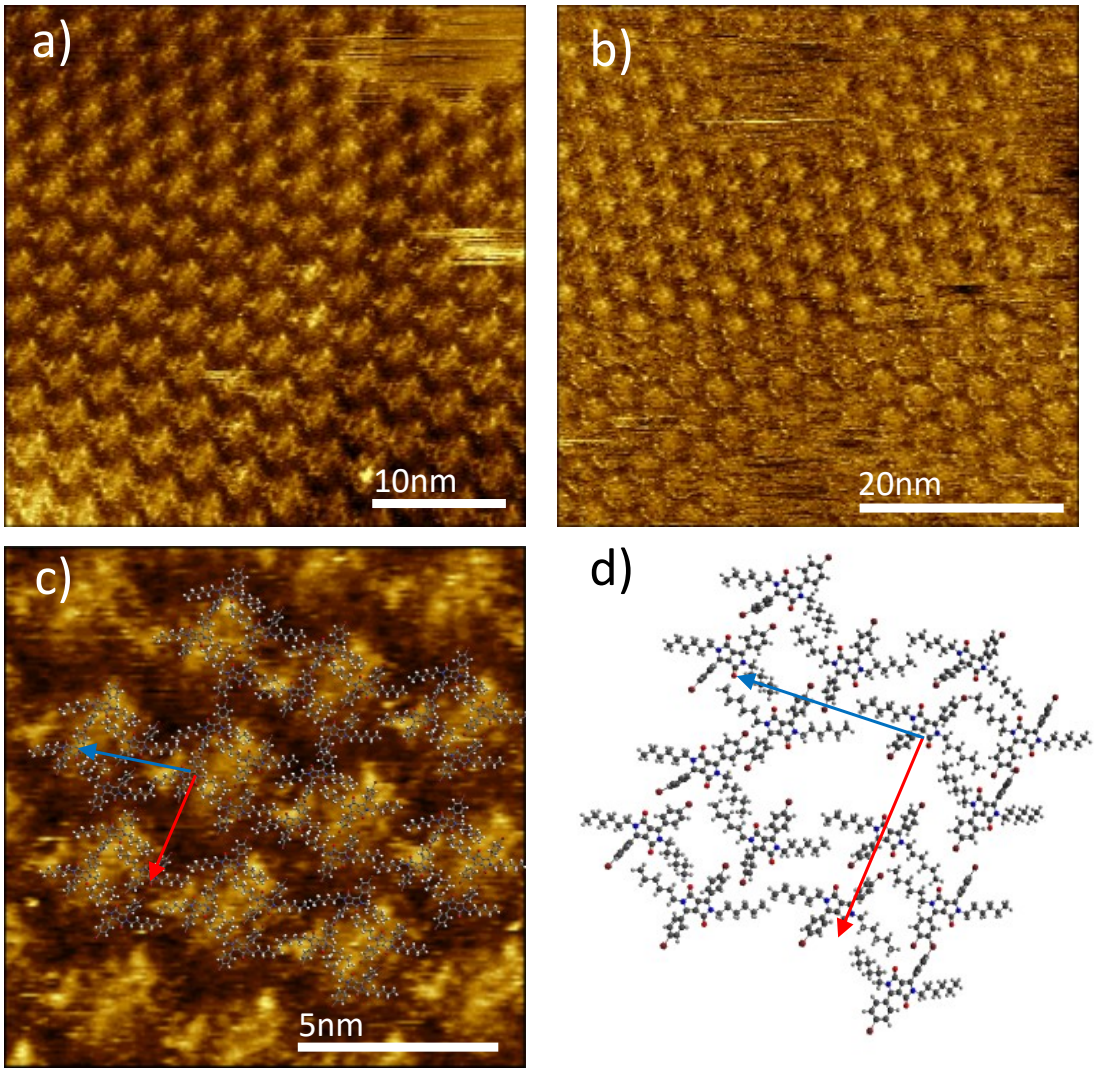

Figure 4.13: a-b) STM images showing structures seen on 500 μg/ml **Br_2Hex_2DPP** solution drop cast onto HOPG. (Sample bias = 1 V, I(set-point) = 0.05 nA) c) Shows the structure from (a) with overlaid proposed **Br_2Hex_2DPP** structure and lattice vectors. The blue arrow representing the horizontal vector was measured to be 3.3 ± 0.2 nm, and the vertical vector was measured to be 2.9 ± 0.1 nm. d) Shows a model of the molecular structure, where the blue length was measured to be 3.1 nm and the red length was measured to be 2.9 nm.

and adventitious carbon are unavoidable in these circumstances, and the presence of solvents and in particular nonanoic acid are necessitous with this preparation technique.

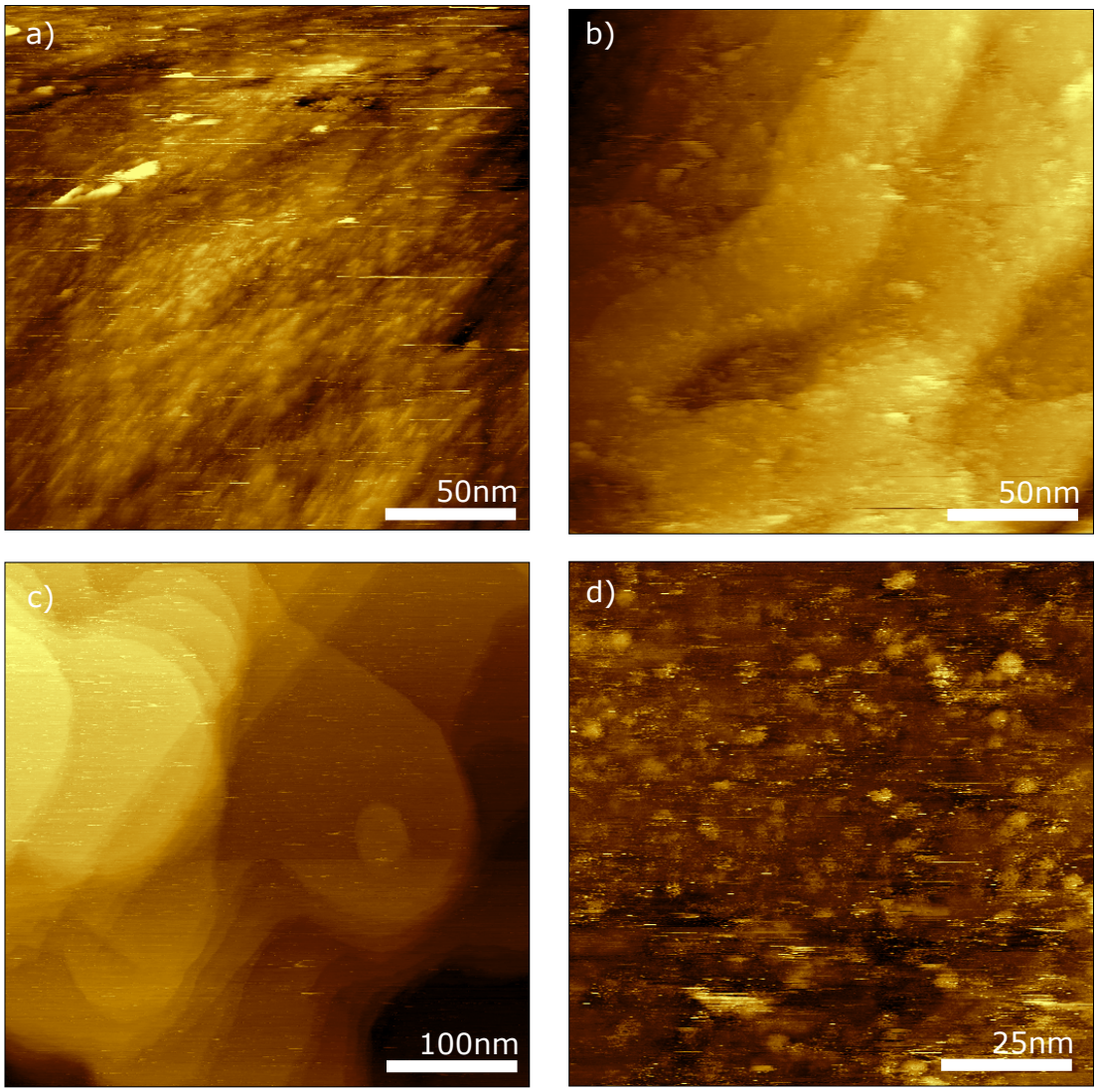

Figure 4.14: STM images of a 500 μg/ml **Br_2Hex_2DPP** solution drop cast onto Au(111) following a variety of annealing techniques (Sample bias = 1 V, Current = 0.05 nA). a) Following a 120°C anneal in a vacuum bubble system. b) Following a 250°C anneal in a vacuum tube. c) Following a 250°C anneal on an open air hotplate. d) Following a 250°C anneal in nitrogen atmosphere tube furnace.

4.4 Conclusion

In conclusion, here I have demonstrated that the on-surface self-assembly and polymerisation of functional DPP species is significantly influenced by specific chemical groups. Here, alkyl chains are observed to influence both the close-packing of the reactant molecules and the ordering of the polymeric product. Similarly, the bromine moieties (selected to facilitate on-surface synthesis) also

influence the stability of the close-packed precursor units, which in turn is likely to affect the reaction pathway and ultimate alignment of the polymeric product. I demonstrate that the alkyl chains play a key role in the alignment of the DPP polymers and show how the thermal stability of these groups is key in maintaining the long-range order of the polymers. In addition, it has been shown that pro-chiral nature of the DPP-based monomers results in homochiral self-assembled structures of the unreacted monomers and the polymer reaction product. It is expected that the alignment of photo sensitive polymers is key to maximising the efficiency of optoelectronic devices, and hence the role of molecular level interactions driving the ordering of these polymers is an important step towards development of such devices.

Chapter 5

Deposition and Characterisation of Large Porphyrin-based Nanorings

In this chapter, the technique of electrospray deposition is explored as a method for allowing the on-surface STM characterisation of thermally unstable complex molecules, in this case a selection of nanorings created via novel in-solution synthesis.

5.1 Electrospray Deposition

In the previous experimental chapter, chapter 4, deposition of a target molecule was achieved via thermal sublimation. This strategy is a common approach for in vacuum deposition of molecules onto a supporting substrate. However, it is not always possible. Larger, more complex molecules are often less stable and liable to decompose before reaching sublimation temperature. The morphology and conformation of these molecules on surfaces is of interest, and so an alternative means of deposition is required. One route to successful deposition of thermally labile molecules is electrospray ionisation. [138] Originally developed as a method of creating ion beams for use within mass spectrometry, [139] the electrospray method was more recently implemented as a method for molecular deposition [140, 141] and has proven highly successful as a deposition method for a variety

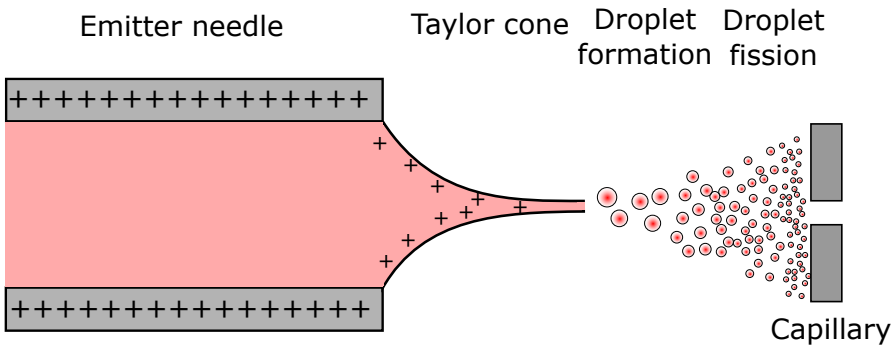

Figure 5.1: Diagram of the process of electrospray. A solution containing the target molecule and a polar solvent passes through a positively biased needle, ionising elements of the solution (most likely the polar solvent). These ions move to the end of the needle forming a Taylor cone, and disperse into droplets as charge build-up exceeds surface tension. These droplets then undergo repeated fission during transit towards the oppositely biased capillary.

of large molecules with complex functionalities. [142–144]

5.1.1 Electrospray Methodology

Put simply, electrospray is the creation of charged droplets, which subsequently undergo fission into smaller and smaller droplets as they move away from an emitter. By creating a fine mist of molecules within a solvent, it is possible to propel the target molecule towards the sample, without the need for sublimation. By placing a sample down-stream of this flow of droplets, one can transfer molecules from solution to a substrate. To achieve this, a solution containing the molecule dissolved in an appropriate solvent/polar solvent mix is pushed through a biased emitter needle of radius 25-50 μm by a syringe pump. The needle is positioned approximately 1-3 mm away from a grounded capillary tube serving as an entrance to the UHV system. The electrospray process occurs in ambient conditions, as evaporation of solvent is a key part of the process, and thus for the technique to apply to UHV science an opening to ambient pressure must be made in the UHV system. The electric field drives the process of spray formation, as will be described below. The setup is shown in Figure 5.1. A high bias of the order of kV is applied to the needle to create an electric field between the needle

and capillary. The magnitude of this electric field is described by: [145]

$$E = \frac{2V}{r \ln \frac{4d}{r}}, \tag{5.1}$$

where V is the applied bias, r is the radius of the emitter needle and d is the distance between the needle and capillary. In an example case, where a positive bias is applied, the electric field causes positive ions to migrate away from the sides of the needle towards the surface of the liquid. This build-up of positive charge leads to a repulsion of the gathered ions into a Taylor cone (see Fig. 5.1). [146] For a sufficiently high electric field, the repulsion between ions is large enough to overcome the surface tension, γ, of the liquid and a spray of ionised droplets is emitted from the end of the cone. The critical point at which the electric field (which created the Taylor cone) is strong enough to cause this, E_{crit}, is: [145]

$$E_{crit} \approx \sqrt{\frac{2\gamma \cos\theta}{\epsilon_0 r}}, \tag{5.2}$$

where ϵ_0 is vacuum permittivity and θ is half the angle of the Taylor cone.

Immediately following emission, the droplets can be quite large, and reduce a great deal in size as they travel towards the capillary. This is due to solvent evaporation, increasing charge density and leading to further droplet fission. The point at which the charge density overcomes the cohesive force is known as the Rayleigh limit and is described by the following: [145]

$$Q_{Ry} = 8\pi\sqrt{\epsilon_0 \gamma R^6}, \tag{5.3}$$

where Q_{Ry} is the charge and R is the radius of the droplet. The droplets repeat this process, becoming smaller and smaller. The end point of this process is debated: Dole *et al.* [147] propose that the droplets undergo repeated fission until a single molecule remains in the droplet, with the final solvent evaporating and leaving a residual charge on the molecule. This is known as the charge residual model. A second model, known as ion evaporation, proposes that once droplets decrease below a certain size (approximately 10 nm), ions within the solvent (including charged molecules) can be emitted into the gas phase from the droplet in a process known as ion evaporation. [148]

The needle emitter is positioned external to the vacuum, at ambient pressure; the spray is aimed towards a capillary leading to the UHV system. Of course,

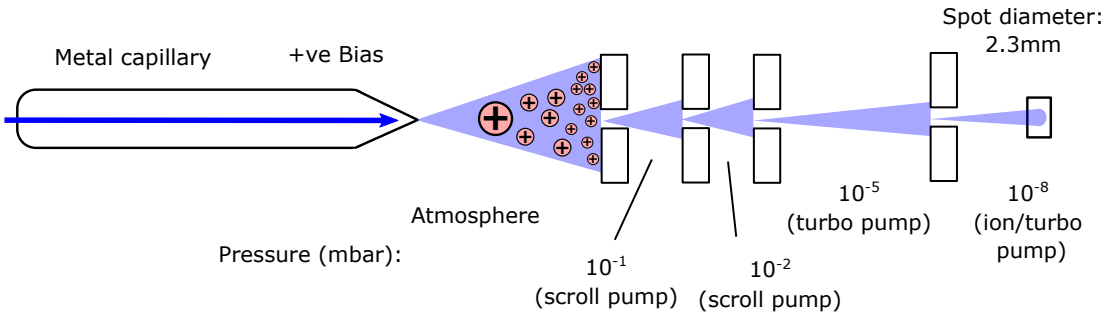

Figure 5.2: The setup of the progressive pumping system typically used to maintain good UHV pressure during electrospray.

the sample needs to remain at UHV pressures to maintain cleanliness. Hence, a series of differentially pumped vacuum chambers are positioned behind the capillary, leading to the sample stage. This setup is shown in Figure 5.2. As can be seen, the ion spray is passed through several apertures, each leading to a chamber with successively lower pressure. This technique, known as differential pumping, allows for the UHV system to be exposed to atmosphere and thus the molecular spray without suffering significant increase in pressure. The interior apertures are so-called "skimmer cones", and are cone-shaped to ensure that only ions travelling straight through the chamber can pass through; in each new low pressure chamber, the beam will expand, so selecting for ions travelling in a straight line is beneficial.

5.1.2 Characterising the Deposition Profile of Electrospray

When performing electrospray deposition, one key difference in relation to depositions *via* thermal sublimation is the uniformity of deposition. Electrospray depositions do not produce uniform coverage, in contrast to what is typically obtained *via* thermal sublimation. Thermal sublimation depositions provide an even coverage across a target sample, due to the distance d from the sample to the sublimator typically being comfortably large enough to provide a deposition spot size greater than the size of the sample. Given a divergence angle θ (half the angle of the emission cone from the central axis of the crucible), the relationship between spot radius R, distance d and aperture radius r is given by the following:

$$R = r + d\tan\theta. \tag{5.4}$$

Hence, a sample of approximately 6.5 mm width will be completely covered in the case where a crucible is with a distance d of 1.75 cm from the sample (in the situation where the divergence angle is 12° and the emission aperture is 3 mm in diameter). [149] Typically the sample-evaporator separation in a UHV setup is around 10-20 cm, so full sample coverage is expected when utilising thermal sublimation. The electrospray setup used in this thesis, has a much narrower angle of divergence upon exiting the last aperture, due to the sequence of skimmer cones. This is approximately 0.25°. The distance to the sample is also a very short 3 cm, and final aperture size 1 mm. Given these values, the spot diameter is calculated to be 2.3 mm.

Characterising a 'Single-Spot' Deposition

Because the deposition spot size of an electrospray deposition is so small, examining the coverage dependence as a function of sample position is of interest; in the context of STM characterisation, electrospray deposition creating areas of differing coverage on one sample could be of use when considering coverage dependent effects. In order to characterize the coverage-position dependence, we perform a spot deposition in the centre of the sample, and acquire a series of STM measurements taken at periodic intervals in a horizontal line across the centre of the sample. As shown in Figure 5.3, it can be seen that deposition results in a large amount of material within the central region, with a decreasing amount visible when moving laterally away from the centre. The deposition pictured followed a 40 min deposition in the centre of the sample at a pressure of 1×10^{-7} mbar. The stepwise STM can be used to estimate the size of the deposition spot.

The images can be categorised into 4 rough regions. Beginning in the very centre, the deposition is mostly too thick to perform STM, with great difficulty imaging and large (apparent height ∼4-5 nm) clumps of indiscernible material. This area (dark red) has a diameter of approximately 0.5 mm, based on the STM images taken. Extending beyond this is a further region where material density is too high for consistent and high quality STM (light red), of approximately 1.3 mm diameter. A sub-monolayer coverage appropriate for imaging individual species is found in the green area, with a diameter of approximately 2.4 mm. While this is

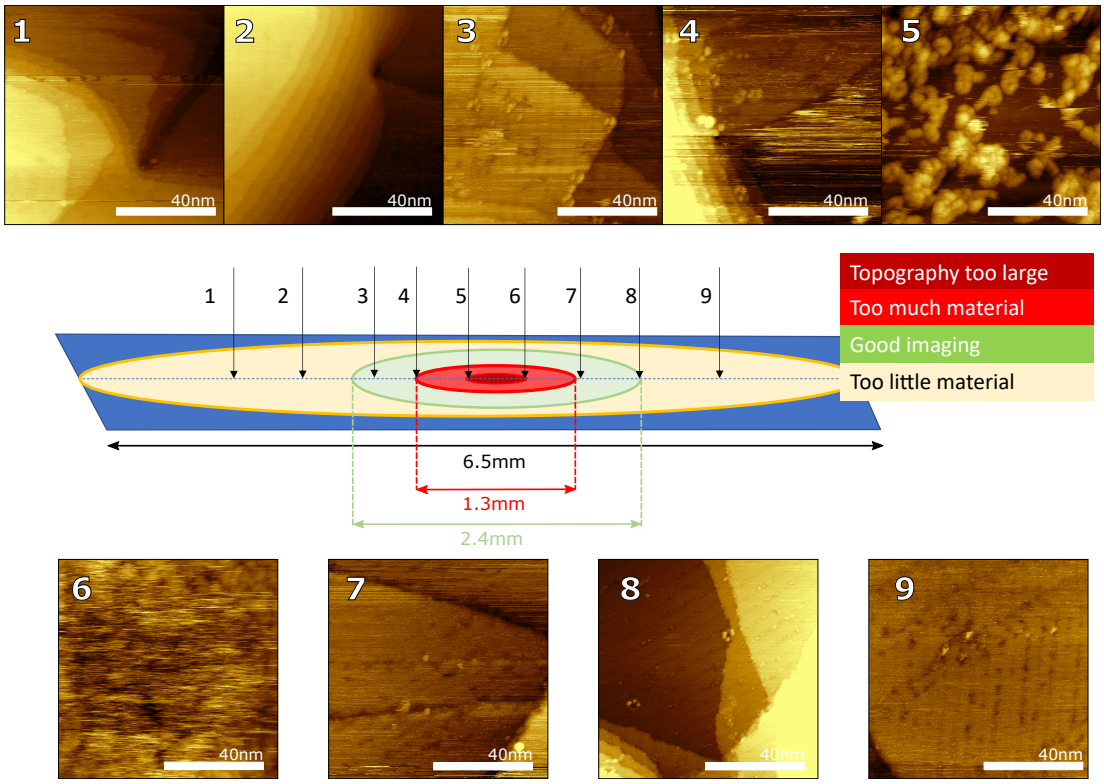

Figure 5.3: Stepwise STM images taken at different lateral positions across a sample prepared with an electrospray spot deposition of *c*-P24b. All images taken at room temperature with the following settings: -1.8V, 15pA.

slightly larger than the calculated spot size, it is possible that material migrates across the surface at room temperature, which this sample was prepared and imaged at, or that solvent dewetting can result in transport of material. The final possibility is that the deposition spot may be larger than calculated, as will be discussed later in this chapter and in chapter 6. The most revealing implication of this coarse-grained analysis is that the electrospray spot itself is non-uniform and gives rise to a significantly higher coverage at the centre. This has significant implications for the potential use of X-ray spectroscopy studies of electrosprayed materials, as the spot size of the X-ray beam could encompass a variety of different levels of coverage. This would affect 'ensemble averaging techniques', such as XPS, which may average over multiple different coverages, providing an inaccurate picture of the experimental situation, depending on the beam profile used at the time. At grazing incidence, for example, any x-ray spot will cover most of a sample in whichever direction the beam is titled.

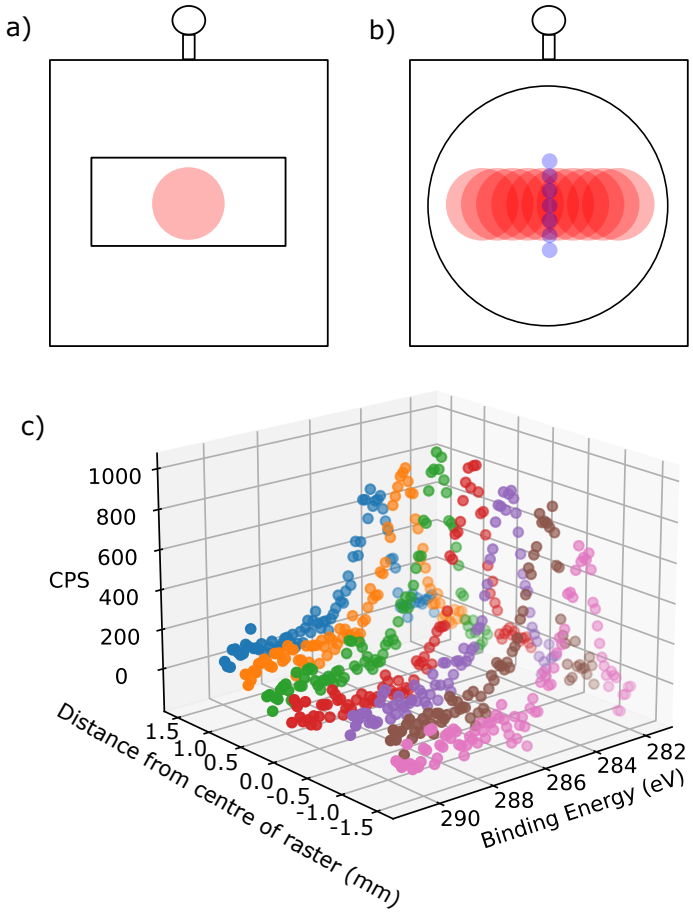

Figure 5.4: a) Scale diagram of a sample plate with an Au(111)-on-mica sample of dimensions 3x6 mm (central rectangle) featuring an electrospray spot deposition (red circle of radius 2.3 mm, in line with expected calculated spot size), such as that shown in Figure 5.3. b) Scale diagram of an electrospray raster deposition (series of red circles of radius 2.3 mm) onto an 8 mm diameter Au (111) single crystal sample (larger black circle). Blue circles mark the locations of the XPS spots (diameter 1mm) from c). c) Stepwise C 1*s* spectra taken across the electrospray raster deposition strip in locations marked by Xs in b); +ve directions are towards the eyelet, -ve is away from the eyelet.

Characterising a 'Raster' Deposition

As a route to obtaining a more uniform coverage, an alternative approach is to perform a raster deposition, whereby the electrospray spot is moved across the sample at regular intervals, creating a larger area of uniform coverage. A schematic comparison of the two deposition approaches can be seen in Figure 5.4a-b). While the spot deposition shown in Figure 5.3 was performed at a

single location for 40 mins, a raster deposition consists of several evenly spaced deposition spots for a shorter time. In Figure 5.4b), the deposition consists of 10 spots 0.5 mm apart, each of which was deposited on for 5 minutes per raster, with a total of three cycles. This means each spot received approximately 15 minutes, and towards the centre most regions overlap at least 3–4 times, albeit at the edge of the deposition spot. This leads to a larger area of more consistent deposition coverage, more appropriate for area-averaged techniques such as X-ray spectroscopy.

As the RT STM used here can only move horizontally across the sample, stepwise C 1*s* XP spectra were taken vertically across this strip, as displayed in Figure 5.4c). The XPS spots were taken at 0.5 mm separation across the deposition spot in the approximate centre of the raster, in order to gauge the width of the strip. Each different colour spectra presented in Figure 5.4c) represents a C 1*s* spectra taken at one of these spots, with blue being the most extreme position 1.5 mm towards the eyelet from the centre of the strip (top in figure 5.4b)), and pink being the most extreme position 1.5 mm away from the eyelet from the centre of the strip. Each of these peaks is located at broadly the same binding energy (284.1 eV), with the peaks taking uniform shape, but differing intensity. The coverage is broadly uniform across the region covered by the calculated 2.3mm deposition spot, with noticeable drop off beyond this limit. While there is a decrease in coverage beyond this point, it is notable that the apparent material dispersal under this method is wider than anticipated, indicating that the deposition spot is larger than calculated. These results do indicate, however, that the creation of a large deposition area of uniform coverage is possible using this method, and hence is suitable for various X-ray spectroscopy techniques; this method is utilised in chapter 6.

5.1.3 Co-deposition of Contaminant Material

When imaging electrosprayed material at room temperature, the deposited species is often clearly visible on the substrate (provided the species itself is not too mobile), allowing for high quality images such as those shown in fig 5.5a). However, upon cooling to 4 K, unresolvable contaminant is visible across the sample, as

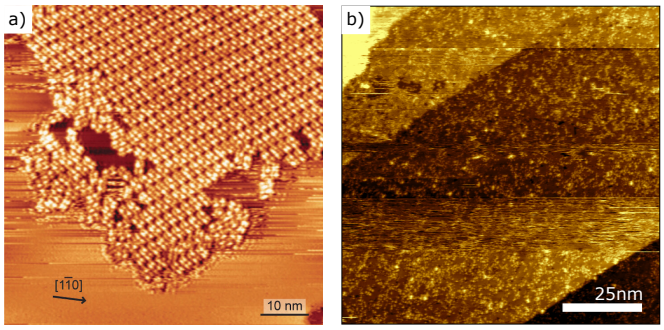

Figure 5.5: a) Image of as deposited molecular precursors on Ag(111), taken at room temperature. Taken from Ran *et al.*. [150] b) Image of toluene+methanol 40 minute spot deposition taken at 4 K. Bias = -1 V, Current set point = 50 pA.

shown in 5.5b). This image was taken following spot deposition of solvents, toluene and methanol, as a control experiment. The contaminant is of unknown origin, but appears to be very mobile on the surface, as it can be found across the breadth of a sample, not just in the deposition area.

Upon annealing to 250 °C, the material appears to desorb. For molecule-substrate systems this can be an issue, as measurements of certain reaction stages triggered before contaminant desorption may not be measured accurately. The relatively high desorption temperature seems to rule out the possibility of the contaminant being the toluene or methanol themselves, as these should evaporate at temperatures below 250°C. Possible sources of contaminant could be impurities within the chosen solvents. It is also possible that the electrospray mechanism itself is contaminated; perhaps inside the many differential pumping chambers, the turbulent flow of solution can attach and remove chemical species from the inside wall of the chambers before eventually depositing them.

While higher purity solvents, or decontamination of the e-spray setup, may solve this issue, an alternative approach is mass-selective electrospray, using principles from mass spectrometry in order to select for a mass associated with the target molecule. This has been applied with success to large organic molecules like proteins, [151] however it has not been broadly adopted in the field of on-surface synthesis. While molecular species can still be imaged in the presence of contaminant, and useful information about morphology can be obtained, the packing of molecules may well be affected by contaminant material. Techniques

like scanning tunnelling spectroscopy (STS) are hampered by a layer of contaminant material, as it is challenging to ascertain which states are from the target molecule and which come from the contaminant.

5.1.4 Applications of the Electrospray Methodology

Electrospray deposition is an extremely useful and versatile tool for the deposition of large, thermally labile molecules into UHV conditions for STM. Due to the non-uniform coverage of spot depositions, these are unsuitable for X-ray spectroscopy; a raster deposition technique produces a larger area of uniform deposition suitable for X-ray spectroscopy. Low temperature STM can be affected by contaminant material, inhibiting techniques such as STS, however useful morphological observations can be made. Within this thesis, electrospray deposition is utilised to investigate two classes of porphyrin-based molecular species: cyclic porphyrin nanorings, discussed below, and porphyrin-graphene nanoribbons, discussed in chapter 6.

5.2 c-P Series Nanorings

Electrospray facilitates the STM imaging and characterisation of the morphology of large target molecules that are not suitable for thermal deposition. Synthetic chemistry provides a route to create a wide array of functional molecules, such as extended polymers hundreds of nanometers in length. [152] While these molecules can be deposited *via* drop-casting or freeze-drying, electrospray allows for deposition into UHV conditions, and thus allows for higher resolution STM imaging. STM characterisation has one advantage over the range of in-solution measurement techniques, which generally rely on averaging over many molecules, that are frequently used to characterise the products of molecules synthesis (mass spectrometry, nuclear magnetic resonance (NMR), gas-liquid chromatography (GLC)). Crucially, the combination of STM and electrospray allows the morphology of a single target molecule to be discerned, and by measuring a range of single molecules, information about the distribution of molecular size and shapes can be ascertained. A key issue, which appears trivial at first glance, is to deter-

mine whether or not a polymer is linear or cyclic. For linear and cyclic polymers, only the terminating monomer unit might be expected to display any chemical difference from the monomers within the body of the polymer and, as such, trying to distinguish between linear and cyclic species by considering the small number of terminating groups can be non-trivial and often outside the scope over techniques which average over many monomers. STM and SPM offer a real space route to identifying the structure of novel molecular species.

One family of molecules that exhibit a cyclic structure are porphyrin nanorings. In several naturally occurring biological systems, light capture is conducted by rings of chlorophyll molecules, of which the central structure is an aromatic porphyrin unit. [153] In order to replicate the exceptional charge transport and light capture properties of these natural systems, porphyrin nanoring structures have been synthesised and investigated. Previous porphyrin nanorings have been unable to replicate the charge transport exhibited by their natural counterparts. [154–156] The molecule shown in Figure 5.6a), labelled *c*-P24b, is an attempt to explore systems which may exhibit novel charge transport behaviour. Synthesized *via* a novel vernier templating route (the process of which is shown in Figure 5.6c-d), as reported by O'Sullivan *et al.* on a similar porphyrin nanoring [157]), this molecule represents the first time a cyclic porphyrin-based structure mimicking the meso-meso linked porphyrin rings found in chlorophyll molecules has been synthesized, and hence provides a route to further understanding the light capture and energy transport properties of these molecules. [158]

The unique aspect of vernier templating is the use of several small template sections, unevenly matched with the porphyrin oligomers in such a way as to add to a coherent whole, allows for the in-solution synthesis of both ring and template, rather than having to create a sometimes extremely large template separately. In traditional template synthesis, the larger the target molecule, the larger the template, until creating such a template becomes a limiting factor in and of itself. This is not the case with vernier templating. In the example in Figure 5.6c), each template features 6 attachment points, and each oligomer features 4 porphyrins. The combination of 2 templates and 3 oligomers forms the vernier complex as shown in 5.6d), with a subsequent covalent coupling step facilitating the forma-

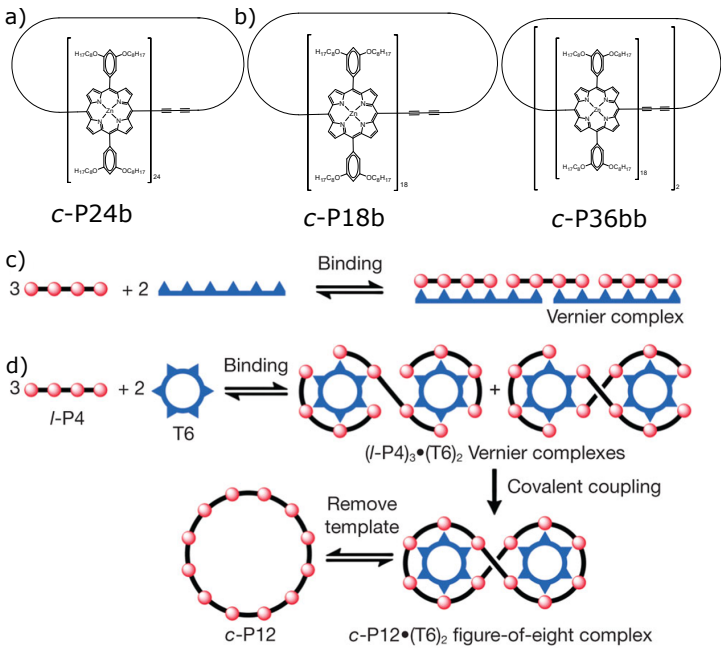

Figure 5.6: a-b) Structures of porphyrin oligomers *c*-P24b, *c*-P18b and *c*-P36bb, where *c* refers to cyclic, PN is the number of porhpyrin units, and b represents the number of butadiyne bridges in the molecule. c-d) Process of vernier templating, taken from O'Sullivan *et al.*. [157] c) Shows the formation of a molecular 3:2 complex of oligomers and template sections. d) Shows the formation of the vernier complex to create a 12 porphyrin macrocycle.

tion of a 12 porphyrin ring. Given that the cyclic structure of these molecules is key to their function, ratifying the cyclic topography was of significant importance. Hence, a need arose for the unique structural characterisation abilities of STM, and electrospray deposition. After the breakthrough synthesis of *c*-P24b, *c*-P18b and *c*-P36bb were also synthesized *via* a similar template method; [159] these structures are shown in Figure 5.6b). Much like *c*-P24b, the cyclic nature of these other *c*-P series nanorings required verification *via* STM characterisation. Each species possesses unique characteristics rendering further investigation desirable: *c*-P18b was the smallest produced in this style, while *c*-P36bb was an unexpected figure-of-8 by-product from the synthesis route. *c*-P18b was of particular interest, as smaller cyclic molecules experience greater strain, and tend towards conformations that favour electron delocalisation, to stabilise the molecule, and thus a smaller molecule is a target for energy transport properties.

In this section, the *c*-P series nanorings are deposited onto an Au(111)-on-

mica sample *via* electrospray deposition and characterised with STM. The initial goal is to determine the cyclic nature of the target molecules, and subsequently characterise structural and conformational motifs.

5.2.1 Experimental Method

All nanoring species were synthesized by the group of Harry L. Anderson, Department of Chemistry, University of Oxford, Chemistry Research Laboratory, Oxford, UK.

Structural characterisation was performed *via* STM. Au on mica samples (Georg Albert PVD GmbH) were cleaned *via* cycles of Ar ion sputtering (20 minutes at 0.75 keV, 8.5×10^{-6} mbar) and annealing (300 °C for 20 minutes). Sample cleanliness was determined *via* XPS prior to deposition. STM data was acquired using an Omicron STM-1 system, with Nanonis control electronics, operating at room temperature under ultra-high vacuum (UHV) conditions: base pressure $< 2\times10^{-9}$ mbar. Imaging was performed using electrochemically etched tungsten tips, functionalised with gold during on-surface tip preparation (bias is applied to the sample).

X-ray photoelectron spectroscopy (XPS) was acquired using a SPECS DeviSim near ambient pressure XPS (NAP-XPS) instrument operating in ultra-high vacuum (UHV) mode at a pressure $< 1\times10^{-9}$ mbar. Spectra were measured using a Phoibos 150 NAP hemispherical analyser with 20 eV pass energy and monochromatic Al Kα X-rays (1486.7 eV). The samples were transported between the STM and XPS sites using a vacuum suitcase at a pressure $<1\times10^{-10}$ mbar.

All nanorings were prepared in 50 µg/mL solutions in toluene/methanol (3:1 ratio). Electrospray deposition was conducted for all samples upon a clean Au(111) substrate *via* electrospray ionization with a Molecularspray UHV4i deposition source. Parameters for each sample are as follows: *c*-P18b was deposited with a solution flow rate of 0.1 mL/hour for 40 minutes in a single spot using a potential of 1.9 kV to initiate the electrospray event (base pressure during deposition was 1 $\times10^{-7}$ mbar). *c*-P24b was deposited with a solution flow rate of between 0.1 and 0.03 mL/hour for 30 minutes in a single spot using a potential of 1.2 kV to initiate the electrospray event (base pressure during deposition

was 2.5×10^{-7} mbar). The *c*-P36bb was deposited with a solution flow rate of between 0.1 and 0.03 mL/hour for 20 minutes in a single spot using a potential of 1.9 kV to initiate the electrospray event (base pressure during deposition was 1×10^{-7} mbar). *cf*P18MM was deposited with a solution flow rate of between 0.1 and 0.03 mL/hour for 20 minutes using a potential of 2 kV to initiate the electrospray event (pressure during deposition was 2 x 10–7 mbar). P18MM was deposited with a solution flow rate of between 0.1 and 0.03 mL/hour for 40 minutes using a potential of 2 kV to initiate the electrospray event (pressure during deposition was 2 x 10–7 mbar). During the deposition of P18MM, the electrospray spot was raster-scanned across the sample.

The *c*-P series rings are covered in the following section, with the P-18 series rings described and covered in section 5.2.4.

5.2.2 Nanoring STM

Following deposition, I obtain morphological data of the various cyclic polymers *via* STM characterisation. In all cases, areas of sub-monolayer coverage were identified, where molecular species were numerous, but with enough separation to allow individual species to be identified and imaged. As can be seen in Figure 5.7a-c), areas of approximately similar coverage were found on each sample. In each case, the cyclic nature of the molecules is clearly visible. All of the c-P series rings exhibit an aperiodic fluctuation in apparent height, shown by the bright features visible around the circumference of each ring. These display no apparent pattern, and vary in both height and number seemingly at random; efforts were made to ascertain whether differing surface adsorption sites affected this characteristic, but no relationship could be established. They are attributed to non-planar structures driven by competition between the preferential adsorption of the plane of the porphyrin with the substrate and steric hindering between neighbouring covalently coupled porphyrins. The steric hindrance between the meso-meso linked porphyrins typically exhibit a rotational angle of between 70-90° in solution, and hence facilitate the planar adsorption of all porphyrin cores upon the substrate. I attribute the variation in appearance to the prevalence of a number of quasi-energetically-degenerate conformational structures or kinetically

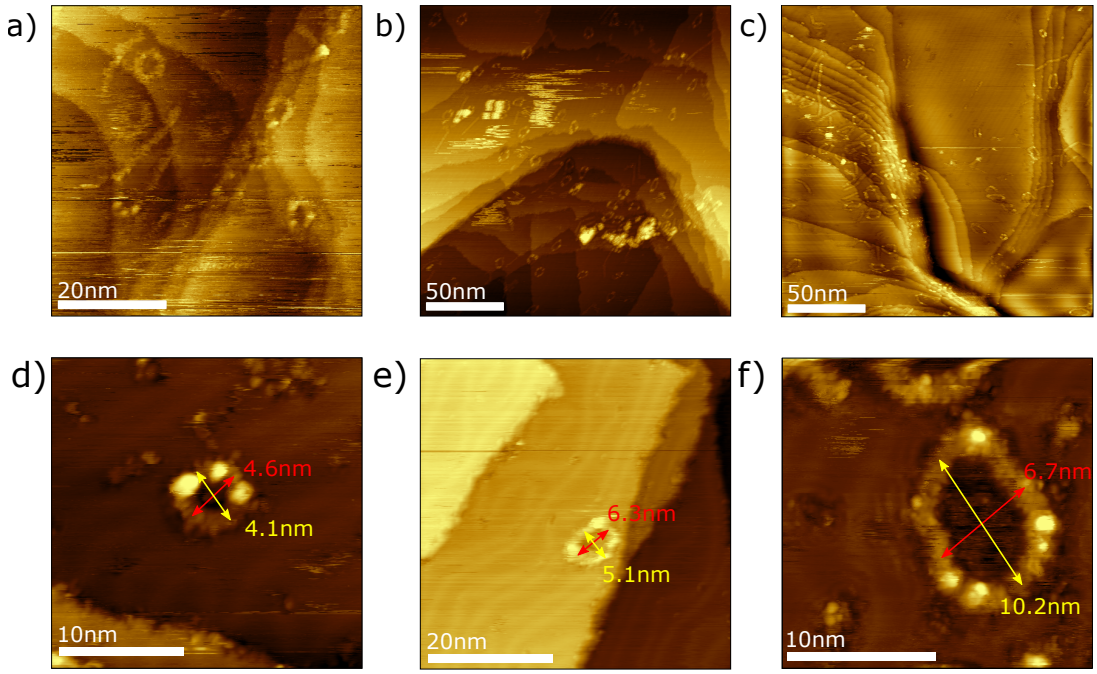

Figure 5.7: a-c) Overview STM images showing coverage of a) *c*-P18b, b) *c*-P24b, and c) *c*-P36bb - this image has had a "polynomial background subtraction" applied during post processing to flatten the image and make all steps visible, causing some unusual brightness fluctuations. These are not representative of the surface states. All images: Sample bias = -1.8 V, Set-point current = 20 pA. d-f) Closer zoom STM images showing measurements of individual species, d)*c*-P18b (-1.8 V, Set-point current = 15 pA), e) *c*-P24b (-1.8 V, Set-point current = 20 pA), and f) *c*-P36bb (-1.8 V, Set-point current = 15 pA).

trapped arrangements.

We now focus on characterising the dimensions of individual cyclic polymers. In Figure 5.7d-f), isolated examples of each species can be seen, with measurements taken across the long and short axis. The dimensions are obtained from the peak-to-peak separation of the features observed in line profiles. Line profiles are taken across the full diameter of the rings, with the major and minor axes being identified visually, as shown in Figure 5.8. Most rings are not perfectly circular; for the purposes of measurement, they are considered ellipses, with a major axis and minor axis. These are represented by a blue and red line, respectively, as shown in inset Figure 5.8c) and applied in 5.8a-b). The line profiles have two clear peaks associated with the ring; in this case, the peak-to-peak separation on

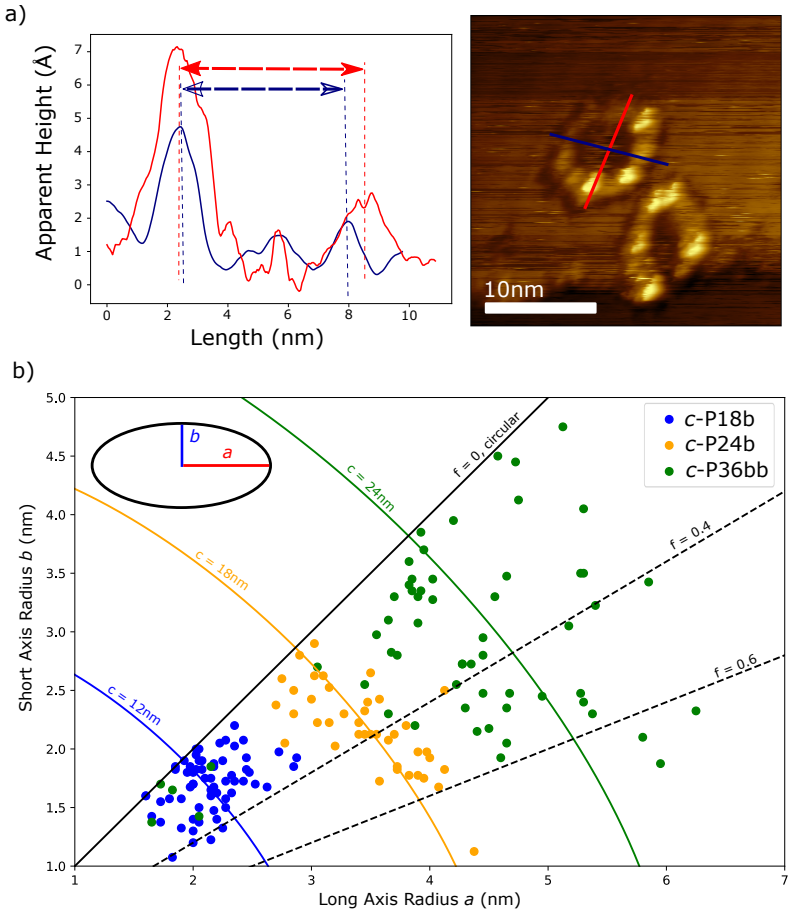

Figure 5.8: a) Line profile across the long and short axis of *c*-P24b species, as shown in associated STM image. (Sample bias = –1.8 V, Set-point current = 20 pA). b) Graph showing the experimentally measured long- and short-axis for *c*-P18b, *c*-P24b and *c*-P36bb nanorings deposited onto Au(111).

the red and blue line profiles are 6.2 nm and 5.7 nm, respectively. By measuring the long and short axis of the rings, information can be gained on the size of the rings, as described below, and by comparing the ratio of the two axes inferences can be made on the flexibility of the rings; greater deviation from circularity can be seen as an indication of molecular flexibility. These measurements were collected for a large number of species for each deposition (The number of individual rings measured for the *c*-P18b, *c*-P24b and *c*-P36bb data sets consists of 41, 38 and 59 molecules, respectively), and the long and short axis plotted against one another in Figure 5.8b). The solid black line represents a flattening ratio f of 0, indicating a circular ring shape; flattening ratio is calculated as $\frac{a-b}{a}$, where a is the long axis and b is the short axis. The dotted lines represent increasing f values,

meaning a more elliptical shape. The blue, orange, and green arcs correspond to an ellipse of fixed circumference; equivalent to the average circumference obtained for each nanoring deposition. As can be seen, the rings cluster into three groups, corresponding to the three molecular species. As the size of the rings increases, so too does the flexibility, as the flattening ratio of the larger rings expands beyond 0.6, whereas for the *c*-P18b species is almost entirely below 0.4. Also worth noting is the apparent presence of smaller species within the *c*-P36bb deposition, as indicated by some green data points appearing in clusters associated with the smaller rings.

The circumference stated here is calculated by the Ramanujan approximation for the circumference of an ellipse c: [160]

$$c \approx \pi[3(a+b) - \sqrt{(3a+b)(a+3b)}]. \tag{5.5}$$

This is a somewhat crude approximation of the circumference of the rings, as (particularly the larger rings) are not particularly symmetrical, and the peak to peak line profiles can be across either wider or narrower parts of the ring; these fluctuations in width are ascribed to horizontally or vertically aligned porphyrins, and so any measurement across these could affect the perceived a and b measurements and lead to inconsistent measurements. In addition, adsorption at step-edge features can affect the perceived geometry of the rings. Primarily, the function of these measurements is to ascertain the flexibility and general size of the rings, and it serves that function well. Some key points stand out from this data: firstly, the *c*-P36bb deposition seems to contain some *c*-P18b and *c*-P24b, which makes some sense as that sample itself was an unintended by-product from *c*-P18b synthesis. Secondly, the larger the rings become, the more flexible they become, tending towards a more elliptical shape. This agrees with the findings of Gotfredsen *et al.* that the smaller porphyrin rings would experience significant tension, holding the rings in a rigid shape. [158]

5.2.3 Adsorption sites and Ring Mobility

Also of interest were the durability and mobility of the rings at room temperature. In this case, when I refer to mobility, I describe the propensity of the molecule

to move on the surface during the imaging process, either thermally induced or pushed by the tip. Preferential adsorption at step edges is an indication that the species may be mobile at this temperature, as they are only observed when trapped in such a preferential adsorption site. Other evidence aside from step edge adsorption can be 'streaking' on the image (scan artefact where part of a single scan line exhibits anomalous apparent height compared to those before and after, appearing as bright or sometimes dark horizontal lines across the image), indicating a molecule moving as it is being scanned, ascribed to tip interaction, or movement of rings between consecutive images. In order to investigate these characteristics, the proportion of rings located on steps, and proportion of broken rings, were recorded, as shown in Table 5.1. *c*-P18b demonstrates a high level of mobility, as evidenced by constant streaking in STM images, examples of which can be seen in Figure 5.7a). The *c*-P18b sample also features a high proportion of rings on step edges. As the rings, like many adsorbates on coinage metals, seem to more favourably adhere to step edges, [161–163] the highly mobile *c*-P18b is unlikely to remain in a single location long enough to image without being adsorbed on a step-edge, explaining this characteristic. The proportion of each species adsorbed to step edges is lower for *c*-P24b than the other *c*-P series rings. This may be due to ring mobility; it seems feasible that the moment of deposition was the only period at which the *c*-P36bb species were able to diffuse across the substrate, before preferentially adsorbing at step edges. Hence, it can be argued that the much lower rate of step edge adsorption of *c*-P24b is due to two factors: firstly, it is not so mobile that it cannot be imaged anywhere but step edges, as is

	c-P18b	*c*-P24b	*c*-P36bb
Proportion of rings adsorbed on step edges	87%	41%	70%
Proportion of broken rings	23%	27%	44%

Table 5.1: Proportion of broken rings and rings adsorbed onto step edges for *c*-P series nanorings. *c*-P18b n=60, *c*-P24b n = 51, *c*-P36bb n =58.

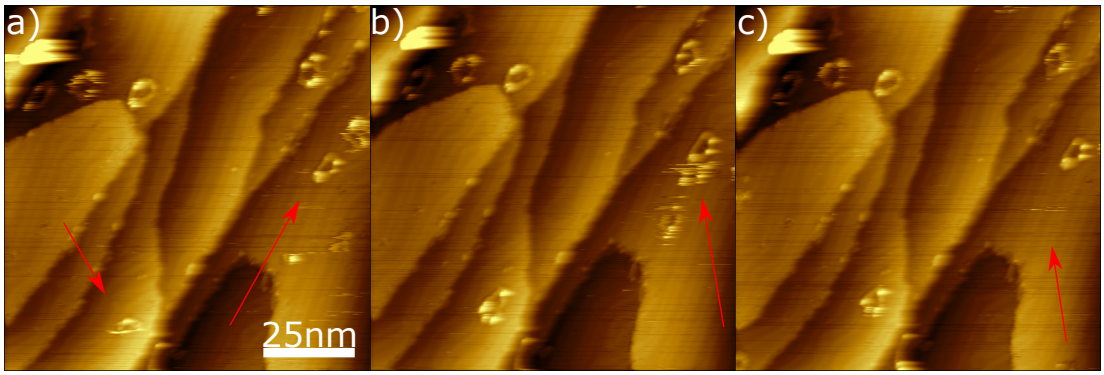

Figure 5.9: Sequential STM images showing apparent motion of individual *c*-P24b species during imaging. Evidence of movement are highlighted by red arrows. (Sample bias = -1.8 V, set point current = 20 pA).

the case with *c*-P18b, and secondly it is mobile enough to not become immobile at room temperature, as is the case with *c*-P36bb. *c*-P24b images demonstrate some characteristic streaking, and although it is not quantified, it seems to a lesser extent than *c*-P18b.

Another piece of evidence for *c*-P24b mobility is seen in Figure 5.9. The *c*-P24b can be imaged moving across the surface in between scans, indicating that diffusion is occurring during imaging. When rings appear and disappear without any streaking of the image or other artefacting, this is considered to be motion without an obvious tip interaction. In some scans, streaks on the image appear, indicating tip-molecule interactions could be causing some ring motion. In some cases, rings move mid image, giving the appearance of a half-ring. These half-rings are a strong indication of tip-ring interaction, as the ring has moved while the tip passes over the molecule; given that the tip state remains consistent during these events, it seems unlikely that the molecular species has completely transferred onto the tip, and is instead simply moving in the presence of the tip. *c*-P36bb in contrast, displays no evidence of motion, with very little observed streaking and no images displaying other characteristics assigned to moving rings.

With respect to the proportion of broken rings, it seems clear that the *c*-P36bb deposition contains a significantly greater preponderance of broken rings in chain structure, with 44%, while the other two species are each at around 25%. A few possible explanations for this phenomenon seem reasonable: firstly, the greater flexibility of these rings could lead to conformational situations that produce

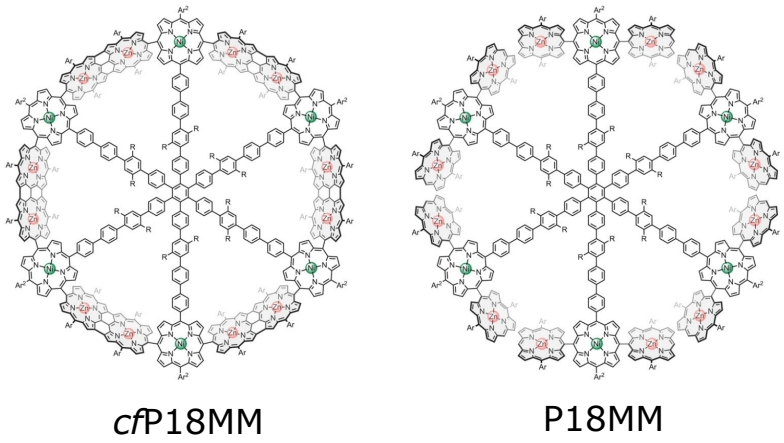

Figure 5.10: Chemical structure of the *cf*P18MM and P18MM nanorings.

greater strain on the molecule. Secondly, it could be that the introduction of the second butadiyne bridge significantly reduces the stability of the molecule, or just the increased size in general. Given the previously discussed phenomenon of greater internal strain leading to increased electron delocalisation, it seems possible that the largest rings may suffer from reduced resilience. Alternatively, it is possible that the sample itself contained a higher proportion of broken rings prior to deposition, as the *c*-P36bb sample was itself a by-product.

Based on the trends in this data, I can draw the following conclusions: as the size of *c*-P series rings increases, the species exhibit greater fragility, and lesser mobility.

5.2.4 P18 Series Nanorings

A further set of nanorings originating from a novel synthesis is the P18 series, namely P18MM and *cf*P18MM, the structures of which are shown in Figure 5.10. Prior to the creation of these molecules, a macrocycle entirely constructed of 5,15-linked porphyrins had never been synthesized. The fused version (*cf*P18MM) is of particular interest due to the theoretical possibility of exceptional electronic delocalisation, leading to extremely high single molecule conductance that is almost independent of length. [164] Once again, their cyclic nature needed to be verified with STM. As described in section 5.2.1, these new rings were deposited *via* electrospray. Figure 5.11 shows that this was accomplished for both species. Figure 5.11a-b) are overview images showing areas of broadly equivalent coverage

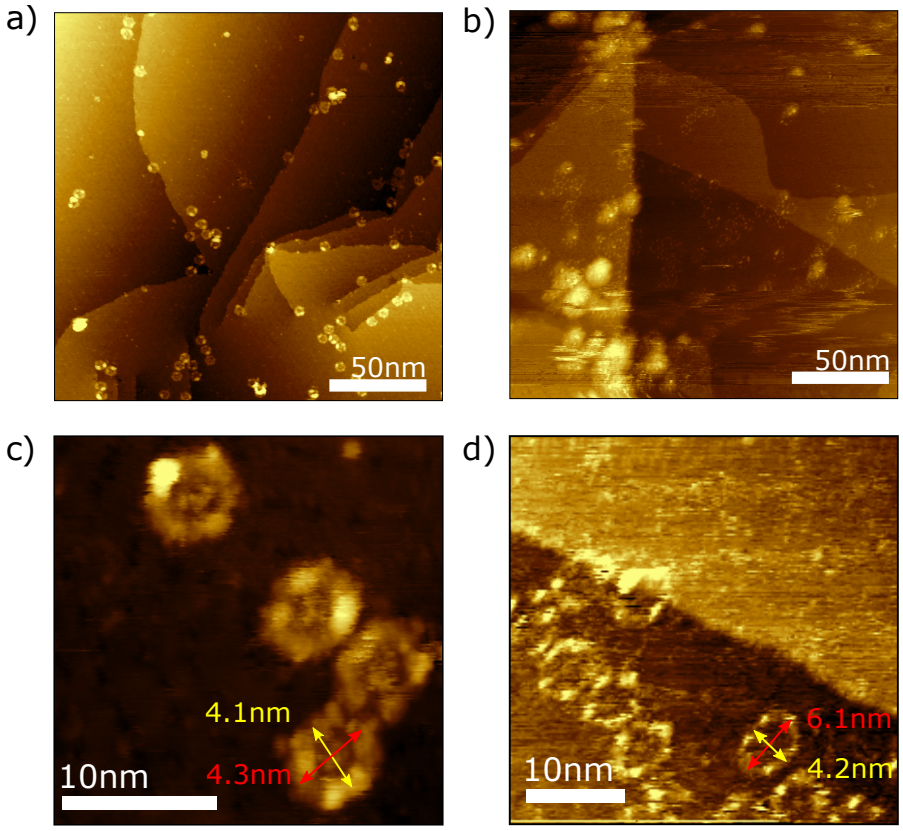

Figure 5.11: STM overview images of the a) *cf*P18MM (Sample bias = –2 V, set-point current = 15 pA) and b) P18MM (Sample bias = –1 V, set-point current = 20 pA) nanorings. Closer zoomed STM images of individual c) *cf*P18MM (Sample bias = –2.0 V, set-point current = 15 pA) and d) P18MM nanorings with associated measurements. (Sample bias = –1.0 V, set-point current = 20 pA)

for each of these nanoring species, with Figure 5.11c-d) showing a closer zoom. Once again, long and short axis measurements are taken, in order to establish information on the size and flexibility of the molecular species; example measurements are shown in Figure 5.11c-d) for each species.

Unfortunately, statistics on the P18MM species were small, with a measurement sample of only 8 rings. Even with such a limited sample size, I can draw some conclusions: an average circumference of 15.4±0.5 nm puts the non-fused ring as significantly larger on surface than the closed-fused *cf*P18MM, with an average circumference of 12.3±0.4 nm (n=60). This is probably due to the porphyrin-porphyrin coupling being a key facet of the bunched up structure of the porphyrin rings discussed in this chapter. Overall, the measurements are quite similar to the similarly structured *c*-P18b, each being a cyclic polymer of

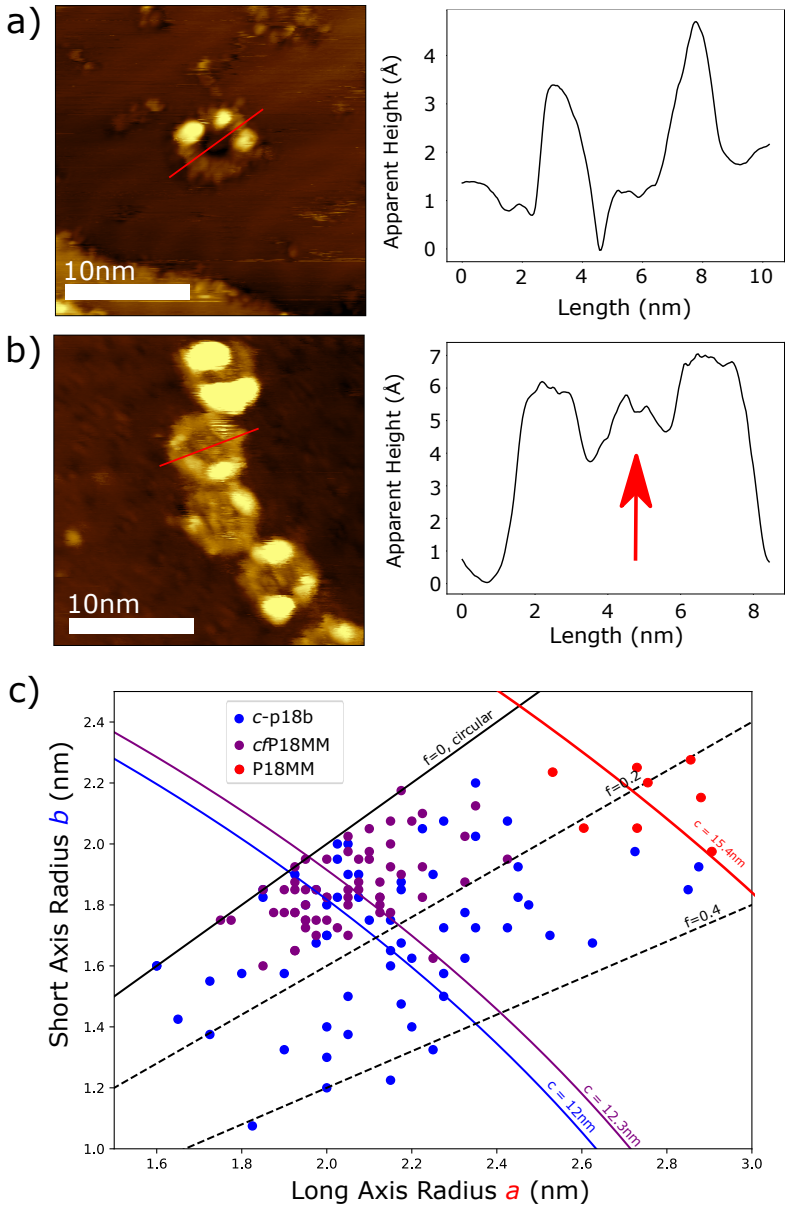

Figure 5.12: STM images of a) *c*-P18b (-1.8 V, Set-point current = 15 pA) and b) *cf*P18MM (-2 V, Set-point current = 15 pA) with associated line profiles marked on the image with red lines. b) Graph showing the experimentally measured long- and short-axis for *c*-P18b, *cf*P18MM and P18MM nanorings deposited onto Au(111)

covalently bonded porphyrins.

As a point of comparison, line profiles across each of these species highlight the manner in which the central template is still visible in STM; this is shown in Figure 5.12. As indicated by the red arrow, a raised feature is present in the centre of the ring, which is not present in the *c*-P18b species. This is attributed

to the presence of the template.

Another aspect to note here is that the apparent height of the ring for *cf*P18MM is generally higher than *c*-P18b, reaching approximately the same height as the periodic raised sections of the *c*-P series nanorings (see Figure 5.8). This lends credence to the suggestion that these bright features are sections of the ring where the porphyrins are twisted upright, as this kind of conformation is likely to be encouraged by the presence of the template, as we expect the rotational flexibility of the monomer units to be curtailed by the template. Figure 5.12 shows the measured dimensions for the two P*N* series nanorings, with *c*-P18b for comparison. Of note is that, while the measured circumference of *cf*P18MM and *c*-P18b are very similar, the *cf*P18MM retains a more circular shape overall, presumably due to the influence of the internal template. The non-fused P18MM is of approximately similar circularity to *c*-P18b. the various measurements of all porphyrin nanorings can be seen in Table 5.2. As can be seen from the table, the presence of the internal template has less of an impact on apparent circumference than the inter-porphyrin bonds of the monomers - *c*-P18b and *cf*P18MM are of an effectively identical average circumference, whereas the unfused P18MM is significantly larger. One area in which the templates do influence the structure is that the most circular species is the closed-fused and templated 18-member ring; it seems clear that both the fusion and the template have some influence on

Species	Number of measured units (n)	Average long axis measurement (nm)	Average short axis measurement (nm)	Average circumference (nm)	Average flattening ratio
c-P18b	63	4.3±0.5	3.4±0.5	12.1±1.3	0.20±0.12
c-P24b	51	6.8±0.9	4.4±0.8	17.9±1.2	0.34±0.18
c-P36bb	59	8.9±1.4	6.0±1.4	23.8±3.0	0.31±0.19
*cf*P18MM	60	4.1±0.3	3.7±0.3	12.3±0.7	0.09±0.05
P18MM	8	5.5±0.3	4.3±0.2	15.4±0.5	0.21±0.06

Table 5.2: Measured characteristics of each porphyrin nanoring species following electrospray deposition.

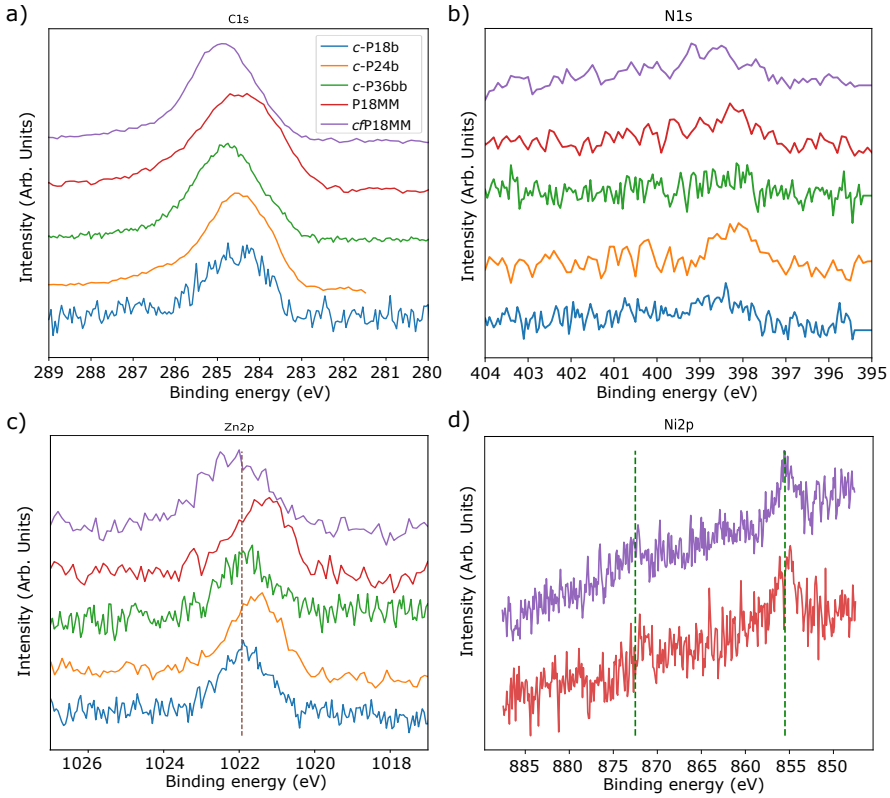

Figure 5.13: XP spectra of each of the electrosprayed nanorings species on Au(111). a) C 1*s* region. b) N 1*s* region. c) Zn 2*p* 3/2 region. Brown dotted line represents literature value for Zn-porphyrin on Au(111). [142] d) Ni 2*p* Region. The green dotted line represents literature value for a thin film of Ni-prophyrin on Cu. [165]

circularity.

5.2.5 Chemical Characterisation via XPS

XPS was performed on each of these samples in order to determine a successful deposition of intact molecules. These spectra are displayed in Figure 5.13. STM offers real space information on molecular structure and dimensions. However, it is non-trivial to robustly identify specific chemical groups within a molecular species. Here, I use XPS to offer a characterisation of the chemical environments present for the deposited molecular species. In our setup, electrospray deposition is conducted in the same UHV system as the XPS; the samples are then transferred to an STM *via* a vacuum suitcase as described in section 5.2.1. XPS is an excellent companion technique for electrospray, as it allows users to determine

whether or not they have completed a successful deposition, more or less in real time, as opposed to waiting to image the sample in STM, which in our experimental setup has a significant associated time cost due to the need to transport the samples.

The C 1s spectra, displayed in Figure 5.13a), are a useful tool for discerning the coverage of deposited material, as the organic target molecules contain a number of carbon atoms, leading to a relatively strong signal. The C 1s peak can be normalised to the native surface peak, such as Au 4f, in a wide scan for a more accurate approximation of coverage. While the coverage does vary across the sample with a spot deposition, the XPS measurements for coverage are always taken on the deposition spot itself, allowing for comparison between samples. The broad environments shown here reveal little information on the nature of the deposited material, but do appear in the expected 284-285.5 eV region for porphyrins on metal surfaces. [166] The N 1s, Zn 2p and Ni 2p regions provide information on the intact nature of the molecules on the surface. For metalated porphyrins, such as those featured in the nanorings, we would expect a single N 1s environment, which is found in each case; if the metal cores of the porphyrins had become detached at some point in the deposition process, we would expect to see 2-3 distinct environments depending on the frequency of any de-metalating process. [166] The metal regions themselves would also display multiple environments if the cores were in the process of losing the atoms, an on-surface and an on-molecule region. In fact, the Zn 2p 3/2 region for each species displays a binding energy in a similar region to that obtained from the literature for a Zn-porphyrin on Au(111), represented with the brown dotted line. [142] Similarly, the Ni 2p region displays peaks in the same region as those found for a thin-film of Ni-Porphyrin on a Cu substrate, represented with the green dotted line. [165]

The XPS measurements were performed with a lab source, producing monochromatic Al Kα X-rays (1486.7 eV). Unfortunately, at this photon energy, the cross-section of many elements is quite small, making high resolution spectra extremely time consuming. As such, the Zn 2p, Ni 2p and particularly the N 1s spectra are poorly resolved. Lab-based XPS may not have the best resolution - that is where

synchrotron radiation comes in, as will be explored in chapter 6. While these limitations do prevent us obtaining high resolution XPS spectra (on a reasonable timescale), we are still able to obtain insights into the nature of the as-deposited molecule by looking for signs of molecular degradation, as described above, and most importantly can do so without requiring synchrotron radiation.

5.2.6 Conclusion

The work detailed in this chapter highlights the unique morphological characterisation properties of STM, often essential in understanding the structure of a target molecule. Specifically, a series of porphyrin-based nanorings were characterised, confirming the cyclic nature of the molecules, and measurements of the size and shape of the molecules were also made. These observations lend credence to the notion that smaller porphyrin nanorings experience a much greater structural tension, holding them in a less flexible and more circular shape. Behaviour of these molecules in relation to their motion, resilience, and preferential site adsorption was also established *via* the collection of STM statistics, indicating a higher degree of on-surface diffusive mobility exhibited by smaller species, alongside higher resilience.

The utility of the electrospray deposition technique is also explored, as an unrivalled method of depositing larger, thermally labile molecules that are more practically synthesized in solution. In combination with XPS, electrospray is proven to be a highly reliable and consistent deposition method for the nanorings studied within this chapter. XPS analysis reveals the technique deposits intact molecules, and monitoring the coverage with XPS allows for a consistent and repeatable coverage. Further to this, the distribution of material following electrospray deposition was also investigated, revealing the concentration gradient of material across the surface following an electrospray deposition and material being deposited far outside the theoretically calculated spot size.

Chapter 6

On-Surface Synthesis of Porphyrin-Graphene Nanoribbons

In this chapter, electrospray deposition is utilised to deposit large, complex molecules synthesized in-solution. Here, polymeric precursor molecules are annealed on-surface to produce a porphyrin-graphene nanoribbon, combining the atomic precision of solution-phase synthetic chemistry with on-surface protocols to enable reaction steps that cannot yet be achieved in solution. Scanning tunnelling microscopy (STM) and photoelectron spectroscopy (PES) are used in concert to characterise the novel porphyrin-fused graphene nanoribbon formed on-surface.

The work contained within this chapter was produced in collaboration with Dr Matthew Edmondson, University of Nottingham Nanoscience group. Specifically, the STM images (including dI/dV maps) taken following the 450 °C anneal were taken by Dr Edmondson. Contributions from Dr Edmondson are indicated within the figure captions where appropriate.

6.1 Porphyrin-graphene Nanoribbons

Graphene nanoribbons (GNRs) possess fascinating electronic properties with the potential for applications within (opto-)electronic devices [167]. Studies of GNRs

often focus upon the on-surface synthesis of extended graphitic polymers formed from the Ullmann-type coupling of halogen functionalised precursors, such as bianthracene units [3]. In common with many on-surface synthesis protocols, the initial, intermediate and product states can be studied by scanning tunnelling microscopy (STM) and atomic force microscopy (AFM) to provide sub-molecular insights into reaction pathways and resultant structures [4]. Recently, the on-surface synthesis of open-shell nanographenes which exhibit $\pi-$magnetism [168] has led to contemplation on their use within spintronic devices and quantum computing architectures [169]. There is also significant interest in achieving doped and heterostructured GNRs, with the aim of allowing tunable bandgap and Fermi-level engineering. The chemical modification of the reactive precursor molecules, which are the building blocks of GNRs, is a widely explored route to providing functional groups at the periphery [170, 171] and within the core of the GNR; boron [172] or nitrogen [173–175] are frequently used as dopant species.

While an on-surface synthesis approach to the formation of GNRs has allowed polymers with a range of structures to be fabricated, there are still significant challenges relating to the selectivity and efficiency of such on-surface reactions. My proposed methodology utilises the atomic precision of solution-phase chemistry to form highly regular polymeric precursor species, and to employ on-surface protocols to enable reaction steps which are not facile in solution (e.g. the dehydrogenative-cyclisation reaction step required to produce conjugated graphitic materials).

Our focus is on the inclusion of porphyrin species within the graphene nanoribbons, giving rise to porphyrin-fused graphene nanoribbons (PGNRs). Porphyrins are robust molecular species, amenable to functionalistaion by pendant chemical groups at the periphery and metalation of the macrocyclic core. Porphyrin species have been well-studied by a number of surface science approaches, including photoelectron spectroscopies (PES) [176] and scanning probe microscopies (including STM and AFM) [177]. The functionalisation of graphene structures has been demonstrated by fusion of tetrapyrroles (free base porphyrins, 2H-P) to the edges of extended graphene structures [178] and by the on-surface synthesis of GNRs with porphyrin units fused at regular distances along the edge of the nanorib-

bon, [179] while the inclusion of porphyrin groups within GNRs has been achieved by on-surface methods, but frequently results in short oligomers [180,181] exhibiting a high defect density [182]. Importantly, the inclusion of metal functionalised porphyrins provides a scheme for doping these graphitic species [181], allowing access to spin states [182,183] and for the incorporation of the catalytic properties of such species [177].

A challenge for a combined solution-phase and on-surface approach is the transfer of large (over 100 nm in length in the case of the polymers used in this work [184]), thermally labile, polymers from solution to the ultra-high vacuum (UHV) environments required for precision PES and STM measurements. Over the last decades, electrospray-based deposition (ESD) procedures have been used to deposit a range of fragile, functional, and polymeric species onto substrates held under UHV conditions [123, 140–142, 151, 157, 185–189]; including graphene nanoribbons [190]. This has provided a route to the characterisation of molecular structure and properties, by combining the spatial resolution of STM and AFM with the chemical and structural sensitivity of PES techniques (e.g. X-ray photoelectron spectroscopy (XPS), near-edge X-ray adsorption fine-structure (NEXAFS) and X-ray standing wave (XSW) techniques) [158, 164, 184, 191].

6.2 Experiments

In this chapter, I employ a combination of ESD, STM, XPS, NEXAFS, and XSW to characterise a novel porphyrin-fused graphene nanoribbon, **PGNR**, formed from the on-surface synthesis of a linear polymer consisting of regularly spaced Ni-porphyrin units linked by sections of aryl rings, nickel(II) porphyrin polymer (**NiPP** - synthesised and characterised as reported previously [184]); designed to fuse together to form graphitic regions between neighbouring Ni-porphyrin units - see Figure 6.1a-b) for proposed reaction scheme. In solution, this final step in synthesis was not possible.

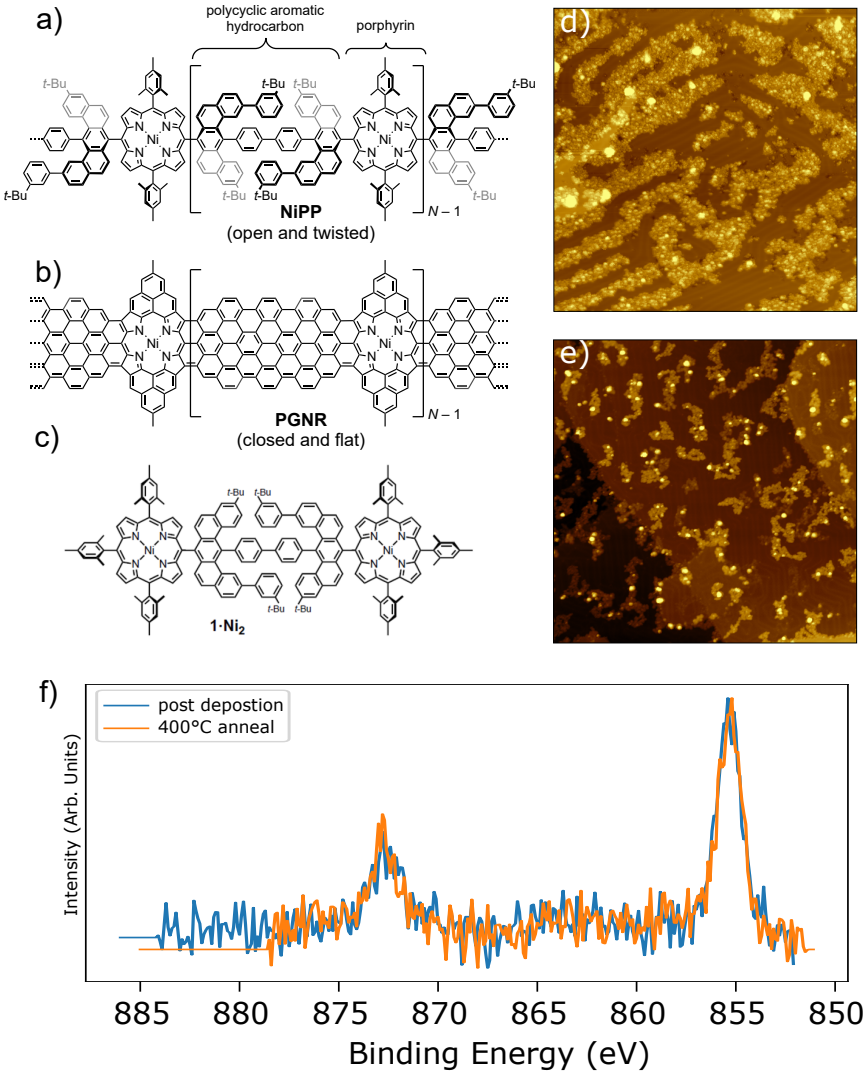

Figure 6.1: Overview of the on-surface synthesis of a porphyrin-fused graphene nanoribbon (**PGNR**). a) Chemical structure of **NiPP**. b) Proposed structure of the reaction product following on-surface synthesis to form **PGNR** (degree of polymerisation is expected to be up to $N = 54$). c) Chemical structure of molecular precursor **1-Ni$_2$**. d) STM image showing surface of Au(111) sample following electrospray deposition of **1-Ni$_2$** (Bias = 0.5 V, Current set point = 100 pA). e) STM image showing surface of Au(111)/**1-Ni$_2$** sample following anneal to 500 °C (Bias = 1.8 V, Current set point = 50 pA). f) XP spectra of the Ni 2*p* region of an **NiPP** sample showing the presence of unchanged Ni 2*p* signal following anneal to 400 °C.

6.2.1 Experimental Details

Synthesis

All nanoribbon precursor species were synthesized by the group of Harry L. Anderson, Department of Chemistry, University of Oxford, Chemistry Research Laboratory, Oxford, UK.

Scanning Tunnelling Microscopy - STM

Scanning tunnelling microscopy (STM) experiments were performed using a Scienta Omicron POLAR low-temperature STM system operating under ultra-high vacuum (UHV) conditions with a base pressure of better than $3x10^{-10}$ mbar. All samples were prepared by the 'single spot' ESD procedure described in section 5.1.2 (electrospray deposition in a single spot for 40 mins) and transferred to the UHV-STM system using a vacuum suitcase (NextGeneration UHV Suitcase, Ferrovac AG). The STM was cooled to liquid helium temperatures, with a sample temperature of 4.7 K. All STM measurements were performed in constant current mode using electrochemically etched tungsten tips optimised by controlled indentation into the Au(111) single crystal substrate [bias applied relative to the sample]. Differential conductance maps were measured in constant current mode and were generated using a lock-in amplifier output that applied a 20 mV signal at 2153 Hz in addition to the sample bias.

XPS, NEXAFS, and NIXSW

Synchrotron-based XPS, as well as NEXAFS and NIXSW measurements, were performed at the I09 beamline [192] at Diamond Light Source. **NiPP**/Au(111) samples were prepared in Nottingham (as described above) and transferred to IO9 *via* a Vacuum Suitcase (NextGeneration UHV Suitcase, Ferrovac AG). The I09 beamline utilises two undulator sources allowing access to 'soft' X-rays (100–2000 eV) and 'hard' X-rays (2100–18000 eV). The 'hard' X-rays were monochromated by a Si double crystal monochromator, and the 'soft' X-ray beam by a plane grating monochromator. The XP spectra were acquired using a VG Scienta EW4000 HAXPES analyser mounted perpendicular to the incoming light (light is linearly

polarised in the horizontal plane). The binding energies were defined relative to the Fermi level of the substrate. Reflectivity curves were obtained from a fluorescent plate mounted in the port through which the synchrotron light is incident. The curves were then acquired using a CCD camera mounted on a window opposite the port. Reflectivity curves were fitted to determine the phase of the X-ray standing wave in addition to modelling peak broadening due to experimental uncertainties. Non-dipolar effects in the photoelectron yield were modelled using a backward-forward asymmetry parameter, Q, derived from the calculations of Nefedov *et al.* [193, 194]. Due to the large acceptance angle of the EW4000 analyser (±30 °) an effective emission angle of 15 ° was used for the (111) reflection, with respect to the surface plane. The hard X-ray had a beam spot size of 0.02 mm^2 and the soft X-ray beam spot size was 0.16 mm^2. The sample used in synchrotron analysis was prepared *via* an electrospray raster deposition, in order to create a larger area of even coverage, as described in section 5.1.2. In this instance, 10 deposition spots 0.5 mm apart were deposited on for 5 mins each, a total of 3 times.

N 1s, C 1s and Ni 2p core level XP spectra were obtained using photon energies of 550 eV, 450 eV, and 1160 eV, respectively. NEXAFS measurements were acquired at the nitrogen K-edge using photon energies in the range 395-420 eV, whilst detecting the photoelectron yield *via* the hemispherical analyser. Angular measurements were acquired at angles of 0° (normal incidence), 85° (grazing incidence), and 55° ('magic angle'). NIXSW measurements were performed using the (111) Bragg plane of the crystal ('hard' X-ray undulator on I09, with a nominal Bragg energy of 2630 eV). Each NIXSW measurement was repeated multiple times (10 times for the C 1s region, and > 8 times for the Ni 2p), with each new measurement performed at a different sample location to avoid beam damage. Before and after each XSW measurement, core level spectra for the C 1s ($h\nu = 2620$ eV) were obtained in order to monitor possible beam damage, with no significant changes observed. The sample was cooled using liquid nitrogen to reduce the effects of beam damage during data acquisition. A reflectivity curve was measured prior to each X-ray standing wave measurement to check the quality of the new areas of the surface and ensure that the energy range of

each spectrum is the same with respect to the Bragg energy. The XP spectra acquired during the XSW measurement are fit with a combination of Gaussian and Doniach-Šunjić line shapes [195], a single chemical environment is fit for both carbon and nitrogen species. The sample was characterised in the as-deposited state, and following annealing to 450°C and 575°C in order to assess the outcome of the on-surface reaction.

6.2.2 STM Characterisation

Prior to the deposition of the complete porphyrin polymer **NiPP**, attempts were made to deposit and conduct on-surface synthesis of a molecular precursor, shown in Figure 6.1c). Unfortunately, the monomer sample featured large islands of unresolvable material often oriented along the herringbone, indistinguishable from contaminant material (as discussed in section 5.1.3, see Figure 6.1d)). Annealing to 500 °C did not result in the intended polymerisation reaction, instead clumps of amorphous material were observed (Figure 6.1e)). XPS confirms that the precursor does not desorb up to temperatures of 400 °C. As can be seen in Figure 6.1f), the Ni 2*p* region displays characteristic peaks of expected binding energy for nickel porphyrin, [165] and remains unchanged in both intensity and binding energy following this anneal.

Focussing now on STM of **NiPP**, it can be seen that following ESD of **NiPP** on to an Au(111) substrate, STM characterisation reveals the presence of long chain-like structures (see Figure 6.2a) - several chains indicated by arrows). The chains exhibit significant flexibility and are observed to run continuously across step-edges and over other chains; similar to the appearance of previously characterised porphyrin-based polymers. [142] The average degree of polymerisation for the deposited material is expected to be about $\bar{N} = 34$ (based upon GPC and MS analysis for a related polymer); equivalent to a polymer length of ∼85 nm (DFT calculations indicate the Ni-Ni separation of neighbouring porphyrins is ~ 2.5 nm) [184]. The deposited chains are observed as continuous polymers which frequently cross; continuous chain lengths of up to 55 nm were observed within the acquired STM data. Between the chains are domains of material that cover the Au(111) surface (highlighted by white-dashed box and inset in Figure 6.2a).

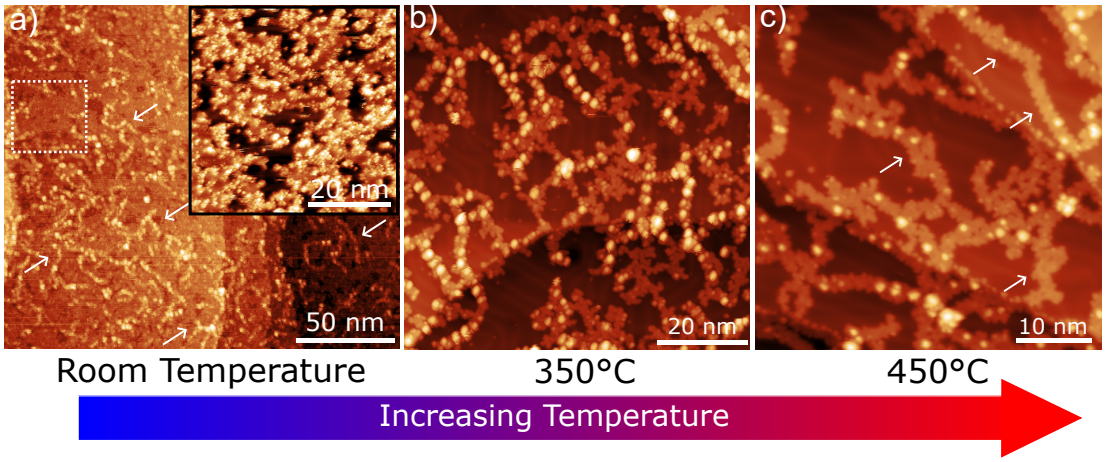

Figure 6.2: Overview of the on-surface synthesis of a porphyrin-fused graphene nanoribbon (**PGNR**). a) as deposited, b) following annealing to 350°C and c) following annealing to 450°C. Image parameters: a) −1.5 V, 50 pA, $T = 78$ K (inset −2.0 V, 50 pA, $T = 78$ K), b) −2.0 V, 50 pA, $T = 4.7$ K, and c) −2.0 V, 20 pA, $T = 4.7$ K.

I assign the material between the chains to the previously discussed co-deposited contaminant. This is attributed to silicon-grease, polydimethylsiloxane, PDMS, although the presence of solvent species, methanol and toluene, is not excluded, due to the previously discussed electrospray contamination. The contaminant is removed after annealing at 350°C (see Figure 6.2b), where clean areas on the Au(111) terraces can now be resolved along with the characteristic herringbone reconstruction [196]. Along the chains, a periodic sequence of bright features are visible, which I assign to the alternating regions of the *polycyclic aromatic hydrocarbon* and *porpyhrin* sections of the polymer chain (see Figure 6.1a). To initiate the on-surface ring-closing reaction which facilitates the formation of **PGNR**, the sample is annealed at 450°C (see Figure 6.2c)). Based on previous studies of on-surface ring-closing reactions [166, 180, 197–199], dehydrocyclisation of **NiPP** is expected to occur at this temperature. It is clear that regions of the chains now have a reduced corrugation (i.e. 'flatter' appearance in STM topographs - see regions highlighted by arrows in Figure 6.2c). However, STM characterisation of the surface reveals bright protrusions along the chains, which I assign to the presence of non ring-closed material [198] and tertiary butyl (tBu) groups.

Additional details of the chains can be obtained by measuring the periodicity

along the length of the polymer chains. Figures 6.3a) and 6.3b) show overview STM images of **NiPP** on Au(111) following annealing to 250°C and 450°C, respectively. The corrugation along the chain can be visualised as a line-profile (the path that the STM tip would follow along the polymer chain) and is shown in Figure 6.3c for **NiPP** and **PGNR** materials. The periodicity of the chains is measured to be as 2.32 nm, for the as deposited material, and 2.40 nm post anneal (see Figure 6.3d), which is in excellent agreement with the expected periodicity of **NiPP** ($\sim$ 2.5 nm [184]). Additionally, close-up STM topographs (Figure 6.3e) reveal the position of the periodic depressions to be at the centre of the porphyrin macrocycle; indicated by red arrows. While the topographs show the cores to appear as depressions, differential conductance maps (dI/dV maps) acquired over the range +2 V to −2 V reveal that at negative sample biases in the range −2 V to −1.2 V, the cores appear bright (Figure 6.3f) which I assign to a contribution from a highest occupied molecular orbital-derived (HOMO-derived) valence band with a significant contribution from the Ni-porphyrin subunit of the nanoribbon. We note that dI/dV spectroscopy measurements of Ni-porphyrin species [200] exhibit a resonant feature over a similar energy range, suggesting that the molecular HOMO may contribute to the HOMO-derived valence band for the **PGNR**.

6.2.3 Photoelectron Spectroscopy

XPS

To facilitate further chemical and structural analysis of the on-surface synthesis of porphyrin-graphene nanoribbons, synchrotron-based XPS, NEXAFS, and XSW measurements were performed. As the **NiPP**/Au(111) sample is prepared by ESD (see experimental section for details) a non-uniform molecular coverage is obtained. Figure 6.4a) shows the variation in XPS signal for the C 1s region as a function of sample position. The intensity of the C 1s signal increases from the edge to the middle of the sample. At the edge of the sample the broad carbon peak is centred at $\sim$ 284.0 eV binding energy (BE) which shifts to higher BE, $\sim$ 284.6 eV, at the centre of the sample (Figure 6.4b) - acquired following annealing to 450°C). The shift to lower BE for lower coverage, at the sample edge, is assigned to increased screening *via* a molecule-substrate interaction. A similar

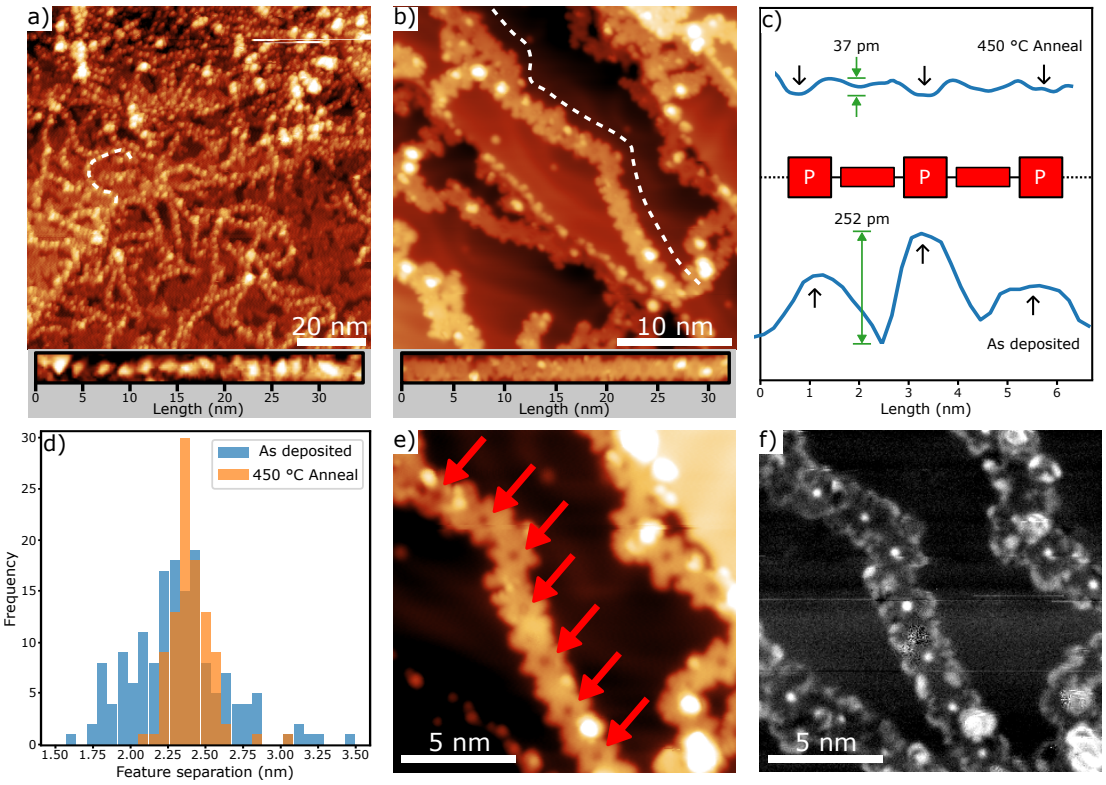

Figure 6.3: Details of periodicity and on-surface synthesis of **PGNR**. STM topographs of (a) **NiPP** following annealing to 250°C, and (b) **PGNR** formed by on-surface synthesis following annealing to 450°C [panels below STM data show topography along the line profiles for the chains indicated within the image]. (c) Line profiles along the **NiPP** and **PGNR** chains; line profiles presented are segments containing two repeat units, acquired along the chains indicated in STM images (a) and (b). (d) Histogram showing the separation between periodic features along **NiPP** and **PGNR**. (e) STM topograph showing a close-up of a **PGNR** section; red arrows indicate features assigned to the centre of the porphyrin macrocycles. (f) dI/dV map of the **PGNR** chain in (e); under these conditions, the Ni atoms at the core of the porphyrin species appear as bright features (assigned to the HOMO of the Ni-Porphyrin subunit). STM image parameters: (a) −2.0 V, 50 pA. (b) −2.0 V, 100 pA. (e,f) −1.9 V and V_{Osc} = 20 mV, 100 pA. All images acquired at 4.7 K. Images e-f) collected by Dr Edmondson. Figures c-d) created by Dr Edmondson.

shift is observed for the Ni $2p_{3/2}$ signal (Figure 6.4c), indicating that at the edge of the sample the Ni atoms at the core of the porphyrin units are interacting

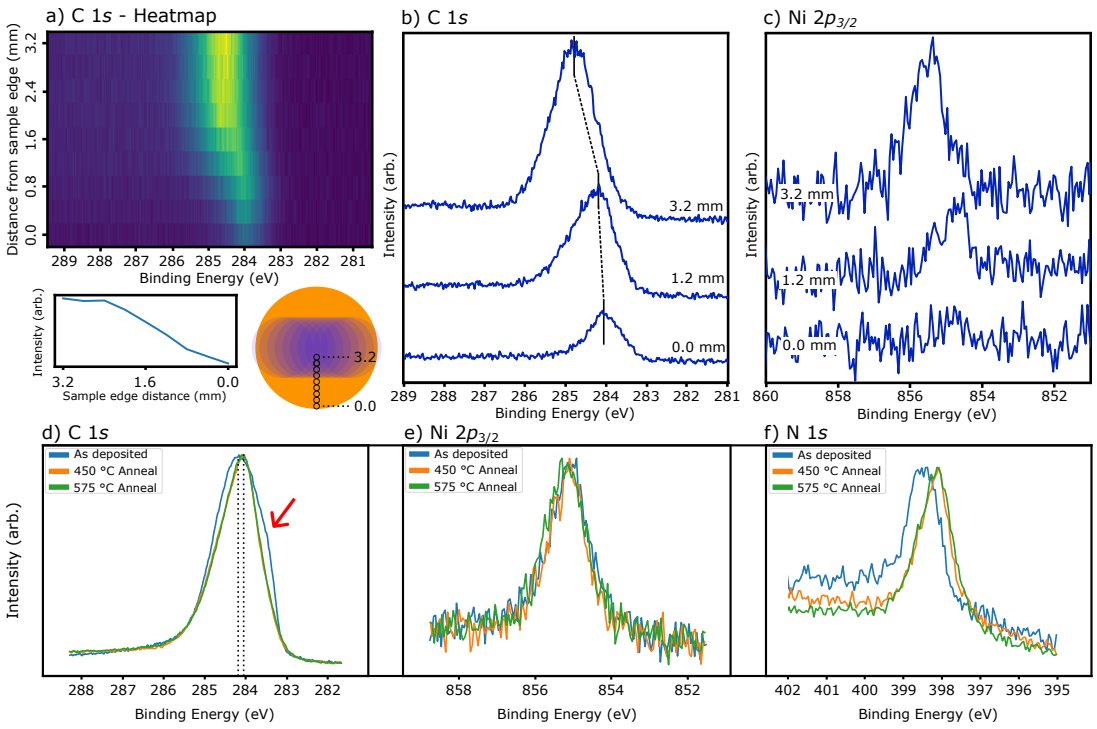

Figure 6.4: XPS characterisation of **NiPP** on Au(111). a) Normal incidence XPS, C 1*s* region, as a function of sample position. Coverage is seen to increase from edge to centre of sample. Inset below shows the Au(111) surface, with the blue overlapping 2 mm deposition spots raster scanned across 10 positions on the surface (acquired after annealing at 575°C). The black circles indicate the location of beam incidence. XP spectra for the b) C 1*s* and c) Ni $2p_{3/2}$ regions (acquired after annealing at 450°C); the position of the C 1*s* peak shifts to lower BE in the lower coverage regions at the edge of the sample. d), e), and f) show XPS of the C 1*s*, Ni $2p_{3/2}$ and N 1*s* regions for as deposited **NiPP** on Au(111) and following annealing to 450°C and 575°C (acquired at positions $>$ 2.0 mm from the sample centre). The red arrow in d) indicates a shoulder, attributed to contaminant material, which is removed following annealing. Figure a) created by Dr Edmondson.

with the substrate, while towards the centre some Ni species are interacting less strongly with the surface which I assign to some sections of the polymer lying either atop contaminant material or regions of polymer.

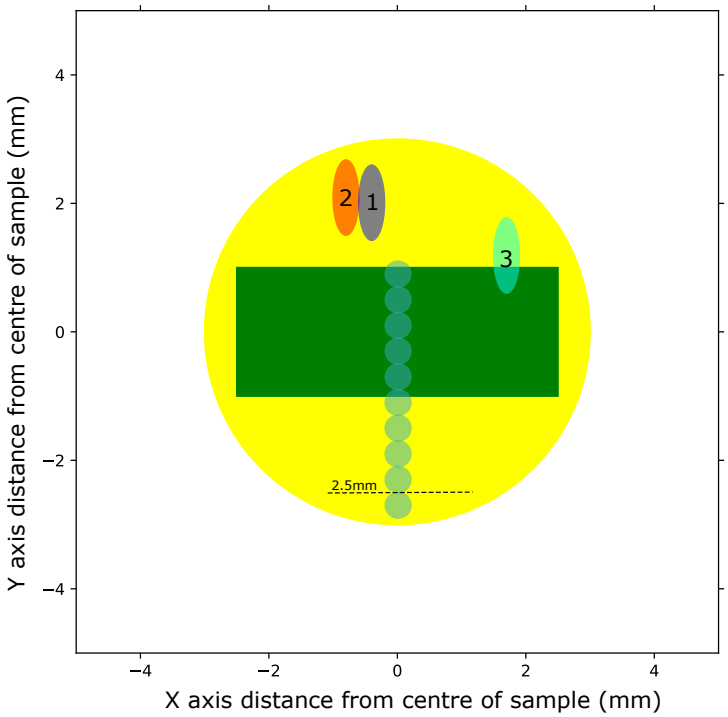

Figure 6.5: Scale diagram showing the position and size of XPS spots on the **NiPP** on Au(111) raster deposition. The theoretical deposition is crudely modelled with the green rectangle, the pre anneal XPS spot (blue/grey) is marked with a 1, the 450 °C spot (red/orange) marked with a 2, and the 575 °C spot (cyan) marked with a 3. The 450 °C normal incidence stepped spots are marked with blue circles.

A Note on XPS Location and Electrospray Raster Deposition

The XP spectra shown in Figure 6.4a-c) were taken at normal incidence, making determining the position of the X-ray spot on the sample fairly trivial; these stepped normal incidence XPS were taken following the 450 °C anneal and above only, and thus cannot be compared to pre-anneal XPS. The high resolution XPS shown in Figure 6.4d-f) were taken at an incidence angle of 70°, as this is the optimal angle for the hemispherical analyser in this system and thus produces the strongest signal. The high resolution spectra were taken in a variety of locations across the sample, so as to avoid beam damage, and at each stage of the anneal. However, due to the manner in which the sample rotates, the relative centre of the sample shifts for each rotation angle, as shown in Figure 6.5. As can be seen, the Y axis position of all three high resolution spots lies off of the theoretical deposition

size (spot size 2.4 mm diameter). Yet in each of these positions, material was found, with Ni 2*p* signal visible to the dashed line, at a distance of roughly twice that expected. This implies that the deposition spot size could be significantly wider than calculated, particularly in the case of a raster deposition, where each motor step could lead to a slight deviation in the position of the deposition spot. In this particular instance, over 30 steps were taken (one for each deposition spot) and any non-linearity in sample motion between depositions would lead to a significant deviation from the expected deposition profile.

With respect to determining the true location of the XPS spots, for future use it should be noted that the centre of the sample spot should be calibrated at each angle at which measurements are taken. A simple geometric model (estimating spot location deviation due to the finite displacement of the sample surface from the axis of rotation) was implemented to obtain relative position of the XPS NEXAFS and XSW measurements. It should also be noted that this calibration needs to be done each time the sample is taken and reinserted into the sample stage, as this can result in a slightly different sample location, with respect to the manipulator axis of rotation, each time.

NEXAFS

Angle-resolved NEXAFS data acquired at the nitrogen K-edge provides information on the structural changes occurring within **NiPP** during the on-surface synthesis of **PGNR** and supports the ring-closing and flattening reaction proposed based upon the STM and XPS data. In common with nitrogen K-edge NEXAFS for metalloporphyrins [201–204], resonances for as-deposited **NiPP** are observed at 398.8 eV (π_1^*), 401.2 eV (π_2^*) and 401.9 eV (π_3^*): see Figure 6.6. Prior to annealing, the polymer shows limited dichroism and the reduction in intensity of the π_1^*, π_2^*, and π_3^* peaks from grazing to normal-incidence indicates an average tilt angle of $\sim$43° (which may correspond to a random ordering) for the core of the porphyrin relative to the plane of the surface (tilt angles obtained *via* the 'ratio method' detailed in reference 103). The π_1^* resonance has previously been assigned to the LUMO (lowest unoccupied molecular orbital) for porphyrin species and DFT studies indicate that this π-type orbital is located exclusively

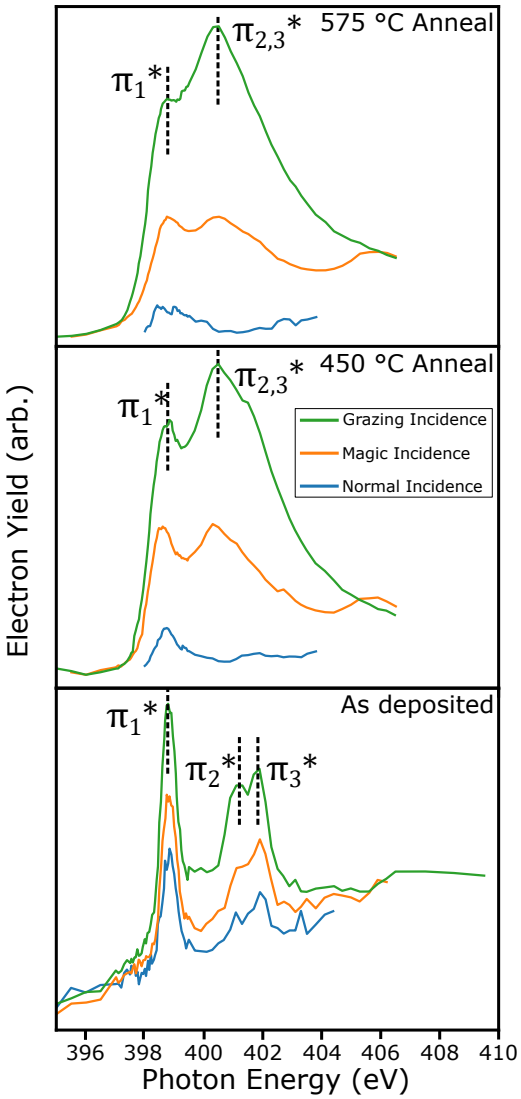

Figure 6.6: Angle-resolved NEXAFS spectra acquired at the nitrogen K-edge for **NiPP** on Au(111) as a function of annealing temperature: as deposited, 450°C anneal, and 575°C anneal. Resonances are labelled and discussed within the main text.

at the porphyrin core, including the nitrogen atoms [202]. The angle of the porphyrin core to the substrate is in agreement with a model where the flexibility of the precursor allows the porphyrin units (containing nitrogen environments) to rotate around the C-C axis connecting them to the 'graphitic precursor-unit' along the length of the polymer (see Figure 6.2a) : similar to the canting of anthracene units within the intermediate reaction step of the on-surface synthesis of a graphene nanoribbon. [3]

Following each of the sequential annealing steps, the NEXAFS data reveals

an increase in dichroism (Figure 6.6) corresponding to a reduction in the angle of the porphyrin core relative to the (111) surface plane. The π_2^* and π_3^* peaks are seen to broaden and merge (labelled as $\pi_{2,3}^*$, 400.5 eV), while the position of the π_1^* resonance is constant around 398.8 eV. After annealing to 450°C the average tilt angle is calculated, from the π_1^* resonance, to be $\sim 28°$, which further reduces to $\sim 22°$ following annealing to 575°C. This confirms that the change in structure observed in STM is linked to flattening (and on-surface ring-closing reaction) where porphyrin species within **PGNR** are roughly parallel to the surface plane. Interestingly, the reduction in intensity of the π_1^* resonance, relative to π_2^*/π_3^* and $\pi_{2,3}^*$, following annealing, indicates an increased interaction with the substrate due to the partial filling of the π_1^* molecular orbital. [203, 205] This reduction in intensity is therefore attributed to a flattening of the nanoribbon and a corresponding enhanced interaction between porphyrin core and metallic substrate (as indicated by the observed shift in BE within the XPS data).

The NEXAFS data here has been curtailed due to the interference of core-level derived photo-electron peaks (as described in section 3.2.3); this issue is shown in Figure 6.7. The presence of these peaks indicates the presence of valence band transitions of comparable energy to that of the auger electrons, at the photon energies used here. These provide no information on unoccupied π^* states and thus must be disregarded. All photon energies below the appearance of the Auger peak can be considered, but those after the appearance of the peak are to be disregarded; the range of photon energies at which this occurs varies with angle of incidence.

NIXSW

Normal incidence X-ray standing wave (NIXSW) analysis was performed upon **NiPP**/Au(111) using the (111) Bragg reflection (nominally 2630 eV). NIXSW is a chemically sensitive technique which allows the structure and adsorption positions of specific chemical elements in specific environments to be addressed. [106]

With NIXSW, the angle of the incident X-ray is held constant, and photon energy instead varied. As described in section 3.2.4, moving through Bragg condition photon energies at normal incidence shifts the nodes of the standing

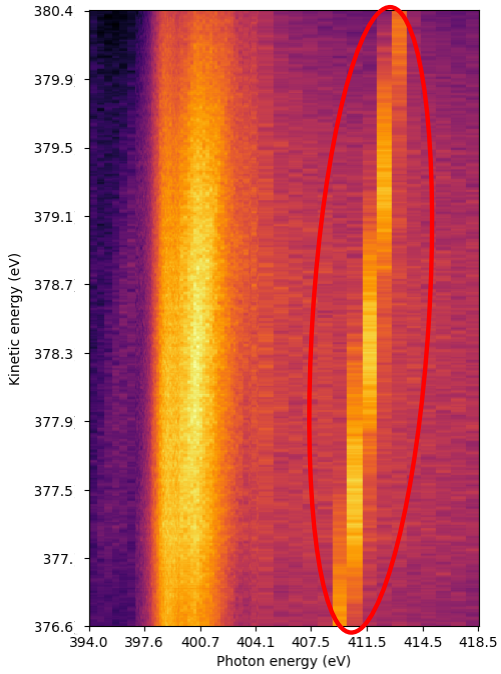

Figure 6.7: Heatmap showing the counts for electrons at different kinetic energies at specific photon energies during the spectra acquisition. A roaming peak is marked with a red circle. This spectrum is for the 70 ° angle on the 575 °C annealed sample.

wave perpendicularly between the targeted crystallographic planes. In a practical sense, this means that once the Bragg condition photon energies of the specific area of the sample is identified, a series of XP spectra are taken in small increments across the range of appropriate photon energies. As the anti-node of the standing wave moves spatially through the position of the target species, the intensity of these XP spectra will increase; hence, a measurement of the intensity of these peaks as the photon energy changes can provide the information required for an XSW measurement. This will provide information on the position of the atomic species relative to the planes the standing wave is reflected from. In this instance, the (111) plane has been chosen, as this lies parallel to the surface plane, and means the XSW should provide us with information relating to the position of the target species relative to their adsorption height on the surface. The XSW absorption profiles for the regions measured in this experiment are shown in Figure 6.8. Each plot contains three elements: the measured reflectivity of the crystal at that specific point (the black line with blue points), the intensity data from

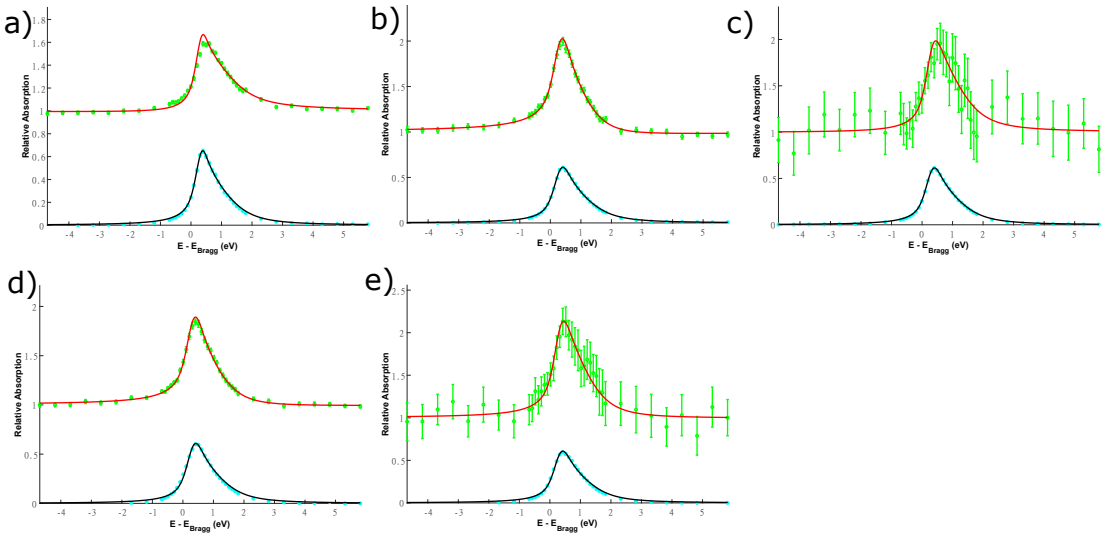

Figure 6.8: XSW adsorption data and fit for: a) the C 1s region pre-anneal, b) the C 1s region post 450 °C anneal, c) the N 1s region post 450 °C anneal, d) the C 1s region post 575 °C anneal, and e) the N 1s region post 575 °C anneal.

the XPS fits taken at different photon energies (the green points), and the XSW fit created by varying the C_f and C_p values with the reflectivity measurement to best fit the green points data (the red line). Hence, in this example, most of the XSW fits closely resemble the reflectivity curve; this is due to the low coherent fraction, as shown in Table 6.1.

Here, I obtain experimental values of C_f and C_p for the nitrogen species within the core of the porphyrin (from the single chemical environment identified within N 1s XPS data) and values for the ensemble of carbon environments. Information

LGNiPNR	Element	C_f	C_p
As deposited	Carbon	0.08±0.02	0.01±0.03
450°C anneal	Carbon	0.19±0.02	0.73±0.03
450°C anneal	Nitrogen	0.2±0.1	0.3±0.1
575°C anneal	Carbon	0.25±0.02	0.45±0.02
575°C anneal	Nitrogen	0.6±0.1	0.36±0.07

Table 6.1: Values for coherent fraction (C_f) and coherent position (C_p) obtained from NIXSW analysis for **NiPP** on Au(111) for the as deposited material, and following sequential annealing to 450°C and 575°C to form **PGNR**.

on the degree of order, coherent fraction (C_f), and the 'average height', coherent position (C_p), of the specific chemical species relative to the projection of the bulk planes (i.e. in the case where no reconstruction, or relaxation, of the substrate occurs, C_p would define the height above the topmost surface layer) are obtained. Conceptually, $C_f \approx 1$ would indicate a single adsorption site for the atomic species probed, while $C_f \approx 0$ suggests adsorption at multiple sites or a random ordering. The coherent position can generally be considered in relation to a mean adsorption height ($d_{h,k,l}$) expressed as a function of the separation of the (h,k,l) planes, $D_{h,k,l}$, such that: $d_{h,k,l} = (n + C_p)D_{h,k,l}$, where n is an integer. The as deposited **NiPP** material exhibits a low value of C_f for carbon species (0.08±0.02), which implies no vertical ordering relative to the surface; i.e. a disordered polymer (note that as the value of C_f is effectively zero no inference can be made from the value of C_p). Following sequential annealing to 450°C and 575°C an increase in the value of C_f is observed (0.19±0.02 to 0.25±0.02), indicating that there is an increase in order but that the carbon species present occupy multiple heights (again, the low coherent fraction means that it is not possible to meaningfully interpret the coherent position). The increase in C_f is in agreement with the expected outcome of forming graphitic material (i.e. an overall flattening of the polymers). In agreement with the STM data presented in Figures 6.2 and 6.3, the relatively low value of C_f indicates incomplete ring-closing within the polymer, which is expected to result in a range of carbon adsorption heights.

Analysis of the nitrogen species by NIXSW reveal that a significant level of order ($C_f = 0.6\pm0.1$) is achieved following annealing to 575°C. This increase in order following annealing (compare with $C_f = 0.2\pm0.1$ prior to annealing) supports the interpretation that the on-surface reaction results in flattening of the porphyrin-graphene nanoribbons. Although this value of C_f does not indicate a high degree of order, it is comparable with studies of tetraphenylporphyrin (TPP) on Au(111) [197] and zinc-porphine (ZnP) on Ag(111) [206] where quasi-2D structures are observed, and as such supports the formation of **PGNR**.

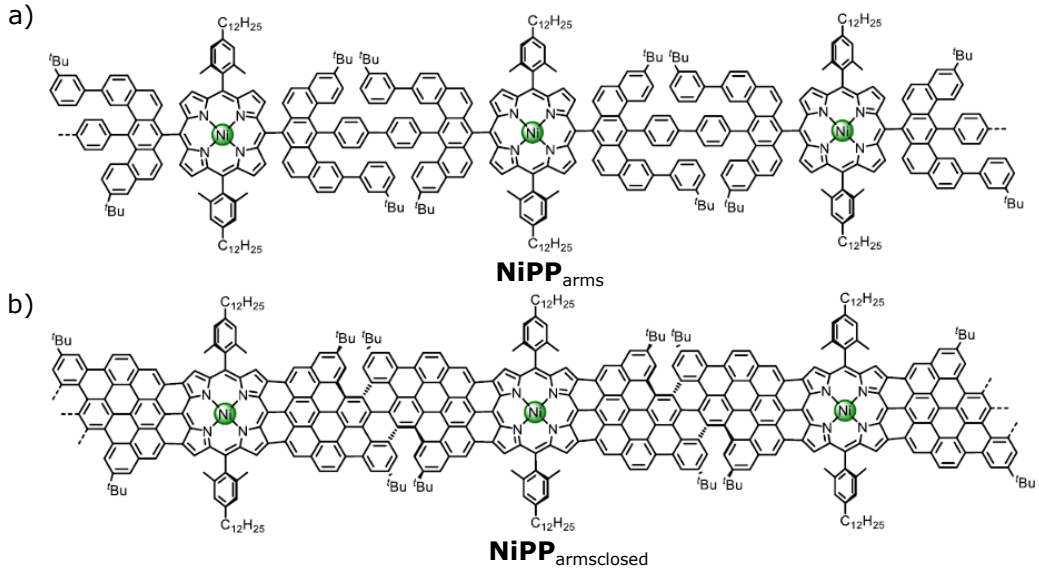

Figure 6.9: Chemical structure of a) **NiPP**$_{arms}$ and b)**NiPP**$_{armsclosed}$.

6.2.4 Functionalisation With Alkyl Chains

In addition to **NiPP**, a second, similar pair of species (referred to here as **NiPP**$_{arms}$ and **NiPP**$_{armsclosed}$) were prepared with alkyl side chains, as shown in Figure 6.9. As can be seen in the Figure, the **NiPP**$_{armsclosed}$ species is further towards the fully graphenated middle section, although the reaction is not yet complete. This species was not soluble in toluene, and so in this section the focus is on **NiPP**$_{arms}$, which was successfully deposited *via* electrospray, much like **NiPP**. The interest in functionalisation with alkyl side chains derives from the capacity of such chains to steer on-surface self-assembly, as discussed in detail in chapter 4.

STM

Two preparations of the **NiPP**$_{arms}$ were made, one spot deposition and one raster deposition. Each deposition displayed evidence of ribbons prior to annealing, but individual ribbons displaying measurable periodicity (as was the case with **NiPP**, see Figure 6.2) were not discernible; this can be seen in Figure 6.10a-b). The different contrasts found in the spot deposition shown in Figure 6.10a) and raster deposition in Figure 6.10b) are attributed to higher coverage on the raster sample; a greater density of ribbon-like structures and no indication of the herringbone structure implies a coverage of at least one monolayer, whereas the area imaged

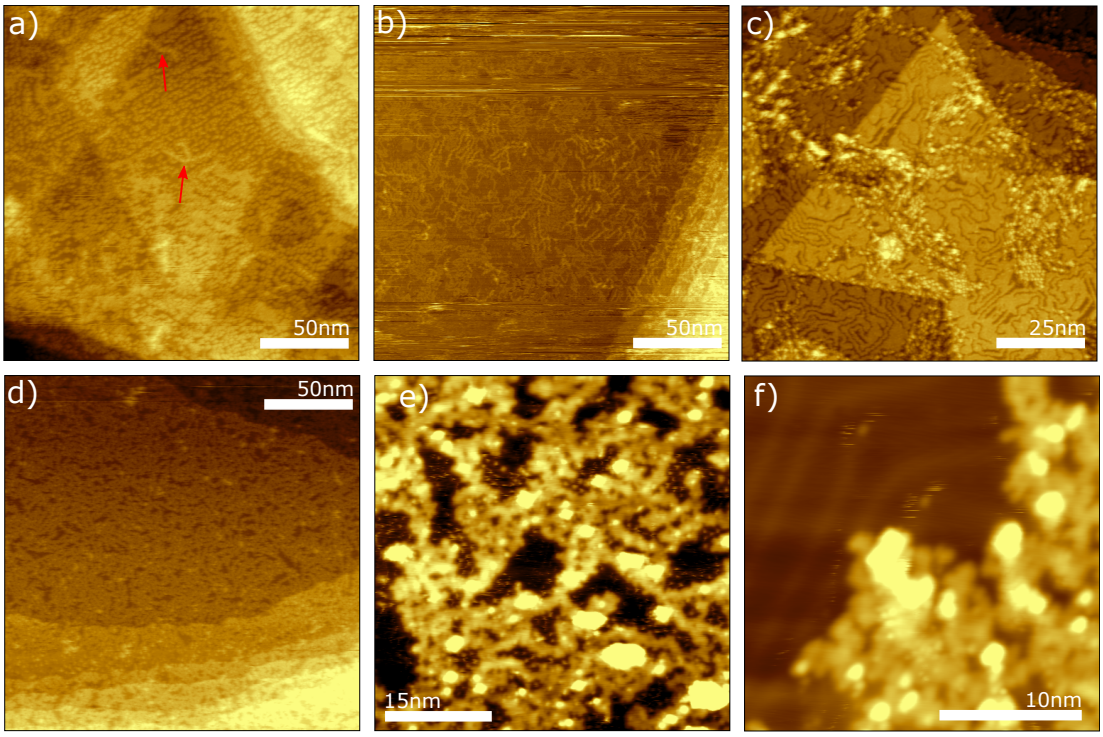

Figure 6.10: STM images of the **NiPP**$_{arms}$ species on Au(111). a) Electrospray spot deposition of **NiPP**$_{arms}$ as deposited. Red arrows highlight possible chains (Bias = -2 V, Set point current = 100 pA). b) Electrospray raster deposition of **NiPP**$_{arms}$ as deposited (Bias = -1.5 V, Set point current = 50 pA) c) **NiPP**$_{arms}$ on Au(111) following anneal to 150°C (Bias = -2 V, Set point current = 50 pA). d) **NiPP**$_{arms}$ on Au(111) following anneal to 350°C (Bias = -2 V, Set point current = 100 pA). e) **NiPP**$_{arms}$ on Au(111) following anneal to 450°C (Bias = -2 V, Set point current = 100 pA). f) Close zoom on **NiPP**$_{arms}$ on Au(111) following anneal to 450°C, with visible herringbone (Bias = -2 V, Set point current = 100 pA).

on the spot deposition appears to be sub-monolayer (of ribbons at least, not of contaminant). Following the anneal to 150 °C, a series of chain-like apparently recessed areas is visible on the sample (Figure 6.10c)). In some instances, the raised areas feature a thickness approximately similar to that expected of the ribbons, as shown in Figure 6.11. The approximate length of the alkyl chains is 1.4 nm, so it is feasible that the measured interspatial gap of 1.3 nm could be accommodated *via* the flexibility of the alkyl side chains. Unfortunately, this phenomenon is not consistent across large areas of the sample, and as the "chain" material exhibits no intra-molecular resolution, it is not possible to draw conclusions about

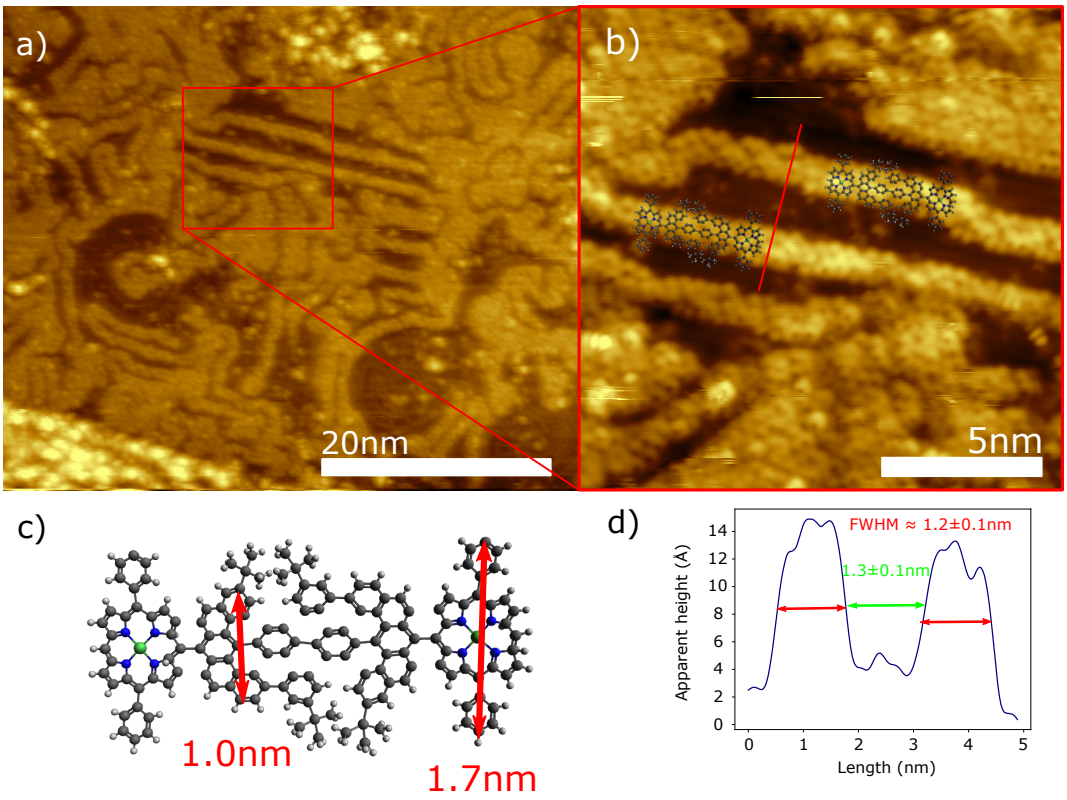

Figure 6.11: a-b) STM image and cutout zoom of apparent ribbon material from **NiPP**$_{arms}$ on Au(111) deposition following anneal to 150 °C, with b) scale overlay of model of single unit of **NiPP**$_{arms}$ (Bias = 2 V, Set point current = 100 pA). c) Model of single unit cell of **NiPP**$_{arms}$ with approximate dimensions based on universal force field model. d) Line profile taken from STM image shown in b) (location indicated by red line), with labelled measurements.

the nature of these unusual structures. Following anneal to 350 °C, much of the contaminant material appears to have desorbed, as shown in Figure 6.10d). A high coverage of close-packed ribbon-like material is visible, with little inter-chain separation and once again no resolvable intramolecular detail. The lack of inter-chain separation and regular packing arrangements perhaps suggests the loss of the alkyl side chains. This can be seen in even greater detail in Figures 6.10e-f), following anneal to 450 °C. The material in these images, while occasionally chain-like, appears to have undergone cross-linking reactions and in some cases (Figure 6.10f)) agglomerated into an entirely unresolvable mass. While this material does exhibit flattening expected from the formation of a graphitic polymer

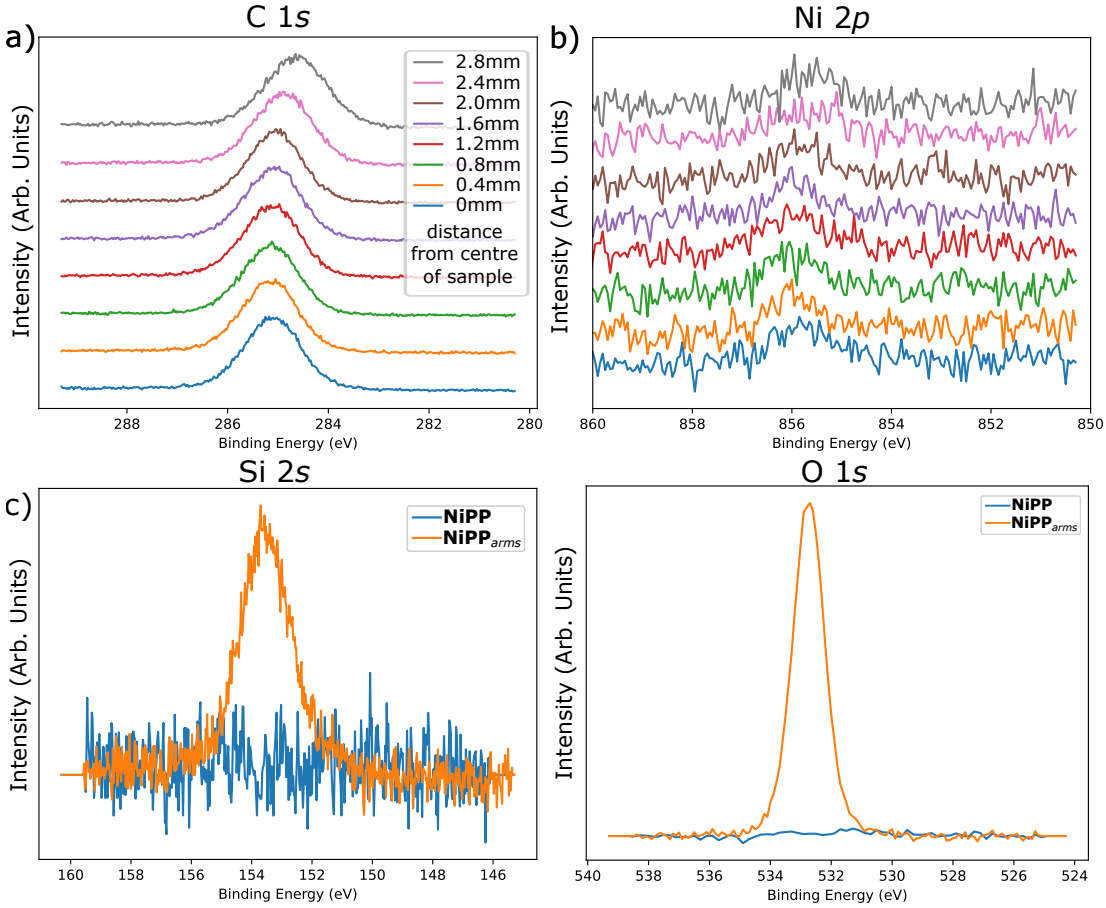

Figure 6.12: XP spectra for the **NiPP**$_{arms}$ species on Au(111). a) C 1*s* region normal incidence spectra moving away from the centre of the sample. b) Ni 2*p* region normal incidence spectra moving away from the centre of the sample. c) Si 2*s* region for **NiPP** following 450 °C anneal (blue) and **NiPP**$_{arms}$ following deposition (orange). d) O 1*s* region for **NiPP** following 450 °C anneal (blue) and **NiPP**$_{arms}$ following deposition (orange).

in line with **NiPP** (apparent height in the order of 0.5-1 Å), due to the complete lack of intramolecular resolution it is once again not possible to determine the character of the system.

XPS

In addition to STM, the **NiPP**$_{arms}$ raster deposition was also subject to XPS analysis following deposition. Some valuable insight was provided *via* comparison with **NiPP** (Figure 6.12). The spatially resolved C 1*s* and Ni 2*p* spectra exhibit the same downward shift in binding energy towards the edge of the sample

as **NiPP**, again attributed to decreasing coverage resulting in an increased surface screening effect. Also of interest is the presence of a significant silicon peak, as shown in Figure 6.12c). This peak is attributed to silicon-grease, as previously discussed in section 6.2.2, as is the strong O1s peak shown in 6.12d). The contrasting **NiPP** spectra in each of these regions is taken following a 450 °C anneal of the sample, indicating that the silicon contaminant has desorbed at these temperatures, matching the observed desorption at around this temperature in the STM. This is assuming that the silicon grease is present in both samples, as the Si 2*s* region was not measured on the **NiPP** until after annealing to 450 °C. Silicone grease is used within the experimental synthesis of these molecules, introducing a clear source of contaminant.

While not as successful as the experiments with **NiPP**, the deposition and analysis of $\mathbf{NiPP}_{arms}$ provided interesting insight into the issues relating to contamination during the electrospray process, and allowed insight into the differing on-surface evolution of a structurally similar molecule, hinting at the generally applicable nature of this approach.

6.3 Conclusion

We have demonstrated that porphyrin doped graphene nanoribbons can be formed *via* a combination of atomically precise solution-based synthesis and on-surface reaction pathways. The conversion of a Ni-porphyrin polymer to a porphyrin-graphene nanoribbon has been characterised by STM, XPS, NEXAFS, and NIXSW providing confirmation that: (i) The conversion of the **NiPP** polymer precursor to **PGNR** proceeds *via* a ring-closing reaction resulting in the 'flattening' of the **PGNR**. (ii) The nitrogen and nickel chemical environments within the porphyrin core, as well as the morphology of the porphyrin macrocycle, remain unchanged during formation of **PGNR** indicating that Ni-porphyrin units are incorporated into the nanoribbon. The combination of solution chemistry with bottom-up synthesis provides routes inaccessible to either method alone.

Chapter 7

At Which Temperature Does a Reaction Occur?

In this chapter, the properties of Ullmann-type coupling reactions of brominated tetraphenylporphyrin (Br_xTPP) on Au(111) and Cu(111) are investigated using a variety of spectroscopic methods, including temperature programmed measurements to provide temporal insights, paired with low temperature STM. Temperature programmed XPS (TP-XPS) is utilised to obtain temporal resolution of reaction progression, and Arrhenius analysis of TP-XPS is employed in a novel method to determine the kinetic properties of these reactions. The role of entropy in this system is also considered. The research highlights the mutability of oft-cited "reaction temperatures" when different rates of heating are applied.

7.1 Temperature Programmed Measurements

By measuring the temporal evolution of a system, significant insight can be obtained into the mechanisms underlying an on-surface process. SPM has been used to monitor evolving systems in real time, such as in the case of porphyrin diffusion, [166, 207, 208] but chemical reactions typically occur at higher temperatures than those at which STM achieves greatest resolution. Hence, a common technique when examining reactions with SPM is heating to a temperature at which a reaction step is expected to occur, cooling back down, and imaging the system at cryogenic temperatures (as has been seen in prior chapters). This route

provides a snap-shot of the system at the initial, final, and intermediate stages of the reaction, but 'real time' monitoring of the reaction progress is precluded. An alternative approach is to utilise XPS to monitor the reaction. Here, the upper limit on temperature for these measurements is determined by factors such as melting point of the substrate material, and hence a much larger temperature range is accessible. Therefore, the system can be continuously monitored over the course of a reaction as the temperature of a sample is increased.

Observing the development of reactions as a function of temperature has been a focus of much work in the field of mass spectrometry (MS). This is achieved *via* a technique known as temperature-programmed desorption (TPD). Here, the chemical species desorbing from the substrate are characterised using MS and the reaction is investigated by measuring the reaction products which leave the surface. Key to this approach is a well defined ramp rate, where the temperature is increased until the reaction progresses to completion. The ramp rate is then changed, and the system measured again, at a few different rates. TPD has previously been utilised to investigate the progression of on-surface Ullmann-type coupling, [209, 210] and has also been used to determine kinetic properties of species desorption *via* varying ramp rates. [16]

7.1.1 Arrhenius Analysis

Arrhenius analysis has previously been used to determine the kinetic properties of desorbing molecules in temperature programmed desorption (TPD) experiments. [16] Considering the desorption of a species as a first order reaction process, the Arrhenius equation for the desorption of species X, with concentration $[X]$ is as shown below, where A is the Arrhenius prefactor, E_a is the activation energy, T is the temperature and k_B is the Boltzmann constant:

$$\frac{d[X]}{dt} = -A[X]e^{\frac{-E_a}{k_B T}}. \tag{7.1}$$

If the sample is heated with a linear rate, β Ks^{-1}, starting with an initial temperature of T_0, the temperature after t seconds is given by:

$$T = T_0 + \beta t. \tag{7.2}$$

Combining Eqns. 7.1 and 7.2:

$$\frac{d[X]}{dT} = -\frac{A}{\beta}[X]e^{\frac{-E_a}{k_B T}}. \tag{7.3}$$

In a TPD context, the $\frac{d[X]}{dt}$ is considered proportional to the mass spectrometry signal. In TP-XPS, the signal we use is the area under an XPS peak (P_X) assigned to the particular chemical environment (in the case of this investigation, a Br $3d$ region peak assigned to the Br-TPP environment), as below:

$$\Delta P_x = \frac{d[P_x]}{dt} \propto -\frac{d[X]}{dt}. \tag{7.4}$$

Within a temperature ramp, the maximum reaction rate occurs at T_m. This occurs when the rate of change of peak area is 0, like so:

$$\frac{d\Delta P_x}{dT} = 0 = \frac{d}{dT}[\frac{A}{\beta}[X]e^{\frac{-E_a}{k_B T_m}}], \tag{7.5}$$

differentiating and rearranging to a linear form:

$$\ln \frac{T_m^2}{\beta} = \ln \frac{E_a}{k_B A} + \frac{E_a}{k_B T_m}. \tag{7.6}$$

In this form, $\ln \frac{T_m^2}{\beta}$ plotted against $\frac{1}{T_m}$ to produce a straight line with gradient $\frac{E_a}{k_B}$ and intercept $\frac{E_a}{k_B A}$, thereby allowing calculation of activation energy.

In the context of a TPD experiment, this can be applied in the following manner: firstly, a signature for the reaction must be identified. In this case, it will be a reaction product of a certain mass. Then, a series of ramp rates must be applied, with the reaction signature being continuously measured. The temperature at which the rate of change of reaction signature peaks can be identified from this data at each rate, and this information can be used in the form of equation 7.6 to acquire E_a and A for the desorption of the molecule in question.

7.1.2 Temperature-Programmed XPS

In the context of TP-XPS, the reaction signature would be the changing intensity of an XPS peak relating to the targeted chemical reaction. Ullmann-type coupling has been examined with a combination of STM and TP-XPS on several occasions; [74,75,211] and in the example shown in Figure 7.1, on two surfaces, investigated by Fritton *et al.*. [95] In this case, the tri-brominated organic molecule

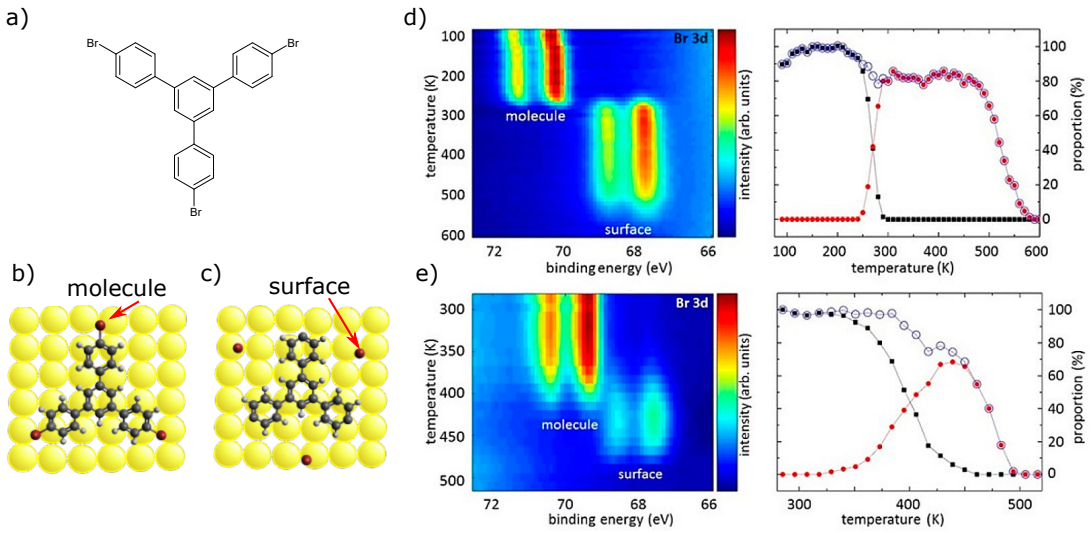

Figure 7.1: a) Chemical structure of TBB. b-c) Diagram showing the bromine environments labelled as on-molecule and on-surface. Br 3*d* TP-XPS Data of brominated molecule TBB on d) Ag(111) and e) Au(111). Accompanying graphs show the relative intensities of peaks assigned to molecule-bound (black) and surface-bound (red) Br. The clear markers indicate total Br intensity. Taken from Fritton *et al.* [95]

deposited on Ag(111) and Au(111) is being investigated in a typical Ullmann-type coupling reaction. As is shown in Figure 7.1, TP-XPS of the Br 3*d* region shows in clear temporal detail the debromination of the molecule and the subsequent Br desorption. Given a clear reaction indicator exists in the XPS, the temperature at which the reaction can be said to occur can be discerned from this data. In this case, a clear shift in binding energy in the Br 3*d* region occurs when the bromine detaches from the molecule and is adsorbed on the surface. On Au(111), the Br $3d_{3/2}$ shifts from 70.4 eV to 68.6 eV, and on Ag(111) from 71.4 eV to 68.7 eV; these match literature values for a transition from an organo-halide species to a chemisorbed bromine. [131, 212, 213] This technique has previously been applied for Ullmann-type coupling reactions. [214]

At Which Temperature Does a Reaction Occur?

An overlooked aspect of reaction temperature is that the rate of heating influences the temperature at which the peak reaction rate occurs. In experiments such as

those covering Ullmann-type coupling reactions, a reaction temperature is often cited. This can be derived from TP-XPS, or stepwise heating of the sample; such measurements are reported in Table 2.2 in section 2.2.2. Of course, as can be seen from the Arrhenius rate analysis described above, this statement of a reaction temperature alone is entirely inadequate to fully describe a system. The changing peak rate of reaction temperature with ramp rate has also been observed with Ullmann-type reactions, as Di Giovannantonio *et al.* observed significant shifting ($\approx$ 10 K) noted from a ramp rate difference of just 0.5 °Cs^{-1}. [211]

The varying rate of heating in different experimental setups could explain the disparate dehalogenation temperatures discussed in section 2.2.2, Figure 2.6; it is clear from the Arrhenius analysis that ramp rate information should also be listed to provide a more complete picture of the conditions in which a reaction has taken place. Ideally, an experimental technique should provide kinetic parameters of the reaction, such as E_a and A to more completely describe the system.

In this chapter, an understanding of the morphological and chemical development of the target system, Br$_x$TPP on Au(111) and Cu(111), is developed through the application of stepwise STM, NEXAFS and XPS at different temperatures. Following this, the kinetic properties of the dehalogenation reaction are examined *via* Arrhenius analysis of temporally resolved TP-XPS, allowing for a more accurate characterisation of reaction steps than a simple statement of reaction temperature. Entropy and enthalpy are identified as key parameters for comparing reactions, and this novel technique allows these parameters to be determined, opening up new avenues for potential molecule/substrate tailoring towards specific on-surface processes, increasing both efficiency and selectivity.

7.2 Experimental Methods

7.2.1 Sample Preparation

Br$_x$TPP was synthesized by the group of Neil Champness, The University of Birmingham, School of Chemistry, University Rd W, Birmingham, UK, B15 2TT.

Cu(111) and Au(111) surfaces were both prepared in ultra-high vacuum (UHV) conditions, base pressure 7.7×10^{-10} mbar, by cycles of sputtering and annealing

(sputter 1 keV for 20 minutes, anneal to 550 °C and held for 5 minutes before returning to room temperature.) For spectroscopy, the Cu(111) was annealed in 2×10^{-6} mbar of O_2, and the resultant clean surfaces were characterised with XPS to show no contaminant species present. Thermal depositions of Br_xTPP onto nitrogen cooled single crystal Cu(111) surface (approx. sample temperature of -180 °C) was performed with a Knudsen-type evaporator (250°C, 5-15 mins). Nominally identical coverages (sub-monolayer) were obtained by comparing the relative intensities of metal and adsorbate (C 1s) features. On Au(111), the same deposition parameters were used, albeit with the crystal held at room temperature. Assignment of sub-monolayer coverage was supported by STM characterization.

7.2.2 Details of the FlexPES Beamline

All spectroscopy experiments were performed at MAX IV in Lund, Sweden, at the Surface and Materials Science (SMS) Branch of the FlexPES beamline. [215] FlexPES is situated on the 1 GeV storage ring and used a planar undulator and collimated plane-grating monochromator to deliver photons with energy range 40-1500 eV. The beam spot on the SMS branch was defocused to produce a spot of 1×0.4 mm^2. The defocused beam was used for all measurements reported, to limit any radiation damage to the samples. No radiation damage was detected on either of the samples (this was determined *via* continuous C 1s measurement under photon flux, with no variation in spectra intensity or shape). Base pressure did not exceed 1×10^{-9} mbar in the experimental chamber during the experiment.

The experimental station at FlexPES features a Scienta SES-2002 hemispherical analyser (Scienta Omicron) positioned 40° from the incident photon beam, which was used for the photoelectron spectroscopy. PES measurements were taken at normal emission. A home-built partial electron yield (PEY) microchannel plate (MCP) detector was used for X-ray absorption measurements. NEXAFS measurements were taken in partial electron yield (PEY) mode using the MCP detector. For the N K-edge a retardation potential of 300 V was used and for C K-edge a potential of 220 V was used to suppress the contributions of low energy electrons in the background. On the Au(111) system all measurements

aside from the TP-XPS were carried out at RT, while on the Cu(111) system all measurements aside from the TP-XPS, were carried out at -180°C.

7.3 Stages of Ullmann-type Coupling on Cu(111) and Au(111)

7.3.1 Introduction

In this section, TP-XPS is used in concert with sequential NEXAFS and STM to gain insight into the evolution of the Ullmann-type coupling reaction exhibited by Br_xTPP (structure shown in Figure 7.2) on Au(111) and Cu(111) surfaces. These techniques allow temporal chemical characterisation, paired with high-resolution topographical and conformational information. The on-surface reactions of porphyrins are of great interest as molecular building blocks in bottom-up on-surface assembly, due to their interesting chemical properties. [15, 84, 177] Alongside the various stages of Ullmann-type coupling reactions, as described in section 2.2.2, electrocyclic ring-closing [198, 216, 217] has often been reported with phenyl-functionalised porphyrin species, and self or trans metallation is also commonly observed. [197, 218, 219] Here, I look at a complex multi-step system, where several intra- and inter-molecular reaction steps are initiated (as summarized in Figure 7.2 and discussed in detail below). I investigate these multi-step reactions on Au(111) and Cu(111) and identify the effects of the two substrates on the progression of this on-surface reaction, utilising STM and TP-XPS.

7.3.2 STM Characterisation

STM images acquired following deposition Br_xTPP onto Au(111) and Cu(111) show that species with 0,1,2,3 and 4 bromine atoms are visible, indicating that all species (x=0-4) are present. This is expected as the synthesis route will yield a mixture of species. Br_2TPP is the most frequently observed molecular species; within solution-phase synthesis, Br_2TPP is expected to be the majority product, [220] and it is therefore unsurprising that this is the most frequently observed species within the STM measurements. This can be seen in Figure 7.2a+e).

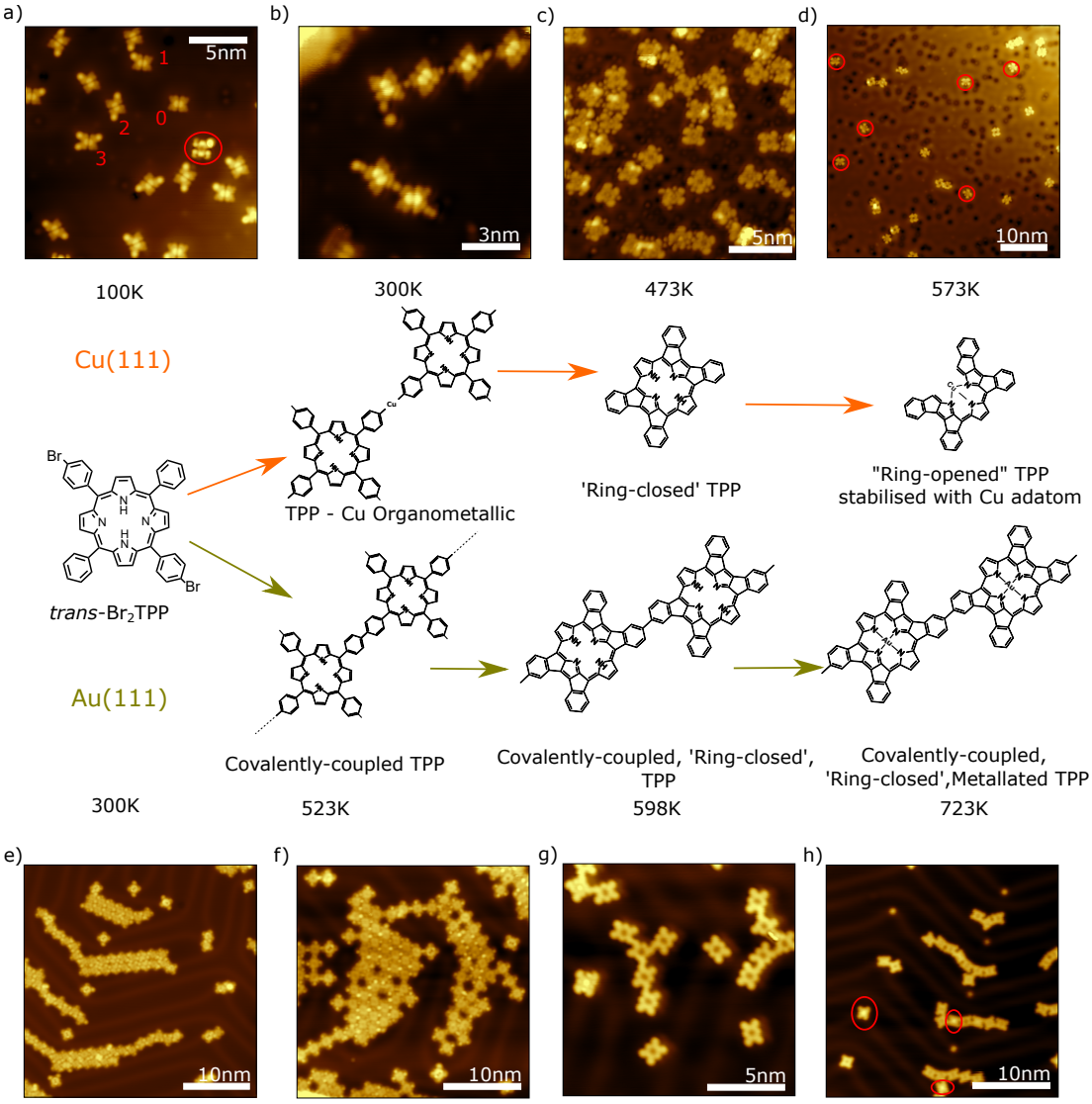

Figure 7.2: Summary of the reactions of Br_xTPP on Cu(111) (a-d) and Au(111) (e-h), with accompanying STM. STM parameters: a) Bias = -1 V, Current = 50 pA.b) Bias = -1 V, Current = 150 pA.c) Bias = 1 V, Current = 250 pA.d) Bias = -1.6 V, Current = 300 pA.e) Bias = 0.5 V, Current = 100 pA.f) Bias = 0.5 V, Current = 300 pA.g) Bias = -0.1 V, Current = 100 pA.h) Bias = -1.4 V, Current = 100 pA. STM images on Au(111) acquired by Matt Edmondson [223]

In agreement with previous studies, the bright protrusions can be assigned to the location of bromine atoms on the molecule. [15, 84, 221, 222] On Cu(111), the porphyrins are predominantly isolated, or in small clusters, with no visible aggregation into island formations. This behaviour has been observed previously, and is attributed to a strong molecule-substrate interaction and dipole formation. [224] These individual porphyrins adopt two conformations on surface: a “saddle”

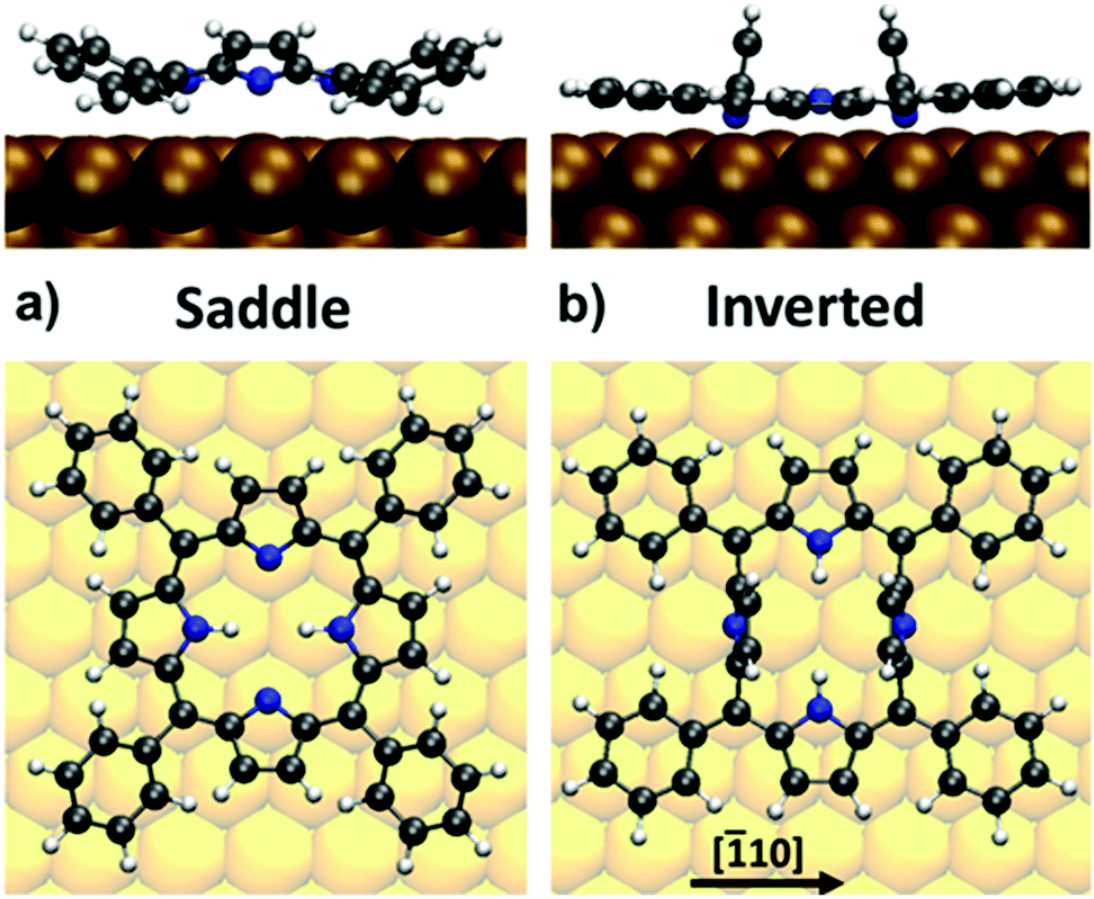

Figure 7.3: Two conformational geometries of 2HTPP on Cu(111), derived from DFT calculations by Lepper *et al.*, with Figure also produced by Lepper *et al.* [227] a) Shows a conventional "saddle-shape" adsorption geometry and (b) an "inverted" adsorption geometry with two pyrrole rings in "upright" configuration.

shape (as shown in the red circle Figure 7.2a)), [225] and an "inverted" structure which predominates, at a ratio of 3:1 (N=233; these statistics acquired by Ailish Gray). [72, 226]. These two conformations are shown in Figure 7.3, as reported by Lepper *et al.* [227]

On Au(111), the porphyrins more readily aggregate into islands, with a small proportion instead becoming trapped in energetically preferable elbow sites. [6] This is attributed to the higher sample temperature during deposition and the weaker surface-molecule interaction expected on Au(111). The stabilisation of non-halogenated TPP species has previously been assigned to π-H interactions. [166] Here the presence of halogen atoms may provide additional stabilisation *via* a halogen-binding motif. [40,128] Individual molecules are pinned at "elbow" sites

in the characteristic herringbone reconstruction, [196] exhibiting the aforementioned "saddle" shape. The close-packed islands reside in the face-centred cubic (fcc) regions of the surface; this is a known phenomenon, and has been described in terms of the difference in diffusion barriers between fcc and hcp regions. [6]

Following annealing of the Au(111) and Cu(111) surfaces (to 523 K and 300 K, respectively - as expected all reaction steps occur at a lower temperature on Cu as compared to Au [8]) the debromination step of the Ullmann-type coupling reaction is initiated. On Cu(111), this results in the formation of an organometallic intermediate (supported by XPS as shown in section 7.3.3) predominantly consisting of short chains, as shown in Figure 7.2b); this result is in agreement with the literature. [70, 77] At this temperature, the "saddle" shape is entirely absent, indicating a preference for the "inverted" conformation once dehalogenated. On Au(111), the molecule exhibits covalent coupling at the same temperature at which dehalogenation is first observed; as in the literature, the MOF appears less stable on Au than Cu. [15, 64] Bright features observed within the close-packed islands (Figure 7.2f)) are attributed to still-attached Br atoms, indicating incomplete dehalogenation at this temperature. Further annealing results in longer covalently bonded polymers and further dehalogenation.

After the formation of MOFs or covalently linked polymers, further annealing (473K on Cu(111), 598K on Au(111)) results in ring-closing reactions on both surfaces, as shown in Figure 7.2c&g). A variety of ring closed isomers are formed, of the same form as those reported by Cirera *et al.*. [216] Ring-closing reactions are cyclodehyrdogenation reactions, whereby the porphyrin planarizes; schematics of two example species are shown in Figure 7.4. On Au(111), the porphyrins within covalently linked polymer chains exhibit ring-closing, showing the relative stability of the recently formed C-C coupling between neighbouring porphyrins compared to the barrier for cyclodehydrogenation, which gives rise to the ring-closed porphyrinoids. These staggered energy barriers allow for the sequential nature of the on-surface reaction.

Additionally, following further heating, partial metallation occurs, as shown by the ringed molecules in Figure 7.2h) - the bright cores are attributed to the incorporation of a surface Au atom into the central macrocycle (this phenomenon

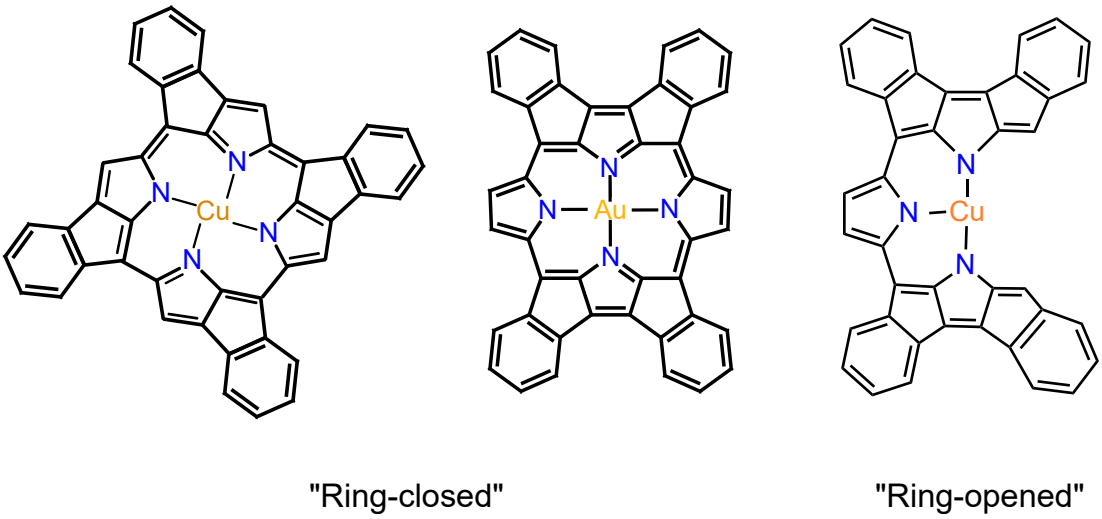

Figure 7.4: Schematics of ring-closed and ring-opened metalated tetraphenyl porphyrins.

is also shown in Figure 7.4). Metallation is a process whereby a tetraphenylporphyrin species takes a metal atom from the substrate into the macrocycle core of the molecule and results in a metalated species. On Cu(111), the MOF structures are observed to break up, and individual porphyrins begin the intramolecular ring-closing reaction at 473K (Figure 7.2c)); the bright features are attributed to incomplete ring-closing. [166] Upon further annealing, the "ring-opened" species, mediated by a surface adatom and circled in Figure 7.2d), predominates. A schematic of the ring-opened structure is shown in Figure 7.4. Once again, metallation is indicated by a bright protrusion in the centre of the molecule; this is supported by XPS, as reported below. These ring-opened structures have been previously reported on Cu(111). [217]

Also observed on Cu(111) following the 573 K anneal were molecular chains, such as seen in Figure 7.5a). At this temperature, the MOF has broken down, and individual ring-closed species predominate, but short molecular chains are occasionally seen. The lack of order in these chains indicates that the coupling is not Ullmann-type, as the bonding seems non-site-specific, as opposed to at the brominated sites on the pendant aryl rings as expected for Ullmann-type coupling. In order to ascertain the nature of these features, manipulation was performed using the STM 'tip'. This was achieved by reducing the tip-sample separation, disabling the feedback, and manually directing tip motion across the chain. As

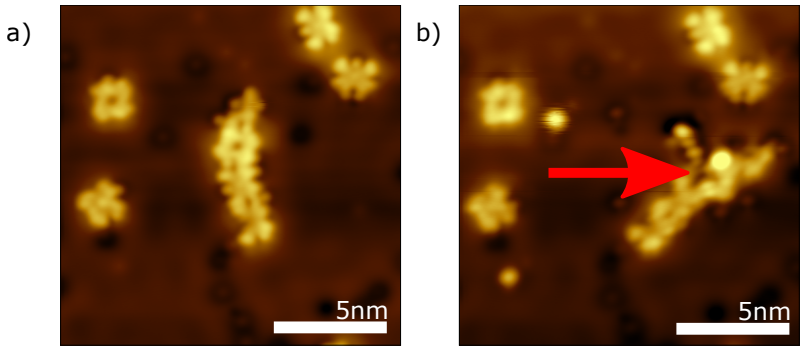

Figure 7.5: STM images showing molecular chain a) before and b) after tip manipulation. STM parameters: Bias = -1.6 V, Current = 300 pA.

can be seen in Figure 7.5b), the chain was damaged by the tip manipulation, but no individual units were detached. This resilience is a strong indicator of covalent bonding, alongside the XPS discussed below.

7.3.3 Stepwise Spectroscopy: snapshots of an on-surface reaction

Chemical evolution of a reaction: XPS characterisation

XPS and NEXAFS spectra were taken at different annealing stages to provide additional chemical and orientational information on the developing system. Specifically targeted temperatures were used to trigger the desired reaction stages, in much the same manner as the previously discussed STM. Beginning with the C 1s region, several key stages in the reaction can be seen, as shown in Figure 7.6. The C 1s region contains information on the chemistry and thus the structure of the carbon in the target molecule; as the molecule is organic, this is the overwhelming proportion of constituent atoms, and hence this region is of great interest. The C 1s spectra for as deposited Br$_x$TPP, on both Au(111) and Cu(111), exhibit a broad asymmetric peak arising from the multitude of carbon environments (Fig. 7.6a and d). Here I initially list the expected carbon environments and go on to interpret the experimental data in light of these expected spectroscopic features. Six distinct chemical environments are assigned (highlighted within the chemical structures in Fig. 7.6), they can be described as follows: atoms in the phenyl rings (PhC, blue), atoms in aromatic sections of the core (ArC, cyan), atoms

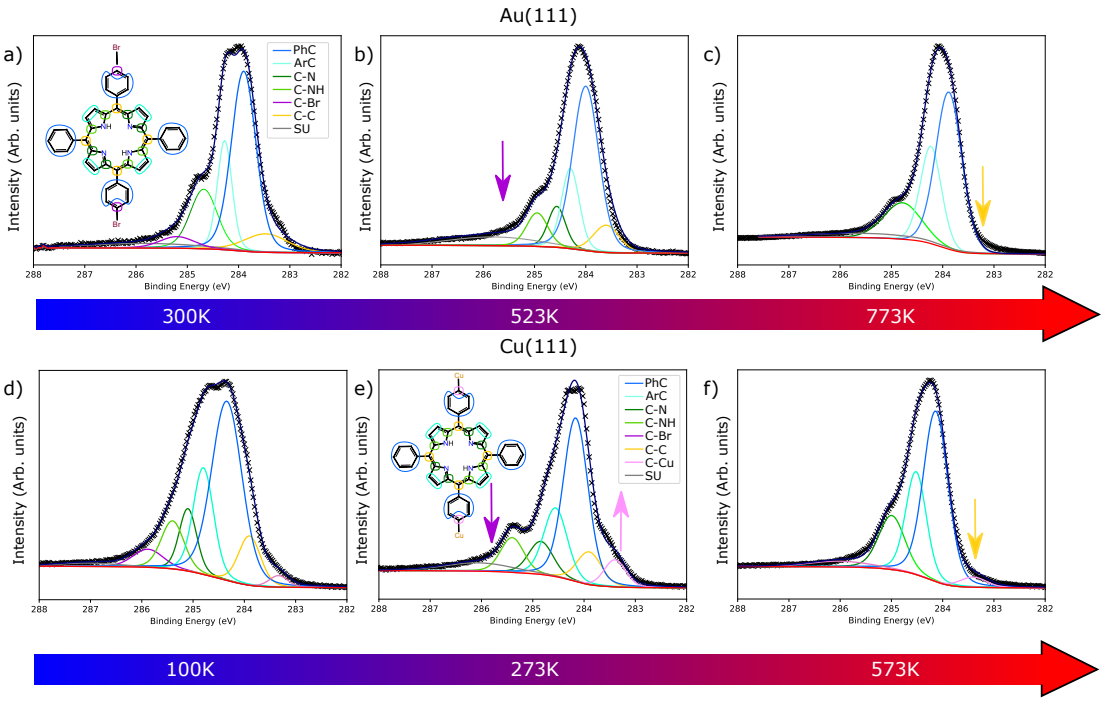

Figure 7.6: XP spectra in the C 1*s* region for Br$_x$TPP on Au(111) (a-c) and Cu(111) (d-f).

bonded with nitrogens (aminic C-NH, iminic C-N, both green), atoms bonded with bromine (C-Br, purple) and carbon-carbon bonded atoms (C-C, yellow). In accordance with the literature, a high binding energy shoulder is assigned to the C-Br environment, and a low binding energy shoulder to the organometallic environment. [95, 166, 191, 228] The methodology behind the assignment of the peaks is described by Nardi *et al.*, including the notable lower binding energy C-C peak. [229] Using the number of atoms in each environment to define peak areas relative to one another, a convincing model of the C 1*s* region can be assembled; these environments can be seen labelled in Figure 7.6a+e). In addition, I note that carbon atoms adjacent to the two different nitrogen environments (−N= and −N−H) are expected to exhibit different BEs when there is a significant difference between the chemical environment of the nitrogen species (e.g. strong interaction with substrate atoms) [229].

On Cu(111), where a strong interaction between −N= and the substrate has previously been observed, ([72, 226, 227]) I assign the carbon species adjacent to nitrogen atoms (labelled here as C_N and C_{NH}) to different BEs (285.1 eV and 285.3 eV respectively). On Au(111), where a strong interaction between −N= and

substrate is not expected, a single peak at 284.8 eV is assigned. This distinction between C_N and C_{NH} is an important feature and provides details of the progress of the on-surface reaction following annealing.

As the reaction progresses, I look for evidence of covalent bonding or MOF formation; as previously mentioned, the signals for these changes are shoulders appearing at high or low binding energy respectively. On Au(111), the organometallic region is not visible, due to either the relative instability of the MOF or poor peak separation from the main body of the C 1*s*. What can be seen is the elimination of the C-Br peak upon annealing to 523 K; also notable in this step is the separation of the two C-N environments, possibly caused by distortion of the saddle shape (at this temperature, ring-closing is not expected to have occurred, but the shift in the C-N environments indicates a less extreme positional change for these environments) during covalent bonding as the molecule moves out of the saddle shape. Subsequent annealing to 773 K results in the elimination of the C-C peak (Figure 7.6c)), indicating a ring-closing reaction as the intensity shifts to the aromatic carbon peak ArC, in good agreement with the previously discussed STM.

On Cu(111), a similar picture emerges: after annealing to 273 K, the C-Br peak diminishes (shown in Figure 7.6b&e) by a purple arrow), and after further annealing (in this case 573 K) the C-C peak also reduces (shown in Figure 7.6c&f) by a yellow arrow). Notable differences begin in Figure 7.6d), where the C-N peaks can be seen to be separate, caused by the inverted conformation of the porphyrins on Cu(111). One key difference between Cu(111) and Au(111) can be seen in Figure 7.6e), where the organometallic peak C-Cu can be clearly seen at the low binding energy position as expected (pink arrow). The final state shown in Figure 7.6f) is very similar to that on Au(111), as the system consists predominantly of ring-closed covalently-coupled polymer chains.

The C 1*s* region undergoes various changes for each surface as the reaction progresses; these changes are listed in Table 7.1. In both cases, a decrease in the high binding energy C-Br peak indicates a dehalogenation has occurred. On Cu(111), clear evidence of MOF formation is seen, with the prominent C-Cu peak arising; this is absent on Au(111). Ring-closing can be observed *via* the decreasing

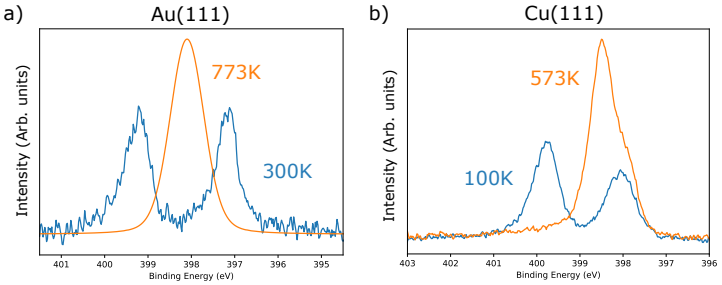

Figure 7.7: XP spectra in the N 1s region for Br$_x$TPP on Au(111) a) and Cu(111) b).

C-C peak, common to both surfaces, and further conformational changes can be derived from changing C-N environments.

In order to monitor the metallation of the porphyrin species, the N 1s region was also measured, both before and after the anneal, as shown in Figure 7.7. This merging of two N 1s peaks into one is highly characteristic of porphyrin metallation and supports the possible metalation indicators visible in the STM. On Au(111), the N 1s spectra exhibits a 4 environment split (attributed to TPP located on and off the top of adatoms) transitioning to a single, clearly defined peak associated with a self-metalated porphyrin found in the literature. [197] The four environments can be seen in Figure 7.7a) as two large peaks, representing the iminic (lower binding energy) and aminic (higher binding energy) positions, each with a smaller shoulder on the higher binding energy side caused by ad-

Surface	Reaction stage	Temp (K)	C 1s signature
Au(111)	Debromination	523	Decrease in Br-C peak, splitting of C-N peaks
Au(111)	Ring-closing	773	Decrease in C-C peak
Cu(111)	Debromination	273	Decrease in Br-C peak, widening of gap between C-N peaks
Cu(111)	MOF formation	273	Increase in C-Cu peak
Cu(111)	Ring-closing	573	Decrease in C-C peak

Table 7.1: Changes in C 1s XPS region for Br$_x$TPP on Cu(111) and Au(111) at various stages of anneal.

sorption atop adatoms. On Cu(111), the pre anneal N 1s split is more uneven, favouring the higher binding energy peak associated with pyrrolic nitrogen. This is ascribed in the literature to an electron diffraction effect caused by the inverted porphyrin confirmation; as the lone pair on the iminic nitrogen atoms are pointed towards the surface, they suffer significant scattering. [203] After annealing, a single peak with a significant shoulder is formed, again in accordance with the literature. [203] The lopsided nature of this metalated peak could be due to the aforementioned ring-opened porphyrins creating a different environment to a fully metalated porphyrin.

Structural characterisation: NEXAFS

In addition to the XPS, angle resolved NEXAFS were acquired at various stages of the on-surface reaction (i.e. following step-wise annealing of the sample). NEXAFS provide information on the energy levels of π^* and σ^* orbitals; angle resolved NEXAFS provides specific information on the orientation of the bonds related to the π^* and σ^* orbitals relative to the surface, as described in section 3.2.3. For porphyrin species, C K-edge measurements may be used to probe unoccupied π states associated with the macrocyclic core, or phenyl legs and therefore may provide details on the average orientation of the core or legs relative to the surface. Figure 7.8 details the C K-edge NEXAFS spectra taken at various stages of anneal on both surfaces. It is non-trivial to definitively assign resonances to specific structural moieties within Br_xTPP, however it is common for the first π^* resonance to be associated with the anti-bonding orbitals in the macrocyclic core of the porphyrin. [202,230] Here the focus is on the use of angle-resolved NEXAFS to determine conformational information during the reaction. On Au(111), the C 1s NEXAFS spectra (Figure 7.8a-c) display clear changes in π^* orbital structure, indicating chemical reactions have indeed taken place. Angle-resolved NEXAFS may provide information on the orientation of molecular bonds with respect to the surface by considering the variation in intensity of a specific resonance as a function of the angle of incidence for the X-ray source.

For any molecular orientation one may plot the expected variation in intensity as a function of angle of incidence (see Figure 7.8d)), and by plotting the measured

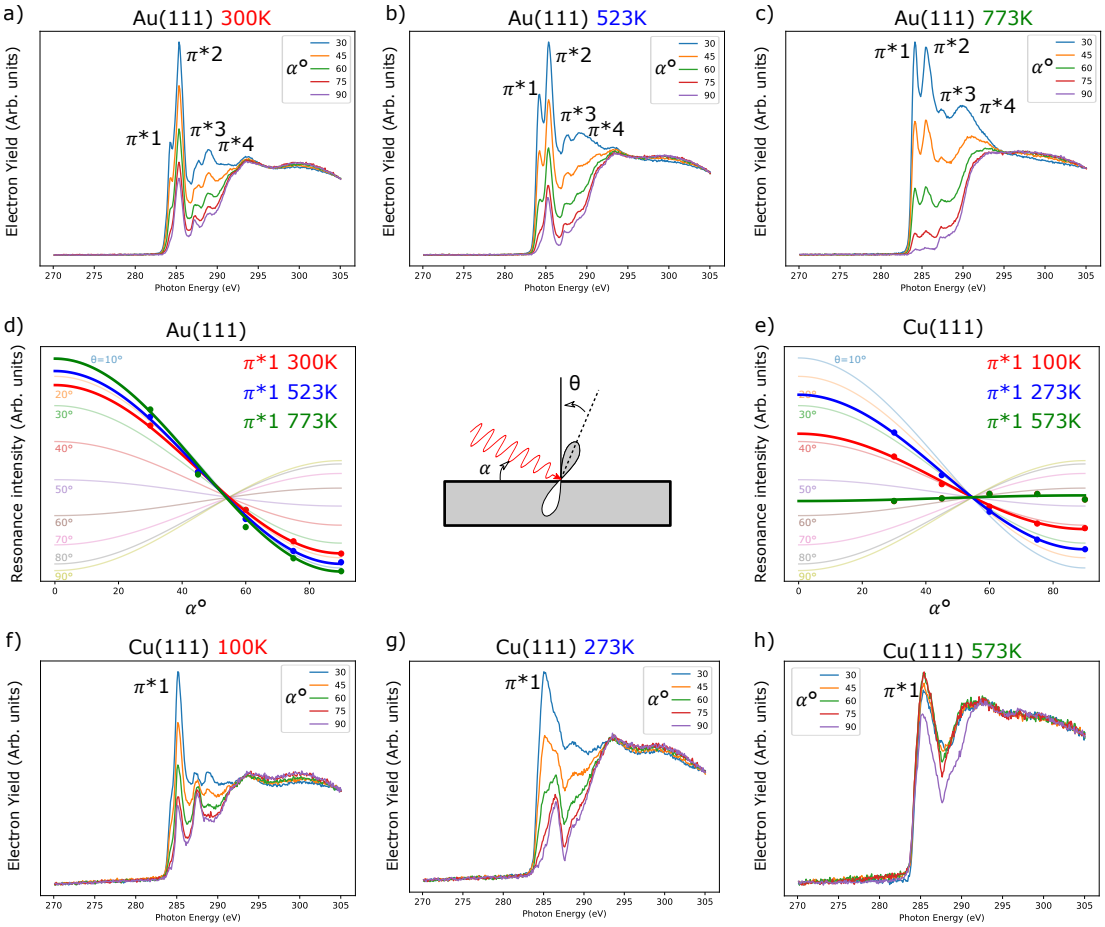

Figure 7.8: NEXAFS spectra in the C K-edge region for Br$_x$TPP on Au(111) a-c) and Cu(111) e-h). Also included are plots of normalised resonance intensity with calculated bond angle plot for d) Au(111) and e) Cu(111).

data one can identify the optimal fit. Figure 7.8d) shows a plot of intensities for the π^*1 peak at different anneal temperatures, showing a clear reduction in angle to surface normal θ with increasing anneal temperature. As the π^* orbitals are perpendicular to the molecular plane we therefore deduce that the molecule aligns more closely to the surface plane following each annealing step. This pattern presents itself across the various identifiable C K-edge resonance peaks, as shown in Table 7.2.

This pattern of the molecule progressively flattening over the course of the anneals matches both the STM and XPS descriptions, with covalent coupling and particularly ring-closing expected to flatten the molecule. The initially adopted saddle shape (as assigned by STM and supported by the NEXAFS result of a 20-40° angles) is no longer physically possible once the phenyl appendages are

bonded in plane with the central macrocycle.

On Cu(111), the resonance peaks are less clearly distinguished, with significant changes to the number and appearance of resonant peaks as the anneal temperature is increased. The dominant π^*1 resonance feature becomes broader at each of the three annealing stages (indicating significant changes in the electronic structure at the core of the molecule). At 273 K, the molecule displays some flattening; this is ascribed to the shift from saddle to inverted conformation, which results in planarisation of the molecule. At 573 K the calculated angle is 55°. A 55° angle can occur if the bond is at 55°, or if the bond angles are entirely disordered, meaning the molecule is disordered on the surface. This behaviour is ascribed to the molecule agglomerating onto step edges at high temperatures, a phenomenon observed on Cu(111) in STM when the coverage is low ($\leq$0.5 ML). This phenomenon is shown in Figure 7.9.

The N K-edge NEXAFS follow a similar pattern on Cu(111), but differs on Au(111), as shown in Table 7.2 and Figure 7.10. In porphyrin species, nitrogen atoms are found only in the core. In the saddle shape, these atoms are roughly

Region	Surface	Temp (K)	π^*1 θ°	π^*2 θ°	π^*3 θ°	π^*4 θ°
C K-edge	Au(111)	300	23.3±2.7	37.8±0.6	35.2±1.1	39.1±0.8
C K-edge	Au(111)	523	16.7±5.5	33.1±0.9	28.7±1.75	35.4±1
C K-edge	Au(111)	773	3.8±4.2	8.9±5.5	25.2±2.2	31.2±1.3
N K-edge	Au(111)	300	21.7±0.1	24±0.2	n/a	n/a
N K-edge	Au(111)	523	23.4±0.2	26.7±0.5	n/a	n/a
N K-edge	Au(111)	773	29.3±0.9	25.5±0.4	n/a	n/a
C K-edge	Cu(111)	100	37.9±0.3	n/a	n/a	n/a
C K-edge	Cu(111)	273	26.4±0.1	n/a	n/a	n/a
C K-edge	Cu(111)	573	55.8±0.1	n/a	n/a	n/a
N K-edge	Cu(111)	100	49±0.2	55.7±0.3	n/a	n/a
N K-edge	Cu(111)	273	55.9±0.2	57.1±0.2	n/a	n/a
N K-edge	Cu(111)	573	55.7±0.2	55.9±0.5	n/a	n/a

Table 7.2: Calculated angles of π^* orbitals to the surface normal for different NEXAFS resonance peaks.

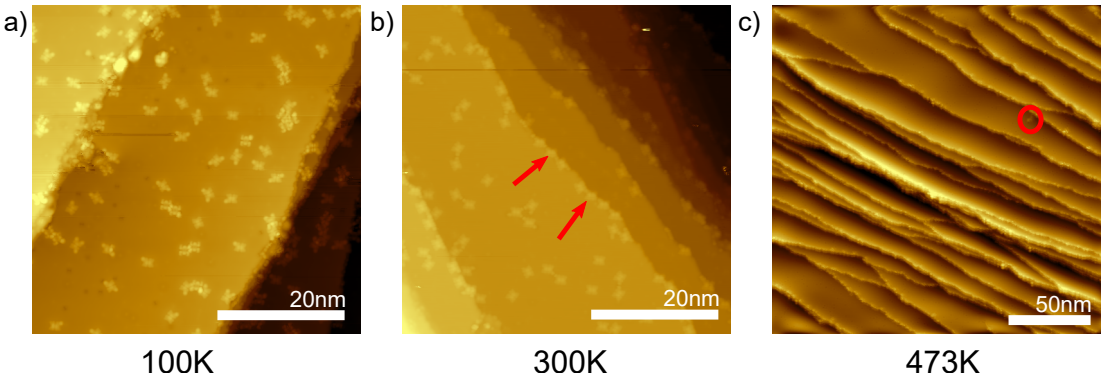

Figure 7.9: STM images of Br_xTPP on Cu(111) at various stages of anneal and the gradual migration towards step edges on a low coverage (<0.5ML) preparation. Highlighted with the arrows are porphyrin species adsorbed onto the step edges. Highlighted with the red circle is a single porphyrin species adsorbed onto a terrace site in the overview scan. a) Bias = -1.0 V, Set point current = 50 pA. b) Bias = -1.0 V, Set point current = 150 pA. c) Bias = -1.0 V, Set point current = 250 pA.

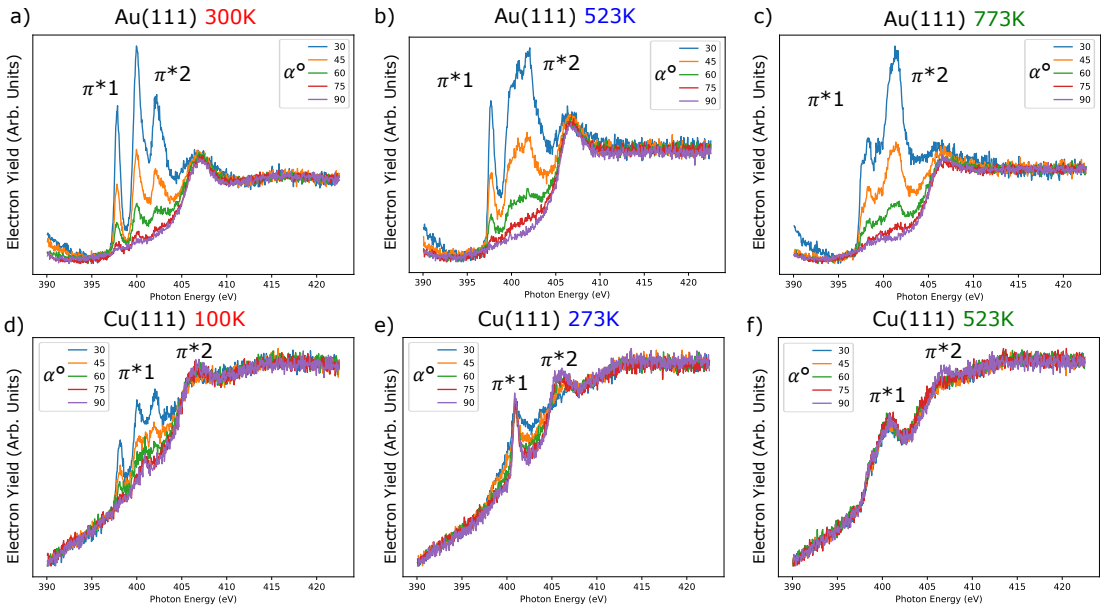

Figure 7.10: NEXAFS spectra in the N K-edge for Br_xTPP on Au(111) a-c) and Cu(111) d-f).

planar, albeit with the iminic and aminic species tilted slightly differently. On Au(111), while showing clear changes in electronic structure, demonstrates no significant change in bond orientation over the course of the anneal is observed; this implies that the nitrogen bonds are not in plane with the porphyrin macrocycle,

remaining in the saddle shape throughout, until ring closing occurs, which also does not lead to homogenous nitrogen orbital tilt. The XPS for the sample these NEXAFS were taken from displayed incomplete ring closing at the time the final NEXAFS was taken, so this data is not representative of a metalated system. The inverted structure features huge variation in bond angle between the iminic and aminic nitrogens, which seems likely to cause the disordered signal seen at all stages of the Cu(111) annealing process. The N K edge NEXAFS arrives at a uniform 55° position following anneal, perhaps indicative of the evolution of all species into the inverted position, in agreement with the STM.

7.3.4 TP-XPS

Temperature programmed measurements allow observation of a targeted reaction in real time. In the case of XPS, these measurements enable temporal insight into the evolution of core level spectra over the course of a reaction, rather than stopping the reaction at predetermined temperatures to capture snapshot, as is the case with the stepwise XPS described previously. The temperature range over which the measurements on the Cu(111) samples were taken was chosen to include the dehalogenation reaction of the Br_xTPP, shown graphically in Figure 7.11a), approximately 173-273 K. The characteristic carbon-bromine spin-orbit doublet at binding energies of 71.4 eV and 70.5 eV is observed, and transitions to a lower set of binding energies over the course of the reaction, at 69.7 eV and 68.7 eV (as seen in Figure 7.11c), with the C-Br environment labelled "Br-TPP" and the bromine-copper environment labelled Br-Cu). This shift to a lower binding energy is associated with breaking of the C-Br bonds, as the higher energy environment is typically associated with a C-Br environment. [70] This indicates successful deposition of the intact molecule and subsequent dehalogenation reaction. Other regions of interest for TP-XPS investigation in this system include the N 1*s* region, due to the metalation expected on both Cu(111) and Au(111), and any potential shift caused by the transition from saddle to inverted conformations. Additionally, the C 1*s* region contains higher and lower binding energy shoulders associated with the MOF and Br-C bond (as described in section 7.3.3 whose progress could be tracked *via* TP-XPS.

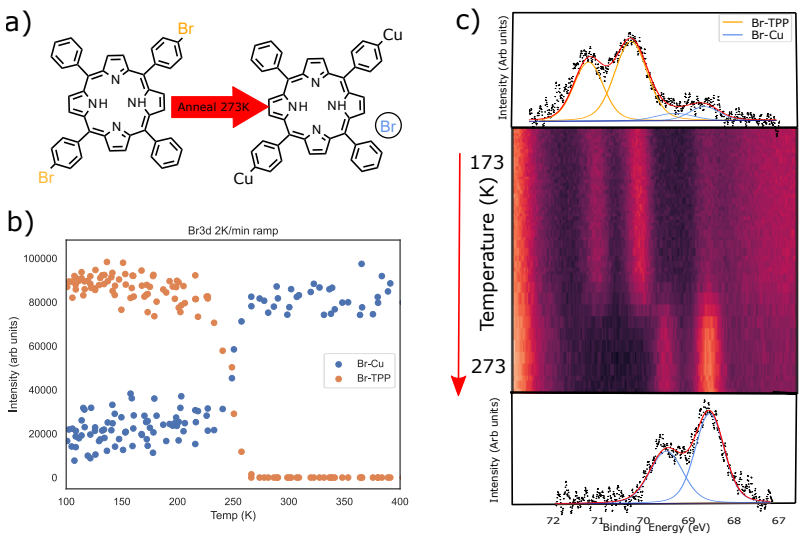

Figure 7.11: a) Reaction scheme showing the dehalogenation of Br_xTPP on Cu(111) following anneal to 273 K, and subsequent metal-organic formation. b) A TP-XPS heat map diagram and XPS peaks fit before and after, showing the change in intensity of XPS peaks in the Br 3*d* region associated with Br on molecule (Orange) and on Cu(111) (Blue). c) Intensity plot for fitted peaks for Br 3*d* signal on and off molecule, against temperature.

For each ramp, the TP-XPS Br 3*d* region is fitted with peaks associated with both Br on the molecule and Br on the surface. Figure 7.11c) features an example heat map, with appended single spectra from the start and end of the ramp. The shift associated with dehalogenation is clearly seen, and the intensity of the respective doublets (measured as area under the fitted peaks) is plotted against temperature, as shown in Figure 7.11b).

An example map for the Br 3*d* and N 1*s* regions on Au(111) and Cu(111) can be seen in Figure 7.12. From these heat maps, it is possible to discern a reaction temperature at which certain changes occur, such as dehalogenation or Br desorption. As mentioned in the introduction to this chapter, this temperature varies with rate of heating; for the remainder of the chapter, I discuss how kinetic parameters can be obtained *via* an Arrhenius analysis of the Br 3*d* and C 1*d* signals.

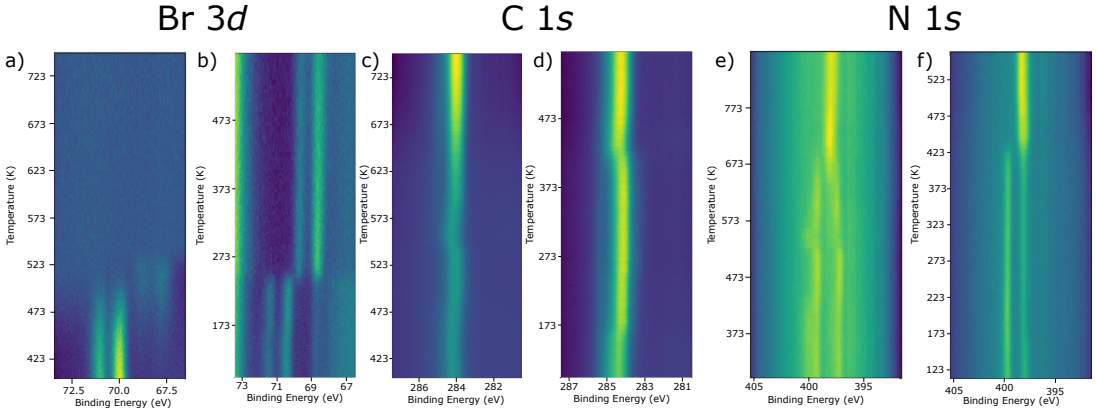

Figure 7.12: Heat maps showing TP-XPS for various regions on both surfaces.a) Br 3*d* Au(111). b) Br 3*d* Cu(111). c) C 1*s* Au(111). d) C 1*s* Cu(111). e) N 1*s* Au(111). f) N 1*s* Cu(111).

7.4 Dehalogenation of Br$_x$TPP on Cu(111)

7.4.1 Introduction

Building on section 7.1.1, here a novel application of Arrhenius analysis to investigate the kinetic properties of reactions is applied to the dehalogenation of Br$_x$TPP on Cu(111), establishing the viability of the use of TP-XPS Arrhenius analysis as a companion technique for TPD and DFT. Lackinger recently proposed a similar approach to TP-XPS in a theoretical analysis [231], using simulated data to discern the viability of determining kinetic properties by least squares fitting decay curves of the form shown in equation 7.3, varying E and A. While the paper concludes that a large number of experiments would be required in order to reduce the error on such a fit, the methodology within this chapter provides a route by which the TPD-inspired multiple ramp rate Arrhenius analysis can be used to narrow the window for possible fitting parameters for E_a and A.

7.4.2 Analysis of a 1st order reaction

As previously described in section 7.2, the Br 3*d* region is fitted with doublet peaks relating to bromine attached to the molecule (Br-TPP) and bromine on-surface (Cu-Br) (Figure 7.11). The intensity of the peaks assigned to these two environments can be plotted as a function of temperature, as shown in 7.13a). By

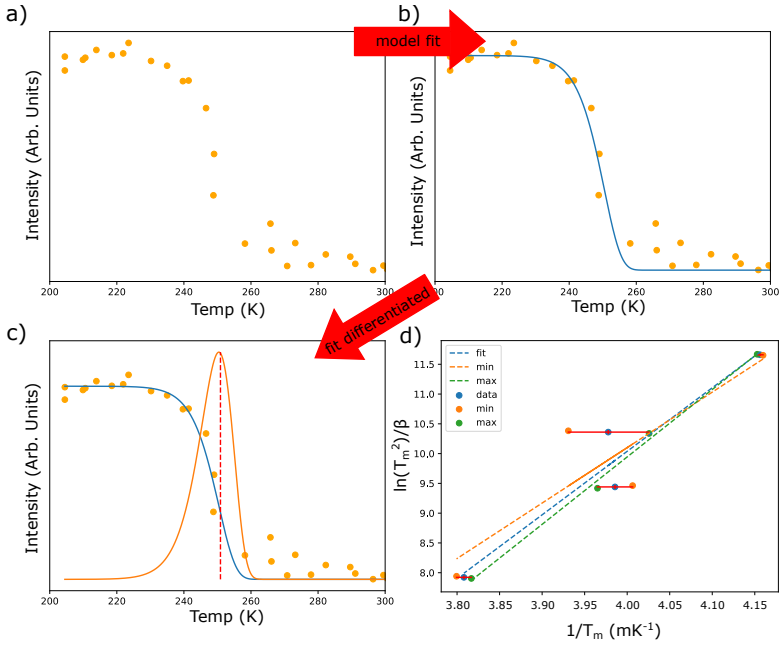

Figure 7.13: a) Intensity plots for Br-TPP intensity decrease for $\beta = 5$ K/min. b) A fit of the form shown in equation 7.3 is fit to the data. c) Fitted curve is differentiated and T_m extracted from the peak position. d) Arrhenius plot for the Br-TPP signal decrease on Cu(111).

considering the dehalogenation of Br_xTPP on Cu(111) as a first order Arrhenius process, the decrease in intensity of the C-Br peaks can be modeled using the relationship between activation energy of the reaction step and the temperature ramp rate (Eqn.7.3). A decay of this form is fitted to the data. The temperature at which the rate of reaction is maximised, T_m, is found when the curve is numerically differentiated with respect to temperature, as shown in Figure 7.13a-c). Once T_m is acquired for a single ramp rate β, this can be repeated for several different ramp rates and information on the variation of T_m with β. As expected, T_m increases with β, and subsequently a straight line plot of $\ln \frac{T_m^2}{\beta}$ against $\frac{1}{T_m}$ can be made, as shown in Figure 7.13d). As discussed in section 7.1.1, the gradient of this curve contains E_a, and the intercept A. Minimum and maximum values are calculated from best fit lines through the data points in their most extreme positions, given the associated error, as shown, resulting in a range of values for E_a and A.

Here I focus on the debromination step of the Ullmann-type coupling reaction of Br_xTPP on Cu(111). We may consider this process *via* three correlated XPS

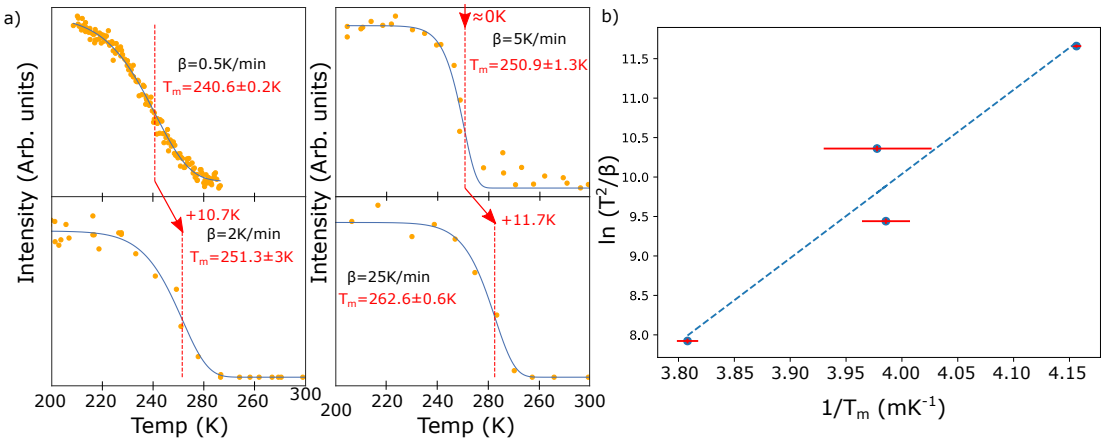

Figure 7.14: a) Intensity plots for Br-TPP intensity decrease for $\beta = 0.5$K/min, 2K/min, 5K/min, 25K/min and subsequent shift in T_m. b) Arrhenius plot for the Br-TPP signal decrease on Cu(111).

signatures: in the Br 3*d* region, Br-TPP decreasing, indicating the scission of the C-Br bond, and Br-Cu signal increasing, indicating the formation of a surface bound bromine species (regions defined in section 7.3.4 Figure 7.11), and within the C 1*s* region, the loss of the higher binding energy shoulder assigned to C-Br may also be considered.

Firstly, I will consider the Br 3*d* region. Table 7.3 shows the resulting E_a and A values obtained from the fitting procedure outlined above (using β of 0.5 Kmin^{-1}, 2 Kmin^{-1}, 5 Kmin^{-1}, 25 Kmin^{-1}) for the Br 3*d* region.

The values for E_a and A obtained for the Br-TPP and Cu-Br TP-XPS measurements are shown in Table 7.3. As shown in Figure 7.11b), it is apparent that the Br-TPP and Cu-Br signals are correlated. It is therefore reasonable to propose

	Br-Cu E_a(eV)	Br-Cu A (Hz)	Br-TPP E_a(eV)	Br-TPP A (Hz)
Min	0.73	1.4×10^{14}	0.80	5.7×10^{15}
Mid	0.89	4.2×10^{17}	0.92	1.6×10^{18}
Max	1.12	2.1×10^{22}	0.98	2.5×10^{19}

Table 7.3: Values for E_a and A for Br 3*d* dehalogenation signals. Minimum and maximum values from best fits through points in the most extreme positions allowed by error in T_m.

that the reaction steps of Br leaving the TPP molecule and forming a new Cu-Br bond are simultaneous. This is further supported by the fact that the calculated activation energies, obtained from the change in these two signals, yield similar activation energies (in the range 0.73-1.12 eV). These experimental values are close to agreement with DFT derived values in the literature (∼0.7 eV). [93, 232]

One could consider an alternative approach to acquiring E_a and A by fitting the TP-XPS data, detailing the change in peak intensity, with the equation of the form in Eqn. 7.3 and allowing E_a and A to vary. This is the approach described by Lackinger, [231] however in this chapter the method differs. I apply such an approach while limiting the parameter space to only allow for values of E_a and A permitted by the Arrhenius analysis. A grid search algorithm where E_{a} and A were varied independently, within the range calculated in the Arrhenius plot, was applied and value for the 'goodness of fit' (root mean squared deviation (RMSD)) obtained. The RMSD of each of these combinations is plotted in a 2D map of the form shown in Figure 7.15a). In these heat maps, the x-axis is a range of A values and the y-axis is a range of E_a values. Each point on the grid represents the RMSD fit quality of a curve of the form shown in Eqn.7.3 with the data, with a combination of E_a and A values indicated by the X-Y coordinates of that position in the grid. A smaller value represents a better fit and the limit has been capped at 1. It is therefore apparent that there exists a wide range of pairs of E_a and A which provide reasonable fits to the TP-XPS data.

Let us consider the consequences of performing a least squares fit of the form shown in Eqn.7.3 to the data, applying no constraints to the range of values for E_a and A. This would result in an infinite range of combinations of E_a and A values that would provide acceptable fits to the data. Hence, we can initially consider a range of reasonable values; 0-2 eV for E_a (positive, in line with DFT calculations) and 10^1-10^{20} Hz (positive, ranging from ≈ 0 to significantly above the standard value of 10^{12} Hz).

While a minimum can be identified from these large grids, the value of the "best fit" alone in identifying the kinetic properties of the reaction is tenuous as good fits can be obtained from a wide range of possible combinations. This was noted by Lackinger in his theoretical examination of the technique [231], but

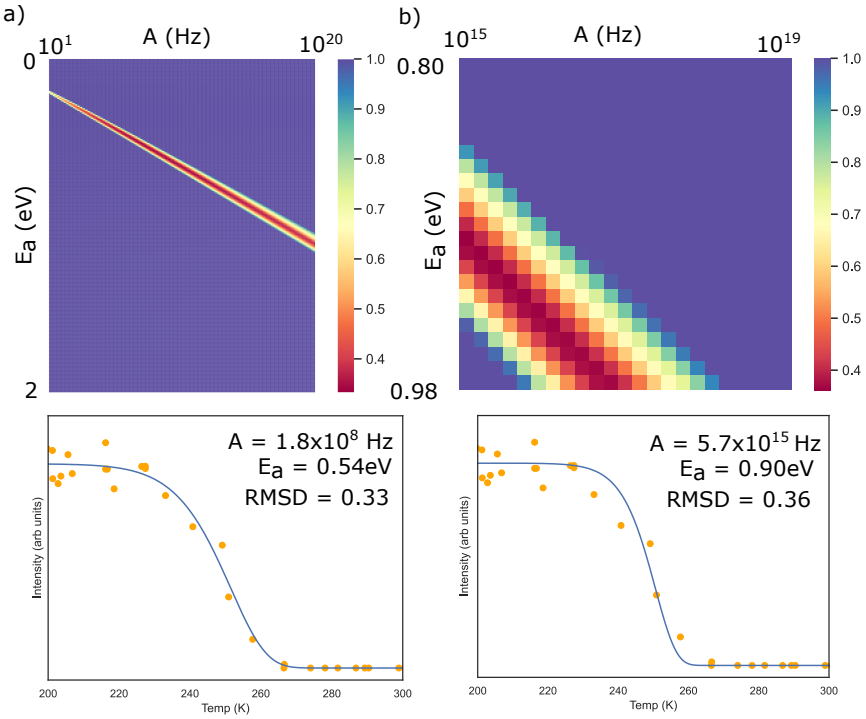

Figure 7.15: a) 2D map showing the RMSD for fits created by different combinations of values of E_a and A (with the range 0-2eV and 10^1-10^{20} Hz respectively), and the resulting best fit, for the Br-TPP Br 3d signal with $\beta = 2$ Kmin^{-1}. b) As for a), but with a limited range of E_a and A as determined from the Arrhenius analysis (E_a = 0.8-0.98 eV and $A = 5.7 \times 10^{15}$-2.5×10^{19})

by using the narrower range of values produced by the Arrhenius analysis, the quality of this range can be assessed - simplistically, if there are no good fits within the range predicted by Arrhenius analysis, then the model does not fit the data. Figure 7.15b) demonstrates that the narrower parameter windows can provide a fit of extremely high quality, closely comparable to the best found in a wider range; the RMSD value of the 'best fit' for the full range and the 'Arrhenus range' can be compared and seen to be very similar. Crucially, fits within an Arrhenius range yield average values of E_a (0.92±0.02 eV) and A ($5\times10^{16\pm1}$ Hz) which are in good agreement with expected values.

7.4.3 2nd Order Reaction Steps

For the majority of cases discussed above, the TP-XPS data showing the debromination step of the Ullmann-type coupling reaction is in good agreement with a

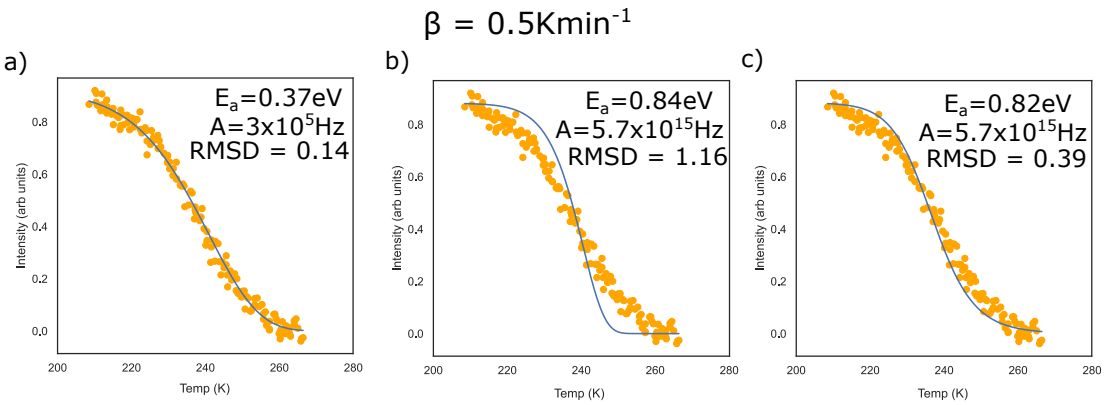

Figure 7.16: Fits to the $\beta = 0.5$ Kmin^{-1} Br$_x$TPP dehalogenation signal using different models and parameters. a) Uses a first order Arrhenius model, with a broad range of possible values. b) Also uses the first order Arrhenius model, albeit with the narrower range of values provided by the Arrhenius plot. c) Uses the same narrow window, but using the second order Arrhenius model.

first-order reaction process. The change in intensity of the Br 3d peaks is well modelled by equation Eqn.7.3 - indicating that the reaction step being considered appears to only depend upon the concentration of the unreacted Br$_x$TPP molecule. For the $\beta = 2, 5, 25$ Kmin^{-1} rates, the form looks good, but in the instance of the $\beta = 0.5$ Kmin^{-1} rate, however, the slope of the decay is too steep when utilising the first-order Arrhenius model within the narrower range of values. As shown in Figure 7.16a), the 1st order model works well when E_a and A can vary freely, but when restricted to the narrower range provided by the Arrhenius analysis, the model cannot account for the shallow slope. While the 1st

β(Kmin^{-1})	1st order wide range RMSD	1st order Arrhenius range RMSD	2nd order narrow range RMSD
0.5	0.13	1.17	0.39
2	0.33	0.36	0.35
5	0.10	0.10	0.09
25	0.02	0.03	0.03

Table 7.4: RMSD values for best fits using different models and fitting parameter windows for the Br-TPP decrease from the Br 3d region.

order model can indeed fit the data, the E_a value being so much lower than other cases and the A value being far below that expected at even room temperature indicates that this model is inadequate to describe the system. Grossman *et al.*, having performed a similar experiment, suggest treating the process of dehalogenation as a second order process whereby diffusing surface adatoms act as the second reaction species. [92] Taking the second order Eqn. from Lord *et al.* : [16]

$$\frac{d[X]}{dt} = -A[X]^n e^{\frac{-E_a}{RT}}, \tag{7.7}$$

where n is reaction order, we can apply this model to the $\beta = 0.5$ Kmin^{-1} data, as shown in Figure 7.16c). As can be seen, this results in a significantly better fit, and the fit is better or equal at all values of β (table 7.4). It should be noted that a second order process that occurs in the presence of sufficient quantities of one of the two rate limiting elements will appear as a first-order reaction; it is possible that the 'faster' ramp rates lead to an abundance of one of the two species (in effect leading to a 'steady state' of the concentration of this reactant). If the second participant in the dehalogenation reaction is indeed metal adatoms, this would imply that for ramp rates $\beta = 2$, 5, 25 Kmin^{-1}, metal adatoms are available in such abundance that the second order reaction becomes a pseudo-first order reaction. Conversely, this means for the $\beta = 0.5$ Kmin^{-1} ramp, this is not the case. The most likely reason for this is that because at lower ramp rates, the temperature at which the maximum reaction rate occurs is lower, causing lower adatom availability. It is also possible that non-uniform sample preparation could be the cause; while the depositions were very similar, the coverage on the $\beta = 0.5$ Kmin^{-1} ramp is higher than the rest (see Figure 7.17). The number of available adatoms could also be affected by the stochastic nature of sputter/anneal cycles, with individual preparations creating a surface with more or less step-edges (as step-edges are the most likely source of adatoms, a reduction in step-edge features is expected to correlate with a reduction in adatom availability).

Changing to the second order model has implications for the Arrhenius plot as the coverage now features in the linearised form the Arrhenius derived relationship (obtained from Eqn. 7.7); while values for T_m do not change, the term $\ln \frac{T_m^2}{\beta}$ becomes $\ln \frac{T_m^2[X]}{\beta}$. This alteration does not affect the value of the gradient (in

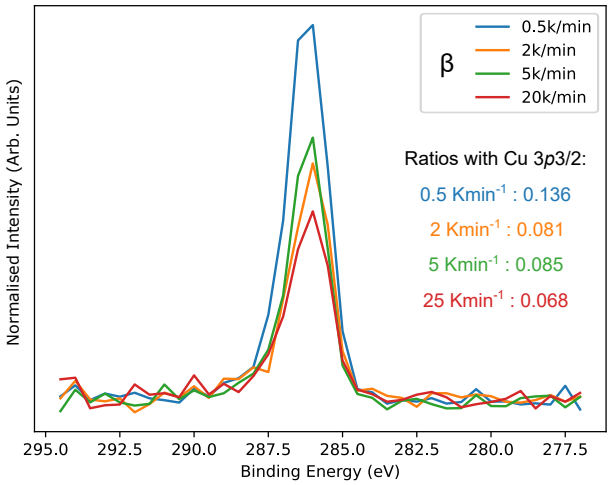

Figure 7.17: The C 1s region of overview XP spectra, normalised with respect to the Cu 3p split peak on the same overview, for each ramp rate.

the cases where all initial concentrations are equal), leading to identical values of E_a, the position of the line is shifted in y, affecting the intercept (and thus A). Figure 7.18a) showcases the impact of varying the coverage on the Arrhenius plot. Changing the coverage from 1 to 0.1 increases the A value by one order of magnitude, perhaps unsurprising given that the coverage term is included multiplicatively. If each of the samples were prepared at a significantly different initial coverage, the points would lie on a different line, affecting the gradient and therefore the calculated values of E_a and A. These samples were prepared uniformly (as seen in Figure 7.18), with an expected coverage of around 0.3-0.6 ML based on STM data, shifting the range of A values from 5.7×10^{15}-2.5×10^{19} Hz to a maximum of 9.6×10^{15}-4.2×10^{19} Hz for the Br$_x$TPP decrease signal, for these purposes considered negligible. Another consideration relating to coverage when utilising a second order model is the influence of the initial coverage on the shape of the decay. In order to determine the impact of this feature on values of E_a, a grid search algorithm was established to vary both E_a and initial coverage at a set value of A. Example heat maps for three different A values are shown in Figure 7.18b). As can be seen, varying coverage between 0.1 and 1 results in very little variation in E_a, with each A value producing an E_a variation of 0.05 eV. Given these effects have negligible impact, I will use the range provided by the rate plots for first and second order models.

Applying the grid search technique with the second order model, and selecting

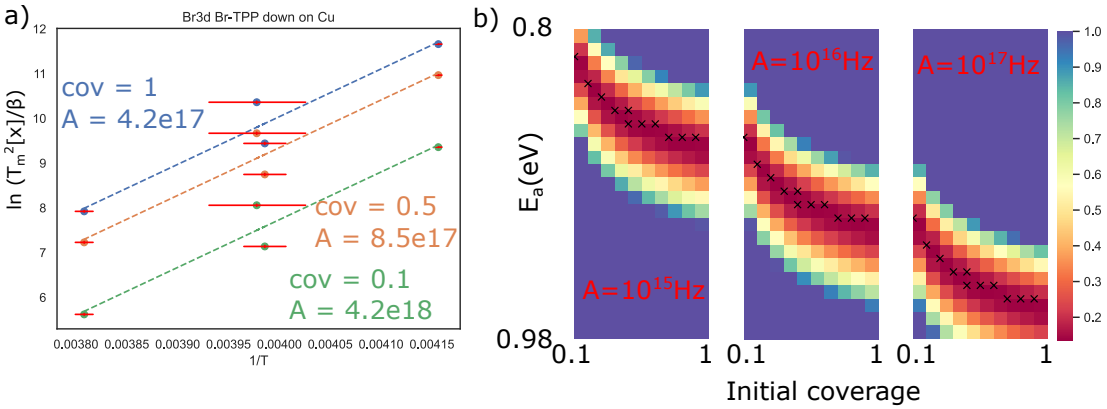

Figure 7.18: a) Shows the influence of changing initial coverage on Arrhenius plot y position. b) Heat maps showing RMSD values for different initial coverages and values of E_a at different values of A. The black crosses mark value combinations providing an RMSD value within ±10% of best fit.

for value combinations providing an RMSD value within ±10% of best fit, as shown in Figure 7.19, we can narrow our range of possible parameters yet further: each ramp rate has a very similar window of acceptable results. These results, displayed in Table 7.5, demonstrate remarkable consistency. Averaging the results gives these values: 0.91 eV with ±0.03 eV as the error on the mean, with A of $4.1\times10^{16\pm1}$ Hz. This calculated value is slightly higher than the literature value of 0.7 eV, but overall the technique is able to provide a precise result with small errors, albeit at a large time cost. [93, 232]

β(Kmin^{-1})	Ea(eV)	A range (Hz)
0.5	0.84 ±0.02	5.7×10^{15}-3.8×10^{16}
2	0.93 ±0.06	5.7×10^{15}-8.1×10^{17}
5	0.93 ±0.06	5.7×10^{15}-1.0×10^{18}
25	0.94 ±0.05	1.7×10^{16}-8.1×10^{17}

Table 7.5: E_a and A value ranges from grid search using 2nd order Arrhenius model within parameters of Arrhenius plot, for the Br-TPP decrease from the Br 3d region.

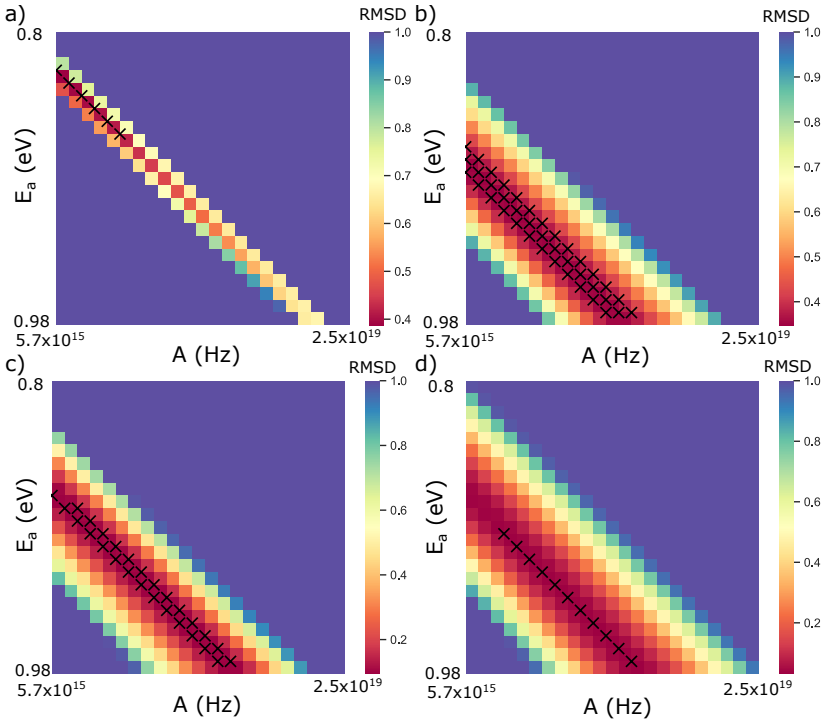

Figure 7.19: Grid search heat maps showing the RMSD for fits of the second order Arrhenius model to the Br-TPP decrease in the Br 3*d* region, within the value range provided by the Arrhenius plot. The black crosses mark value combinations providing an RMSD value within ±10% of best fit. a) $\beta = 0.5$ Kmin^{-1} b) $\beta = 2$ Kmin^{-1} c) $\beta = 5$ Kmin^{-1} d) $\beta = 25$ Kmin^{-1}.

7.4.4 A Consideration of Enthalpy and Entropy: The Eyring Model

As previously described in section 7.3.3, the C 1*s* region contains a higher binding energy shoulder associated with the C-Br bond, and a lower binding energy shoulder associated with the C-Cu MOF formation. Hence, isolating and monitoring the behaviour of these elements could provide further insight into the dehalogenation reaction. The C 1*s* environment for Br$_x$TPP peak assignment is as shown in Figure 7.20a-b). The development of the C 1*s* region over the course of a full ramp can be seen in Figure 7.20c). Changes in the position and intensity of the different peaks during the course of the ramp means that fitting is a complex and multi-stage process. During the full ramp, several reaction stages are expected, changing the intensities of the different peaks. Based on STM data previously discussed in section 7.3, the expected changes to the molecule are as

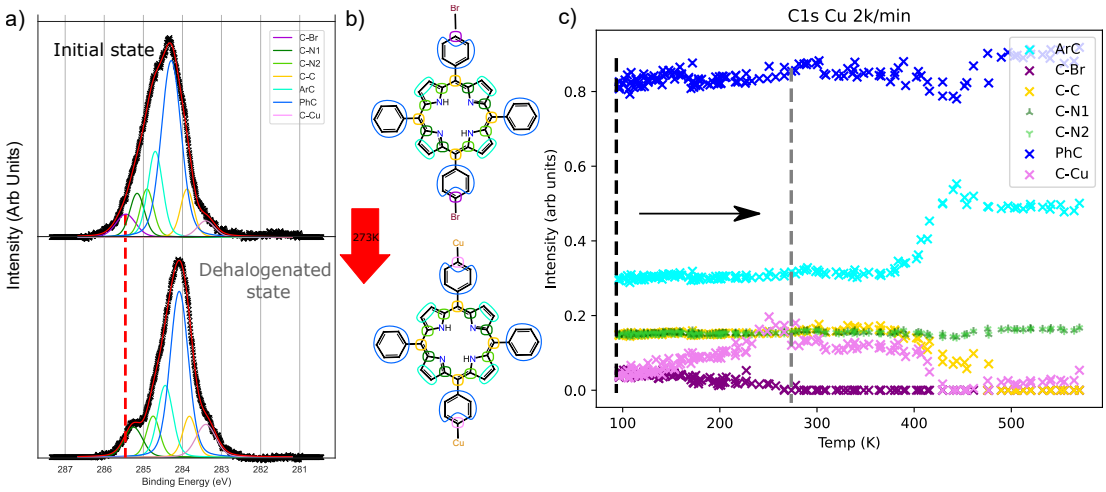

Figure 7.20: a) XP spectra for the C 1s region of Br$_x$TPP on Cu, as deposited and following 273K anneal. b) Molecular diagram of Br$_x$TPP with labelled regions associated with different peaks in the C 1s XPS region. c) Shows the intensity of different peaks in the C 1s region varying with temperature for the $\beta = 2$ Kmin^{-1} ramp.

follows: dehalogenation, formation of organometallic intermediate, ring-closing, Ullmann-type coupling, and metallation. Having fit high resolution XPS, as described in section 7.3, at different stages of the anneal, peak assignments need to be adjusted in stages in order to fit the data and adjust to the changing environments. In order to accurately model the system, peak areas are locked relative to the number of carbon atoms in each environment, and assigned a binding energy range. As over the course of the ramp, the peaks change, the areas are selectively unlocked as fitting parameters, allowing the peaks to shift in line with the data. When these changes are made is at the discretion of the investigator, however with an understanding of the system and monitoring of fit quality with each stage it becomes clear when the model needs to be adjusted. While this technique may seem overly prescriptive, with well justified peak assignments and sufficiently distinct peaks, it is possible to discern reaction signals from even as complicated a system as this.

Decreasing intensity of the C-Br signal, and conversely increasing intensity of the C-Cu signal, are both signatures of dehalogenation in much the same way as the Br 3d signals, albeit more challenging to extract. The dehalogenation and organometallic formation are relatively straightforward to assign, with the

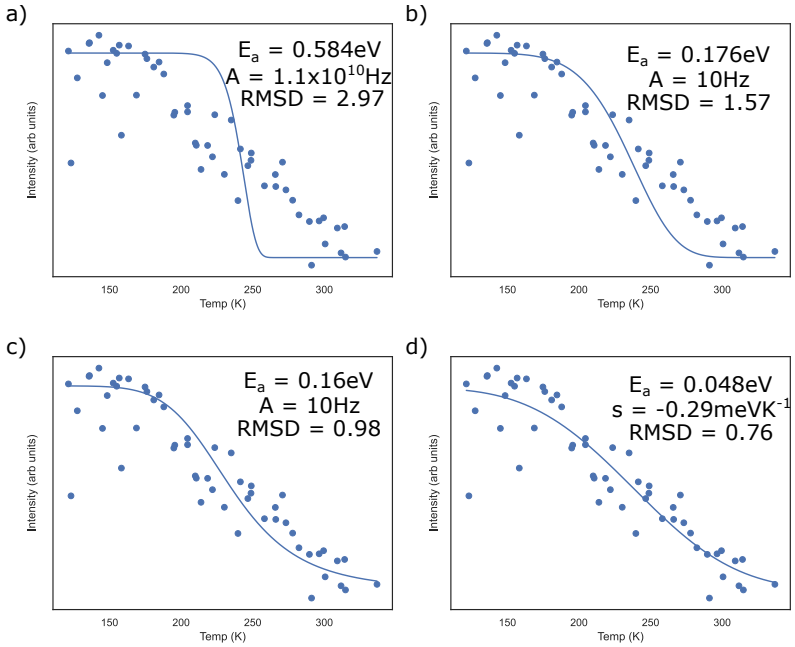

Figure 7.21: Different models and grid search windows for the decreasing intensity of the C 1s Br-C signal for the $\beta = 5$ Kmin^{-1} ramp. a) 1st order Arrhenius model with "reasonable" values for A. b) 1st order Arrhenius model with wide range of values for A. c) 2nd order Arrhenius model with wide range of values for A. d) 2nd order Eyring model with calculated A and range of S values.

aforementioned low and high binding energy shoulders increasing and decreasing respectively. Another possible reaction signal in the C 1s data is the increase in the peak assigned to aromatic carbon, and accompanying decrease in C-C peak intensity at around 400K. This behaviour could be associated with ring closing, as a homogenisation of these environments would be expected. In future experiments, with higher resolution XPS or perhaps a target molecule with a less complex C 1s environment, it should be possible to utilise these measurements to discern reaction steps like ring closing. For this section, I will look at the declining Br-C signal, as it is the most obvious change and pairs well with the Br 3d dehalogenation signals.

To extract the variation in intensity for this peak, the same technique was utilised as described in section 7.4.2. Figure 7.21 shows the intensity data captured for the decreasing C 1s Br-C signal intensity for the $\beta = 5$ Kmin^{-1} ramp. Firstly, I attempt to fit such curves as a first order reaction. Running a grid search algorithm with reasonable parameters (E_a:0-2 eV, A: $1 \times 10^{10} - 10^{22}$ Hz) for a first

order reaction results in the poor fit shown in Figure 7.21a), indicating that this is not a first order reaction. Expanding the search parameters such that I include "unreasonable" A values (1^{10} the lower limit) improves the fit (Figure 7.21b)), but results in an exceptionally low attempt frequency, which is non-trivial to interpret. Considering a second order model improves the fit, (Figure 7.21c)) but still suffers the same issue with low attempt frequency. Hence, we now consider if there is a realistic origin for such a low attempt frequency.

One approach is to consider the influence of entropy. The Arrhenius equation is an empirical relationship, developed through observation. As such, pre-exponential factor A, often referred to as the attempt frequency, is an empirical relationship between the temperature and rate coefficient. In essence, it describes the physical reality that increasing the temperature of a system increases the rate of reaction, and has been calculated to be roughly 1×10^{12} Hz at room temperature. The Eyring equation is of similar form to the Arrhenius equation, albeit based on statistical thermodynamics rather than empirical observation. The Eyring equation is as follows:

$$k = \frac{k_B T}{h} e^{\frac{-\Delta H}{k_B T}} e^{\frac{\Delta S}{k_B}}, \tag{7.8}$$

where k is the reaction rate constant, S is the entropy of activation, and ΔH is enthalpy change, for our purposes closely analogous to the activation energy E_a. Put into a similar format as described earlier, for a TP-XPS rate equation, it takes this form:

$$\frac{d[X]}{dT} = -\frac{1}{\beta} \frac{k_B T}{h} [X]^n e^{\frac{-\Delta H}{k_B T}} e^{\frac{\Delta S}{k_B}}. \tag{7.9}$$

Previously, Ullmann-type coupling has been described with the Eyring equation when explaining the difference in dehalogenation rate on Au(111) and Ag(111); Fritton *et al.* utilise a form of the Eyring equation at thermodynamic equilibrium to explain a slower rate of dehalogenation on Au(111). [95]

Figure 7.21d) demonstrates the increased fit quality possible when implementing an Eyring model. Using the Eyring model, two parameters are varied, ΔH and ΔS, in much the same way as E_a and A could be varied with the Arrhenius model. Given a broad value window for ΔH (0-2 eV, chosen to mirror E_a values from Arrhenius analysis) and ΔS ($\pm$ 5 meVK^{-1}, chosen as Fritton *et al.*

found the entropy contribution in the order of meV [95]), a grid search was conducted for combinations of values creating the best fit with the data, using the RMSD as described in section 7.4.2. The fit gains a better RMSD value than any Arrhenius model, and provides an explanation for the low A value; comparing equations 7.7 and 7.9, we can discern that $A = \frac{-\Delta H}{k_B T} e^{\frac{\Delta S}{k_B}}$. When $S = 0$, we regain the standard value for A; however, when this is not the case, the value of prefactor A can be affected. In the case of the C 1s Br-C signal, the best fits were obtained with an exceptionally low prefactor. This is only possible with the incorporation of the $e^{\frac{\Delta S}{k_B}}$ term, and only for negative values of ΔS. For this ramp, factor $\frac{k_B T}{h} = 4.8 \times 10^{12}$ Hz, in line with expectations for the A value, and factor $e^{\frac{\Delta S}{k_B}} = 2.4 \times 10^{-15}$ Hz. When considered within the context of transition state theory, a negative change in entropy indicates that there is a reduced number of degrees of freedom when moving from the initial to transition state. Such a reduction could come from the confinement of an adatom species, forming a complex with a molecule prior to debromination. Previously, entropic effects have been observed to alter the rate of diffusion for coupled porphyrins, and has been attributed to a reduction in flexibility at the transition state (a negative change in entropy). [233]

Returning to the Br 3d TP-XPS data, we can replace the Arrhenius fits with the Eyring fits. In all cases, the entropy term obtained is 'small' (<0.1 meV) and positive (which would have the effect of increasing the perceived attempt frequency), as shown in Table 7.6. The results from this table clearly demonstrate the difference in entropy change between the C 1s and Br 3d signal in the Eyring model. In all cases for Br 3d signals, the entropy term is smaller and positive, having the effect of increasing the apparent attempt frequency. In the case of the C 1s signals, the entropy term is larger and negative. The $\beta = 0.5$ Kmin^{-1} ramp is not included in these fits, as the data does not capture the pre-change constant intensity region necessary for appropriate modelling. Initially, the change in C 1s and Br 3d signals was attributed to a single reaction step, this step being the cleavage of the C-Br bond. However, it is well established that Ullmann-type coupling reactions progress *via* a MOF intermediate. The intermediate is known to be stable on Ag(111) and Cu(111), and less experimental examples on

Au(111) (further information in section 2.2.2). It is also generally accepted that these structures contain adatom species. [191] Therefore, I postulate that the cleavage of the C-Br bond is a two-step process. Firstly involving the interaction of an adatom with the C-Br bond, and a second step which involves the breaking of the bond and subsequent removal of the Br from the molecule and onto the surface. A similar process has been suggested by Grossman *et al.*(see Figure 2.8). [92] My model of this process is shown in Figure 7.22.

We can see this two-step process by considering the TP-XPS data for the intensity change in C 1s (C-Br bond) and Br 3d (B-TPP and Cu-Br) for BrxTPP on Cu(111): Figure 7.23. This figure shows the Br 3*d* Br-TPP and Br-Cu and C 1*s* Br-C signal intensity changing for β = 0.5, 2, 5, 25 Kmin^{-1}. In each of these, the C 1*s* Br-C signal begins to decrease at a lower temperature than the Br 3*d* signals, or in the case of the 0.5 ramp is progressing at a greater rate at an earlier temperature. For the Br 3*d* signal, I observe that the decrease in Br-TPP (orange) and increase in Cu-Br (green) mirror each other and are therefore describe the same process (analysis above shows that we get the same activation parameters when we analyse the Br-TPP and Cu-Br signals). The C 1*s* C-Br signal clearly differs in form. The clear drop in C 1*s* C-Br intensity in the β = 2

β(Kmin^{-1}), region	2nd order Arrhenius RMSD	2nd order Eyring RMSD	ΔH (eV)	ΔS (meVK^{-1})	$e^{\frac{\Delta S}{k_B}}$ (Hz)
0.5, Br 3*d* Br$_x$TPP	0.39	0.35	0.80	0.03	10^1
2, Br 3*d* Br$_x$TPP	0.35	0.35	0.80	0.02	10^1
5, Br 3*d* Br$_x$TPP	0.09	0.08	0.82	0.04	10^2
25, Br 3*d* Br$_x$TPP	0.03	0.03	0.94	0.09	10^5
2, C 1*s* BrC	0.007	0.005	0.02	-0.26	10^{-14}
5, C 1*s* BrC	0.98	0.76	0.05	-0.29	10^{-14}

Table 7.6: RMSD and ΔS values for best fits from 2nd order Arrhenius and Eyring equations. The quoted ΔH and ΔS values are taken from the mid-point of the range of value combinations providing a fit within 10% of the lowest RMSD value.

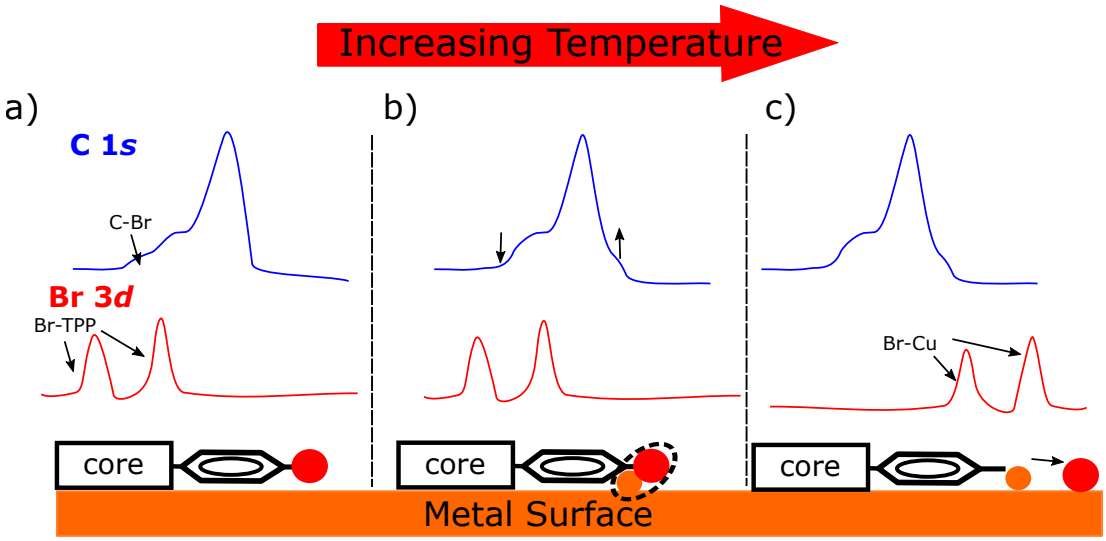

Figure 7.22: Diagram of the proposed model for dehalogenation of Br_xTPP on Cu(111), with idealised XPS spectra showcasing characteristic changes expected at each reaction stage. a) Shows the intact molecule as deposited on the surface. b) Shows the Bromine atom forming a metal-organic coordination with a surface adatom, causing the Br-C shoulder to decrease, and Br-Cu shoulder to increase in the C 1s region. c) Shows the dehalogenated molecule forming a metal-organic coordination with the surface adatom, and the bromine atom separately adsorbed onto the Cu(111) surface. This change is seen in the Br 3d region as the split peak shifts to a lower binding energy following removal from the molecule.

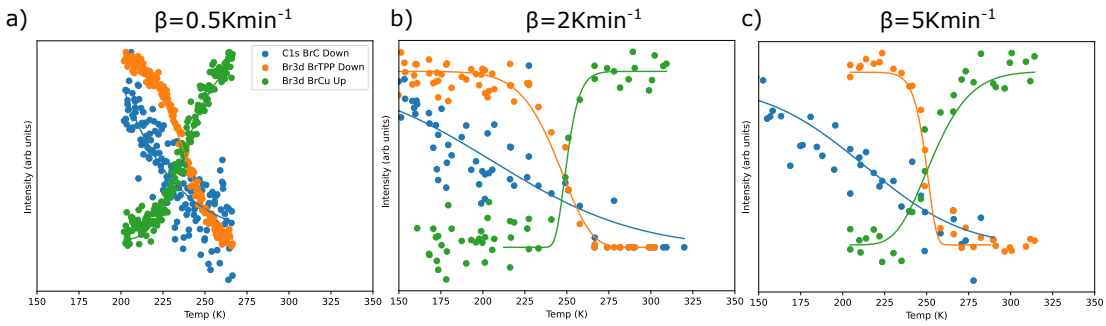

Figure 7.23: C 1s and Br 3d dehalogenation signals overlaid for different β.

and 5 Kmin^{-1} ramps occurs at a lower temperature than the decrease in the Br 3d Br-TPP signal, supporting the assertion that the changes in the C 1s signal relate to the first step in a two-step process. At these rates, this change occurring before the Br 3d change aligns well with the observed 1st order behaviours of these two ramp rates. For the 0.5 Kmin^{-1} rate, we see an overlap between the change

in intensity for C 1s and Br 3d, which potentially explains why for this slower ramp rate, the Br 3d data only achieves a satisfactory fit with 2nd order reaction kinetics.

This information supports the following model: that the dehalogenation of Br_xTPP on Cu(111) is indeed a two-step reaction. The initial step in this process is the capture of Cu adatoms, as indicated by the decreasing C-Br peak intensity in the C 1s region : ΔH = 0.02-0.05 eV, ΔS=-0.26-0.29 meVK^{-1}. This extremely low enthalpic barrier and negative change in entropy (linked to adatom capture and subsequent loss of freedom) clearly distinguish this stage from the subsequent stage witnessed in the Br 3d region. The cleavage of the C-Br bond, as evidenced by the Br 3d signals, is this second stage : ΔH = 0.84±0.03 eV, ΔS=0.05±0.02 meVK^{-1}. The very small, positive entropic contribution clearly differentiates from the initial stage, and the energy barrier is similar to that seen in DFT models in the literature. [93, 232]

The relationship between these two reaction steps can be observed for the different ramp rates investigated. At faster rates ($\beta > 0.5$ Kmin^{-1}), adatom capture occurs before Br-C cleavage, causing the reaction to behave as a pseudo-first order process. At slower rates, the two processes overlap, causing the reaction to change in character to a second order reaction. Crucially, the role of entropy in the first reaction step is indicated by a low attempt frequency (as compared to expected values). By considering the Eyring formulation of an activated process we may understand this reduced attempt frequency in terms of a significant reduction in entropy at the transition state: the reduction in entropy is driven by the loss of conformational flexibility and degrees of freedom during adatom capture.

7.5 Conclusion

This chapter shows that the simplistic, but often posed, question "at which temperature does a reaction occur?" is unhelpful (despite the fact that this is often the only parameter reported in on-surface studies of reactions). Reaction progress is significantly affected by the rate of heating, shifting maximum rate of reaction

temperature T_m. A more suitable way to define reaction barriers for on-surface processes is therefore required. I propose that characterisation in terms of the Arrhenius parameters A and E_a, or the entropic and enthalpic parameters from the Eyring formulation of transition state theory is required.

Here, I present proof of concept for adaptation of TPD Arrhenius analysis to enable TP-XPS characterisation of systems. By capturing temporally resolved XPS data, and assigning changes in specific peak intensities to particular chemical reactions, we can apply Arrhenius-based analysis and acquire data on the pre-factor A and activation energy E_a. Specifically, we propose that the dehalogenation of Br_xTPP on Cu(111) is a two-stage reaction. I propose a mechanism of adatom capture as the rate limiting step, affecting the rate of decay in instances where the ramp rate β is too low. Ultimately, this technique provides a spectroscopic doorway into elusive kinetic properties of on-surface reactions, and as in the case described here, can reveal previously unknown multi-stage elements to reactions. Currently, most activation energies for on-surface reactions are modelled with DFT, rather than based on experimental observation; this technique can be used to confirm or disprove such models and provide insight into new reaction pathways.

Chapter 8

Conclusions

The work detailed in this thesis builds upon the state-of-the-art, and expands, scientific understanding within the field of on-surface synthesis. Primarily, the work aims to develop a better understanding of the synthetic pathways, allowing efficient and effective creation of target molecules, either on-surface or in combination with in-solution chemistry.

The first experimental chapter, chapter 4, focussed on the polymerisation of a DPP based precursor monomer functionalised with aryl halide groups and hexyl chains. The influence of surface-induced chirality and aklyl side chains of the molecule on the as-deposited self-assembled structure was characterised through STM, with a model created to fit the measured lattice dimensions whilst following typical self-assembly motifs and obeying steric limitations. Upon annealing, an Ullmann-type coupling reaction was observed, and the influence of the self-assembled structure on the extended polymer network was considered. Further annealing resulted in degradation of the molecule, resulting in a degeneration of the ordered surface state and eventual cross-linking. A key aspect of this chapter is that useful conclusions on the structure of a molecular system can be inferred from details of the molecular lattice and molecular modelling, without relying on sub-molecular resolution.

In the second experimental chapter, chapter 5, the electrospray deposition method is explored as a route towards using surface analysis techniques on larger, more complex molecules too thermally labile to be deposited *via* thermal sublimation. The character and size of the deposition spot is examined, with spectro-

scopic and STM data combining to provide insight on the spread of material. Following this, the STM characterisation of several uniquely synthesized porphyrin nanorings is described, with information on the flexibility of these molecules estimated based on morphological distortion.

In chapter 6, electrospray deposition is once again utilised, this time in order to facilitate the combination of in-solution and on-surface reactions to create novel synthetic pathways. A porphyrin nanoribbon precursor, synthesised in solution, was transferred to a surface and subsequently annealed; this allowed intra-porphyrin graphitic sections to form, creating the targeted porphyrin-graphene nanoribbon. This step was not possible in solution, nor was the formation of the porphyrin nanoribbon *via* on-surface coupling of monomer units, proving the unique versatility of combining the two techniques, with the assistance of electrospray deposition. The nanoribbon species were also interrogated with spectroscopic techniques such as X-ray standing wave (XSW) and near-edge X-ray absorption fine spectroscopy (NEXAFS). These studies informed our understanding of the adsorption of the molecule and evolution of the system during the graphene formation.

Finally, the last experimental chapter, chapter 7, covered a novel experimental approach towards determining the kinetic properties of a prototypical on-surface chemical reaction, namely the Ullmann-type coupling of Br functionalised tetraphenyl porphyrin (TPP) on Cu(111). *via* the use of temperature programmed XPS (TP-XPS), Arrhenius analysis was performed in order to extract activation energy E_a and attempt frequency. By developing this approach to consider the Eyring formulation of transition state theory parameters for the entropic and enthalpic barriers were ascertained. The investigation led to the consideration of the Ullmann-type coupling reaction on Cu(111) as a second order reaction, with Cu(111) adatoms performing the role of a rate limiting reactant species. This aspect of Ullmann-type coupling is oft-debated, and the novel method described in this chapter provides an avenue of insight into this common question. Alongside this, a comparison of the reaction progress on Cu(111) and Au(111) was presented, comparing the stepwise XPS and NEXAFS for the species on each surface.

Overall, the work contained in this thesis furthers the understanding of on-surface reactions, from the topological characterisation of individual species at different stages of a reaction, to the marriage of in-solution and on-surface reaction pathways, concluding with a novel method for obtaining experimental insight into bond enthalpy, a potentially more useful metric for application in the field of molecular synthesis than the oft-cited reaction temperatures that permeate the literature.

On-surface synthesis is an area of burgeoning importance, and the techniques applied in combination as described in this thesis can be implemented to augment our understanding of processes key to controlling the efficiency and selectivity of a range of on-surface processes.

Bibliography

[1] G Binnig, H Rohrer, Ch. Gerber, and E Weibel. 7 X 7 Reconstruction on Si(111) Resolved in Real Space. *Phys. Rev. Lett.*, 50(2):120–123, 1983.

[2] Eigler D. M. and Schweizer E. K. Positioning single atoms with a scanning tunnelling microscope. *Nature*, 344:524–526, 1990.

[3] Jinming Cai, Pascal Ruffieux, Rached Jaafar, Marco Bieri, Thomas Braun, Stephan Blankenburg, Matthias Muoth, Ari P. Seitsonen, Moussa Saleh, Xinliang Feng, Klaus Müllen, and Roman Fasel. Atomically precise bottom-up fabrication of graphene nanoribbons. *Nature*, 466(7305):470–473, 2010.

[4] Adam Sweetman, Neil R. Champness, and Alex Saywell. On-surface chemical reactions characterised by ultra-high resolution scanning probe microscopy. *Chemical Society Reviews*, 49(13):4189–4202, 2020.

[5] Leo Gross, Z L Wang, D Ugarte, Fabian Mohn, Nikolaj Moll, W a Heer, P Vincent, Peter Liljeroth, C Journet, Gerhard Meyer, V T Binh, M Poot, H S J Van Der Zant, A Aguasca, A Bachtold, K Kim, A Zettl, P Hung, H W C Postma, M Bockrath, X Blase, and S Roche. The Chemical Structure of a Molecule Resolved by Atomic Force Microscopy. *Science*, 325:1110–4, 2009.

[6] Matthew Edmondson and Alex Saywell. Molecular Diffusion and Self-Assembly: Quantifying the Influence of Substrate hcp and fcc Atomic Stacking. *Nano Letters*, 22(20):8210–8215, 2022.

[7] Holly Walen, Da Jiang Liu, Junepyo Oh, Hyunseob Lim, J. W. Evans, Yousoo Kim, and P. A. Thiel. Self-organization of S adatoms on Au(111): $\sqrt{3R30°}$rows at low coverage. *Journal of Chemical Physics*, 143(1), 2015.

[8] Marco Bieri, Manh-Thuong Nguyen, Oliver Gröning, Jinming Cai, Matthias Treier, Kamel Aït-Mansour, Pascal Ruffieux, Carlo A Pignedoli, Daniele Passerone, Marcel Kastler, Klaus Müllen, and Roman Fasel. Two-Dimensional Polymer Formation on Surfaces: Insight into the Roles of Precursor Mobility and Reactivity. *Journal of the American Chemical Society*, 132(46):16669–16676, 2010.

[9] Albertus P.H.J. Schenning and E. W. Meijer. Supramolecular electronics; nanowires from self-assembled /*pi*-conjugated systems. *Chemical Communications*, (26):3245–3258, 2005.

[10] Yuning Li, Prashant Sonar, Leanne Murphy, and Wei Hong. High mobility diketopyrrolopyrrole (DPP)-based organic semiconductor materials for organic thin film transistors and photovoltaics. *Energy and Environmental Science*, 6(6):1684–1710, 2013.

[11] Fabian D. Natterer, Kai Yang, William Paul, Philip Willke, Taeyoung Choi, Thomas Greber, Andreas J. Heinrich, and Christopher P. Lutz. Reading and writing single-atom magnets. *Nature*, 543(7644):226–228, 2017.

[12] Jean-Marie Lenh. Supramolecular Chemistry - Scope and Perspectives - Molecules - Supermolecules - Molecular Devices. *Nobel lecture*, pages 444–491, 1987.

[13] Steven De Feyter and Frans C. De Schryver. Two-dimensional supramolecular self-assembly probed by scanning tunneling microscopy. *Chemical Society Reviews*, 32(3):139–150, 2003.

[14] K.S. Feu, F.F. De Assis, S. Nagendra, and R.A. Pilli. The nobel prize in chemistry 2016: Molecular machines. *Quimica Nova*, 40(1), 2017.

[15] Leonhard Grill, Matthew Dyer, Leif Lafferentz, Mats Persson, Maike V. Peters, and Stefan Hecht. Nano-architectures by covalent assembly of molecular building blocks. *Nature Nanotechnology*, 2(11):687–691, 2007.

[16] Frances M. Lord and J. S. Kittelberger. On the determination of activation energies in thermal desorption experiments. *Surface Science*, 43(1):173–182, 1974.

[17] Johannes A.A.W. Elemans, Shengbin Lei, and Steven De Feyter. Molecular and supramolecular networks on surfaces: From two-dimensional crystal engineering to reactivity. *Angewandte Chemie - International Edition*, 48(40):7298–7332, 2009.

[18] Tibor Kudernac, Shengbin Lei, Johannes A.A.W. Elemans, and Steven De Feyter. Two-dimensional supramolecular self-assembly: Nanoporous networks on surfaces. *Chemical Society Reviews*, 38(2):402–421, 2009.

[19] Pearl N. Dickerson, Amber M. Hibberd, Nuri Oncel, and Steven L. Bernasek. Hydrogen-bonding versus van der Waals interactions in self-assembled monolayers of substituted isophthalic acids. *Langmuir*, 26(23):18155–18161, 2010.

[20] Yi Hu, Kai Miao, Li Xu, Bao Zha, Xinrui Miao, and Wenli Deng. Effects of alkyl chain number and position on 2D self-assemblies. *RSC Advances*, 7(51):32391–32398, 2017.

[21] Lokamani, Jeffrey Kelling, Robin Ohmann, Jörg Meyer, Tim Kühne, Gianaurelio Cuniberti, Jannic Wolf, Guido Juckeland, Thomas Huhn, Peter Zahn, Francesca Moresco, and Sibylle Gemming. Describing chain-like assembly of ethoxygroup-functionalized organic molecules on Au(111) using high-throughput simulations. *Scientific Reports*, 11(1):1–9, 2021.

[22] Samuel Paul Jarvis, Mohammad Abdur Rashid, Adam Sweetman, Jeremy Leaf, Simon Taylor, Philip Moriarty, and Janette Dunn. Intermolecular artifacts in probe microscope images of C60 assemblies. *Physical Review B - Condensed Matter and Materials Physics*, 92(24), 2015.

[23] S. Berner, M. De Wild, L. Ramoino, A. Baratoff, H. J. Güntherodt, S. Ivan, H. Suzuki, D. Schlettwein, and A. Jung. Adsorption and two-dimensional phases of a large polar molecule: Sub-phthalocyanine on Ag(111). *Physical Review B - Condensed Matter and Materials Physics*, 68(11):1–11, 2003.

[24] Jun Motojima, Naoko Suzuki, Hideyuki Tsukada, and Takashi Yokoyama. Adsorption and self-assembly of hexa-tert-butyl-hexa-peri-hexabenzocoronene on the si(111)-3×3-Ag surface. *Surface Science*, 713(May):121905, 2021.

[25] Jacob N Israelachvili. Van der Waals Forces. In Jacob N Israelachvili, editor, *Intermolecular and Surface Forces (Third Edition)*, chapter 6, page iii. Academic Press, San Diego, 3rd edition, 2011.

[26] Steven De Feyter, Atsushi Miura, Sheng Yao, Zhijian Chen, Frank Würthner, Pascal Jonkheijm, Albertus P.H.J. Schenning, E. W. Meijer, and Frans C. De Schryver. Two-dimensional self-assembly into multicomponent hydrogen-bonded nanostructures. *Nano Letters*, 5(1):77–81, 2005.

[27] Pierangelo Metrangolo, Hannes Neukirch, Tullio Pilati, and Giuseppe Resnati. Halogen bonding based recognition processes: A world parallel to hydrogen bonding. *Accounts of Chemical Research*, 38(5):386–395, 2005.

[28] Ludwig Bartels. Tailoring molecular layers at metal surfaces. *Nature Chemistry*, 2(2):87–95, 2010.

[29] RP Sijbesma and EW Meijert. Self-assembly of well-defined structures by hydrogen bonding. *Current Opinion in Colloid and interface science*, 4(1):24–32, 1999.

[30] James A. Theobald, Nell S. Oxtoby, Michael A. Phillips, Nell R. Champness, and Peter H. Beton. Controlling molecular deposition and layer structure with supramolecular surface assemblies. *Nature*, 424(6952):1029–1031, 2003.

[31] Peng Lei, Jing Fei Hou, Yu Chuan Xiao, Feng Ying Zhao, Xiao Kang Li, Ke Deng, and Qing Dao Zeng. On-Surface Self-Assembled Structural Transformation Induced by Schiff Base Reaction and Hydrogen bonds. *Langmuir*, 37(12):3662–3671, 2021.

[32] Paul A. Staniec, Luís M.A. Perdigão, Alex Saywell, Neil R. Champness, and Peter H. Beton. Hierarchical organisation on a two-dimensional supramolecular network. *ChemPhysChem*, 8(15):2177–2181, 2007.

[33] José Abad, José I. Martínez, Paula Gómez, Miriam Más-Montoya, Luis Rodríguez, Albano Cossaro, Alberto Verdini, Luca Floreano, José A. Martín-Gago, David Curiel, and Javier Méndez. Two-Dimensional Self-Assembly Driven by Intermolecular Hydrogen Bonding in Benzodi-7-azaindole Molecules on Au(111). *Journal of Physical Chemistry C*, 127(24):11591–11599, 2023.

[34] Rico Gutzler, Chaoying Fu, Afshin Dadvand, Yun Hua, Jennifer M. MacLeod, Federico Rosei, and Dmitrii F. Perepichka. Halogen bonds in 2D supramolecular self-assembly of organic semiconductors. *Nanoscale*, 4(19):5965–5971, 2012.

[35] Gabriella Cavallo, Pierangelo Metrangolo, Roberto Milani, Tullio Pilati, Arri Priimagi, Giuseppe Resnati, and Giancarlo Terraneo. The halogen bond. *Chemical Reviews*, 116(4):2478–2601, 2016.

[36] Fabien Silly, Christine Viala, and Jacques Bonvoisin. Two-Dimensional Halogen-Bonded Porous Self-Assembled Nanoarchitectures of Copper β-Diketonato Complexes. *Journal of Physical Chemistry C*, 122(30):17143–17148, 2018.

[37] David Peyrot and Fabien Silly. On-Surface Synthesis of Two-Dimensional Covalent Organic Structures versus Halogen-Bonded Self-Assembly: Competing Formation of Organic Nanoarchitectures. *ACS Nano*, 10(5):5490–5498, 2016.

[38] Zechao Yang, Lukas Fromm, Tim Sander, Julian Gebhardt, Tobias A. Schaub, Andreas Görling, Milan Kivala, and Sabine Maier. On-Surface Assembly of Hydrogen- and Halogen-Bonded Supramolecular Graphyne-Like Networks. *Angewandte Chemie - International Edition*, 59(24):9549–9555, 2020.

[39] Bao Zha, Xinrui Miao, Pei Liu, Yumeng Wu, and Wenli Deng. Concentration dependent halogen-bond density in the 2D self-assembly of a thienophenanthrene derivative at the aliphatic acid/graphite interface. *Chemical Communications*, 50(64):9003–9006, 2014.

[40] James Lawrence, Gabriele C. Sosso, Luka Dordevic, Harry Pinfold, Davide Bonifazi, and Giovanni Costantini. Combining high-resolution scanning tunnelling microscopy and first-principles simulations to identify halogen bonding. *Nature Communications*, 11(1):7–13, 2020.

[41] Vadia Foziya Yusuf, Naved I. Malek, and Suresh Kumar Kailasa. Review on Metal-Organic Framework Classification, Synthetic Approaches, and Influencing Factors: Applications in Energy, Drug Delivery, and Wastewater Treatment. *ACS Omega*, 7(49):44507–44531, 2022.

[42] Qitang Fan, J. Michael Gottfried, and Junfa Zhu. Surface-Catalyzed C-C Covalent Coupling Strategies toward the Synthesis of Low-Dimensional Carbon-Based Nanostructures. *Accounts of Chemical Research*, 48(8):2484–2494, 2015.

[43] D. Ecija, M. Marschall, J. Reichert, A. Kasperski, D. Nieckarz, P. Szabelski, W. Auwärter, and J. V. Barth. Dynamics and thermal stability of surface-confined metal-organic chains. *Surface Science*, 643:91–97, 2016.

[44] U Schlickum, R Decker, F Klappenberger, G Zoppellaro, and S Klyatskaya. Metal - Organic Honeycomb Nanomeshes with Tunable Cavity Size. *Nano Letters*, 7(12), 2007.

[45] Matthias Marschall, Joachim Reichert, Alexander Weber-Bargioni, Knud Seufert, Willi Auwärter, Svetlana Klyatskaya, Giorgio Zoppellaro, Mario Ruben, and Johannes V. Barth. Random two-dimensional string networks based on divergent coordination assembly. *Nature Chemistry*, 2(2):131–137, 2010.

[46] T.L. Cottrell. *The Strengths of Chemical Bonds*. Butterworth, London, 1958.

[47] J A Kerr. Bond Dissociation Energies by Kinetic Methods. *Chemical Reviews*, 66(5):465–500, 1966.

[48] Sidney W. Benson. Papers — III Bond Energies. *Journal of Chemical Education*, 42(9):502–518, 1965.

[49] B B Darwent. *Bond Dissociation Energies in Simple Molecules*. Bond Dissociation Energies in Simple Molecules. U.S. National Bureau of Standards, 1970.

[50] Qiang Sun, Renyuan Zhang, Jun Qiu, Rui Liu, and Wei Xu. On-Surface Synthesis of Carbon Nanostructures. *Advanced Materials*, 30(17):1–12, 2018.

[51] Qian Shen, Hong Ying Gao, and Harald Fuchs. Frontiers of on-surface synthesis: From principles to applications. *Nano Today*, 13:77–96, 2017.

[52] Yi Qi Zhang, Nenad Kepčija, Martin Kleinschrodt, Katharina Diller, Sybille Fischer, Anthoula C. Papageorgiou, Francesco Allegretti, Jonas Björk, Svetlana Klyatskaya, Florian Klappenberger, Mario Ruben, and Johannes V. Barth. Homo-coupling of terminal alkynes on a noble metal surface. *Nature Communications*, 3:1–8, 2012.

[53] Hong Ying Gao, Dingyong Zhong, Harry Mönig, Hendrik Wagner, Philipp Alexander Held, Alexander Timmer, Armido Studer, and Harald Fuchs. Photochemical glaser coupling at metal surfaces. *Journal of Physical Chemistry C*, 118(12):6272–6277, 2014.

[54] Philipp Alexander Held, Hong Ying Gao, Lacheng Liu, Christian Mück-Lichtenfeld, Alexander Timmer, Harry Mönig, Dennis Barton, Johannes Neugebauer, Harald Fuchs, and Armido Studer. On-Surface Domino Reactions: Glaser Coupling and Dehydrogenative Coupling of a Biscarboxylic Acid To Form Polymeric Bisacylperoxides. *Angewandte Chemie - International Edition*, 55(33):9777–9782, 2016.

[55] Lei Dong, Pei Nian Liu, and Nian Lin. Surface-Activated Coupling Reactions Confined on a Surface. *Accounts of Chemical Research*, 48(10):2765–2774, 2015.

[56] Qiang Sun, Liangliang Cai, Yuanqi Ding, Lei Xie, Chi Zhang, Qinggang Tan, and Wei Xu. Dehydrogenative Homocoupling of Terminal Alkenes on Copper Surfaces: A Route to Dienes. *Angewandte Chemie - International Edition*, 54(15):4549–4552, 2015.

[57] F Ullmann and Jean Bielecki. Ueber Synthesen in der Biphenylreihe. *Berichte der deutschen chemischen Gesellschaft*, 34(2):2174–2185, may 1901.

[58] Carlo Sambiagio, Stephen P. Marsden, A. John Blacker, and Patrick C. McGowan. Copper catalysed Ullmann type chemistry: From mechanistic aspects to modern development. *Chemical Society Reviews*, 43(10):3525–3550, 2014.

[59] Todd D Nelson and R David Crouch. Cu, Ni, and Pd Mediated Homocoupling Reactions in Biaryl Syntheses: The Ullmann Reaction, 2004.

[60] Carlo Sambiagio, Stephen P. Marsden, A. John Blacker, and Patrick C. McGowan. Copper catalysed Ullmann type chemistry: From mechanistic aspects to modern development. *Chemical Society Reviews*, 43(10):3525–3550, 2014.

[61] Chris J. Judd, Neil R. Champness, and Alex Saywell. An On-Surface Reaction Confined within a Porous Molecular Template. *Chemistry - A European Journal*, 24(1):56–61, 2018.

[62] J. Björk. Reaction mechanisms for on-surface synthesis of covalent nanostructures. *Journal of Physics Condensed Matter*, 28(8), 2016.

[63] Marco Bieri, Stephan Blankenburg, Milan Kivala, Carlo A. Pignedoli, Pascal Ruffieux, Klaus Müllen, and Roman Fasel. Surface-supported 2D heterotriangulene polymers. *Chemical Communications*, 47(37):10239–10241, 2011.

[64] Thomas Faury, Sylvain Clair, Mathieu Abel, Frédéric Dumur, Didier Gigmes, and Louis Porte. Sequential linking to control growth of a surface covalent organic framework. *Journal of Physical Chemistry C*, 116(7):4819–4823, 2012.

[65] Rico Gutzler, Luis Cardenas, Josh Lipton-Duffin, Mohamed El Garah, Laurentiu E. Dinca, Csaba E. Szakacs, Chaoying Fu, Mark Gallagher, Martin Vondráček, Maksym Rybachuk, Dmitrii F. Perepichka, and Federico Rosei. Ullmann-type coupling of brominated tetrathienoanthracene on copper and silver. *Nanoscale*, 6(5):2660–2668, 2014.

[66] Fabian Queck, Ondrej Krejčí, Philipp Scheuerer, Felix Bolland, Michal Otyepka, Pavel Jelínek, and Jascha Repp. Bonding Motifs in Metal-Organic Compounds on Surfaces. *Journal of the American Chemical Society*, 140(40):12884–12889, 2018.

[67] Johannes V. Barth. Molecular architectonic on metal surfaces. *Annual Review of Physical Chemistry*, 58:375–407, 2007.

[68] M. Lackinger. Surface-assisted Ullmann coupling. *Chemical Communications*, 53(56):7872–7885, 2017.

[69] Qitang Fan, Tao Wang, Liming Liu, Jin Zhao, Junfa Zhu, and J. Michael Gottfried. Tribromobenzene on Cu(111): Temperature-dependent formation of halogen-bonded, organometallic, and covalent nanostructures. *Journal of Chemical Physics*, 142(10), 2015.

[70] Min Chen, Jie Xiao, Hans Peter Steinrück, Shiyong Wang, Weihua Wang, Nian Lin, Wolfgang Hieringer, and J. Michael Gottfried. Combined photoemission and scanning tunneling microscopy study of the surface-assisted ullmann coupling reaction. *Journal of Physical Chemistry C*, 118(13):6820–6830, 2014.

[71] Andrea Basagni, Francesco Sedona, Carlo A. Pignedoli, Mattia Cattelan, Louis Nicolas, Maurizio Casarin, and Mauro Sambi. Molecules-oligomers-nanowires-graphene nanoribbons: A bottom-up stepwise on-surface cova-

lent synthesis preserving long-range order. *Journal of the American Chemical Society*, 137(5):1802–1808, 2015.

[72] Juan Carlos Moreno-López, Duncan John Mowbray, Alejandro Pérez Paz, Rodrigo Cezar De Campos Ferreira, Alisson Ceccatto Dos Santos, Paola Ayala, and Abner De Siervo. Roles of Precursor Conformation and Adatoms in Ullmann Coupling: An Inverted Porphyrin on Cu(111). *Chemistry of Materials*, 31(8):3009–3017, 2019.

[73] J. A. Lipton-Duffin, O. Ivasenko, D. F. Perepichka, and F. Rosei. Synthesis of polyphenylene molecular wires by surface-confined polymerization. *Small*, 5(5):592–597, 2009.

[74] Gianluca Galeotti, Marco Di Giovannantonio, Josh Lipton-Duffin, Maryam Ebrahimi, Stefano Tebi, Alberto Verdini, Luca Floreano, Yannick Fagot-Revurat, Dmitrii F. Perepichka, Federico Rosei, and Giorgio Contini. The role of halogens in on-surface Ullmann polymerization. *Faraday Discussions*, 204:453–469, 2017.

[75] Marco Di Giovannantonio, Mohamed El Garah, Josh Lipton-Duffin, Vincent Meunier, Luis Cardenas, Yannick Fagot Revurat, Albano Cossaro, Alberto Verdini, Dmitrii F. Perepichka, Federico Rosei, and Giorgio Contini. Insight into organometallic intermediate and its evolution to covalent bonding in surface-confined ullmann polymerization. *ACS Nano*, 7(9):8190–8198, 2013.

[76] Hermann Walch, Rico Gutzler, Thomas Sirtl, Georg Eder, and Markus Lackinger. Material- and orientation-dependent reactivity for heterogeneously catalyzed carbon-bromine bond homolysis. *Journal of Physical Chemistry C*, 114(29):12604–12609, 2010.

[77] Qitang Fan, Cici Wang, Yong Han, Junfa Zhu, Wolfgang Hieringer, Julian Kuttner, Gerhard Hilt, and J. Michael Gottfried. Surface-assisted organic synthesis of hyperbenzene nanotroughs. *Angewandte Chemie - International Edition*, 52(17):4668–4672, 2013.

[78] Ke Ji Shi, Ding Wang Yuan, Cheng Xin Wang, Chen Hui Shu, Deng Yuan Li, Zi Liang Shi, Xin Yan Wu, and Pei Nian Liu. Ullmann Reaction of Aryl Chlorides on Various Surfaces and the Application in Stepwise Growth of 2D Covalent Organic Frameworks. *Organic Letters*, 18(6):1282–1285, 2016.

[79] Yuxuan Lin, Mengxiao Diao, Jingxin Dai, Zhen Xu, Xinwei Zhao, Xiaojie Wen, Lingbo Xing, Xiong Zhou, Qiwei Chen, Jing Liu, and Kai Wu. Molecular insight into on-surface chemistry of an organometallic polymer. *Physical Chemistry Chemical Physics*, 25(2):1006–1013, 2022.

[80] Ming Xi and Brian E Bent. Iodobenzene on Cu(111): formation and coupling of adsorbed phenyl groups. *Surface Science*, 278(1):19–32, 1992.

[81] Marco Bieri, Matthias Treier, Jinming Cai, Kamel Aït-Mansour, Pascal Ruffieux, Oliver Gröning, Pierangelo Gröning, Marcel Kastler, Ralph Rieger, Xinliang Feng, Klaus Müllen, and Roman Fasel. Porous graphenes: Two-dimensional polymer synthesis with atomic precision. *Chemical Communications*, (45):6919–6921, 2009.

[82] Johanna Eichhorn, Thomas Strunskus, Atena Rastgoo-Lahrood, Debabrata Samanta, Michael Schmittel, and Markus Lackinger. On-surface Ullmann polymerization via intermediate organometallic networks on Ag(111). *Chemical Communications*, 50(57):7680–7682, 2014.

[83] Chen Hui Shu, Yan He, Ruo Xi Zhang, Jian Le Chen, An Wang, and Pei Nian Liu. Atomic-scale visualization of stepwise growth mechanism of metal-alkynyl networks on surfaces. *Journal of the American Chemical Society*, 142(39):16579–16586, 2020.

[84] L. Lafferentz, V. Eberhardt, C. Dri, C. Africh, G. Comelli, F. Esch, S. Hecht, and L. Grill. Controlling on-surface polymerization by hierarchical and substrate-directed growth. *Nature Chemistry*, 4(3):215–220, 2012.

[85] Han Zhu, Xuhan Zhou, Shenwei Chen, Zizhao Liu, Ye Tao, and Dingyong Zhong. On-Surface Reaction of 1,4-Dibromo-2,5-Diiodobenzene on Au(111) and Ag(100). *Journal of Physical Chemistry C*, 127(12):5783–5790, 2023.

[86] Matthias Koch, Marie Gille, Andreas Viertel, Stefan Hecht, and Leonhard Grill. Substrate-controlled linking of molecular building blocks: Au(111) vs. Cu(111). *Surface Science*, 627:70–74, 2014.

[87] P. J. Robinson and K. A. Holbrook. Why gold is the noblest of all the metals. *Nature*, 376(July):238–240, 1995.

[88] Alex Saywell, Jutta Schwarz, Stefan Hecht, and Leonhard Grill. Polymerization on Stepped Surfaces: Alignment of Polymers and Identification of Catalytic Sites. *Angewandte Chemie*, 124(21):5186–5190, 2012.

[89] Qitang Fan, Liming Liu, Jingya Dai, Tao Wang, Huanxin Ju, Jin Zhao, Julian Kuttner, Gerhard Hilt, J. Michael Gottfried, and Junfa Zhu. Surface Adatom Mediated Structural Transformation in Bromoarene Monolayers: Precursor Phases in Surface Ullmann Reaction. *ACS Nano*, 12(3):2267–2274, 2018.

[90] Chris J. Judd, Sarah L. Haddow, Neil R. Champness, and Alex Saywell. Ullmann Coupling Reactions on Ag(111) and Ag(110); Substrate Influence on the Formation of Covalently Coupled Products and Intermediate Metal-Organic Structures. *Scientific Reports*, 7(1):1–7, 2017.

[91] Antti J. Mäkinen, James P. Long, Neil J. Watkins, and Zakya H. Kafafi. Sexithiophene adlayer growth on vicinal gold surfaces. *Journal of Physical Chemistry B*, 109(12):5790–5795, 2005.

[92] Lukas Grossmann, Manuela Hocke, Gianluca Galeotti, Giorgio Contini, Luca Floreano, Albano Cossaro, Amit Ghosh, Michael Schmittel, Johanna Rosen, Wolfgang M. Heckl, Jonas Björk, and Markus Lackinger. Mechanistic insights into on-surface reactions from isothermal temperature-programmed X-ray photoelectron spectroscopy. *Nanoscale*, pages 7612–7625, 2024.

[93] Jonas Björk, Felix Hanke, and Sven Stafström. Mechanisms of halogen-based covalent self-assembly on metal surfaces. *Journal of the American Chemical Society*, 135(15):5768–5775, 2013.

[94] Jonas Björk, Manfred Matena, Matthew S. Dyer, Mihaela Enache, Jorge Lobo-Checa, Lutz H. Gade, Thomas A. Jung, Meike Stöhr, and Mats Persson. STM fingerprint of molecule-adatom interactions in a self-assembled metal-organic surface coordination network on Cu(111). *Physical Chemistry Chemical Physics*, 12(31):8815–8821, 2010.

[95] Massimo Fritton, David A. Duncan, Peter S. Deimel, Atena Rastgoo-Lahrood, Francesco Allegretti, Johannes V. Barth, Wolfgang M. Heckl, Jonas Björk, and Markus Lackinger. The Role of Kinetics versus Thermodynamics in Surface-Assisted Ullmann Coupling on Gold and Silver Surfaces. *Journal of the American Chemical Society*, 141(12):4824–4832, 2019.

[96] Ivar Giaever and Karl Megerle. Study of Superconductors by Electron Tunneling. *Physical Review*, 122(4):1101–1111, 1961.

[97] G. Binnig, H. Rohrer, Ch Gerber, and E. Weibel. Tunneling through a controllable vacuum gap. *Applied Physics Letters*, 40(2):178–180, 1982.

[98] J Bardeen. Tunnelling from a Many-Particle Point of View. *Phys. Rev. Lett.*, 6(2):57–59, 1961.

[99] J. Tersoff and D. R. Hamann. Theory of the scanning tunneling microscope. *Physical Review B*, 31(2):805–813, 1985.

[100] C. Julian Chen. Origin of atomic resolution on metal surfaces in scanning tunneling microscopy. *Physical Review Letters*, 65(4):448–451, 1990.

[101] Kai Siegbahn. Electron spectroscopy for atoms, molecules, and condensed matter. *Science*, 217(4555):111–121, 1982.

[102] Joachim Stöhr. Principles, Techniques, and Instrumentation of NEXAFS. In *NEXAFS Spectroscopy*, chapter 5. Springer Berlin, Heidelberg, 1992.

[103] J. Stöhr and D. A. Outka. Determination of molecular orientations on surfaces from the angular dependence of near-edge x-ray-absorption fine-structure spectra. *Physical Review B*, 36(15):7891–7905, 1987.

[104] Nam Koo Kim, Young Hwan Min, Seokhwan Noh, Eunkyung Cho, Gitaeg Jeong, Minho Joo, Seh Won Ahn, Jeong Soo Lee, Seongtak Kim, Kyuwook Ihm, Hyungju Ahn, Yoonmook Kang, Hae Seok Lee, and Donghwan Kim. Investigation of Thermally Induced Degradation in CH3NH3PbI3 Perovskite Solar Cells using In-situ Synchrotron Radiation Analysis. *Scientific Reports*, 7(1):1–9, 2017.

[105] Andre Authier. Dynamical Theory of X-Ray Diffraction. In *International Tables for Crystallography*, volume 11, pages 534–551. Wiley, 2001.

[106] D. P. Woodruff. Surface structure determination using x-ray standing waves. *Reports on Progress in Physics*, 68(4):743–798, 2005.

[107] Yaping Zang, Suman Ray, E. Dean Fung, Anders Borges, Marc H. Garner, Michael L. Steigerwald, Gemma C. Solomon, Satish Patil, and Latha Venkataraman. Resonant Transport in Single Diketopyrrolopyrrole Junctions. *Journal of the American Chemical Society*, 140(41):13167–13170, 2018.

[108] Chaoying Fu, Patrick J. Beldon, and Dmitrii F. Perepichka. H-Bonding Control of Supramolecular Ordering of Diketopyrrolopyrroles. *Chemistry of Materials*, 29(7):2979–2987, 2017.

[109] Sara J. Krivickas, Chiho Hashimoto, Junya Yoshida, Akira Ueda, Kazuyuki Takahashi, John D. Wallis, and Hatsumi Mori. Synthesis of racemic and chiral BEDT-TTF derivatives possessing hydroxy groups and their achiral and chiral charge transfer complexes. *Beilstein Journal of Organic Chemistry*, 11:1561–1569, 2015.

[110] Céline Réthoré, Narcis Avarvari, Enric Canadell, Pascale Auban-Senzier, and Marc Fourmigué. Chiral molecular metals: Syntheses, structures, and properties of the AsF6- salts of racemic (±)-, (R)-, and (S)-tetrathiafulvalene-oxazoline derivatives. *Journal of the American Chemical Society*, 127(16):5748–5749, 2005.

[111] Akinori Honda, Yoshinori Tamaki, and Kazuo Miyamura. The Effects of Noncovalent Interactions on Surface Structures Formed by Diketopyrrolopy-

rrole Pigment and Its Alkyl-Derivatives on HOPG Substrate. *Bulletin of the Chemical Society of Japan*, 88(7):969–975, 2015.

[112] Chaoying Fu, Francine Bélanger-Gariépy, and Dmitrii F. Perepichka. Supramolecular ordering of difuryldiketopyrrolopyrrole: The effect of alkyl chains and inter-ring twisting. *CrystEngComm*, 18(23):4285–4289, 2016.

[113] Leonhard Grill and Stefan Hecht. Covalent on-surface polymerization. *Nature Chemistry*, 12(2):115–130, 2020.

[114] Tao Wang and Junfa Zhu. Confined on-surface organic synthesis: Strategies and mechanisms. *Surface Science Reports*, 74(2):97–140, 2019.

[115] Lander Verstraete and Steven De Feyter. 2D Self-assembled molecular networks and on-surface reactivity under nanoscale lateral confinement. *Chemical Society Reviews*, 50(10):5884–5897, 2021.

[116] Xuechao Li, Haitao Ge, Renjie Xue, Minghui Wu, and Lifeng Chi. Anchoring and Reacting On-Surface to Achieve Programmability. *JACS Au*, 2(1):58–65, 2022.

[117] Mendel In't Veld, Patrizia Iavicoli, Sam Haq, David B. Amabilino, and Rasmita Raval. Unique intermolecular reaction of simple porphyrins at a metal surface gives covalent nanostructures. *Chemical Communications*, (13):1536–1538, 2008.

[118] Sam Haq, Felix Hanke, John Sharp, Mats Persson, David B. Amabilino, and Rasmita Raval. Versatile bottom-up construction of diverse macromolecules on a surface observed by scanning tunneling microscopy. *ACS Nano*, 8(9):8856–8870, 2014.

[119] Christophe Nacci, Francisco Ample, David Bleger, Stefan Hecht, Christian Joachim, and Leonhard Grill. Conductance of a single flexible molecular wire composed of alternating donor and acceptor units. *Nature Communications*, 6(May), 2015.

[120] Dmitry Skidin, Tim Erdmann, Seddigheh Nikipar, Frank Eisenhut, Justus Krüger, Florian Günther, Sibylle Gemming, Anton Kiriy, Brigitte Voit,

Dmitry A Ryndyk, Christian Joachim, Francesca Moresco, and Gianaurelio Cuniberti. Tuning the conductance of a molecular wire by the interplay of donor and acceptor units. *Nanoscale*, 10(36):17131–17139, 2018.

[121] Xiangzhi Meng, Lacheng Liu, Fátima García, Berta Álvarez, Dolores Pérez, Hong Ying Gao, Diego Pena, and Harald Fuchs. Effect of Central π-System in Silylated-Tetraynes on σ-Bond Metathesis on Surfaces. *Journal of Physical Chemistry C*, 122(11):6230–6235, 2018.

[122] Sylvain Clair and Dimas G. De Oteyza. Controlling a Chemical Coupling Reaction on a Surface: Tools and Strategies for On-Surface Synthesis. *Chemical Reviews*, 119(7):4717–4776, 2019.

[123] Chris J. Judd, Dmitry V. Kondratuk, Harry L. Anderson, and Alex Saywell. On-Surface Synthesis within a Porphyrin Nanoring Template. *Scientific Reports*, 9(1):1–8, 2019.

[124] Kyeongwoon Chung, Min Sang Kwon, Brendan M. Leung, Antek G. Wong-Foy, Min Su Kim, Jeongyong Kim, Shuichi Takayama, Johannes Gierschner, Adam J. Matzger, and Jinsang Kim. Shear-triggered crystallization and light emission of a thermally stable organic supercooled liquid. *ACS Central Science*, 1(2):94–102, 2015.

[125] David B. Amabilino, Steven De Feyter, Roberto Lazzaroni, Elba Gomar-Nadal, Jaume Veciana, Concepció Rovira, Mohamed M. Abdel-Mottaleb, Wael Mamdouh, Patrizia Iavicoli, Krystallia Psychogyiopoulou, Mathieu Linares, Andrea Minoia, Hong Xu, and Josep Puigmartí-Luis. Monolayer self-assembly at liquid-solid interfaces: Chirality and electronic properties of molecules at surfaces. *Journal of Physics Condensed Matter*, 20(18), 2008.

[126] Karl Heinz Ernst. Molecular chirality at surfaces. *Physica Status Solidi (B) Basic Research*, 249(11):2057–2088, 2012.

[127] R. Raval. Chiral expression from molecular assemblies at metal surfaces: Insights from surface science techniques. *Chemical Society Reviews*, 38(3):707–721, 2009.

[128] Joan Teyssandier, Kunal S. Mali, and Steven De Feyter. Halogen Bonding in Two-Dimensional Crystal Engineering. *ChemistryOpen*, 9(2):225–241, 2020.

[129] Luis Perdigao. LMAPper - https://sourceforge.net/projects/spm-and-mol-viewer/, 2019.

[130] Marcus D Hanwell, Donald E Curtis, David C Lonie, Tim Vandermeersch, Eva Zurek, and Geoffrey R Hutchison. Avogadro: an advanced semantic chemical editor, visualization, and analysis platform. *Journal of Cheminformatics*, 4(1):17, 2012.

[131] Arunabh Batra, Dean Cvetko, Gregor Kladnik, Olgun Adak, Claudia Cardoso, Andrea Ferretti, Deborah Prezzi, Elisa Molinari, Alberto Morgante, and Latha Venkataraman. Probing the mechanism for graphene nanoribbon formation on gold surfaces through X-ray spectroscopy. *Chemical Science*, 5(11):4419–4423, 2014.

[132] Konstantin A. Simonov, Nikolay A. Vinogradov, Alexander S. Vinogradov, Alexander V. Generalov, Elena M. Zagrebina, Nils Mårtensson, Attilio A. Cafolla, Tomas Carpy, John P. Cunniffe, and Alexei B. Preobrajenski. Effect of substrate chemistry on the bottom-up fabrication of graphene nanoribbons: Combined core-level spectroscopy and STM study. *Journal of Physical Chemistry C*, 118(23):12532–12540, 2014.

[133] Dimas G. De Oteyza, Aran García-Lekue, Manuel Vilas-Varela, Néstor Merino-Díez, Eduard Carbonell-Sanromà, Martina Corso, Guillaume Vasseur, Celia Rogero, Enrique Guitián, Jose Ignacio Pascual, J. Enrique Ortega, Yutaka Wakayama, and Diego Peña. Substrate-Independent Growth of Atomically Precise Chiral Graphene Nanoribbons. *ACS Nano*, 10(9):9000–9008, 2016.

[134] Marco Di Giovannantonio, Qiang Chen, José I. Urgel, Pascal Ruffieux, Carlo A. Pignedoli, Klaus Müllen, Akimitsu Narita, and Roman Fasel. On-Surface Synthesis of Oligo(indenoindene). *Journal of the American Chemical Society*, 142(30):12925–12929, 2020.

[135] Tuan Anh Pham, Fei Song, Manh Thuong Nguyen, Zheshen Li, Florian Studener, and Meike Stöhr. Comparing Ullmann Coupling on Noble Metal Surfaces: On-Surface Polymerization of 1,3,6,8-Tetrabromopyrene on Cu(111) and Au(111). *Chemistry - A European Journal*, 22(17):5937–5944, 2016.

[136] Gianluca Galeotti, Marco Di Giovannantonio, Andrew Cupo, Sarah Xing, Josh Lipton-Duffin, Maryam Ebrahimi, Guillaume Vasseur, Bertrand Kierren, Yannick Fagot-Revurat, Damien Tristant, Vincent Meunier, Dmitrii F. Perepichka, Federico Rosei, and Giorgio Contini. An unexpected organometallic intermediate in surface-confined Ullmann coupling. *Nanoscale*, 11(16):7682–7689, 2019.

[137] Alex Saywell, Wojciech Greń, Grégory Franc, André Gourdon, Xavier Bouju, and Leonhard Grill. Manipulating the conformation of single organometallic chains on Au(111). *Journal of Physical Chemistry C*, 118(3):1719–1728, 2014.

[138] Leonhard Grill. Large molecules on surfaces: deposition and intramolecular STM manipulation by directional forces. *Journal of Physics: Condensed Matter*, 22(8):084023, 2010.

[139] John B Fenn, Matthias Mann, Chin Kai Meng, Shek Fu Wong, and Craig M Whitehouse. Electrospray Ionization for Mass Spectrometry of Large Biomolecules. *Science*, 246(4926):64–71, 1989.

[140] Stephan Rauschenbach, Frank L. Stadler, Eugenio Lunedei, Nicola Malinowski, Sergej Koltsov, Giovanni Costantini, and Klaus Kern. Electrospray ion beam deposition of clusters and biomolecules. *Small*, 2(4):540–547, 2006.

[141] Stephan Rauschenbach, Ralf Vogelgesang, N. Malinowski, Jürgen W. Gerlach, Mohamed Benyoucef, Giovanni Costantini, Zhitao Deng, Nicha Thontasen, and Klaus Kern. Electrospray ion beam deposition: Soft-landing and fragmentation of functional molecules at solid surfaces. *ACS Nano*, 3(10):2901–2910, 2009.

[142] Alex Saywell, Johannes K. Sprafke, Louisa J. Esdaile, Andrew J. Britton, Anna Rienzo, Harry L. Anderson, James N. O'Shea, and Peter H. Beton. Conformation and packing of porphyrin polymer chains deposited using electrospray on a gold surface. *Angewandte Chemie - International Edition*, 49(48):9136–9139, 2010.

[143] T. Zambelli, Y. Boutayeb, F. Gayral, J. Lagoute, N. K. Girdhar, A. Gourdon, S. Gauthier, M. J. Blanco, J. C. Chambron, V. Heitz, and J. P. Sauvage. Deposition of large organic molecules in ultra-high vacuum: A comparison between thermal sublimation and pulse-injection. *International Journal of Nanoscience*, 3(3):331–341, 2004.

[144] Nouf Alharbi, Jack Hart, and James N. O'Shea. The adsorption and XPS of triphenylamine-based organic dye molecules on rutile TiO_2(110) prepared by UHV-compatible electrospray deposition. *Surface Science*, 735(May):122323, 2023.

[145] P Kebarle and Y Ho. On the Mechanism of Electrospray Mass Spectrometry. *Electrospray Ionization Mass Spectrometry*, pages 3–63, 1997.

[146] Matthias S. Wilm and Matthias Mann. Electrospray and Taylor-Cone theory, Dole's beam of macromolecules at last? *International Journal of Mass Spectrometry and Ion Processes*, 136(2-3):167–180, 1994.

[147] Malcolm Dole, L. L. Mack, R. L. Hines, Department Of Chemistry, R. C. Mobley, L. D. Ferguson, and M. B. Alice. Molecular beams of macroions. *The Journal of Chemical Physics*, 49(5):2240–2249, 1968.

[148] B. A. Thomson and J. V. Iribarne. Field induced ion evaporation from liquid surfaces at atmospheric pressure. *The Journal of Chemical Physics*, 71(11):4451–4463, 1979.

[149] Kentax GmbH. Operating instructions for Evaporator TCE-BSC and variable power supply unit, 2012.

[150] Wei Ran, Andreas Walz, Karolina Stoiber, Peter Knecht, Hongxiang Xu, Anthoula C. Papageorgiou, Annette Huettig, Diego Cortizo-

Lacalle, Juan P. Mora-Fuentes, Aurelio Mateo-Alonso, Hartmut Schlichting, Joachim Reichert, and Johannes V. Barth. Depositing Molecular Graphene Nanoribbons on Ag(111) by Electrospray Controlled Ion Beam Deposition: Self-Assembly and On-Surface Transformations. *Angewandte Chemie - International Edition*, 61(14), 2022.

[151] Paul Fremdling, Tim K. Esser, Bodhisattwa Saha, Alexander A. Makarov, Kyle L. Fort, Maria Reinhardt-Szyba, Joseph Gault, and Stephan Rauschenbach. A Preparative Mass Spectrometer to Deposit Intact Large Native Protein Complexes. *ACS Nano*, 16(9):14443–14455, 2022.

[152] Baozhong Zhang, Roger Wepf, Karl Fischer, Manfred Schmidt, Sébastien Besse, Peter Lindner, Benjamin T. King, Reinhard Sigel, Peter Schurtenberger, Yeshayahu Talmon, Yi Ding, Martin Kröger, Avraham Halperin, and A. Dieter Schlüter. The largest synthetic structure with molecular precision: Towards a molecular object. *Angewandte Chemie - International Edition*, 50(3):737–740, 2011.

[153] Richard J. Cogdell, Andrew Gall, and Jürgen Köhler. The architecture and function of the light-harvesting apparatus of purple bacteria: From single molecules to in vivo membranes. *Quarterly Reviews of Biophysics*, 39(3):227–324, 2006.

[154] Hyun Sun Cho, Hanju Rhee, Jae Kyu Song, Chang Ki Min, Masayoshi Takase, Naoki Aratani, Sung Cho, Atsuhiro Osuka, Taiha Joo, and Dongho Kim. Excitation energy transport processes of porphyrin monomer, dimer, cyclic trimer, and hexamer probed by ultrafast fluorescence anisotropy decay. *Journal of the American Chemical Society*, 125(19):5849–5860, 2003.

[155] Myung Seok Choi, Tomoko Yamazaki, Iwao Yamazaki, and Takuzo Aida. Bioinspired Molecular Design of Light-Harvesting Multiporphyrin Arrays. *Angewandte Chemie - International Edition*, 43(2):150–158, 2003.

[156] Naoki Aratani, Dongho Kim, and Atsuhiro Osuka. Discrete cyclic porphyrin arrays as artificial light-harvesting antenna. *Accounts of Chemical Research*, 42(12):1922–1934, 2009.

[157] Melanie C. O'Sullivan, Johannes K. Sprafke, Dmitry V. Kondratuk, Corentin Rinfray, Timothy D.W. Claridge, Alex Saywell, Matthew O. Blunt, James N. O'Shea, Peter H. Beton, Marc Malfois, and Harry L. Anderson. Vernier templating and synthesis of a 12-porphyrin nano-ring. *Nature*, 469(7328):72–75, 2011.

[158] Henrik Gotfredsen, Jie Ren Deng, Jeff M. Van Raden, Marcello Righetto, Janko Hergenhahn, Michael Clarke, Abigail Bellamy-Carter, Jack Hart, James O'Shea, Timothy D.W. Claridge, Fernanda Duarte, Alex Saywell, Laura M. Herz, and Harry L. Anderson. Bending a photonic wire into a ring. *Nature Chemistry*, 14(12):1436–1442, 2022.

[159] Jeff M. Van Raden, Jie Ren Deng, Henrik Gotfredsen, Janko Hergenhahn, Michael Clarke, Matthew Edmondson, Jack Hart, James N. O'Shea, Fernanda Duarte, Alex Saywell, and Harry L. Anderson. Template-Directed Synthesis of Strained meso-meso-Linked Porphyrin Nanorings. *Angewandte Chemie - International Edition*, 63(14), 2024.

[160] Srinivasa Ramanujan. *Collected Papers of Srinivasa Ramanujan*. Cambridge University Press, 1927.

[161] Lizhi Zhang, Zhihai Cheng, Qing Huan, Xiaobo He, Xiao Lin, Li Gao, Zhitao Deng, Nan Jiang, Qi Liu, Shixuan Du, Haiming Guo, and Hong Jun Gao. Site- and configuration-selective anchoring of iron-phthalocyanine on the step edges of Au(111) surface. *Journal of Physical Chemistry C*, 115(21):10791–10796, 2011.

[162] X. Chen, E. R. Frank, and R. J. Hamers. Spatially and rotationally oriented adsorption of molecular adsorbates on Ag(111) investigated using cryogenic scanning tunneling microscopy. *Journal of Vacuum Science and Technology B: Microelectronics and Nanometer Structures Processing, Measurement, and Phenomena*, 14(2):1136–1140, 1996.

[163] Marta E. Cañas-Ventura, Wende Xiao, Daniel Wasserfallen, Klaus Müllen, Harald Brune, Johannes V. Barth, and Roman Fasel. Self-assembly of pe-

riodic bicomponent wires and ribbons. *Angewandte Chemie - International Edition*, 46(11):1814–1818, 2007.

[164] Marcin A. Majewski, Wojciech Stawski, Jeff M. Van Raden, Michael Clarke, Jack Hart, James N. O'Shea, Alex Saywell, and Harry L. Anderson. Covalent Template-Directed Synthesis of a Spoked 18-Porphyrin Nanoring**. *Angewandte Chemie - International Edition*, 62(18), 2023.

[165] G. I. Svirskiy, N. N. Sergeeva, S. A. Krasnikov, N. A. Vinogradov, Yu N. Sergeeva, A. A. Cafolla, A. B. Preobrajenski, and A. S. Vinogradov. Electronic structure of nickel porphyrin NiP: Study by X-ray photoelectron and absorption spectroscopy. *Physics of the Solid State*, 59(2):368–377, 2017.

[166] Matthew Edmondson, Eleanor S. Frampton, Chris J. Judd, Neil R. Champness, Robert G. Jones, and Alex Saywell. Order, disorder, and metalation of tetraphenylporphyrin (2H-TPP) on Au(111). *Chemical Communications*, 58(42):6247–6250, 2022.

[167] Zongping Chen, Akimitsu Narita, and Klaus Müllen. Graphene Nanoribbons: On-Surface Synthesis and Integration into Electronic Devices. *Advanced Materials*, 32(45):1–26, 2020.

[168] Dimas G. De Oteyza and Thomas Frederiksen. Carbon-based nanostructures as a versatile platform for tunable π-magnetism. *Journal of Physics : Condensed Matter*, 34(44), 2022.

[169] Xinran Wang, Haomin and Wang, Hui Shan and Ma, Chuanxu and Chen, Lingxiu and Jiang, Chengxin and Chen, Chen and Xie, Xiaoming and Li, An-Ping and Wang. Graphene nanoribbons for quantum electronics. *Nature Reviews Physics*, 3(12):791—-802, 2021.

[170] Eduard Carbonell-Sanromà, Jeremy Hieulle, Manuel Vilas-Varela, Pedro Brandimarte, Mikel Iraola, Ana Barragán, Jingcheng Li, Mikel Abadia, Martina Corso, Daniel Sánchez-Portal, Diego Peña, and Jose Ignacio Pascual. Doping of Graphene Nanoribbons via Functional Group Edge Modification. *ACS Nano*, 11(7):7355–7361, 2017.

[171] Daniel J. Rizzo, Meng Wu, Hsin Zon Tsai, Tomas Marangoni, Rebecca A. Durr, Arash A. Omrani, Franklin Liou, Christopher Bronner, Trinity Joshi, Giang D. Nguyen, Griffin F. Rodgers, Won Woo Choi, Jakob H. Jørgensen, Felix R. Fischer, Steven G. Louie, and Michael F. Crommie. Length-Dependent Evolution of Type II Heterojunctions in Bottom-Up-Synthesized Graphene Nanoribbons. *Nano Letters*, 19(5):3221–3228, 2019.

[172] Shigeki Kawai, Shohei Saito, Shinichiro Osumi, Shigehiro Yamaguchi, Adam S. Foster, Peter Spijker, and Ernst Meyer. Atomically controlled substitutional boron-doping of graphene nanoribbons. *Nature Communications*, 6:6–11, 2015.

[173] Ethan Chi Ho Wen, Peter H. Jacobse, Jingwei Jiang, Ziyi Wang, Steven G. Louie, Michael F. Crommie, and Felix R. Fischer. Fermi-Level Engineering of Nitrogen Core-Doped Armchair Graphene Nanoribbons. *Journal of the American Chemical Society*, 145(35):19338–19346, 2023.

[174] Yi Zhang, Yanfang Zhang, Geng Li, Jianchen Lu, Xiao Lin, Shixuan Du, Reinhard Berger, Xinliang Feng, Klaus Müllen, and Hong Jun Gao. Direct visualization of atomically precise nitrogen-doped graphene nanoribbons. *Applied Physics Letters*, 105(2), 2014.

[175] Rémy Pawlak, Xunshan Liu, Silviya Ninova, Philipp D'Astolfo, Carl Drechsel, Sara Sangtarash, Robert Häner, Silvio Decurtins, Hatef Sadeghi, Colin J. Lambert, Ulrich Aschauer, Shi Xia Liu, and Ernst Meyer. Bottom-up Synthesis of Nitrogen-Doped Porous Graphene Nanoribbons. *Journal of the American Chemical Society*, 142(29):12568–12573, 2020.

[176] J. Michael Gottfried. Surface chemistry of porphyrins and phthalocyanines. *Surface Science Reports*, 70(3):259–379, 2015.

[177] Willi Auwärter, David Écija, Florian Klappenberger, and Johannes V. Barth. Porphyrins at interfaces. *Nature Chemistry*, 7(2):105–120, 2015.

[178] Yuanqin He, Manuela Garnica, Felix Bischoff, Jacob Ducke, Marie Laure Bocquet, Matthias Batzill, Willi Auwärter, and Johannes V. Barth. Fus-

ing tetrapyrroles to graphene edges by surface-assisted covalent coupling. *Nature Chemistry*, 9(1):33–38, 2017.

[179] Feifei Xiang, Yanwei Gu, Amogh Kinikar, Nicolò Bassi, Andres Ortega-Guerrero, Zijie Qiu, Oliver Gröning, Pascal Ruffieux, Carlo Pignedoli, Klaus Müllen, and Roman Fasel. Zigzag Graphene Nanoribbons with Periodic Porphyrin Edge Extensions. *preprint*, pages 1–41, 2024.

[180] Luis M. Mateo, Qiang Sun, Shi Xia Liu, Jesse J. Bergkamp, Kristjan Eimre, Carlo A. Pignedoli, Pascal Ruffieux, Silvio Decurtins, Giovanni Bottari, Roman Fasel, and Tomas Torres. On-Surface Synthesis and Characterization of Triply Fused Porphyrin–Graphene Nanoribbon Hybrids. *Angewandte Chemie - International Edition*, 59(3):1334–1339, 2020.

[181] Xuelei Su, Zhijie Xue, Gang Li, and Ping Yu. Edge State Engineering of Graphene Nanoribbons. *Nano Letters*, 18(9):5744–5751, 2018.

[182] Jingcheng Li, Niklas Friedrich, Nestor Merino, DImas G. De Oteyza, DIego Peña, David Jacob, and Jose Ignacio Pascual. Electrically Addressing the Spin of a Magnetic Porphyrin through Covalently Connected Graphene Electrodes. *Nano Letters*, 19(5):3288–3294, 2019.

[183] Jingcheng Li, Nestor Merino Díez, E. C. Sanromà, Manuel Vilas-Varela, Dimas G. De Oteyza, Diego Peña, Martina Corso, and Jose Ignacio Pascual. Survival of spin state in magnetic porphyrins contacted by graphene nanoribbons. *Science Advances*, 4(2):1–6, 2018.

[184] Qiang Chen, Alessandro Lodi, Heng Zhang, Alex Gee, Hai I. Wang, Fanmiao Kong, Michael Clarke, Matthew Edmondson, Jack Hart, James N. O'Shea, Wojciech Stawski, Jonathan Baugh, Akimitsu Narita, Alex Saywell, Mischa Bonn, Klaus Müllen, Lapo Bogani, and Harry L. Anderson. Porphyrin-fused graphene nanoribbons. *Nature Chemistry*, 16(7):1133–1140, 2024.

[185] Andrew J. Pollard, Edward W. Perkins, Nicholas A. Smith, Alex Saywell, Gudrun Goretzki, Anna G. Phillips, Stephen P. Argent, Hermann Sachdev,

Frank Müller, Stefan Hüfner, Stefan Gsell, Martin Fischer, Matthias Schreck, Jürg Osterwalder, Thomas Greber, Simon Berner, Neil R. Champness, and Peter H. Beton. Supramolecular assemblies formed on an epitaxial graphene superstructure. *Angewandte Chemie - International Edition*, 49(10):1794–1799, 2010.

[186] Zhitao Deng, Nicha Thontasen, Nikola Malinowski, Gordon Rinke, Ludger Harnau, Stephan Rauschenbach, and Klaus Kern. A close look at proteins: Submolecular resolution of two- and three-dimensionally folded cytochrome c at surfaces. *Nano Letters*, 12(5):2452–2458, 2012.

[187] Stefania Moro, Nicholas Siemons, Oscar Drury, Daniel A. Warr, Thomas A. Moriarty, Luís M.A. Perdigão, Drew Pearce, Maximilian Moser, Rawad K. Hallani, Joseph Parker, Iain McCulloch, Jarvist M. Frost, Jenny Nelson, and Giovanni Costantini. The Effect of Glycol Side Chains on the Assembly and Microstructure of Conjugated Polymers. *ACS Nano*, 16(12):21303–21314, 2022.

[188] Daniel A. Warr, Luís M.A. Perdigão, Harry Pinfold, Jonathan Blohm, David Stringer, Anastasia Leventis, Hugo Bronstein, Alessandro Troisi, and Giovanni Costantini. Sequencing conjugated polymers by eye. *Science Advances*, 4(6):2–7, 2018.

[189] James F. Ponder, Hu Chen, Alexander M.T. Luci, Stefania Moro, Marco Turano, Archie L. Hobson, Graham S. Collier, Luís M.A. Perdigão, Maximilian Moser, Weimin Zhang, Giovanni Costantini, John R. Reynolds, and Iain McCulloch. Low-Defect, High Molecular Weight Indacenodithiophene (IDT) Polymers Via a C-H Activation: Evaluation of a Simpler and Greener Approach to Organic Electronic Materials. *ACS Materials Letters*, 3(10):1503–1512, 2021.

[190] Sebastian Scherb, Antoine Hinaut, Xuelin Yao, Alicia Götz, Samir H. Al-Hilfi, Xiao Ye Wang, Yunbin Hu, Zijie Qiu, Yiming Song, Klaus Müllen, Thilo Glatzel, Akimitsu Narita, and Ernst Meyer. Solution-Synthesized

Extended Graphene Nanoribbons Deposited by High-Vacuum Electrospray Deposition. *ACS Nano*, 17(1):597–605, 2023.

[191] Chris J. Judd, Filipe L.Q. Junqueira, Sarah L. Haddow, Neil R. Champness, David A. Duncan, Robert G. Jones, and Alex Saywell. Structural characterisation of molecular conformation and the incorporation of adatoms in an on-surface Ullmann-type reaction. *Communications Chemistry*, 3(1), 2020.

[192] Tien Lin Lee and David A. Duncan. A Two-Color Beamline for Electron Spectroscopies at Diamond Light Source. *Synchrotron Radiation News*, 31(4):16–22, 2018.

[193] C. J. Fisher, R. Ithin, R. G. Jones, G. J. Jackson, D. P. Woodruff, and B. C.C. Cowie. Non-dipole photoemission effects in x-ray standing wavefield determination of surface structure. *Journal of Physics Condensed Matter*, 10(35), 1998.

[194] V. I. Nefedov, V. G. Yarzhemsky, I. S. Nefedova, M. B. Trzhaskovskaya, and I. M. Band. The influence of non-dipolar transitions on the angular photoelectron distribution. *Journal of Electron Spectroscopy and Related Phenomena*, 107(2):123–130, 2001.

[195] S. Doniach and M. Sunjic. Many-electron singularity in X-ray photoemission and X-ray line spectra from metals. *Journal of Physics C: Solid State Physics*, 3(2):285–291, 1970.

[196] J. V. Barth, H. Brune, G. Ertl, and R. J. Behm. Scanning Tunneling Microscopy Observations on the Reconstructed Au(111) Surface. *Physical Review B*, 42(15):9307, 1990.

[197] Eleanor S. Frampton, Matthew Edmondson, Chris J. Judd, David A. Duncan, Robert G. Jones, and Alex Saywell. Self-metalation of tetraphenyl porphyrin on Au(111): Structural characterisation via X-ray standing wave analysis. *Inorganica Chimica Acta*, 558(August):121718, 2023.

[198] Alissa Wiengarten, Julian A. Lloyd, Knud Seufert, Joachim Reichert, Willi Auwärter, Runyuan Han, David A. Duncan, Francesco Allegretti, Sybille Fischer, Seung Cheol Oh, Özge Saglam, Li Jiang, Saranyan Vijayaraghavan, David Écija, Anthoula C. Papageorgiou, and Johannes V. Barth. Surface-Assisted Cyclodehydrogenation; Break the Symmetry, Enhance the Selectivity. *Chemistry - A European Journal*, 21(35):12285–12290, 2015.

[199] Jianchen Lu, Binbin Da, Wei Xiong, Renjun Du, Zhenliang Hao, Zilin Ruan, Yong Zhang, Shijie Sun, Lei Gao, and Jinming Cai. Identification and electronic characterization of four cyclodehydrogenation products of H2TPP molecules on Au(111). *Physical Chemistry Chemical Physics*, 23(20):11784–11788, 2021.

[200] Lieve G. Teugels, L. Gaby Avila-Bront, and S. J. Sibener. Chiral domains achieved by surface adsorption of achiral nickel tetraphenyl- or octaethylporphyrin on smooth and locally kinked Au(111). *Journal of Physical Chemistry C*, 115(6):2826–2834, 2011.

[201] Robby Büchner, Mattis Fondell, Robert Haverkamp, Annette Pietzsch, Vinícius Vaz da Cruz, and Alexander Föhlisch. The porphyrin center as a regulator for metal-ligand covalency and π hybridization in the entire molecule. *Physical Chemistry Chemical Physics*, 23(43):24765–24772, 2021.

[202] Norman Schmidt, Rainer Fink, and Wolfgang Hieringer. Assignment of near-edge x-ray absorption fine structure spectra of metalloporphyrins by means of time-dependent density-functional calculations. *Journal of Chemical Physics*, 133(5):1–14, 2010.

[203] K. Diller, F. Klappenberger, M. Marschall, K. Hermann, A. Nefedov, Ch Wöll, and J. V. Barth. Self-metalation of 2H-tetraphenylporphyrin on Cu(111): An x-ray spectroscopy study. *Journal of Chemical Physics*, 136(1), 2012.

[204] Iulia Cojocariu, Henning Maximilian Sturmeit, Giovanni Zamborlini, Albano Cossaro, Alberto Verdini, Luca Floreano, Enrico D'Incecco, Matus Stredansky, Erik Vesselli, Matteo Jugovac, Mirko Cinchetti, Vitaliy Feyer,

and Claus Michael Schneider. Evaluation of molecular orbital symmetry via oxygen-induced charge transfer quenching at a metal-organic interface. *Applied Surface Science*, 504(October 2019):144343, 2020.

[205] Giovanni Zamborlini, Matteo Jugovac, Albano Cossaro, Alberto Verdini, Luca Floreano, Daniel Lüftner, Peter Puschnig, Vitaliy Feyer, and Claus M. Schneider. On-surface nickel porphyrin mimics the reactive center of an enzyme cofactor. *Chemical Communications*, 54(95):13423–13426, 2018.

[206] Aleksandr Baklanov, Johannes T. Küchle, David A. Duncan, Paul T.P. Ryan, Reinhard J. Maurer, Martin Schwarz, Eduardo Corral Rascon, Ignacio Piquero-Zulaica, Huynh Thien Ngo, Alexander Riss, Francesco Allegretti, and Willi Auwärter. Zinc-Porphine on Coinage Metal Surfaces: Adsorption Configuration and Ligand-Induced Central Atom Displacement. *Journal of Physical Chemistry C*, 127(15):7501–7512, 2023.

[207] H. Marbach and H. P. Steinrücka. Studying the dynamic behaviour of porphyrins as prototype functional molecules by scanning tunnelling microscopy close to room temperature. *Chemical Communications*, 50(65):9034–9048, 2014.

[208] J V Barth. Transport of adsorbates at metal surfaces: from thermal migration to hot precursors. *Surface Science Reports*, 40(3):75–149, 2000.

[209] Ming Xi and Brian E. Bent. Mechanisms of the Ullmann Coupling Reaction in Adsorbed Monolayers. *Journal of the American Chemical Society*, 115(16):7426–7433, 1993.

[210] Jong Liang Lin and Brian E. Bent. Carbon-halogen bond dissociation on copper surfaces: Effect of alkyl chain length. *Journal of Physical Chemistry*, 96(21):8529–8538, 1992.

[211] Marco Di Giovannantonio, Massimo Tomellini, Josh Lipton-Duffin, Gianluca Galeotti, Maryam Ebrahimi, Albano Cossaro, Alberto Verdini, Neerav Kharche, Vincent Meunier, Guillaume Vasseur, Yannick Fagot-Revurat, Dmitrii F. Perepichka, Federico Rosei, and Giorgio Contini. Mechanistic

Picture and Kinetic Analysis of Surface-Confined Ullmann Polymerization. *Journal of the American Chemical Society*, 138(51):16696–16702, 2016.

[212] Luis Cardenas, Rico Gutzler, Josh Lipton-Duffin, Chaoying Fu, Jaclyn L. Brusso, Laurentiu E. Dinca, Martin Vondráček, Yannick Fagot-Revurat, Daniel Malterre, Federico Rosei, and Dmitrii F. Perepichka. Synthesis and electronic structure of a two dimensional π-conjugated polythiophene. *Chemical Science*, 4(8):3263–3268, 2013.

[213] Yu Jui Wu, Wei Hua Wang, and Chao Ming Chiang. Identification of surface allenyl and its transformation into propargyl with C3H3Br adsorption by rairs on Ag(111). *Langmuir*, 18(5):1449–1452, 2002.

[214] Gianluca Galeotti, Marco Di Giovannantonio, Josh Lipton-Duffin, Maryam Ebrahimi, Stefano Tebi, Alberto Verdini, Luca Floreano, Yannick Fagot-Revurat, Dmitrii F. Perepichka, Federico Rosei, and Giorgio Contini. The role of halogens in on-surface Ullmann polymerization. *Faraday Discussions*, 204:453–469, 2017.

[215] Alexei Preobrajenski, Alexander Generalov, Gunnar Öhrwall, Maxim Tchaplyguine, Hamed Tarawneh, Stephan Appelfeller, Eleanor Frampton, and Noelle Walsh. FlexPES: a versatile soft X-ray beamline at MAX IV Laboratory. *Journal of Synchrotron Radiation*, 30:831–840, 2023.

[216] Borja Cirera, Bruno De La Torre, Daniel Moreno, Martin Ondráček, Radek Zbořil, Rodolfo Miranda, Pavel Jelínek, and David Écija. On-Surface Synthesis of Gold Porphyrin Derivatives via a Cascade of Chemical Interactions: Planarization, Self-Metalation, and Intermolecular Coupling. *Chemistry of Materials*, 31(9):3248–3256, 2019.

[217] Felix Bischoff, Alexander Riss, Georg S. Michelitsch, Jacob Ducke, Johannes V. Barth, Karsten Reuter, and Willi Auwärter. Surface-Mediated Ring-Opening and Porphyrin Deconstruction via Conformational Distortion. *Journal of the American Chemical Society*, 143(37):15131–15138, 2021.

[218] C. Bürker, A. Franco-Cañellas, K. Broch, T. L. Lee, A. Gerlach, and F. Schreiber. Self-metalation of 2H-tetraphenylporphyrin on Cu(111) stud-

ied with XSW: Influence of the central metal atom on the adsorption distance. *Journal of Physical Chemistry C*, 118(25):13659–13666, 2014.

[219] Michael Röckert, Stefanie Ditze, Michael Stark, Jie Xiao, Hans Peter Steinrück, Hubertus Marbach, and Ole Lytken. Abrupt coverage-induced enhancement of the self-metalation of tetraphenylporphyrin with Cu(111). *Journal of Physical Chemistry C*, 118(3):1661–1667, 2014.

[220] Roger Kadish, Karl and Smith, Kevin M and Guilard. *The Porphyrin Handbook: Chlorophylls and Bilins: Biosynthesis, Synthesis and Degradation*. Elsevier, 2012.

[221] S. P. Jarvis, S. Taylor, J. D. Baran, D. Thompson, A. Saywell, B. Mangham, N. R. Champness, J. A. Larsson, and P. Moriarty. Physisorption Controls the Conformation and Density of States of an Adsorbed Porphyrin. *Journal of Physical Chemistry C*, 119(50):27982–27994, 2015.

[222] Catherine M. Doyle, Sergey A. Krasnikov, Natalia N. Sergeeva, Alexei B. Preobrajenski, Nikolay A. Vinogradov, Yulia N. Sergeeva, Mathias O. Senge, and Attilio A. Cafolla. Evidence for the formation of an intermediate complex in the direct metalation of tetra(4-bromophenyl)-porphyrin on the Cu(111) surface. *Chemical Communications*, 47(44):12134–12136, 2011.

[223] Edmondson. *Characterising on-surface processes with spatial and temporal resolution: Porphyrins and Phthalocyanines*. PhD thesis, University of Nottingham, 2023.

[224] Geoffrey Rojas, Xumin Chen, Cameron Bravo, Ji Hyun Kim, Jae Sung Kim, Jie Xiao, Peter A. Dowben, Yi Gao, Xiao Cheng Zeng, Wonyoung Choe, and Axel Enders. Self-assembly and properties of nonmetalated tetraphenyl-porphyrin on metal substrates. *Journal of Physical Chemistry C*, 114(20):9408–9415, 2010.

[225] Johannes Mielke, Felix Hanke, Maike V. Peters, Stefan Hecht, Mats Persson, and Leonhard Grill. Adatoms underneath single porphyrin molecules on Au(111). *Journal of the American Chemical Society*, 137(5):1844–1849, 2015.

[226] P. T.P. Ryan, P. L. Lalaguna, F. Haag, P. L. Lalaguna, P. Ding, M. M. Braim, J. V. Barth, T. L. Lee, D. P. Woodruff, F. Allegretti, and D. A. Duncan. Validation of the inverted adsorption structure for free-base tetraphenyl porphyrin on Cu(111). *Chemical Communications*, 56(25):3681–3684, 2020.

[227] Michael Lepper, Julia Köbl, Tobias Schmitt, Martin Gurrath, Abner De Siervo, M. Alexander Schneider, Hans Peter Steinrück, Bernd Meyer, Hubertus Marbach, and Wolfgang Hieringer. "inverted" porphyrins: A distorted adsorption geometry of free-base porphyrins on Cu(111). *Chemical Communications*, 53(58):8207–8210, 2017.

[228] Matthias Lischka, Massimo Fritton, Johanna Eichhorn, Vijay S. Vyas, Thomas Strunskus, Bettina V. Lotsch, Jonas Björk, Wolfgang M. Heckl, and Markus Lackinger. On-Surface Polymerization of 1,6-Dibromo-3,8-diiodpyrene - A Comparative Study on Au(111) Versus Ag(111) by STM, XPS, and NEXAFS. *Journal of Physical Chemistry C*, 122(11):5967–5977, 2018.

[229] Marco Nardi, Roberto Verucchi, Claudio Corradi, Marco Pola, Maurizio Casarin, Andrea Vittadini, and Salvatore Iannotta. Tetraphenylporphyrin electronic properties: A combined theoretical and experimental study of thin films deposited by SuMBD. *Physical Chemistry Chemical Physics*, 12(4):871–880, 2010.

[230] K. Diller, F. Klappenberger, F. Allegretti, A. C. Papageorgiou, S. Fischer, A. Wiengarten, S. Joshi, K. Seufert, D. Écija, W. Auwärter, and J. V. Barth. Investigating the molecule-substrate interaction of prototypic tetrapyrrole compounds: Adsorption and self-metalation of porphine on Cu(111). *Journal of Chemical Physics*, 138(15):0–9, 2013.

[231] Markus Lackinger. Possibilities and Limitations of Kinetic Studies in On-Surface Synthesis by Real Time X-ray Photoelectron Spectroscopy. *ChemPhysChem*, 202400156:1–7, 2024.

[232] Jannis Jung and Doreen Mollenhauer. Theoretical Studies of the Mechanism of Ullmann Coupling of Naphthyl Halogen Derivatives to Binaphtyl on Coinage Metals. *Journal of Physical Chemistry C*, 127(41):20284–20300, 2023.

[233] Florian Buchner, Jie Xiao, Elisabeth Zillner, Min Chen, Michael Röckert, Stefanie Ditze, Michael Stark, Hans Peter Steinrück, J. Michael Gottfried, and Hubertus Marbach. Diffusion, rotation, and surface chemical bond of individual 2 H-tetraphenylporphyrin molecules on Cu(111). *Journal of Physical Chemistry C*, 115(49):24172–24177, 2011.